UiO : University of Oslo

Solveig Næss

Biophysical modeling of electric and magnetic brain signals

Thesis submitted for the degree of Philosophiae Doctor

Department of Informatics
Faculty of Mathematics and Natural Sciences

2021

Acknowledgements

This work was conducted at the Centre for Integrative Neuroplasticity (CINPLA) and the Department of Informatics at the University of Oslo, Simula Research Laboratory, and the University of California, San Diego, through the SUURPh programme.

First of all, I would like to thank my inspiring supervisors Gaute, Torbjørn and Marianne. Thanks for exciting projects, availability, support, and steady guidance.

Thanks to the organizers of the SUURPh programme and my fellow SUURPhers for fantastic support, and to Anders for an exciting research stay in San Diego.

Thanks to all the members of CINPLA. In particular, thanks to my awesome office-mates: Marte Julie and Elise. A special thanks to Marte Julie, Eirik and Marie for invaluable backing in the final weeks of writing. Finally, thanks so much to family and friends for all support along the way!

Solveig Næss
Oslo, July 2021

Abstract

When we think and feel, the nerve cells (neurons) in the brain communicate by means of electric messages. We can listen to these neural conversations by recording resulting electric and magnetic signals on the outside of the head. The electric signals can be measured with small electrodes placed on the scalp, a method known as electroencephalography (EEG), while magnetic fields can be recorded with magnetoencephalography (MEG). Even though EEG and MEG are widely used techniques for studying cognition and disease in the human brain, we know surprisingly little about the neural origin of these signals.

We can get an overview of the electrical activity in the neural symphony by studying the current dipole moment capturing the melody of the network. To illustrate: if you know which tune is played on stage, you will have a good idea of what one can hear from the outside of the concert hall. Correspondingly, the current dipole moment can be applied for modeling EEG and MEG signals measured outside of the head. Furthermore, it is possible to simulate neural activity with detailed neuron models reconstructed from experimental data. However, the possibility to predict non-invasive brain recordings by calculating the current dipole moment from detailed neural activity has not yet been taken full advantage of.

This thesis presents a forward modeling framework for computing EEG and MEG signals, with methods firmly grounded in the underlying biophysics. Specifically, In Paper I, we present analytical formulas and available python code for computing electric brain signals from a current dipole moment in a simplified head consisting of four concentric spheres. In Paper II, we expand the open-source python-package LFPy, allowing for current dipole calculations from morphologically reconstructed neurons and neural populations. LFPy 2.0 includes methods for computing electric potentials on top of the brain (electrocorticography), as well as EEG and MEG signals. In Paper III, we apply methods from Paper I and II to compute the current dipole moment and the resulting electric brain signals from biophysically detailed single cells and existing neural simulations. We demonstrate how the presented modeling framework opens the door for exploring the neural origin of electric and magnetic brain signals.

List of Papers

Paper 1

Næss, S.[†], Chintaluri, C.[†], Ness, T.V., Dale, A.M., Einevoll, G.T., and Wójcik, D.K. 'Corrected four-sphere head model for EEG signals'. In: *Frontiers in Human Neuroscience* vol. 11, (2017), 00490. DOI: 10.3389/fnhum.2017.00490.

Paper 2

Hagen, E.[†], Næss, S.[†], Ness, T.V. and Einevoll, G.T. 'Multimodal modeling of neural network activity: computing LFP, ECoG, EEG, and MEG signals with LFPy 2.0'. In: *Frontiers in Neuroinformatics* vol. 12, (2018), 00092. DOI: 10.3389/fninf.2018.00092.

Paper 3

Næss, S., Halnes, G., Hagen, E., Hagler Jr., D.J., Dale, A.M., Einevoll, G.T., and Ness, T.V. 'Biophysically detailed forward modeling of the neural origin of EEG and MEG signals'. In: *NeuroImage* vol. 225, (2021), 117467. DOI: 10.1016/j.neuroimage.2020.117467

[†]These authors have contributed equally to this work.

Contents

Chapter 1

Introduction

1.1 What is this thesis about?

If there were a window in the back of the head so that we could see through hair, skin, scalp, and some membranes, we would stare in at the jelly-like, wrinkled, walnut-shaped brain. The outermost, folded part of the brain is known as the neocortex and is home to billions of nerve cells, named *neurons* [1]. The main feature of neurons is that they are brilliant at communicating. When we think and feel, the neurons are talking, exchanging information in highly complex networks.

In order to hear what the other cells in the network are saying, a large part of the neuron body consists of branch-like input structures named dendrites. The dendrites harbor thousands of connections, called synapses, receiving messages from other cells. When a synaptic input arrives, signals are forwarded from the dendrites down to the headquarters, called the soma. The soma will then decide whether to pass the information on to tens of thousands of other cells through the output cable called the axon (see Figure 1.1). This information is encoded by means of electric signals [2–4].

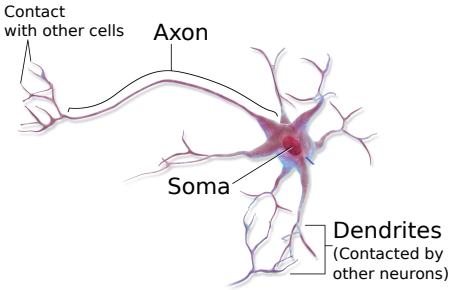

Fig 1.1. Illustration of neuron morphology. A neuron receives input from other cells through the synapses on the dendrites, and electric signals are forwarded to the soma. If the membrane potential in the soma reaches a threshold value, an action potential will travel down the axon and submit an electric signal to the other neurons in the network. The figure is adapted from The Blausen Gallery, 2014 [5], and was published earlier in Næss, 2015 [6].

The reason why neurons have anything to do with electricity is that the brain and all the nerve cells are soaked in a soup called cerebrospinal fluid. If we could zoom in on the cerebrospinal fluid, we would see ions such as sodium, potassium, and chloride. Ions are charged particles, and typically there is more positive charge on the outside of the cell than on the inside. The membrane is effectively

a capacitor charged by ions, similar to the membrane setting up the voltage in a battery. The voltage drop over the cell membrane is known as the *membrane potential* and is quite constantly ~ −70 mV when the neuron is resting. When a neuron receives synaptic input from other cells, however, small *ion channels* in the membrane are unlocked. Ions will move through the ion channels, and alter the membrane potential, also giving rise to capacitive currents. Ionic and capacitive currents are collectively called *transmembrane currents*. The neuron is an electrically connected whole: a dendritic transmembrane current will lead to axial currents inside the neuron and potentially affect the membrane potential in the entire cell, including the soma. If the somatic membrane potential reaches a certain threshold, an army of ion channels opens, and an action potential is generated. The action potential is a sharp membrane deflection that will travel all the way down the axon, activating the thousands of synapses on the connected cells.

From physics, we know that currents set up electric and magnetic fields. This means that neural activity in the brain generates electric and magnetic signals that can be measured in the clinic. The magnetic signals can be detected with magnetoencephalography (MEG), while electroencephalogram (EEG), electrodes on top of the scalp, and electrocorticography (ECoG), electrodes on top of the brain, can record the resulting electric potential (see Figure 1.2). It is even possible to measure electric potentials by inserting electrodes into the brain. These intracranial recordings are typically split into the low-frequency part of the signal, known as *local field potentials* (LFP), and the high-frequency part, *multi-unit activity* (MUA) [7–12]. While MUA is used to study *spikes* [13, 14] (the extracellular signature of action potentials), the LFPs are thought to reflect the slower synaptic currents [10, 15, 16]. This thesis focuses on EEG signals, but we will also touch in on the other measurement modalities.

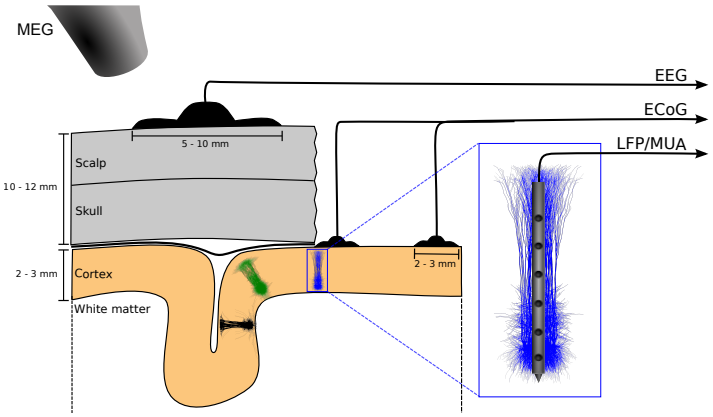

Fig 1.2. Recording techniques for electric and magnetic brain signals. Illustration of MUA/LFP, ECoG, EEG and MEG recordings, measuring electric and magnetic signals generated by neural populations in neocortex. Figure courtesy of Torbjørn V. Ness.

Since neurons speak the language of electricity, they can be modeled using electric circuits [9, 17]. This means that we can use well-known laws of physics to describe the neural conversations with mathematics! Implementing the right equations (most often on a computer), we can simulate neural activity through mathematical modeling.

Going from neural activity to measurable brain signals is an example of *forward modeling*, predicting measurements from underlying neural activity, as opposed to *inverse modeling*, where the goal is to approximate neural activity from measurements. The standard forward modeling scheme for predicting potentials in neural tissue involves (i) computing the transmembrane currents from a neural simulation, and (ii) plugging these into an equation giving the resulting electric potential. For predictions of potentials in the vicinity of the modeled neuron(s), we assume that the tissue is infinitely large and that the electric conductivity of tissue is independent of location and direction. However, when modeling EEG signals, the distance from neuron to electrode is increased, and we need to take into account that current flow is medium-dependent. For example, the current flows more easily through the high-conductivity cerebrospinal fluid than through the more resistant skull. In addition, the shapes of the different geometries of the head will affect the potential on the scalp. The geometries and conductivities of the different parts of the head can be incorporated into EEG modeling by applying a *head model*. The input to such head models is typically not the transmembrane currents readily available from neuron simulations, but rather a position-weighted sum of the transmembrane currents, known as the *current dipole moment*.

The focus of this thesis is to model the link between EEG and MEG signals and the underlying neural activity, by computing the current dipole moment from biophysically detailed neural simulations.

1.2 Motivation

Most of what we know about how the brain works comes from animal studies, where recording electrodes are implanted in brain tissue. For obvious ethical reasons, intracranial recordings on humans are restricted to special clinical cases, including small brain tumors and drug-resistant epilepsy. Even though we can learn a lot from animal studies, we will eventually need to study humans to understand the human brain [16]. Since no surgery is required for EEG and MEG recordings, these techniques are obvious candidates for studying human brain activity.

Brain-generated electric signals are relatively easy to measure. Already in 1875, Richard Caton recorded electric signals from the top of animal brains [18]. The first human EEG was recorded about 50 years later by Hans Berger [19]. Since then, EEG has been used for diagnosing brain diseases such as epilepsy, brain tumors, and dementia, and it has also been an important tool in psychology. Despite the widespread use of EEG, it is clear that we know very little about the origin of these electric signals. As Michael X. Cohen spells out in “Where does

EEG come from and what does it mean?", we know "shockingly little about the answer to this question" [20].

When analyzing EEG signals, it is common to either compare the recordings to other brain activity measures or to look for correlations between signals and presented stimulus. In the past decades, however, we have realized that measurement physics must play a more prominent role in neuroscience [21].

In general, physics-type modeling of measurable brain signals is crucial for bridging scales in neuroscience: from nanoscale molecular dynamics in single ion channels to the meter-long axonal cables. To understand the biophysical origin of measurements, we need to develop mathematical models of the biological systems we measure from [12, 14]. In addition to revealing insights about the origin of clinical recordings, modeling what we can measure can make it possible to compare simulations with clinical data. This is important for obtaining a better understanding of model limitations and improving the models.

Specifically, setting up a framework for modeling EEG and MEG signals from biophysically detailed neural activity is important for understanding where these signals come from [22], answering the first part of Cohen's question [20]. Furthermore, one can test different hypotheses in a virtual laboratory by applying the framework to various types of neural simulations, to shed light on part two of the question: "What does it mean?".

In short, modeling EEG and MEG signals from detailed neural simulations is essential for understanding the human brain and helping improve methods for diagnosing human brain diseases.

1.3 My contribution

The first person to model the source of EEG as a current dipole moment was M. A. B. Brazier in 1949 [23, 24]. She computed scalp potentials with a model known as the *current dipole approximation*. Both approximating the head as an infinite homogeneous space and a homogeneous sphere, she looked into how the shape and conductivity of the head model affected the EEG signal. Her work is followed by many others representing different parts of the head by adding more concentric, spherical shells with various conductivity to the head model [1, 25–33].

In the past decades, advanced imaging techniques have opened for replacing the spherical head models with realistic head reconstructions. By plugging the current dipole into a realistic head model, EEG signals can be computed with numerical methods such as the boundary element method [34, 35] or the finite element method [36].

Until recently, EEG forward models have mainly been applied for solving the inverse problem, focusing on finding the dipole strength, location, and orientation that can explain the recordings. Even though this work is very important for finding, for example, where epileptic seizures originate in the brain, there is still unexploited potential in EEG forward modeling. If we replace more or less

arbitrary dipoles with dipoles computed from detailed neuron simulations, we can link EEG recordings with the neural activity generating these signals.

The starting point for today's advanced simulations of neural activity was laid by Professor William Thomson (also known as Lord Kelvin) when developing the cable theory for the (transatlantic) telegraph cable in 1855 [9]. In the early 1900s, neuroscientists started looking at neurons as pieces of electric cable (see summary in [9]). Detailed passive membrane mechanisms, as described by Rall [37] and others, and active mechanisms, as modeled by Hodgkin, Huxley and Katz [17, 38] to name a few, were later incorporated in the simulations. Building on this, Rall used a forward modeling scheme based on transmembrane currents to calculate extracellular potentials from neuron models with simplified cell morphologies [39, 40]. In 1999, Holt and Koch computed spikes from reconstructed morphologies of pyramidal neurons [8]. Later, the forward modeling scheme was applied not only to look at spikes [41], but also LFP signals [13, 42]. At the same time, we have seen rapid development in large network simulations of morphologically detailed neuron models [43] and point neuron networks (approximating each neuron as a single point) [12, 44, 45]. Thanks to initiatives such as the Project MindScope at the Allen Institute for Brain Science, the Blue Brain Project, and the EU Human Brain Project, we now have access to a vast amount of detailed reconstructed neurons and network simulations [21]. These neuron models can be downloaded and used in neuron simulations by applying easily accessible neuron simulation tools such as NEURON [46] and GENESIS [47]. In other words, the road lies open for detailed simulations of neural activity.

Other studies have looked into current dipole calculations from detailed single-cell simulations [14, 22, 48] and from networks of neurons with simplified morphologies [49]. In this thesis, however, we predict EEG and MEG signals by computing the current dipole moment from neural simulations of both single cells and neural populations, based on morphologically reconstructed neuron models. The findings were published in three papers: Paper I and II outline an EEG/MEG modeling framework, and Paper III demonstrates how the framework can be applied for answering questions about the biophysical origin of EEG and MEG signals. The work has already been applied for linking the mechanisms of schizophrenia to EEG signals in the papers by Mäki-Marttunen et al., 2019 [50, 51][1] and summarized in our recent book chapter [52].

Research objectives

The overall goal of this work was to investigate the biophysical link between electrical activity in the brain and measurable electric and magnetic brain signals. Specifically, we aim to meet the following research objectives: Paper I) provide an available version of the four-sphere head model; Paper II) upgrade the open-source python-package LFPy, enabling ECoG, EEG and MEG calculations from biophysically detailed neural network simulations; Paper III) investigate the applicability of the current dipole approximation for ECoG and EEG calculations,

[1] I made contributions to these papers, but they are not included in my thesis.

and explore contributions from neural activity to EEG and MEG signals by using the frameworks provided in Paper I and II.

Chapter 2

Theoretical background

This chapter lays the physics foundation for the theory presented in Paper I-III. Here, I explain the two-step modeling scheme for electric potentials in the brain: (i) how to calculate transmembrane currents from multicompartmental modeling, and (ii) how to model electric potentials with volume conductor theory. I dedicate a section to the current dipole approximation, including the full derivation and a note on what we lose by choosing this approximate alternative, before introducing the concept of head models. Finally, I present basic magnetic field theory. If you are not interested in the physics details, you can jump to Chapter 3.

2.1 How to model transmembrane currents

The electric and magnetic signals playing the main parts in this thesis are generated by electric currents resulting from neural activity in the brain. These currents can be modeled with *multicompartmental modeling*, where we split the neuron morphology into multiple compartments. Each compartment must be so small that we can assume the electric potential to be the same within the whole compartment. Because the cell membrane has both resistive and capacitive properties, we represent each compartment by an electric RC-circuit. The circuit is driven by the voltage difference between the actual membrane potential and the resting potential (see Figure 2.1).

From Kirchhoff's current law, we know that the total current entering and leaving a compartment must be zero, as described by the cable equation [2, 4, 8, 9]:

$$g_{n,n+1}(V_{n+1} - V_n) - g_{n-1,n}(V_n - V_{n-1}) = C_n \frac{dV_n}{dt} + \sum_j I_n^j. \tag{2.1}$$

The axial conductance between compartment n and compartment $n+1$ is denoted by $g_{n,n+1}$, while V_n is the membrane potential and C_n is the membrane capacitance of compartment n. The cable equation says that the axial current from neighboring compartments (left-hand side) must equal the total current entering and escaping through the membrane, that is the transmembrane current (right-hand side). The total transmembrane current I_n in compartment n includes both the capacitive current (first term on right-hand side) and the sum of ionic currents I_n^j crossing the membrane through j types of ion channels [2, 15]:

$$I_n = C_n \frac{dV_n}{dt} + \sum_j I_n^j. \tag{2.2}$$

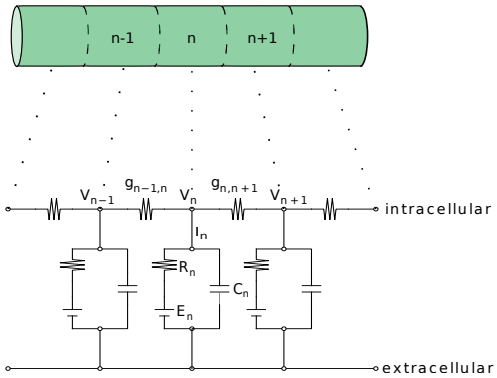

Fig 2.1. Illustration of multicompartmental modeling. A dendritic stick is split up into compartments. The compartment size must be so small that we can assume the whole compartment to have the same membrane potential. Each compartment is represented by an electric RC-circuit, with membrane potential V_n, membrane resistance R_n, membrane capacitance C_n and resting potential E_n. The axial, intracellular conductance between compartments is denoted $g_{n,n+1}$. First published in Næss, 2015 [6].

The next equation shows how we can calculate the current dipole moment $\mathbf{p}$ as a weighted sum of the transmembrane currents:

$$\mathbf{p} = \sum_n I_n \mathbf{r}_n, \tag{2.3}$$

where $\mathbf{r}_n$ is the position of transmembrane current I_n. Note that the current dipole moment alternatively can be calculated from axial currents:

$$\mathbf{p} = \sum_n I_n^a \mathbf{d}_n, \tag{2.4}$$

where each axial current I_n^a has traveled a distance $\mathbf{d}_n$. The current dipole moment is key to EEG and MEG modeling, and we'll get better acquainted with this guy in Section 2.2.3.

2.2 Volume conductor theory

The reason for starting this theory chapter with currents, and not zooming all the way into ions, is that EEG is a macroscopic measure: It is neither possible to know the exact location of all charges in the brain, nor is it necessary, since Debye shielding and electroneutrality of tissue make sure that single charge contributions to measured electric potentials are negligible [1, 53]. This means that we can safely use currents as our starting point for volume conductor theory.

Additionally, volume conductor theory relies on a second coarse-graining assumption. Neural tissue is densely packed with neurons, and extracellular space makes up only ~ 20% of tissue [54]. Extracellular currents will typically travel both extracellularly and intracellularly [55], and modeling the exact current pathways would require knowledge of the tissue microstructure. On a macroscopic scale of ~ tens of micrometers, we can instead average over reference volumes large enough to contain both extracellular space and several neurites [56]. In other words, we assume that the current sees the tissue as a smooth volume conductor with constant conductivity [1, 57].

Note that in the Papers 1-3, we used the terms "extracellular space" and "extracellular conductivity", while "tissue outside of the modeled neurons" and "tissue conductivity" would have been more precise.

In this section, I first derive the Poisson equation for volume conductors, before giving the solution for the electric potential in an infinite, homogeneous conductor.

2.2.1 From Maxwell to Poisson

In order to describe electromagnetic signals on the macroscopic scale, we start out with the macroscopic version of Maxwell's equations [56]:

$$\nabla \cdot \mathbf{D} = \rho, \tag{2.5}$$

$$\nabla \times \mathbf{E} = -\frac{\partial \mathbf{B}}{\partial t}, \tag{2.6}$$

$$\nabla \cdot \mathbf{B} = 0, \tag{2.7}$$

$$\nabla \times \mathbf{H} = \mathbf{i} + \frac{\partial \mathbf{D}}{\partial t}. \tag{2.8}$$

Here, $\mathbf{D}$ (C/m^2) is the displacement field set up by the unbound charge density ρ (C/m^3), $\mathbf{E}$ (V/m) is the electric field, $\mathbf{B}$ (T) is the magnetic field and $\mathbf{H}$ (A/m) is the magnetizing field induced by the unbound current density $\mathbf{i}$ (A/m^2).

The conductive medium in the brain is linear in both the magnetic and electric sense [1]. This means that the magnetization of the medium is proportional to the magnetic field, that is $\mathbf{B} = \mu\mathbf{H}$, and polarization of the medium is proportional to the electric field: $\mathbf{D} = \epsilon\mathbf{E}$. Consequently, we can go on with the macroscopic formulation of Maxwell's equations for linear media [58]:

$$\nabla \cdot \mathbf{E} = \frac{\rho}{\epsilon}, \tag{2.9}$$

$$\nabla \times \mathbf{E} = -\frac{\partial \mathbf{B}}{\partial t}, \tag{2.10}$$

$$\nabla \cdot \mathbf{B} = 0, \tag{2.11}$$

$$\nabla \times \mathbf{B} = \mu\mathbf{i} + \mu\epsilon\frac{\partial \mathbf{E}}{\partial t}. \tag{2.12}$$

Equation 2.9 is known as Gauss law and says that a net free charge density ρ will generate a diverging electric field. Further, Faraday's law (Equation 2.10) states that a rotation (curl) of the electric field will be induced by a temporal change in the magnetic field $\mathbf{B}$. In Gauss law for magnetism (2.11), equivalent to (2.9), the divergence of the magnetic field is 0, since magnetic monopoles do not exist. Finally, Ampère's circuit law (2.12) describes how a current density of free charges $\mathbf{i}$ and a temporal change in the electric field will both induce a magnetic field.

Taking the divergence of both sides of Equation 2.12, we arrive at the following expression, since $\nabla \cdot \nabla \times \mathbf{B}$ is zero:

$$\nabla \cdot (\mathbf{i} + \epsilon \frac{\partial \mathbf{E}}{\partial t}) = 0. \tag{2.13}$$

The second term on the left-hand side of Equation 2.13 is known as the displacement current, and is due to capacitive effects in the medium. Consequently, we see $\mathbf{i} + \epsilon \frac{\partial \mathbf{E}}{\partial t} = \mathbf{i}_{\text{tot}}$ as the total current of unbound and bound charges. Equation 2.13 is, therefore, equivalent to the current continuity equation, ensuring that the net flux of total current in a single point is zero:

$$\nabla \cdot \mathbf{i}_{\text{tot}} = 0. \tag{2.14}$$

In volume conductor theory, it is common to split the total current (density) into two parts: the primary current $\mathbf{i}_{\text{s}}$ and the resulting tissue current $\mathbf{i}_{\text{t}}$ [59],

$$\mathbf{i}_{\text{tot}} = \mathbf{i}_{\text{s}} + \mathbf{i}_{\text{t}}. \tag{2.15}$$

As explained in Nunez & Srinivasan, 2006 [1] and Gratiy et al., 2017 [60], volume conductor theory is based on dividing the conductor into two subdomains: (i) the intracellular space plus the membrane of the neurons that we model, and (ii) the rest, which resembles the tissue in the infinite homogeneous case. The primary current is here a trick used to avoid dealing with boundary conditions on the surface of the cellular domain. In volume conductor theory, it is common to express the negative divergence of the primary current density in terms of the *current source density* C:

$$C = -\nabla \cdot \mathbf{i}_{\text{s}}, \tag{2.16}$$

where C is given in A/m^3. The current source density represents the electric current entering and escaping the tissue.

With all this in place, we obtain the continuity equation for volume conductor theory, by inserting Equations 2.15 and 2.16 into Equation 2.14:

$$\nabla \cdot \mathbf{i}_{\text{t}} = C. \tag{2.17}$$

Next, we assume that the tissue current is solely dependent on the current sources. This means that we do not consider volume currents due to bulk flow, since the interstitial fluid is incompressible [60]. Further, we rely on the assumption that concentration gradients are negligible in extracellular space, so that we do not

have to take diffusion currents into account [15, 61]. In the brain, it is also safe to assume that magnetic fields won't affect the tissue currents [1]. Moreover, fluctuations in the electric fields in the brain are relatively slow, meaning that the displacement current is also negligible (see Hämäläinen et al. 1993 [16]). These arguments support the well-known observation that the tissue current can be expressed by Ohms law:

$$\mathbf{i}_{\mathrm{t}} = \sigma \mathbf{E}. \tag{2.18}$$

Due to the low frequencies in brain activity, we can safely assume that $\partial \mathbf{B}/\partial t$ is negligible, and therefore apply the quasistatic version of Faraday's law (Equation 2.10):

$$\nabla \times \mathbf{E} = 0. \tag{2.19}$$

ensuring a conservative electric field.

We see from combining Stokes' theorem,

$$\iint_{\Omega} \nabla \times \mathbf{E} \cdot d\mathbf{a} = \oint_{\partial\Omega} \mathbf{E} \cdot d\mathbf{l}, \tag{2.20}$$

with Equation 2.19, that the circle integral along a closed loop in the (conservative) electric field $\mathbf{E}$ is zero,

$$\oint_{\partial\Omega} \mathbf{E} \cdot d\mathbf{l} = 0,$$

and we can define the electric potential as

$$\Phi(\mathbf{r}) = -\int_{O}^{\mathbf{r}} \mathbf{E} \cdot d\mathbf{l}. \tag{2.21}$$

Further, we can express the potential difference over a path from $\mathbf{a}$ to $\mathbf{b}$ in a conservative field $\mathbf{E}$ as

$$\Phi(\mathbf{b}) - \Phi(\mathbf{a}) = -\int_{\mathbf{a}}^{\mathbf{b}} \mathbf{E} \cdot d\mathbf{l}. \tag{2.22}$$

From the fundamental theorem, we know that

$$\Phi(\mathbf{b}) - \Phi(\mathbf{a}) = \int_{\mathbf{a}}^{\mathbf{b}} \nabla\Phi \cdot d\mathbf{l}. \tag{2.23}$$

Comparing 2.22 with 2.23, we see that the electric field can be expressed as the negative gradient of the electric potential:

$$\mathbf{E} = -\nabla\Phi, \tag{2.24}$$

when $\frac{\partial \mathbf{B}}{\partial t} \approx 0$. Finally, we can insert Ohm's law (2.18) into the continuity equation (2.17) and replace $\mathbf{E}$ with $-\nabla\Phi$, to obtain the Poisson equation for electric potentials:

$$\nabla \cdot \sigma \nabla \Phi = -C. \tag{2.25}$$

2.2.2 Electric potential in infinite homogeneous medium

In this section, we find a solution for the Poisson equation in an infinite, homogeneous medium. This means that we assume the head to be a volume conductor where the conductivity σ is a scalar independent of position. Consequently, we can write the Poisson equation on the following form:

$$\nabla^2\Phi = -\frac{C}{\sigma}. \tag{2.26}$$

First, we want to find the electric potential Φ from a current source I_1 at location $\mathbf{r}_1$ with current source density $C = i_1\delta(\mathbf{r}-\mathbf{r}_1)$. We start by integrating both sides of Equation 2.26 over a volume Ω containing the current source I_1:

$$\iiint_{\Omega} \nabla^2\Phi d\Omega = -\frac{1}{\sigma}\iiint_{\Omega} i_1\delta(\mathbf{r}-\mathbf{r}_1)d\Omega.$$

The integral on the right-hand side gives us the current source I_1. On the left-hand side, we apply the divergence theorem, such that:

$$\oiint_S \nabla\Phi(\mathbf{r})\cdot d\mathbf{S} = -\frac{I_1}{\sigma} \tag{2.27}$$

We choose our integration surface S to be a sphere with center $\mathbf{r}_1$ and radius $R = |\mathbf{r}-\mathbf{r}_1|$. Since the potential from a point source spatially only depends on the distance R from the source, $\Phi(\mathbf{r}) = \Phi(R)$, we can write the potential gradient as $\nabla\Phi(\mathbf{r}) = d\Phi(\mathbf{r})/dR\ \hat{\mathbf{R}}$. Here, $\hat{\mathbf{R}}$ is the unit vector orthogonal to the surface increment $d\mathbf{S} = dS\ \hat{\mathbf{R}}$, and our expression reduces to

$$\frac{d\Phi}{dR}\oiint_S dS = \frac{d\Phi}{dR}4\pi R^2 = -\frac{I_1}{\sigma}.$$

Next, we integrate $d\Phi = -I_1/(4\pi\sigma R^2)dR$ from ∞ to R, and obtain the expression

$$\Phi(R) = \frac{I_\mathrm{k}}{4\pi\sigma R}. \tag{2.28}$$

Substituting R with $|\mathbf{r}-\mathbf{r}_1|$, we arrive at:

$$\Phi(\mathbf{r}) = \frac{I_1}{4\pi\sigma|\mathbf{r}-\mathbf{r}_1|}. \tag{2.29}$$

Since the medium is linear, electric potentials sum linearly and the electric potential at location $\mathbf{r}$ from N current sources I_k positioned at $\mathbf{r}_\mathrm{k}$ can be expressed by the sum [14]:

$$\Phi(\mathbf{r}) = \sum_{\mathrm{k}=1}^{\mathrm{N}} \frac{I_\mathrm{k}}{4\pi\sigma|\mathbf{r}-\mathbf{r}_\mathrm{k}|}. \tag{2.30}$$

When modeling electric potentials in close vicinity of the neuron, Equation 2.30 is often a safe choice. When modeling EEG-signals, on the other hand, it can be useful to base the computations on the current dipole approximation, instead.

2.2.3 Current dipole approximation in homogeneous medium

This thesis revolves around the current dipole moment (Equation 2.3), and how the current dipole moment can be utilized for electric potential predictions through the current dipole approximation. I will therefore derive the current dipole approximation, emphasizing which constraints underlie the approximation, and what we lose by choosing the approximation over the exact solution given in Equation 2.30.

2.2.3.1 Derivation of the current multipole expansion

In order to derive the current dipole approximation for infinitely large volume conductors with constant conductivity, we must first derive the current multipole expansion. The current multipole expansion is an infinite series that can be used for approximating the electric potential from a set of currents, by calculating a finite set of terms. If you're not interested in the details of the derivation, you can jump to Equation 2.35. In Figure 2.2, we illustrate a volume containing N currents I_k at position $\mathbf{r}_k$. The center of the volume is $\mathbf{r}_c = \sum_{k=1}^{N} \frac{\mathbf{r}_k}{N}$. We are interested in the electric potential measured with a simulated point electrode located a distance $R = |\mathbf{R}| = |\mathbf{r}_c - \mathbf{r}|$ away from the current distribution.

Our goal is to derive an alternative to Equation. 2.30, by writing $\frac{1}{|\mathbf{r}-\mathbf{r}_k|} = \frac{1}{R_k}$ as an infinite series. The term R_k denotes the distance between current I_k at $\mathbf{r}_k$ and the electrode position $\mathbf{r}$. The first step is applying the cosine rule,

$$R_k^2 = R^2 + r_{ck}^2 - 2Rr_{ck}\cos\theta_k. \tag{2.31}$$

where $r_{ck} = |\mathbf{r}_{ck}|$ is the magnitude of the distance vector between the volume center $\mathbf{r}_c$ and current location $\mathbf{r}_k$, and θ_k is the angle between $\mathbf{r}_{ck}$ and $\mathbf{R}$ (see Figure 2.2). Next, we rearrange Equation 2.31 to obtain the following expression for R_k:

$$\begin{aligned} R_k^2 &= R^2\big[1 - \frac{r_{ck}}{R}2\cos\theta_k + \big(\frac{r_{ck}}{R}\big)^2\big], \\ \implies R_k &= R\sqrt{1 - 2h\cos\theta_k + h^2} \quad \forall h = \frac{r_{ck}}{R}. \end{aligned}$$

This gives us:

$$\frac{1}{|\mathbf{r} - \mathbf{r}_k|} = \frac{1}{R_k} = \frac{1}{R\sqrt{1 - 2h\cos\theta_k + h^2}}.$$

Here, we notice that $\frac{1}{\sqrt{1-2h\cos\theta_k+h^2}}$ is the generating function for the Legendre polynomials, meaning that

$$\frac{1}{\sqrt{1 - 2h\cos\theta_k + h^2}} = \sum_{l=0}^{\infty} h^l P_l(\cos\theta_k) \qquad \forall \quad |h| = |\frac{r_{ck}}{R}| < 1. \tag{2.32}$$

We can now express $\frac{1}{|\mathbf{r}-\mathbf{r}_k|}$ as an infinite series:

$$\frac{1}{|\mathbf{r} - \mathbf{r}_k|} = \frac{1}{R}\sum_{l=0}^{\infty}\big(\frac{r_{ck}}{R}\big)^l P_l(\cos\theta_k) \qquad \forall \quad R > r_{ck}. \tag{2.33}$$

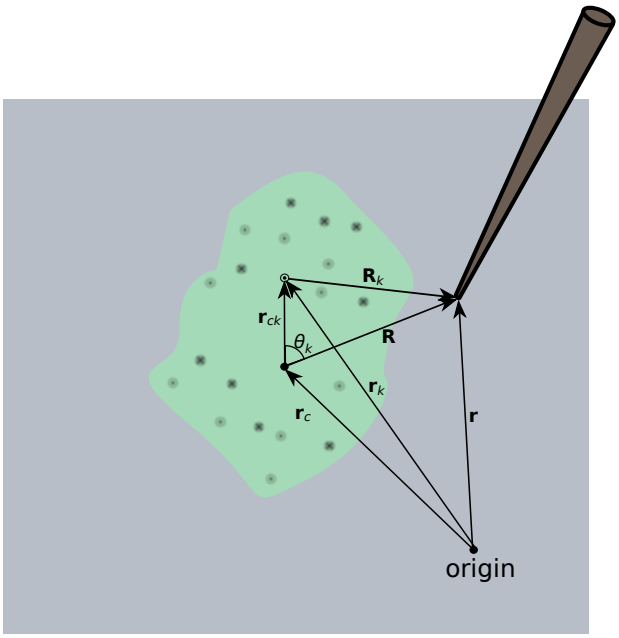

Fig 2.2. Electric potential from volume of current sinks and sources. A volume of point current sinks and sources generates an electric potential measured with the electrode in $\mathbf{r}$, a distance $\mathbf{R}$ away from the center of the volume located at $\mathbf{r}_c$. Current source k has the location $\mathbf{r}_k$, a distance $\mathbf{r}_{ck}$ away from the volume center. The distance vector from volume center to electrode is called $\mathbf{R}$, and the angle between $\mathbf{R}$ and $\mathbf{r}_{ck}$ is denoted by θ_k.

Here, P_l are the Legendre polynomials, such that:

$$\begin{aligned} P_0(\cos\theta_k) &= 1, \\ P_1(\cos\theta_k) &= \cos\theta_k, \\ P_2(\cos\theta_k) &= \frac{3}{2}\cos^2\theta_k - \frac{1}{2}, \\ P_3(\cos\theta_k) &= \frac{5}{2}\cos^3\theta_k - \frac{3}{2}\cos\theta_k, \\ &\vdots \end{aligned}$$

By inserting Equation 2.33 into Equation 2.30, we arrive at the current multipole expansion:

$$\Phi(R) = \frac{1}{4\pi\sigma}\frac{1}{R}\sum_{k=1}^{N} I_k \sum_{l=0}^{\infty}\left(\frac{r_{ck}}{R}\right)^l P_l(\cos\theta_k) \quad \forall\ R > r_{ck}. \tag{2.34}$$

Note that current multipole expansion 2.34 is equivalent to Equation 2.30 when the measurement point is further away from the volume center than any of the current sources. Writing out the first terms, we obtain:

$$\begin{aligned}\Phi(R) = \frac{1}{4\pi\sigma}\Bigg[&\frac{1}{R}\sum_{k=1}^{N} I_k \\ &+ \frac{1}{R^2}\sum_{k=1}^{N} I_k r_{ck}\cos\theta_k \\ &+ \frac{1}{R^3}\sum_{k=1}^{N} I_k r_{ck}^2\left(\frac{3}{2}\cos^2\theta_k - \frac{1}{2}\right) \\ &+ \frac{1}{R^4}\sum_{k=1}^{N} I_k r_{ck}^3\left(\frac{5}{2}\cos^3\theta_k - \frac{3}{2}\cos\theta_k\right) + \ldots\Bigg] \quad \forall R > r_{ck}.\end{aligned} \tag{2.35}$$

The first four terms of the current multipole expansion are known as the monopole Φ^{mono}, dipole Φ^{dipole}, quadrupole $\Phi^{\text{quadrupole}}$ and octupole Φ^{octupole} contributions, respectively [1]:

$$\Phi = \Phi^{\text{monopole}} + \Phi^{\text{dipole}} + \Phi^{\text{quadrupole}} + \Phi^{\text{octupole}} + \ldots \tag{2.36}$$

2.2.3.2 Derivation of the current dipole approximation

The electric potential from a set of current sinks and sources can be approximated by solely using the dipole contribution term of the multipole expansion. Note that nothing is lost by omitting the monopole contribution, since the sink and source currents for a whole number of neurons must sum to zero:

$$\Phi^{\text{monopole}} = \frac{1}{4\pi\sigma}\frac{1}{R}\sum_k I_k = 0.$$

We take a closer look at the dipole contribution term:

$$\Phi^{\text{dipole}} = \frac{1}{4\pi\sigma}\frac{1}{R^2}\sum_k I_k r_{ck}\cos\theta_k.$$

From the scalar product identity, we see that $r_{ck}\cos\theta_k = \mathbf{r}_{ck}\cdot\hat{\mathbf{R}}$, where $\hat{\mathbf{R}} = \mathbf{R}/\mathrm{R}$, such that:

$$\begin{aligned}\Phi^{\text{dipole}} &= \frac{1}{4\pi\sigma}\frac{1}{R^2}\sum_k I_k \mathbf{r}_{ck}\cdot\hat{\mathbf{R}} \\ &= \frac{1}{4\pi\sigma}\frac{1}{R^2}\sum_k I_k(\mathbf{r}_k - \mathbf{r}_c)\cdot\hat{\mathbf{R}} \\ &= \frac{1}{4\pi\sigma}\frac{1}{R^2}\left(\sum_k I_k \mathbf{r}_k\cdot\hat{\mathbf{R}} - \sum_k I_k \mathbf{r}_c\cdot\hat{\mathbf{R}}\right).\end{aligned}$$

Since $\sum_k I_k \mathbf{r}_k = \mathbf{p}$ and $\sum_k I_k = 0$, we obtain the current dipole approximation:

$$\Phi \approx \Phi^{\text{dipole}} = \frac{1}{4\pi\sigma} \frac{\mathbf{p} \cdot \hat{\mathbf{R}}}{\mathrm{R}^2} = \frac{1}{4\pi\sigma} \frac{\mathrm{p} \cos\theta}{R^2}, \tag{2.37}$$

where θ is the angle between $\mathbf{p}$ and $\mathbf{R}$. Remember that the multipole expansion is valid under the constraint $\mathrm{R} > r_{ck}$. Applying the current dipole approximation, however, we neglect the higher-order terms, and this calls for stricter constraints. We see from Equation 2.35 that the higher-order contributions decay faster with R, and it is commonly assumed that the current dipole approximation is good when $R >> r_{ck}$. In the next section we want to get a better intuition about when R is *large enough*, by looking at the quadrupole and octupole contributions ($\Phi^{\text{quadrupole}}$, Φ^{octupole}) from a current sink-source pair.

2.2.3.3 What do we lose by using the current dipole approximation?

We find the quadrupole contribution from a current sink I_1 at r_1 and a current source I_2 at r_2 from Equation 2.35:

$$\Phi^{\text{quadrupole}} = \frac{1}{4\pi\sigma} \frac{1}{R^3} \left[I_1 r_{c1}^2 \left(\frac{3}{2} \cos^2\theta_1 - \frac{1}{2} \right) + I_2 r_{c2}^2 \left(\frac{3}{2} \cos^2\theta_2 - \frac{1}{2} \right) \right]. \tag{2.38}$$

Here, we conveniently place the center of the volume $\mathbf{r}_\mathrm{c}$ halfway between the source I_1 and the sink $I_2 = -I_1$, such that $r_{c1} = r_{c2}$. This leads to $\theta_2 = \pi - \theta_1 \implies \cos\theta_2 = -\cos\theta_1$ and $\cos^2\theta_2 = \cos^2\theta_1$. The quadrupole contribution from a sink-source pair is therefore 0. Notice that Legendre polynomials with $l = 4, 6, 8, ...$ contain $\cos\theta_k$ raised to the power of an even number. Consequently, the multipole contribution term number 3, 5, 7, 9, etc is always zero for a sink-source pair.

Now, we go on to the octupole contribution from the sink-source pair I_1, I_2 at $\mathbf{r}_1$, $\mathbf{r}_2$, applying the fourth term of Equation 2.35:

$$\Phi^{\text{octupole}} = \frac{1}{4\pi\sigma} \frac{1}{R^4} \left[I r_{c1}^3 \left(\frac{5}{2} \cos^3\theta_1 - \frac{3}{2} \cos\theta_1 \right) - I r_{c2}^3 \left(\frac{5}{2} \cos^3\theta_2 - \frac{3}{2} \cos\theta_2 \right) \right].$$

We continue to choose $\mathbf{r}_c$ to be the midpoint between $\mathbf{r}_1$ and $\mathbf{r}_2$, such that $r_{c2} = r_{c1} = \frac{d}{2}$ (where d is the distance between $\mathbf{r}_1$ and $\mathbf{r}_2$), and $\cos\theta_2 = -\cos\theta_1$:

$$\begin{aligned}
\Phi^{\text{octupole}} &= \frac{1}{4\pi\sigma} \left[I \frac{d}{2}^3 \left(\frac{5}{2} \cos^3\theta_1 - \frac{3}{2} \cos\theta_1 \right) - I \frac{d}{2}^3 \left(\frac{5}{2} \cos^3\theta_1 - \frac{3}{2} \cos\theta_1 \right) \right] \\
&= \frac{1}{4\pi\sigma} \frac{I d^3}{R^4} \frac{\left(5\cos^3\theta_1 - 3\cos\theta_1 + 5\cos^3\theta_1 - 3\cos\theta_1 \right)}{16} \\
&= \frac{1}{4\pi\sigma} \frac{I d^3}{R^4} \frac{5\cos^3\theta_1 - 3\cos\theta_1}{8}.
\end{aligned}$$

Next, we rename $\theta_1 = \theta$, so that θ is the angle between $\mathbf{p}$ and $\mathbf{R}$. From Equation 2.4 we know that $p = Id$ and arrive at the following expression for the octupole contribution from a sink-source pair:

$$\Phi^{\text{octupole}} = \frac{1}{4\pi\sigma} \frac{p}{R^2} \frac{d^2}{R^2} \frac{5\cos^3\theta - 3\cos\theta}{8}.$$

Finally, we compare the octupole contribution to the dipole contribution when calculating the potential from a sink-source pair:

$$\left|\frac{\Phi^{\text{octupole}}}{\Phi^{\text{dipole}}}\right|_{\max} = \left|\frac{d^2}{R^2}\frac{5\cos^2\theta - 3}{8}\right|_{\max} = \frac{3}{8}\frac{d^2}{R^2}.$$

For a sink-source pair, the octupole contribution is the largest non-zero term that we neglect when applying the current dipole approximation, since the monopole and quadrupole contributions are zero. (See Plonsey and Barr, 2007 [62], page 36 for a similar reflection.)

Nunez and Srinivasan [1] suggest that it is reasonable to apply the current dipole approximation for distances $R > 3d$ or $R > 4d$. The maximal octupole contribution for a sink-source pair when measuring at a distance $R = 3d$ is $\Phi^{\text{octu}}(R = 3d) = \frac{1}{24}\Phi^{\text{dipole}}$, and $\Phi^{\text{octu}}(R = 4d) = \frac{3}{128}\Phi^{\text{dipole}}$ at a distance $R = 4d$. This means that neglecting the octupole contribution from a sink-source pair we lose a portion of the electric potential, that amounts to somewhere between $\sim 0.8\%$ and $\sim 4\%$ of the dipole contribution from a sink-source pair.

Even though we also neglect higher order terms (the 32-pole, the 128-pole, etc), keep in mind that these terms will decay even more rapidly with distance from the source ($1/R^6$, $1/R^8$, ...).

2.2.4 Head Models

EEG signals are affected by the shapes and conductivities of the different parts of the head. In order to include this when modeling EEG signals, we need to use an appropriate head model.

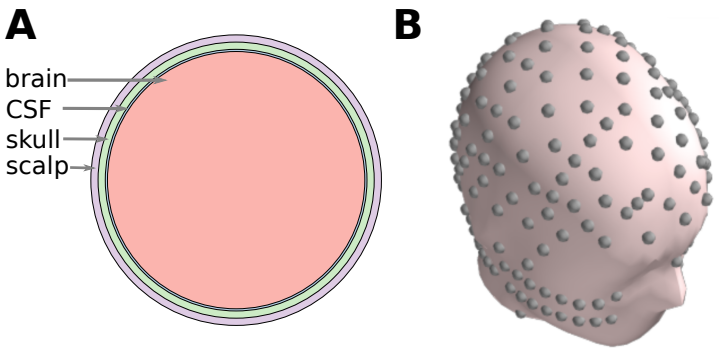

Fig 2.3. Head model illustrations. **A**: The four-sphere model consisting of four concentric shells: brain, CSF, skull and scalp, where the conductivity can be set individually for each shell [1]. **B**: Illustration of the detailed New York Head model, constructed from high-resolution, anatomical MRI-images from 152 heads [63].

A head model splits the head into subspaces, such that the conductivity can be set specifically for each subspace. This means that σ in Equation 2.26 takes

different values, depending on which subspace we are in. Further, the solution must obey the following boundary conditions: (i) current must be continuous on the boundaries, (ii) the potential must be continuous on the boundaries, and (iii) no current can escape the head.

For simple, symmetric head models, one can find an analytical solution for the Poisson equation. The four-sphere head model is an example of such a model, consisting of four concentric shells, representing brain, CSF, skull and scalp, where the conductivity can be set individually for each shell [1, 27, 28, 33] (See Figure 2.3 A). For more detailed head models based on MRI-data from human heads (for example, the New York Head model [63] illustrated in 2.3 B), there is no analytical solution, and this calls for numerical methods, such as the *finite element method* (FEM).

2.2.5 Finite element method solution of the Poisson equation

Here follows a brief introduction to the finite element method, which should be sufficient to understand the verification in Paper 1. For a more rigorous explanation, see Logg et al., 2012 [64] or Langtangen and Logg, 2017 [65].

In order to apply the finite element method, we first need to do some calculus to formulate our problem on the so-called *variational form*. We start out with the Poisson equation (2.26):

$$\nabla^2 \Phi = -\frac{C}{\sigma}. \tag{2.39}$$

Here, we denote the volume of the head model Ω with boundary $\partial\Omega$. Now, we multiply both sides of the Poisson equation with an arbitrary function v and integrate over the domain Ω:

$$\int_\Omega \nabla^2 \Phi \; v \; d\Omega = -\int_\Omega \frac{C}{\sigma} \; v \; d\Omega \tag{2.40}$$

Rewriting $\nabla^2 \Phi \; v = \nabla \cdot (\nabla \Phi \; v) - \nabla \Phi \cdot \nabla \; v$ and applying the divergence theorem, we end up with the expression

$$-\int_\Omega \nabla \Phi \cdot \nabla v \; d\Omega + \int_{\delta\Omega} (\nabla \Phi \; v) \cdot d\mathbf{S} = -\int_\Omega \frac{C}{\sigma} \; v \; d\Omega. \tag{2.41}$$

Since there is no current flow over the boundary, $\nabla \Phi = 0$ on $\partial\Omega$, which means that the boundary integral is zero, leaving us with with

$$\int_\Omega \nabla \Phi \cdot \nabla v \; d\Omega = \int_\Omega \frac{C}{\sigma} \; v \; d\Omega. \tag{2.42}$$

We can now write Equation 2.39 on the variational form:

$$a(\Phi, v) = L(v), \tag{2.43}$$

where

$$a(\Phi, v) = \int_\Omega \nabla \Phi \cdot \nabla \; v \; d\Omega, \tag{2.44}$$

and

$$L(v) = \int_{\Omega} \frac{C}{\sigma}\, v \; d\Omega. \tag{2.45}$$

We want to find a solution Φ such that Equation 2.43 is valid for all v. (It can be shown that Φ will then also be a solution of Equation 2.39, see for example Logg, 2012 [64].) The finite element method consists in defining a *finite dimensional function space* V_h and restricting Φ and v to be contained in this function space $\Phi, v \in V_h$. The good thing about operating in a finite dimensional function space, is that 2.43-2.45 is now a linear system of equations, that can be solved with regular linear algebra on a computer.

In order to obtain a finite dimensional function space V_h for approximating the solution, we divide the physical domain into subdomains, and define a set of basis functions on each subdomain (also called finite elements[1]). The basis functions must be continuous on each subdomain, and can for example be chosen to be second order polynomials. For a 3D problem like ours, each subdomain is typically chosen to be a tetrahedron. In other words, our head model would be discretized into a 3D grid (mesh) of tetrahedrons. The equation system can now be solved applying designated software such as FEniCS [66].

2.2.6 Magnetic fields in the brain

Currents in the brain do not only set up electric potentials, they also generate magnetic fields. This section outlines how we can compute the magnetic field from neural current sources, as described in Ilmoniemi and Sarvas, 2019 [67] and Hämäläinen et al., 1993 [16]. With the help of some calculus and the assumption that the current density goes to 0 at infinity, the Ampère-Laplace law for computing magnetic fields can be derived from Faraday's induction law [58]:

$$\mathbf{B}(\mathbf{r}) = \frac{\mu_0}{4\pi} \int \mathbf{i}(\mathbf{r}') \times \frac{\mathbf{r} - \mathbf{r}'}{|\mathbf{r} - \mathbf{r}'|^3} dV'. \tag{2.46}$$

We want to take a look at the contributions from the primary current and the volume current separately. For this purpose, it is convenient to write Equation 2.46 on a different form. First, we make use of the following identities [16, 67]:

(i) $(\mathbf{r} - \mathbf{r}')/|\mathbf{r} - \mathbf{r}'|^3 = \nabla' 1/|\mathbf{r} - \mathbf{r}'|$, and

(ii) $\mathbf{i}(\mathbf{r}') \times \nabla'(1/|\mathbf{r} - \mathbf{r}'|) = (\nabla' \times \mathbf{i}(\mathbf{r}'))/|\mathbf{r} - \mathbf{r}'| - \nabla' \times (\mathbf{i}(\mathbf{r}')/|\mathbf{r} - \mathbf{r}'|)$,

obtaining:

$$\mathbf{B}(\mathbf{r}) = \frac{\mu_0}{4\pi} \int \frac{\nabla' \times \mathbf{i}(\mathbf{r}')}{|\mathbf{r} - \mathbf{r}'|} dV' - \frac{\mu_0}{4\pi} \int \nabla' \times \frac{\mathbf{i}(\mathbf{r}')}{|\mathbf{r} - \mathbf{r}'|} dV'. \tag{2.47}$$

[1] NB: Note that the term *finite element* can either mean subdomain or the type of basis function applied or the subdomain-basis-function pair.

Evaluating the integral in the second term above, we can apply Stokes' theorem, such that:

$$\text{(iii)} \quad -\int \nabla' \times (\mathbf{i}(\mathbf{r}')/|\mathbf{r}-\mathbf{r}'|)dV = \int \mathbf{i}(\mathbf{r}')/|\mathbf{r}-\mathbf{r}'| \times d\mathbf{S},$$

which equals zero if $\mathbf{i}(\mathbf{r}')$ goes to zero sufficiently fast, when $\mathbf{r} \to \infty$, and we obtain:

$$\mathbf{B}(\mathbf{r}) = \frac{\mu_0}{4\pi} \int \frac{\nabla' \times \mathbf{i}(\mathbf{r}')}{|\mathbf{r}-\mathbf{r}'|} dV'. \tag{2.48}$$

Next, we express the total current density as the sum of the primary current density and the resulting volume current density $\mathbf{i} = \mathbf{i}_s - \sigma\nabla V$, giving

$$\mathbf{B}(\mathbf{r}) = \frac{\mu_0}{4\pi} \int \frac{\nabla' \times \mathbf{i}_s(\mathbf{r}')}{|\mathbf{r}-\mathbf{r}'|} dV' - \frac{\mu_0}{4\pi} \int \frac{\nabla' \times \sigma\nabla' V}{|\mathbf{r}-\mathbf{r}'|} dV'. \tag{2.49}$$

Finally, we use the calculus steps described above in reverse order on the first term, and the relation $\nabla' \times \sigma\nabla' V = \nabla'\sigma \times \nabla' V$ (since $\nabla' \times \nabla' V = 0$) in the second term, such that

$$\mathbf{B}(\mathbf{r}) = \mathbf{B}_0 - \frac{\mu_0}{4\pi} \int \frac{\nabla'\sigma \times \nabla' V}{|\mathbf{r}-\mathbf{r}'|} dV', \tag{2.50}$$

where

$$\mathbf{B}_0(\mathbf{r}) = \frac{\mu_0}{4\pi} \int \frac{\mathbf{i}_s(\mathbf{r}') \times (\mathbf{r}-\mathbf{r}')}{|\mathbf{r}-\mathbf{r}'|^3} dV'. \tag{2.51}$$

In an infinite homogeneous conductor $\nabla'\sigma = 0$, and there will be no contribution from volume currents, meaning that the magnetic field is solely due to primary currents $\mathbf{B} = \mathbf{B}_0$. In a spherically symmetric head model, the radial part of the magnetic field is independent of volume currents, and can be computed with Equation 2.51 (see Nunez and Srinivasan, 2006 [1], Appendix C).

The primary current density from a current dipole $\mathbf{p}$ at position $\mathbf{r}_p$ can be expressed as:

$$\mathbf{i}_p = \mathbf{p}(\mathbf{r}_p)\delta(\mathbf{r}-\mathbf{r}_p). \tag{2.52}$$

Inserting Equation (2.52) into Equation (2.51), we obtain

$$\begin{aligned} \mathbf{B}_p &= \frac{\mu_0}{4\pi} \int \frac{\mathbf{p}(\mathbf{r}_p) \times (\mathbf{r}-\mathbf{r}_p)\delta(\mathbf{r}-\mathbf{r}_p)}{|\mathbf{r}-\mathbf{r}_p|^3} \\ &= \frac{\mu_0}{4\pi} \frac{\mathbf{p}(\mathbf{r}_p) \times (\mathbf{r}-\mathbf{r}_p)}{|\mathbf{r}-\mathbf{r}_p|^3}. \end{aligned} \tag{2.53}$$

Having computed the current dipole moment from a neuron simulation, the resulting MEG contribution can be approximated with Equation 2.53, assuming an infinite homogeneous head model.

Chapter 3

Summary of papers

Paper I

3.1 Corrected four-sphere head model for EEG signals

Paper I is a methods paper providing analytical formulas and available python code for computing the electric potential in the four-sphere head model. The reason for writing this paper, was that we found errors in the Nunez and Srinivasan, 2006 [1] and the Srinivasan, 1998 [33] formulations of the four-sphere model, when implementing their solutions. The paper presents the corrected analytical formulas, including the full derivation. In addition to analytical verifications, the model solution was validated with the finite element method. The scripts for both the analytical and the numerical solution are available on GitHub for forward modeling of electric potentials or benchmarking of finite or boundary element predictions of EEG. This work also laid the foundation for implementing the four-sphere head model into LFPy 2.0 (Paper II). See Appendix A for comments on convergence and agreement with another model solution.

Paper II

3.2 Multimodal modeling of neural network activity: computing LFP, ECoG, EEG, and MEG signals with LFPy 2.0

In paper II, we present the second release of the open-source python package LFPy [15]: LFPy is a tool for computing extracellular potentials from neural activity, running on top of the NEURON simulation environment [46]. While the first release was restricted to electric potentials from single-neuron activity in media with constant conductivity, the second version opens for predictions of multiple measurement modalities, including ECoG, EEG, and MEG, from neural networks.

In order to facilitate EEG, and MEG calculations, we included methods for reducing arbitrary neural activity into a single current dipole moment (either from transmembrane or axial currents) in a framework here referred to as the *dipole framework*. The dipole framework can be applied not only for single cells but also neural populations, with network simulations now enabled in LFPy 2.0. Next, we incorporated two methods from Ness et al., 2015 [68] allowing for (i) electric potential calculations in anisotropic brain tissue, and (ii) calculating potentials subject to step-wise changes in tissue conductivity, for example, those

recorded by multielectrode arrays and ECoG. EEG calculations were enabled with the implementation of the analytical four-sphere model from Paper I. By developing methods for calculating many small current dipoles from a single neuron simulation, we also facilitated ECoG calculations with the four-sphere head model. These multiple current dipoles were also utilized for calculating magnetic fields measured close to the neuron. Finally, we included a method for approximating MEG signals.

Demonstration of the new LFPy features was done by simulating an example network with 5500 neurons from the reconstructed somatosensory cortex column by Markram et al., 2015 [69]. Multimodal measurement calculations were then carried out, showing how the neural network simulation contributed to LFP, ECoG, EEG, and MEG signals.

Errata: In this paper, it is incorrectly stated that the we applied a spherically symmetric head model for the MEG calculations. Instead, all MEG calculations assumed that the volume conductor was an infinite homogeneous space, and were carried out with the Biot-Savart law for a current dipole moment. All references to the four-sphere model or spherically symmetric model regarding MEG calculations should have been replaced with references to an infinite homogeneous model.

Paper III

3.3 Biophysically detailed forward modeling of the neural origin of EEG and MEG signals

In Paper III, we applied methods implemented in Paper I and II, for investigating the link between neural activity and electric brain signals. We illustrated that EEG modeling consists of two cleanly separated steps: i) reducing neural simulations to a single current dipole moment and ii) applying the current dipole moment for calculating the resulting EEG signals. Even though we here focused on EEG signals, the current dipole moments can easily be combined with frameworks for MEG calculations (see Ilmoniemi and Sarvas, 2019 [67]).

Investigating the applicability of the current dipole approximation, we verified that the dipole framework is a good candidate for calculating EEG signals, and that the framework is less suitable for ECoG calculations. Importantly, we demonstrated how a biophysically detailed neuron simulation can be reduced to a single dipole, and that this is a powerful approach for studying single-cell contributions to EEG signals. Next, we illustrated how the dipole framework straightforwardly can be applied for large neural populations. This opened for a single current dipole moment compactly representing EEG contributions from a neural network. Finally, we showed how current dipole moments from single cells or large-scale network activity can be combined with the complex New York Head model to compute EEG signals with a very high level of biophysical

detail [63]. Available python code for applying the New York Head model was also implemented in LFPy.

Chapter 4

Discussion

The long history and widespread use of electric and magnetic brain recordings have been no guarantee for understanding exactly what kind of neural conversations lead to these signals. The underlying physics of EEG and MEG is, however, well understood and was reviewed, for example, in the important works of Nunez and Srinivasan, 2006 [1] and Hämäläinen et al., 1993 [16]. How neural conversations spit out transmembrane currents and how current dipole moments give rise to EEG and MEG is well-established knowledge. Still, one thing missing has been a framework for computing the current dipole moment from arbitrary neuron simulations, allowing for calculations of EEG/MEG from networks of morphologically reconstructed neuron models.

Calculations of current dipole moments from biophysically detailed neuron models have been carried out before to study contributions to EEG/MEG from single spiking cells [22], and to investigate how the current dipole moment is affected by the location of synaptic input [15, 48]. In several studies, the current dipole moments computed from a pre-defined network of minimally sufficient neuron models (simplified neuron morphologies with few compartments) link measured EEG and MEG to neural activity [22, 70–74]. This framework is now available through an easily accessible software tool; the Human Neocortical Neurosolver (HNN) [49]. While this tool may be an obvious choice for easy comparison with clinical recordings, HNN is (for now) not compatible with EEG or MEG calculations from simulations of morphologically detailed neuron models reconstructed from experimental data. The dipole framework presented here gives the opportunity to reduce biophysically detailed simulations of arbitrary neural activity to a single current dipole moment.

I like to think that the current dipole moment gives an overview of the electrical activity in the neural symphony, by capturing the melody of the network. If you know which tune is played on stage, you will have a good idea of what one can hear from the outside of the concert hall. Correspondingly, in Paper III, we see that from only inspecting the current dipole moment, we obtain a good intuition about the resulting electric and magnetic signals that can be recorded outside of the head.

Next, I will illustrate the importance of the dipole framework by discussing ongoing and future applications and giving some thoughts on the outlook of EEG/MEG modeling.

4.1 Applications

In contrast to a broken bone or nearsightedness, it is difficult to know where to begin if you want to *measure* a psychiatric disorder such as schizophrenia. Several studies, including Çavuş et al., 2012 [75] and Light et al., 2013 [76], have shown that EEG recordings can reveal differences between the way healthy controls and schizophrenia patients process visual and auditory stimuli [77]. With genome-wide association studies identifying genetic variants linked to schizophrenia [78], we have started to look into the underlying mechanisms of these differences in EEG signals. In the papers by Maki-Märttunen et al., 2019 [50, 51], we investigated how EEG signals depend on ion channel mechanisms linked to schizophrenia-associated genetic loci, by applying the dipole framework on biophysically detailed neuron models. Our group is part of ongoing efforts aiming to predict EEG signals comparable to clinical data, contributing to the young field of computational psychology [51].

In the future, we hope that EEG can be used not only for understanding and diagnosing brain disorders, but also for studying the neural activity underpinning more general brain functions such as learning, by, for example, following the lead provided by Suzuki and Larkum, 2017 [79]. Their study revealed that dendritic calcium spikes (that are associated with certain learning mechanisms) can be detected with EEG. Since we showed in Paper III that we can model the putative EEG contribution from calcium spikes, calcium spikes appears a good candidate for comparing simulations with measurements.

Another example of how the dipole framework can be used is the work of Martínez-Cañada et al., 2021 [80]. In this study, they apply the dipole framework for generating benchmark EEG data from a network simulation, to investigate whether EEG signals can be predicted with measures readily available from point-neuron network simulations. This work is important because point-neuron network simulations is a very common tool for studying neural populations (the generators of EEG signals) [21].

The dipole framework described here is in the process of being implemented as part of the open-access simulation tools developed by the EU Human Brain Project, through the EBRAINs platform. As soon as this is in place, anyone, anywhere, can compute the current dipole moment from large-scale biophysically detailed neural simulations. They can further model EEG signals with the four-sphere or New York Head model implementation in LFPy, or plug their dipole moment into any head model of their choice. Such available modeling frameworks will hopefully lead to more EEG and MEG modeling, based on different networks resembling different cell types, brain areas, and firing patterns.

Building on future advances in network modeling, it would be exciting to study cell-type-specific contributions to EEG and MEG. When exploring how various neuron types in different brain areas contribute to the dipole moment, we could look to experimentally mapped out connections of different neuron populations and nest back what drives various EEG and MEG signatures.

4.2 Outlook

What can we learn from EEG and MEG signals? The popularity of scalp potentials, in particular, is not due to straightforward interpretation of the recordings, but rather because the technology is very available: EEG equipment is relatively cheap, the recordings are easy to perform, and above all, they are non-invasive. The reason for the difficulties we have interpreting these signals is twofold: i) EEG is very much a global measure, meaning that the signals stem from neural activity in various large networks, and it is not an easy task to tell contributions from different populations apart; ii) there is a long way from the source to the electrode, meaning that information will be lost on the way. These disadvantages are, however, inherent in the non-invasiveness of EEG. Of course, it would be easier to study the brain if we could implant numerous electrodes into brain tissue, but that is simply not an option. We have to study the brain with the technology we have, not the technology we wish to have, and computational modeling is key to make the most of the data at hand.

With an available EEG/MEG-modeling framework in place, one could hope that computing EEG/MEG signals comparable to clinical data was now plug and play. This is, unfortunately, not the case. The main obstacle in realistic EEG modeling lies within simulating network activity imitating real neural conversations spanning multiple brain areas. When modeling even a small piece of cortex, the number of neurons is very high, there is a huge variability within neural populations, and the number of potential model parameters is daunting [21]. As Traub et al., 2015 [81] puts it: “[...] the only way to proceed is through a state of denial that any of the difficulties need be fatal.”

Specifically, in this work, EEG/MEG calculations were computed from a maximum number of 80000 neurons, giving a maximum current dipole moment of about 0.1 nAm. In order to approximate EEG signals that are comparable to clinical recordings, the current dipole moment must be in the $10-100$ nAm range for event-related potentials, and $100-1000$ nAm for low-frequency EEG [22, 49, 72, 73]. This would require neuron simulations on the order of 100 million to a billion neurons [82]. Apart from dipole magnitude, it is essential for comparison with clinical recordings that the computations are not based on single dipoles, but rather whole sheets of dipoles representing multiple brain areas [1, 82].

Nonetheless, these are exciting times for EEG modeling: The steady increase in computational power, improved understanding of how neurons are connected, and the growing amount of available biophysically detailed neuron models make the future of network modeling look promising. Importantly, we are now at the point where we can start predicting non-invasive measurements with computer simulations [21]. As Cohen states in his paper titled "Where does EEG come from and what does it mean?": "Now is the time to start answering the title question" [20]. Simultaneously recording LFP and EEG in animal studies would be an ideal starting point for comparing recordings with data simulated with the dipole framework. Further, modeling multiple measurement modalities will be an

important step on the way to constraining the potential underlying mechanisms. Hopefully, the dipole framework can help us demystify the neural origin of non-invasive brain signals in the future.

Bibliography

[1] Nunez, P. L. and Srinivasan, R. *Electric fields of the brain*. 2nd. New York: Oxford University Press, 2006.

[2] Sterratt, D., Graham, B., Gillies, A., and Willshaw, D. *Principles of computational modeling in neuroscience*. Cambridge: Cambridge University Press, 2011.

[3] Koch, C. and Segev, I. "The role of single neurons in information processing". In: *Nature Neuroscience* vol. 3 (2000).

[4] Dayan, P. and Abbott, L. F. *Theoretical neuroscience, computational and mathematical modeling of neural analysis*. Cambridge, Massachusetts: The MIT Press, 2001.

[5] *Medical gallery of Blausen Medical 2014*. 'https://commons.wikimedia.org/wiki/File:Blausen_0672_NeuralTissue.png'.

[6] Næss, S. "Biophysical modeling of EEG signals from neurons in the brain". MA thesis. Norwegian University of Life Science, Ås, 2015.

[7] Pettersen, K. H. and Einevoll, G. T. "Amplitude variability and extracellular low-pass filtering of neuronal spikes". In: *Biophysical Journal* vol. 94 (2008).

[8] Holt, G. R. and Koch, C. "Electrical interactions via the extracellular potential near cell bodies". In: *Journal of Computational Neuroscience* vol. 6 (1999).

[9] Rall, W. "Core conductor theory and cable properties of neurons". In: *Comprehensive Physiology* (2011).

[10] Buzsáki, G., Anastassiou, C. A., and Koch, C. "The origin of extracellular fields and currents–EEG, ECoG, LFP and spikes." In: *Nature reviews, Neuroscience* vol. 13, no. 6 (2012).

[11] Gaute T. Einevoll and Jaeger, D. (Ed) and Jung, R. (Ed). *Encyclopedia of computational neuroscience, forward modeling of extracellular potentials*. New York: Springer Reference, 2013.

[12] Einevoll, G. T., Kayser, C., Logothetis, N. K., and Panzeri, S. "Modelling and analysis of local field potentials for studying the function of cortical circuits". In: *Nature Reviews, Neuroscience* vol. 14 (2013).

[13] Pettersen, K. H., Hagen, E., and Einevoll, G. T. "Estimation of population firing rates and current source densities from laminar electrode recordings". In: *Journal of Computational Neuroscience* vol. 24, no. 3 (2008).

[14] Lindén, H., Pettersen, K. H., and Einevoll, G. T. “Intrinsic dendritic filtering gives low-pass power spectra of local field potentials”. In: *Springer Science+Business Media* vol. 29 (2010).

[15] Lindén, H., Hagen, E., Łęski, S., Norheim, E. S., Pettersen, K. H., and Einevoll, G. T. “LFPy: a tool for biophysical simulation of extracellular potentials generated by detailed model neurons”. In: *Frontiers in Neuroinformatics* vol. 7 (2014).

[16] Hämäläinen, M., Haari, R., Ilmoniemi, R. J., Knuutila, J., and Lounasmaa, O. V. “Magnetoencephalography — theory, instrumentation, and application to noninvasive studies of the working human brain”. In: *Reviews of Modern Physics* vol. 65 (1993).

[17] Hodgkin, A. L. and Huxley, A. F. “A quantitative description of membrane current and its application to conduction and excitation in nerve”. In: *The Journal of Physiology* vol. 117, no. 4 (1952).

[18] Caton, R. “The electric currents of the brain.” In: *British Medical Journal*, no. 2 (1875).

[19] Berger, H. “Über das Elektreenkephalogramm des Menschen”. In: *Arch. Psychiatr. Nervenkr.*, no. 87 (1929).

[20] Cohen, M. X. “Where does EEG come from and what does it mean?” In: *Trends in Neurosciences* vol. 40, no. 4 (2017).

[21] Einevoll, G. T., Destexhe, A., Diesmann, M., Grün, S., Jirsa, V., Kamps, M. de, Migliore, M., Ness, T. V., Plesser, H. E., and Schürmann, F. “The scientific case for brain simulations”. In: *Neuron* vol. 102 (2019).

[22] Murakami, S. and Okada, Y. “Contributions of principal neocortical neurons to magnetoencephalography and electroencephalography signals.” In: *The Journal of Physiology* vol. 575, no. Pt 3 (2006).

[23] Brazier, M. A. B. “A study of the electric field at the surface of the head”. In: *Electroencephalography and Clinical Neurophysiology* vol. 2 (1949).

[24] Brazier, M. A. B. “A study of the electrical fields at the surface of the head”. In: *American Journal of EEG Technology* vol. 6, no. 4 (1966).

[25] Wilson, F. N. and Baylay, R. H. “The electric field of an eccentric dipole in a homogeneous spherical conducting medium”. In: *Circulation* vol. 1, no. 1 (1950).

[26] Rush, S. and Driscoll, D. A. “Current distribution in the brain from surface electrodes”. In: *Anesthesia & Analgesia* vol. 47, no. 6 (1968).

[27] Hosek, R. S., Sances, A., Jodat, R. W., and Larson, S. J. “The contributions of intracerebral currents to the EEG and evoked potentials”. In: *IEEE Transactions on Biomedical Engineering*, no. 5 (1978).

[28] Cuffin, B. N. and Cohen, D. “Comparison of the magnetoencephalogram and electroencephalogram”. In: *Electroencephalography and Clinical Neurophysiology* vol. 47, no. 2 (1979).

[29] De Munck, J. "The potential distribution in a layered anisotropic spheroidal volume conductor". In: *Journal of applied Physics* vol. 64, no. 2 (1988).

[30] De Munck, J., Peters, M. J., et al. "A fast method to compute the potential in the multisphere model". In: *IEEE Trans. Biomed. Eng* vol. 40, no. 11 (1993).

[31] Zhang, Z. "A fast method to compute surface potentials generated by dipoles within multilayer anisotropic spheres". In: *Physics in medicine & biology* vol. 40, no. 3 (1995).

[32] Sun, M. "An efficient algorithm for computing multishell spherical volume conductor models in EEG dipole source localization". In: *IEEE Transactions on Biomedical Engineering* vol. 44, no. 12 (1997).

[33] Srinivasan, R., Nunez, P. L., and Silberstein, R. B. "Spatial filtering and neocortical dynamics: estimates of EEG coherence". In: *IEEE Transactions on Biomedical Engineering* (1998).

[34] Hämäläinen, M. and Sarvas, J. "Realistic conductivity geometry model of the human head for interpretation of neuromagnetic data". In: *IEEE Transactions on Biomedical Engineering* vol. 36, no. 2 (1989).

[35] Cuffin, B. N. "A method for localizing EEG sources in realistic head models". In: *IEEE Transactions on Biomedical Engineering* vol. 42, no. 1 (1995).

[36] Yan, Y., Nunez, P., and Hart, R. "Finite-element model of the human head: scalp potentials due to dipole sources". In: *Medical and Biological Engineering and Computing* vol. 29, no. 5 (1991).

[37] Rall, W. "Branching dendritic trees and motoneuron membrane resistivity". In: *Experimental Neurology* vol. 1, no. 5 (1959).

[38] Hodgkin, A. L. and Katz, B. "The effect of sodium ions on the electrical activity of the giant axon of the squid". In: *The Journal of Physiology* vol. 108, no. 1 (1949).

[39] Rall, W. "Electrophysiology of a dendritic neuron model". In: *Biophysical Journal* vol. 2 (1962).

[40] Rall, W. and Shepherd, G. M. "Theoretical reconstruction of field potentials and dendrodendritic synaptic interactions in olfactory bulb." In: *Journal of Neurophysiology* vol. 31, no. 6 (1968).

[41] Gold, C., Henze, D. A., Koch, C., and Buzsáki, G. "On the origin of the extracellular action potential waveform: a modeling study". In: *Journal of Neurophysiology* vol. 95, no. 5 (2006).

[42] Einevoll, G. T., Pettersen, K. H., Devor, A., Ulbert, I., Halgren, E., and Dale, A. M. "Laminar population analysis: estimating firing rates and evoked synaptic activity from multielectrode recordings in rat barrel cortex." In: *Journal of Neurophysiology* vol. 97, no. 3 (2007).

[43] Reimann, M. W., Anastassiou, C. A., Perin, R., Hill, S. L., Markram, H., and Koch, C. "A biophysically detailed model of neocortical local field potentials predicts the critical role of active membrane currents". In: *Neuron* vol. 79, no. 2 (2013).

[44] Lumer, E. D., Edelman, G. M., and Tononi, G. "Neural dynamics in a model of the thalamocortical system. I. Layers, loops and the emergence of fast synchronous rhythms." In: *Cerebral Cortex* vol. 7, no. 3 (1997).

[45] Potjans, T. C. and Diesmann, M. "The cell-type specific cortical microcircuit: relating structure and activity in a full-scale spiking network model." In: vol. 24, no. 3 (2014).

[46] Carnevale, N. T. and Hines, M. L. *The NEURON book*. Cambridge: Cambridge University Press, 2006.

[47] Bower, J. M. and Beeman, D. *The book of GENESIS: exploring realistic neural models with the GEneral NEural SImulation System*. Springer Science & Business Media, 2012.

[48] Ahlfors, S. P. and Wreh II, C. "Modeling the effect of dendritic input location on MEG and EEG source dipoles". In: *Medical and Biological Engineering and Computing* vol. 53, no. 9 (2015).

[49] Neymotin, S. A., Daniels, D. S., Caldwell, B., McDougal, R. A., Carnevale, N. T., Jas, M., Moore, C. I., Hines, M. L., Hämäläinen, M., and Jones, S. R. "Human Neocortical Neurosolver (HNN), a new software tool for interpreting the cellular and network origin of human MEG/EEG data". In: *eLife* vol. 9 (2020).

[50] Mäki-Marttunen, T. et al. "Alterations in schizophrenia-associated genes can lead to increased power in delta oscillations". In: *Cerebral Cortex* vol. 29, no. 2 (2019).

[51] Mäki-Marttunen, T. et al. "Biophysical psychiatry—how computational neuroscience can help to understand the complex mechanisms of mental disorders". In: *Frontiers in Psychiatry* vol. 10 (2019).

[52] Ness, T. V., Halnes, G., Næss, S., Pettersen, K. H., and Einevoll, G. T. "Computing extracellular electric potentials from neuronal simulations". In: (2020). arXiv: 2006.16630.

[53] Grodzinsky, A. *Fields, forces, and flows in biological systems*. Mar. 2011.

[54] Nicholson, C. and Phillips, J. "Ion diffusion modified by tortuosity and volume fraction in the extracellular microenvironment of the rat cerebellum." In: *The Journal of Physiology* vol. 321, no. 1 (1981).

[55] Okada, Y. C., Huang, J.-C., Rice, M. E., Tranchina, D., and Nicholson, C. "Origin of the apparent tissue conductivity in the molecular and granular layers of the in vitro turtle cerebellum and the interpretation of current source-density analysis". In: *Journal of Neurophysiology* vol. 72, no. 2 (1994).

[56] Nicholson, C. and Freeman, J. A. “Theory of current source-density analysis and determination of conductivity tensor for anuran cerebellum”. In: *Journal of Neurophysiology* vol. 38, no. 2 (1975).

[57] Logothetis, N. K., Kayser, C., and Oeltermann, A. “In vivo measurement of cortical impedance spectrum in monkeys: implications for signal propagation”. In: *Neuron* vol. 55, no. 5 (2007).

[58] Griffiths, D. J. “Introduction to electromagnetism”. In: *Prentice-Hall, Englewood Cliffths, NJ, 1989) Section* vol. 10 (1999).

[59] Geselowitz, D. B. “On bioelectric potentials in an inhomogeneous volume conductor”. In: *Biophysical Journal* vol. 7, no. 1 (1967).

[60] Gratiy, S. L., Halnes, G., Denman, D., Hawrylycz, M. J., Koch, C., Einevoll, G. T., and Anastassiou, C. A. “From Maxwell’s equations to the theory of current-source density analysis”. In: *European Journal of Neuroscience* vol. 45, no. 8 (2017).

[61] Koch, C. *Biophysics of computation*. Oxford Univ Press, Oxford, 1999.

[62] Plonsey, R. and Barr, R. C. *Bioelectricity: a quantitative approach*. Springer Science & Business Media, 2007.

[63] Huang, Y. and Parra, L. C. “Fully automated whole-head segmentation with improved smoothness and continuity, with theory reviewed”. In: *PLoS ONE* vol. 10, no. 5 (2015).

[64] Logg, A., Mardal, K.-A., and Wells, G. N. *Automated solution of differential equations by the finite element method*. Vol. 84. Lecture notes in computational science and engineering. Berlin, Heidelberg: Springer Berlin Heidelberg, 2012.

[65] Langtangen, H. P. and Logg, A. *Solving PDEs in Python*. Springer, 2017.

[66] Alnæs, M., Blechta, J., Hake, J., Johansson, A., Kehlet, B., Logg, A., Richardson, C., Ring, J., Rognes, M. E., and Wells, G. N. “The FEniCS project version 1.5”. In: *Archive of Numerical Software* vol. 3, no. 100 (2015).

[67] Ilmoniemi, R. J. and Sarvas, J. *Brain signals: Physics and mathematics of MEG and EEG*. MIT Press, 2019.

[68] Ness, T. V., Chintaluri, C., Potworowski, J., Łęski, S., Głąbska, H., Wójcik, D. K., and Einevoll, G. T. “Modelling and analysis of electrical potentials recorded in microelectrode arrays (MEAs)”. In: *Neuroinformatics* vol. 13, no. 4 (2015).

[69] Markram, H. et al. “Reconstruction and simulation of neocortical microcircuitry”. In: *Cell* vol. 163, no. 2 (2015).

[70] Murakami, S., Zhang, T., Hirose, a., and Okada, Y. C. “Physiological origins of evoked magnetic fields and extracellular field potentials produced by guinea-pig CA3 hippocampal slices”. In: *The Journal of Physiology* vol. 544, no. 1 (2002).

[71] Murakami, S., Hirose, A., and Okada, Y. C. “Contribution of ionic currents to magnetoencephalography (MEG) and electroencephalography (EEG) signals generated by guinea-pig CA3 slices.” In: *The Journal of Physiology* vol. 553, no. Pt 3 (2003).

[72] Jones, S. R., Pritchett, D. L., Stufflebeam, S. M., Hämäläinen, M., and Moore, C. I. “Neural correlates of tactile detection: A combined magnetoencephalography and biophysically based computational modeling study”. In: *Journal of Neuroscience* vol. 27, no. 40 (2007).

[73] Jones, S. R., Pritchett, D. L., Sikora, M. A., Stufflebeam, S. M., Hämäläinen, M., and Moore, C. I. “Quantitative analysis and biophysically realistic neural modeling of the MEG mu rhythm: rhythmogenesis and modulation of sensory-evoked responses.” In: *Journal of Neurophysiology* vol. 102, no. 6 (2009).

[74] Sliva, D. D., Black, C. J., Bowary, P., Agrawal, U., Santoyo, J. F., Philip, N. S., Greenberg, B. D., Moore, C. I., and Jones, S. R. “A prospective study of the impact of transcranial alternating current stimulation on EEG correlates of somatosensory perception”. In: *Frontiers in Psychology* vol. 9, no. NOV (2018).

[75] Çavuş, I., Reinhart, R. M., Roach, B. J., Gueorguieva, R., Teyler, T. J., Clapp, W. C., Ford, J. M., Krystal, J. H., and Mathalon, D. H. “Impaired visual cortical plasticity in schizophrenia”. In: *Biological Psychiatry* vol. 71, no. 6 (2012).

[76] Light, G. A. and Näätänen, R. “Mismatch negativity is a breakthrough biomarker for understanding and treating psychotic disorders”. In: *Proceedings of the National Academy of Sciences* vol. 110, no. 38 (2013).

[77] Owens, E., Bachman, P., Glahn, D. C., and Bearden, C. E. “Electrophysiological endophenotypes for schizophrenia”. In: *Harvard Review of Psychiatry* vol. 24, no. 2 (2016).

[78] Schizophrenia Working Group of the Psychiatric Genomics Consortium. “Biological insights from 108 schizophrenia-associated genetic loci”. In: *Nature* vol. 511, no. 7510 (2014).

[79] Suzuki, M. and Larkum, M. E. “Dendritic calcium spikes are clearly detectable at the cortical surface”. In: *Nature Communications* vol. 8, no. 276 (2017).

[80] Martínez-Cañada, P., Ness, T. V., Einevoll, G. T., Fellin, T., and Panzeri, S. “Computation of the electroencephalogram (EEG) from network models of point neurons”. In: *PLoS Computational Biology* vol. 17, no. 4 (2021).

[81] Traub, R. D., Contreras, D., Cunningham, M. O., Murray, H., LeBeau, F. E., Roopun, A., Bibbig, A., Wilent, W. B., Higley, M. J., and Whittington, M. A. “Single-column thalamocortical network model exhibiting gamma oscillations, sleep spindles, and epileptogenic bursts”. In: *Journal of Neurophysiology* vol. 93, no. 4 (2005).

[82] Nunez, P. L., Nunez, M. D., and Srinivasan, R. “Multi-scale neural sources of EEG: genuine, equivalent, and representative. A tutorial review”. In: *Brain Topography* vol. 32, no. 2 (2019).

Papers

Paper I

Corrected four-sphere head model for EEG signals

I

frontiers in Human Neuroscience

METHODS
published: 18 October 2017
doi: 10.3389/fnhum.2017.00490

Corrected Four-Sphere Head Model for EEG Signals

Solveig Næss[1†], *Chaitanya Chintaluri*[2†], *Torbjørn V. Ness*[3], *Anders M. Dale*[4], *Gaute T. Einevoll*[3,5*] *and Daniel K. Wójcik*[2*]

[1] *Department of Informatics, University of Oslo, Oslo, Norway,* [2] *Department of Neurophysiology, Nencki Institute of Experimental Biology, Warsaw, Poland,* [3] *Faculty of Science and Technology, Norwegian University of Life Sciences, Ås, Norway,* [4] *Departments of Neurosciences and Radiology, University of California, San Diego, La Jolla, CA, United States,* [5] *Department of Physics, University of Oslo, Oslo, Norway*

The EEG signal is generated by electrical brain cell activity, often described in terms of current dipoles. By applying EEG forward models we can compute the contribution from such dipoles to the electrical potential recorded by EEG electrodes. Forward models are key both for generating understanding and intuition about the neural origin of EEG signals as well as inverse modeling, i.e., the estimation of the underlying dipole sources from recorded EEG signals. Different models of varying complexity and biological detail are used in the field. One such analytical model is the *four-sphere model* which assumes a four-layered spherical head where the layers represent brain tissue, cerebrospinal fluid (CSF), skull, and scalp, respectively. While conceptually clear, the mathematical expression for the electric potentials in the four-sphere model is cumbersome, and we observed that the formulas presented in the literature contain errors. Here, we derive and present the correct analytical formulas with a detailed derivation. A useful application of the analytical four-sphere model is that it can serve as ground truth to test the accuracy of numerical schemes such as the Finite Element Method (FEM). We performed FEM simulations of the four-sphere head model and showed that they were consistent with the corrected analytical formulas. For future reference we provide scripts for computing EEG potentials with the four-sphere model, both by means of the correct analytical formulas and numerical FEM simulations.

Keywords: four-sphere model, head model, EEG, dipole source, LFP, FEM

OPEN ACCESS

Edited by:
Francesco Di Russo,
Foro Italico University of Rome, Italy

Reviewed by:
Zhimin Li,
University of Wisconsin-Madison, United States
Moritz Dannhauer,
Scientific Computing and Imaging Institute, United States
Ettore Ambrosini,
Università degli Studi di Padova, Italy

***Correspondence:**
Gaute T. Einevoll
gaute.einevoll@nmbu.no
Daniel K. Wójcik
d.wojcik@nencki.gov.pl

[†]*These authors have contributed equally to this work.*

Received: *18 May 2017*
Accepted: *26 September 2017*
Published: *18 October 2017*

Citation:
Næss S, Chintaluri C, Ness TV, Dale AM, Einevoll GT and Wójcik DK (2017) Corrected Four-Sphere Head Model for EEG Signals. Front. Hum. Neurosci. 11:490. doi: 10.3389/fnhum.2017.00490

1. INTRODUCTION

Electroencephalography (EEG), that is, the recording of electrical potentials at the scalp, has been of key importance for probing human brain activity for more than half a century (Nunez and Srinivasan, 2006; Schomer and da Silva, 2012). The EEG signal is generated by current dipoles set up by transmembrane currents in brain cells, and EEG *forward models* aim to compute the contribution from such current dipoles to the electrical potential recorded by EEG electrodes (Hämäläinen et al., 1993; Sanei and Chambers, 2007). Forward models are useful for generating understanding and intuition about the neural origin of EEG signals. They are also key for inverse modeling, i.e., the estimation of the underlying sources based on recorded EEG signals, and for generation of benchmarking data against which candidate methods for EEG data analysis methods and simulation schemes for EEG can be tested.

While the link between the current sources and the resulting potentials in principle is well described by volume-conductor theory, the practical application of this theory is not easy because the cortical tissue, the cerebrospinal fluid (CSF), the skull, and the scalp, all have different electrical conductivities (Nunez and Srinivasan, 2006).

Different forward modeling schemes approximate the geometries and conductivities of the head with various levels of biological detail. On one side we have the spherical head models that can provide analytical formulas for the EEG potentials generated by current dipoles. At the other side of the spectrum we have numerically comprehensive forward modeling schemes, including realistic geometries and electrical conductivities, even electrically anisotropic tissue (Bangera et al., 2010; Vorwerk et al., 2014). These different forward models come with their different advantages and disadvantages in terms of speed, accuracy and interpretability of results (De Munck et al., 2012).

In this paper, we address the four-sphere head model where the head is modeled as four concentric spherical layers. Here, the four layers represent brain tissue, CSF, skull, and scalp. The Poisson equation, which describes the electric fields of the brain within volume-conductor theory, is solved for each layer separately, and the mathematical solutions are matched at the layer interfaces to obtain an analytical expression for the EEG signal as set up by a current source in the brain tissue. The relatively small number of parameters makes the four-sphere model an obvious candidate for exploring and gaining intuition about the nature of EEG signals. Since the solution is analytical and requires little computation time compared to complex numerical schemes, it can be used to quickly test analysis methods and hypotheses. The most popular version of the four-sphere model was presented in Srinivasan et al. (1998); and later in the classic EEG reference book Electric Fields of the Brain (Nunez and Srinivasan, 2006). This model has been used to generate benchmarking data for testing of EEG signal analysis methods, (e.g., Wong et al., 2008; Chu et al., 2012; Peraza et al., 2012), and it is also useful for validation of more general and numerically comprehensive numerical schemes such as the Boundary Element Method (BEM) (Brebbia et al., 2012) and the Finite Element Method (FEM) (Larson and Bengzon, 2013). The FEM approach is the most general and can, in principle, take into account an arbitrarily complicated spatial distribution of electrical conductivity representing the electrical properties of the head (Bangera et al., 2010; Huang et al., 2016). This is done by building a numerical mesh for the head model with the electrical conductivity specified at each mesh point. The mesh construction is a research problem by itself and several mesh-generation tools are available, which often provide slightly different results (Geuzaine, 2009; Kehlet, 2016). The analytical solution for the four-sphere model can serve as a ground truth for testing of different numerical schemes.

While conceptually clear, the mathematical expression of the four-sphere forward model is quite involved and rederiving the expression we discovered errors in the formulas both in the original paper and in the book. Due to the importance of the four-sphere model, we here derive and provide the correct analytical formulas for future reference. We tested our formulas by verifying that the solutions for neighboring layers matched on the layer boundaries. Moreover, when the conductivities for all the layers in the model were set to the same value, the model reduced to the well-known homogeneous single-sphere model as it should. We also verified that the model solution reduces to the formula for the extracellular potential from a current dipole in an infinite homogeneous space, when the layer radii go to infinity and the conductivities for all model layers are equal (not shown). As an application, we performed FEM simulations of the four-sphere model which were consistent with the corrected analytical formulas.

2. METHODS

2.1. Four-Sphere Model

By assuming the quasi-static approximation of Maxwell's equations and using the well-established volume-conductor theory, the electric potential Φ can be found by solving the Poisson equation (Nunez and Srinivasan, 2006),

$$\nabla \cdot \sigma(\mathbf{r}) \nabla \Phi(\mathbf{r}, t) = -C(\mathbf{r}, t), \tag{1}$$

where $C(\mathbf{r}, t)$ is the density of current sources. $\sigma(\mathbf{r})$ is the position-dependent conductivity of the medium, here assumed to be isotropic so that $\sigma(\mathbf{r})$ is a scalar. The four-sphere model is a specific solution of this equation which assumes that the conductive medium consists of four spherical layers representing specific constituents of the head: brain tissue, CSF, skull, and scalp (**Figure 1A**). In the computations below, these layers are labeled by $s = 1$ to 4, respectively. The conductivity $\sigma_s(\mathbf{r})$ is assumed to be homogeneous, i.e., constant within each layer and independent of frequency (Pettersen et al., 2012). In the examples below we assume the same values of conductivities and concentric shell radii as in Nunez and Srinivasan (2006), see **Table 1**. The solution of Equation (1) is subject to the following boundary conditions (where $s = 1, 2, 3$), assuring continuity of both electrical potential and current across the layer boundaries, and no current escaping the outer layer (Nunez and Srinivasan, 2006):

$$\Phi^{s+1}(r_s) = \Phi^s(r_s) \tag{2}$$

$$\sigma_{s+1} \frac{\partial \Phi^{s+1}}{\partial r}(r_s) = \sigma_s \frac{\partial \Phi^s}{\partial r}(r_s) \tag{3}$$

$$\frac{\partial \Phi^4}{\partial r}(r_4) = 0. \tag{4}$$

2.2. Analytical Solution of the Four-Sphere Head Model

The solution of Equation (1) takes different forms for tangential and radial dipoles, and any dipole can be decomposed into a linear combination of these two. The following derivations are based on Appendix G and H in Nunez and Srinivasan (2006), and are described in more detail in Appendix 1 in Supplementary Materials.

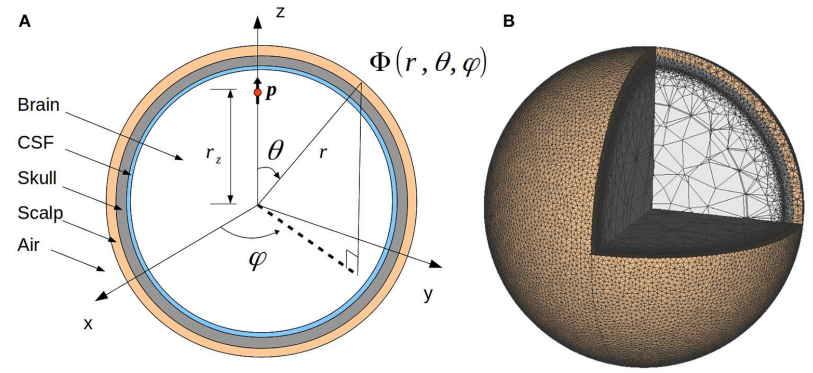

FIGURE 1 | Illustration of the four-sphere head model. **(A)** Cross-section of the four-sphere head model, with the different colors corresponding to the different head layers: brain, CSF, skull, and scalp. The current dipole p is located in the brain layer, at a distance r_Z from the center of the sphere. In all the subsequent figures, the dipole is placed in the $x = 0$ plane, at the z-axis ($r_Z = 7.8$ cm). **(B)** Mesh of the four-sphere model used in the FEM simulations illustrating the different electrical conductivity values for each of the spheres.

TABLE 1 | Radii and electrical conductivities of the present four-sphere model.

Labels	Name	Radius (cm)	σ (S/m)
1	Brain	7.9	$\sigma_{\text{brain}} = 0.33$
2	CSF	8.0	$5\,\sigma_{\text{brain}}$
3	Skull	8.5	σ_{brain}/K
4	Scalp	9.0	σ_{brain}

σ is the conductivity in each of the specified regions. Three variants of the model were considered with skull conductivity reduced by a factor K (20, 40, or 80) compared to the conductivity of the brain.

2.2.1. Radial dipole

Nunez and Srinivasan (2006) give the following equations for calculating extracellular potentials from a radial dipole in the four sphere model. The potential in the inner sphere, the brain, is given by $\Phi^1(r,\theta)$, while $\Phi^s(r,\theta)$ gives the potential in CSF, skull, and scalp, for $s = 2, 3, 4$, respectively,

$$\Phi^1(r,\theta) = \frac{p}{4\pi\sigma_1 r_z^2}\sum_{n=1}^{\infty}\left[A_n^1\left(\frac{r}{r_1}\right)^n + \left(\frac{r_z}{r}\right)^{n+1}\right] nP_n(\cos\theta) \quad r_z < r \le r_1, \tag{5}$$

$$\Phi^s(r,\theta) = \frac{p}{4\pi\sigma_1 r_z^2}\sum_{n=1}^{\infty}\left[A_n^s\left(\frac{r}{r_s}\right)^n + B_n^s\left(\frac{r_s}{r}\right)^{n+1}\right] nP_n(\cos\theta) \quad r_{s-1} \le r \le r_s. \tag{6}$$

Here, Φ^s is the extracellular potential measured at radius r in shell number s, of external radius r_s, from current dipole moment with magnitude p at radial location r_z. The conductivity of sphere s is denoted by σ_s, A_n^s and B_n^s are coefficients depending on the shell radii and conductivities, and $P_n(\cos\theta)$ is the n-th Legendre Polynomial where θ is the angle between measurement and dipole location vectors. From the boundary conditions listed in Equations (2)–(4), we can compute A_n^s, for $s = 1, 2, 3, 4$ and B_n^s, for $s = 2, 3, 4$, using the notation $\sigma_{ij} \equiv \sigma_i/\sigma_j$ and $r_{ij} \equiv r_i/r_j$:

$$A_n^1 = \frac{\frac{n+1}{n}\sigma_{12} + Z_n}{\frac{n}{\sigma_{12} - Z_n}} r_{z1}^{n+1} \tag{7}$$

$$A_n^2 = \frac{A_n^1 + r_{z1}^{n+1}}{r_{12}^n + r_{21}^{n+1} Y_n} \tag{8}$$

$$B_n^2 = Y_n A_n^2 \tag{9}$$

$$A_n^3 = \frac{A_n^2 + B_n^2}{r_{23}^n + r_{32}^{n+1} V_n} \tag{10}$$

$$B_n^3 = V_n A_n^3 \tag{11}$$

$$A_n^4 = \frac{n+1}{n}\frac{A_n^3 + B_n^3}{\frac{n+1}{n} r_{34}^n + r_{43}^{n+1}} \tag{12}$$

$$B_n^4 = \frac{n}{n+1} A_n^4 \tag{13}$$

$$V_n = \frac{\frac{n}{n+1}\sigma_{34} - \frac{r_{34}^n - r_{43}^{n+1}}{\frac{n+1}{n} r_{34}^n + r_{43}^{n+1}}}{\sigma_{34} + \frac{r_{34}^n - r_{43}^{n+1}}{\frac{n+1}{n} r_{34}^n + r_{43}^{n+1}}} \tag{14}$$

$$Y_n = \frac{\frac{n}{n+1}\sigma_{23} - \frac{\frac{n}{n+1} r_{23}^n - V_n r_{32}^{n+1}}{r_{23}^n + V_n r_{32}^{n+1}}}{\sigma_{23} + \frac{\frac{n}{n+1} r_{23}^n - V_n r_{32}^{n+1}}{r_{23}^n + V_n r_{32}^{n+1}}} \tag{15}$$

$$Z_n = \frac{r_{12}^n - \frac{n+1}{n} Y_n r_{21}^{n+1}}{r_{12}^n + Y_n r_{21}^{n+1}}. \tag{16}$$

Equations (5) and (6) are in accordance with Equations (G.1.9–10) in Appendix G of Nunez and Srinivasan (2006) and Equation (A–1) in Srinivasan et al. (1998), Appendix A. However, some of the above coefficients [Equations (7)–(16)] are different from the ones given in Nunez and Srinivasan (2006) and Srinivasan et al. (1998), see Appendix 1 in Supplementary Materials for specifics.

2.2.2. Tangential dipole

The extracellular potential from a tangential dipole in a concentric-shells model is given by Equation (H.2.1) in Appendix H of Nunez and Srinivasan (2006), and takes the following form:

$$\Phi^1(r,\theta,\varphi) = \frac{-p}{4\pi\sigma_1 r_z^2}\sin\varphi\sum_{n=1}^{\infty}\left[A_n^1\left(\frac{r}{r_1}\right)^n + \left(\frac{r_z}{r}\right)^{n+1}\right]P_n^1(\cos\theta)$$
$$r_z < r \le r_1 \quad (17)$$

$$\Phi^s(r,\theta,\varphi) = \frac{-p}{4\pi\sigma_1 r_z^2}\sin\varphi\sum_{n=1}^{\infty}\left[A_n^s\left(\frac{r}{r_s}\right)^n + B_n^s\left(\frac{r_s}{r}\right)^{n+1}\right]P_n^1(\cos\theta)$$
$$r_{s-1} \le r \le r_s, \quad (18)$$

where φ is the azimuth angle and P_n^1 is the associated Legendre polynomial. When solving for the boundary conditions, Equations (2)–(4), we find that the coefficients A_n^s and B_n^s are the same as for the radial dipole solution, see section 2.2.1.

In the results section we compare our analytical solution and the FEM simulations with the two published formulas for the potential in the four-sphere model given in Appendices G and H in Nunez and Srinivasan (2006), and in Appendix A in Srinivasan et al. (1998). For comparison we also present the approximate solution provided in Appendix G.4 in Nunez and Srinivasan (2006). Note that two corrections were done to the model presented in Srinivasan et al. (1998) before comparison. First of all, the multiplication factor p/σ_1 was inserted in Equation (A-1), necessary to give potentials in units of volts. Secondly, a superscript in Equation (A-8) was changed, such that the right-hand-side included A_n^2 instead of A_n^3, since this was obviously a typographical error. For more details on the different descriptions of the analytical four-sphere model, see Appendix 1 in Supplementary Materials.

2.3. Finite Element Method

To find the numerical solution of the four-sphere model we solved the Poisson equation (Equation (1)) using the FEM. The first step was to construct a 3D numerical mesh representing the four-sphere head model geometry. We used the open-source program `gmsh` (Geuzaine, 2009), optimized using the `netgen` algorithm (Schöberl, 1997). **Figure 1B** shows the resulting mesh corresponding to the set of radii listed in **Table 1**. Note that our 3D FEM model-geometry implementation consists of five spheres: scalp, skull, CSF, and two spheres together representing the brain tissue. However, the two innermost spheres (the innermost having a radius of 6 cm) are set to have the same conductivity, i.e., the value for brain tissue listed in **Table 1**. Thus, the model is effectively still a four-sphere model. We observed, however, that partitioning the four spheres into five and partitioning the inner sphere to a coarser mesh size reduced the overall mesh size and computational time while retaining the accuracy. The resulting mesh comprised of nearly 12.2 million tetrahedrons (2.1 million odd nodes) and we observed that at this resolution, the numerical results had converged.

The dipole source was treated as two point current sources (Dirac δ functions) and the conductivity was set at each mesh point according to **Table 1**. The electrodes were modeled as ideal point electrodes. Finally, the Poisson Equation (1) and the Neumann boundary condition, Equation (4), were solved numerically with FEM. All FEM simulations were done with the open-source program `FEniCS` (Logg et al., 2012; Alnæs et al., 2015), with Lagrange P2 finite elements. The linear systems were solved by the *PETSc Krylov Solver* employed with the *Conjugate Gradient* method, and the *Incomplete LU* factorization preconditioner. In all the cases we tested, the solutions converged in less than 350 iterations when the residual norms were of the order 1e-07.

2.4. Software

We provide the `Python` code to obtain the potentials from a current dipole placed in a four-sphere head model using (i) the analytical formulation and (ii) the numerical method (FEM). This is available under the GNU General Public License version 3 here: https://github.com/Neuroinflab/fourspheremodel. Additionally, the scripts to generate the figures presented in this manuscript are also included. We tested this code in Anaconda Scientific package on a Linux 64 machine. For easy uptake of this resource and verification, we provide the associated `conda` environment, with all the specific libraries necessary to run this software, and a help file.

3. RESULTS

3.1. Comparison between Analytical and FEM Results

EEG potentials were computed on the scalp surface with the analytical four-sphere model $\Phi(r_4,\theta,\phi)$ and compared with the results from the FEM simulations for a current dipole **p**. To mimic a current dipole set up by cortical neurons, a dipole was placed in the brain layer ($s = 1$) of the four-sphere head model, 1 mm below the brain-CSF boundary. We modeled the current dipole to have dipole moment equal to 10^{-7} Am (two point sources of magnitude 100 μA separated by $d = 1$ mm). Three different dipole orientations were tested: a radial dipole parallel to the z-axis, a tangential dipole parallel to the y-axis and a dipole subtending 45 degrees to the z-axis in the $x = 0$ plane, cf. **Figures 2A,E,I**. We found that the analytical and FEM models gave similar results for both radial and tangential dipoles: the absolute value of the difference was more than two orders of magnitude smaller than the computed EEG potential for all dipole orientations (**Figure 2**). While we show results only for one current dipole in three orthogonal orientations for a single

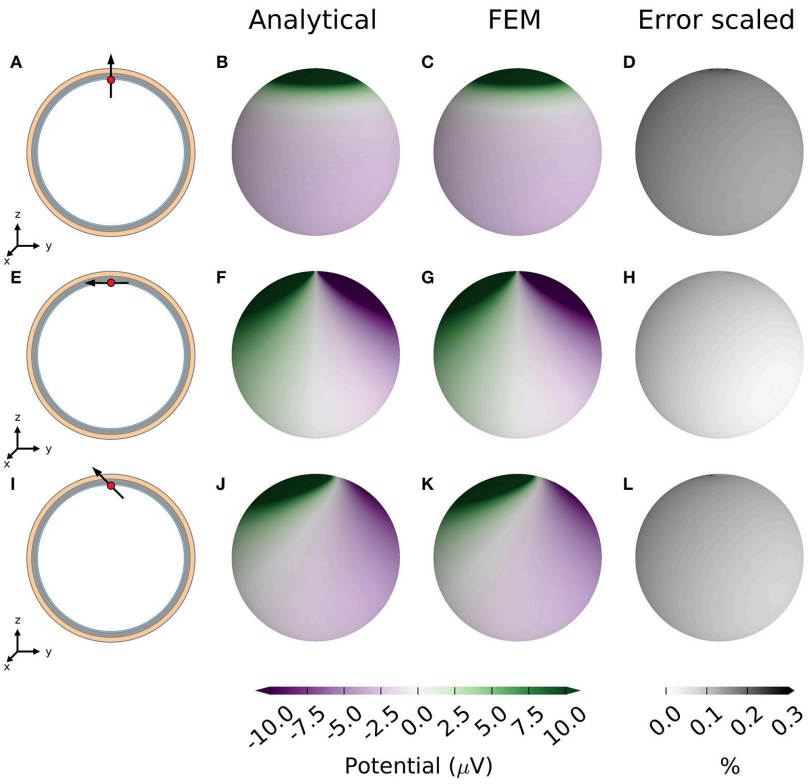

FIGURE 2 | EEG potentials computed with four-sphere model and FEM simulation for radial, tangential, and 45-degree dipole. **(A)** A radial current dipole placed in the brain in the head model as described in **Table 1**. The dipole (black arrow) is located at $\mathbf{r}_Z = [0, 0, 7.8\ \text{cm}]$ (red dot) and has a magnitude 10^{-7} Am to give scalp potentials some tens of microvolts in magnitude, typical for recorded EEG signals. **(B)** Resulting scalp potential calculated with the analytical four-sphere model. **(C)** Scalp potential computed with FEM. **(D)** Absolute difference between results from analytical calculation and FEM, normalized by the global maximum of the magnitude of the potential. The second row, panels **(E–H)** are equivalent to the top row, however for a tangential dipole parallel to the y-axis, in the $x = 0$ plane. The bottom row, panels **(I–L)** are equivalent to the top row, however for a dipole that subtends 45 degrees to the z-axis in the $x = 0$ plane.

position, the scripts provided are generic and accept arbitrary placement, orientation, and moment of the dipole.

A more detailed comparison of EEG potentials predicted by the analytical model and the FEM model is shown in **Figure 3**. Here the computed EEG signal from a radial current dipole is shown for increasing polar angle θ between the current dipole position vector $\mathbf{r}_z$ and the measurement position vector $\mathbf{r}$. The sphere radii and conductivity values are consistent with Nunez and Srinivasan (2006) (**Table 1**). The curve for the analytical results (blue line) overlaps the FEM results (red dots). This figure also demonstrates that previously published formulas give incorrect predictions.

3.2. Limiting Case

As an additional control we tested the limiting case where the conductivity was set to be the same for all four shells, i.e., $\sigma_{\text{brain}} = \sigma_{\text{CSF}} = \sigma_{\text{skull}} = \sigma_{\text{scalp}}$, and equal to that of the brain (**Table 1**). In this case, the resulting scalp potentials should be the same as those calculated from a homogeneous single-sphere head model with radius equal to the scalp radius r_4. For a dipole oriented along the radial direction inside a single homogeneous sphere, the surface potentials are given by Equation (6.7) in Nunez and Srinivasan (2006):

$$\Phi(r_4, \theta) = \frac{p}{4\pi\sigma_1 r_4^2}\left\{\frac{2(\cos\theta - f)}{(1 + f^2 - 2f\cos\theta)^{\frac{3}{2}}} + \frac{1}{f}\left[\frac{1}{(1 + f^2 - 2f\cos\theta)^{\frac{1}{2}}} - 1\right]\right\}, \quad (19)$$

where $f = r_z/r_4$. Comparison between the simplified four-sphere models and the homogeneous single-sphere model showed perfect agreement for the present formulation, while the formulas

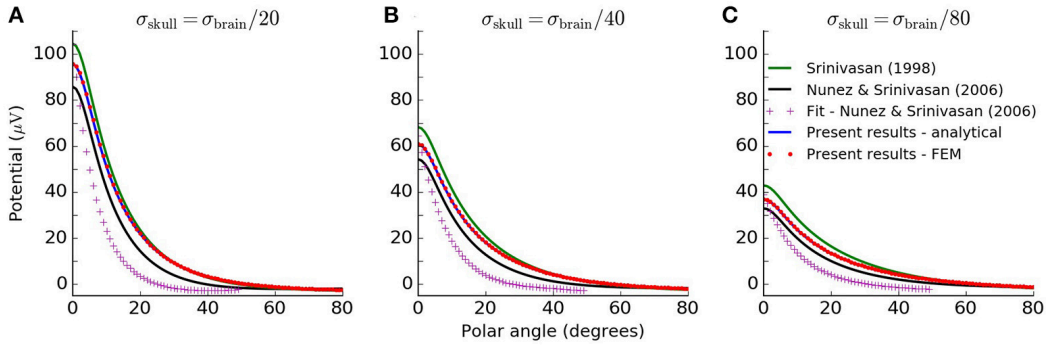

FIGURE 3 | Analytical solution of four-sphere model matches FEM simulation. Scalp potentials from radial current dipole at position $r_z = 7.8$ cm and magnitude 10^{-7} Am to give results in observable range, while still facilitating direct comparison with the original plots in Srinivasan et al. (1998); Nunez and Srinivasan (2006). The resulting scalp potentials are shown for increasing polar angle θ between the current dipole and the measurement position vector. The different lines show calculations with the various formulations of the four-sphere model discussed in this paper, as well as the FEM simulation. The green line shows potentials obtained from Srinivasan et al. (1998), Appendix A, Equations (A1–11). The black line shows results from applying the formulation given in Nunez and Srinivasan (2006), Appendix G, Equations (G.1.9–10) and (G.2.1–10). The approximate solution from Nunez and Srinivasan (2006), Appendix G.4, Equation (G.4.1–3) is given by the pink crosses. The analytical formulation of the four-sphere model presented here is shown in blue, and the FEM simulation is given by the red dots. Panels **A–C** show results for different values of the skull conductivity, i.e., σ_{skull}=$\sigma_{brain}/20$, $\sigma_{brain}/40$ and $\sigma_{brain}/80$, respectively.

listed in Srinivasan et al. (1998) and Nunez and Srinivasan (2006) gave inaccurate predictions (**Figure 4**).

4. DISCUSSION AND CONCLUSIONS

In this note we have revisited the analytical four-sphere model for computing EEG potentials generated by current dipoles in the brain. The main contributions of this paper are the presentation of corrected and validated formulas, as well as the scripts for using them, allowing users to readily apply this important forward model in the field of EEG analysis.

In addition to facilitating the use of the four-sphere model in EEG signal analysis (see, e.g., Wong et al., 2008; Chu et al., 2012; Peraza et al., 2012), the present formulas and scripts will also be a resource for benchmarking comprehensive numerical schemes for computing EEG signals based on detailed head reconstructions using, for example, the FEM (Larson and Bengzon, 2013), or the Boundary Element Method (Brebbia et al., 2012). The FEM approach is not restricted to specific head symmetry assumptions and can take into account an arbitrarily complex spatial distribution of electrical conductivity representing the electrical properties of the head. This is done by constructing a complicated numerical mesh for the head, a task that is often technically challenging. While it is difficult to assure high precision of the given implementation for more complicated and biologically realistic head geometries, the present validated analytical solution for the four-sphere model can serve as one possible ground-truth benchmark. Any FEM or BEM implementation to be trusted, for any analytical model, such as the four-sphere model, should give results in agreement with analytical predictions for different parameter values; here, for example, for various sphere configurations as well as dipole positions and directions. We also provide a set of FEM scripts which model the four-sphere model consistent with the analytical solution.

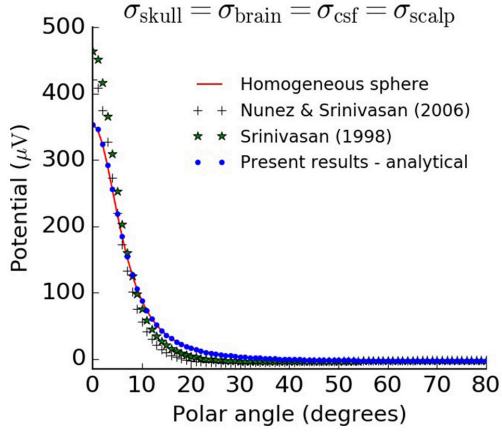

FIGURE 4 | Analytical solution of the four-sphere model satisfies control test for limiting case. Four-sphere model in the limiting case where the conductivity of the skull, CSF, and scalp are equal to the conductivity of the brain, compared to the equivalent model for a single homogeneous sphere, Equation (19). We used a radial dipole of magnitude 10^{-7} Am positioned a distance $r_z = 7.8$ cm away from the center of the sphere, consistent with **Figures 2**, **3**.

Forward models with varying complexity are also used to test the accuracy of inverse methods which estimate the dipole source locations from the potentials and electrode positions. All inverse methods are based on a priori assumptions about the volume and conductivity of the brain. Their implementation requires a forward model encoded either as a lead field matrix or otherwise. The analytical solution of the four-sphere head model provides a way to quickly, yet exhaustively, obtain potentials for a wide range of dipole positions. This makes it an attractive option for testing the accuracy of inverse methods.

AUTHOR CONTRIBUTIONS

SN and TN derived the analytical expressions. CC developed the computational model and did the simulations. AD and GE designed the analytical study. DW designed the computational study. All authors wrote the manuscript.

ACKNOWLEDGMENTS

We thank Paul L. Nunez and Ramesh Srinivasan for useful personal contact. The study received funding from the Simula-UCSD-University of Oslo Research and PhD training (SUURPh) program, funded by the Norwegian Ministry of Education and Research, the European Union Horizon 2020 Research and Innovation Programme under Grant Agreement No. 720270 [Human Brain Project (HBP) SGA1], from the EC-FP7-PEOPLE sponsored NAMASEN Marie-Curie ITN grant 264872 and the Polish National Science Centre's OPUS grant (2015/17/B/ST7/04123).

SUPPLEMENTARY MATERIAL

The Supplementary Material for this article can be found online at: https://www.frontiersin.org/articles/10.3389/fnhum.2017.00490/full#supplementary-material

REFERENCES

Alnæs, M. S., Blechta, J., Hake, J., Johansson, A., Kehlet, B., Logg, A., et al. (2015). The FEniCS Project Version 1.5. *Arch. Numer. Softw.* 3:100. doi: 10.11588/ans.2015.100.20553

Bangera, N. B., Schomer, D. L., Dehghani, N., Ulbert, I., Cash, S., Papavasiliou, S., et al. (2010). Experimental validation of the influence of white matter anisotropy on the intracranial eeg forward solution. *J. Comput. Neurosci.* 29, 371–387. doi: 10.1007/s10827-009-0205-z

Brebbia, C. A., Telles, J. C. F., and Wrobel, L. C. (2012). *Boundary Element Techniques: Theory and Applications in Engineering*. Berlin: Springer Science & Business Media.

Chu, C. J., Kramer, M. A., Pathmanathan, J., Bianchi, M. T., Westover, M. B., Wizon, L., et al. (2012). Emergence of stable functional networks in long-term human electroencephalography. *J. Neurosci.* 32, 2703–2713. doi: 10.1523/JNEUROSCI.5669-11.2012

De Munck, J. C., Wolters, C. H., and Clerc, M. (2012). EEG and MEG forward modeling. *Handb. Neural Activity Measure.* 1, 192–256. doi: 10.1017/CBO9780511979958.006

Geuzaine, C. (2009). Gmsh: a three-dimensional finite element mesh generator with built-in pre- and post-processing facilities. *Int. J. Numer. Methods Eng.* 79, 1309–1331. doi: 10.1002/nme.2579

Hämäläinen, M., Haari, R., Ilmoniemi, R. J., Knuutila, J., and Lounasmaa, O. V. (1993). Magnetoencephalography theory, instrumentation, and application to noninvasive studies of the working human brain. *Rev. Modern Phys.* 65, 413–497. doi: 10.1103/RevModPhys.65.413

Huang, Y., Parra, L. C., and Haufe, S. (2016). The New York Heada precise standardized volume conductor model for EEG source localization and tES targeting. *NeuroImage* 140, 150–162. doi: 10.1016/j.neuroimage.2015.12.019

Kehlet, B. (2016). *mshr*. Available online at: https://bitbucket.org/fenics-project/mshr.

Larson, M. G., and Bengzon, F. (2013). *The Finite Element Method: Theory, Implementation, and Applications*. Berlin; Heidelberg: Springer-Verlag.

Logg, A., Mardal, K.-A., and Wells, G. N., (Eds.). (2012). *Automated Solution of Differential Equations by the Finite Element Method, Volume 84* of *Lecture Notes in Computational Science and Engineering*. Berlin; Heidelberg: Springer.

Nunez, P. L., and Srinivasan, R. (2006). *Electric Fields of the Brain*. New York, NY: Oxford University Press.

Peraza, L. R., Asghar, A. U., Green, G., and Halliday, D. M. (2012). Volume conduction effects in brain network inference from electroencephalographic recordings using phase lag index. *J. Neurosci. Methods* 207, 189–199. doi: 10.1016/j.jneumeth.2012.04.007

Pettersen, K. H., Lindén, H., Dale, A. M., and Einevoll, G. T. (2012). Extracellular spikes and CSD. *Handb. Neural Activity Measure.* 1, 92–135. doi: 10.1017/CBO9780511979958.004

Sanei, S., and Chambers, J. (2007). *EEG Signal Processing, 2007*. The Atrium, Southern Gate, Chichester, West Sussex PO19 8SQ, England: John Wiley & Sons Ltd.

Schöberl, J. (1997). NETGEN an advancing front 2D/3D-mesh generator based on abstract rules. *Comput. Visual. Sci.* 1, 41–52. doi: 10.1007/s007910050004

Schomer, D. L., and da Silva, F. L. (2012). *Niedermeyer's Electroencephalography: Basic Principles, Clinical Applications, and Related Fields*. Philadelphia, PA: Wolters Kluwer Health.

Srinivasan, R., Nunez, P. L., and Silberstein, R. B. (1998). Spatial filtering and neocortical dynamics: estimates of EEG coherence. *IEEE Trans. Biomed. Eng.* 45, 814–826. doi: 10.1109/10.686789

Vorwerk, J., Cho, J.-H., Rampp, S., Hamer, H., Knsche, T. R., and Wolters, C. H. (2014). A guideline for head volume conductor modeling in EEG and MEG. *NeuroImage* 100, 590–607. doi: 10.1016/j.neuroimage.2014.06.040

Wong, D. K., Grosenick, L., Uy, E. T., Guimaraes, M. P., Carvalhaes, C. G., Desain, P., et al. (2008). Quantifying inter-subject agreement in brain-imaging analyses. *NeuroImage* 39, 1051–1063. doi: 10.1016/j.neuroimage.2007.07.064

Conflict of Interest Statement: The authors declare that the research was conducted in the absence of any commercial or financial relationships that could be construed as a potential conflict of interest.

APPENDIX: MATHEMATICAL DERIVATION OF FOUR-SPHERE MODEL

The four-sphere model equations for radial and tangential dipoles are given in Equations (5), (6), (17) and (18). Here we describe how the seven unknown coefficients (Equation (7)–(16) can be determined by the seven boundary conditions (Equations (2)–(4)). We show the calculations for radial dipoles only, however, the derivation presented applies to both radial and tangential dipoles, due to similarity of the models.

We start by finding the derivative of $\Phi^s(r,\theta)$ from Equation (6):

$$\frac{\partial}{\partial r}\Phi^s(r,\theta) = \frac{p}{4\pi\sigma_1 r_z^2}\sum_{n=1}^{\infty}\left[A_n^s\left(\frac{n}{r}\right)\left(\frac{r}{r_s}\right)^n - B_n^s\left(\frac{n+1}{r}\right)\left(\frac{r_s}{r}\right)^{n+1}\right]nP_n(\cos\theta).$$

For the Neumann boundary condition on the scalp boundary, Equation (4), we make use of the relation above, and get:

$$\frac{\partial}{\partial r}\Phi^4(r_4,\theta) = \frac{p}{4\pi\sigma_1 r_z^2}\sum_{n=1}^{\infty}\left[A_n^4\left(\frac{n}{r_4}\right)\left(\frac{r_4}{r_4}\right)^n - B_n^4\left(\frac{n+1}{r_4}\right)\left(\frac{r_4}{r_4}\right)^{n+1}\right]nP_n(\cos\theta) = 0.$$

$$\begin{aligned}
&\Rightarrow A_n^4\left(\frac{n}{r_4}\right) - B_n^4\left(\frac{n+1}{r_4}\right) = 0 \qquad \forall\, n \\
&\Rightarrow B_n^4 = \frac{n}{n+1}A_n^4. \qquad (20)
\end{aligned}$$

Next, we apply the Dirichlet boundary condition on the skull boundary, i.e., Equation (2) for $s = 3$:

$$\Phi^4(r_3) = \Phi^3(r_3)$$

$$\frac{p}{4\pi\sigma_1 r_z^2}\sum_{n=1}^{\infty}\left[A_n^4\left(\frac{r_3}{r_4}\right)^n + B_n^4\left(\frac{r_4}{r_3}\right)^{n+1}\right]nP_n(\cos\theta) = \frac{p}{4\pi\sigma_1 r_z^2}\sum_{n=1}^{\infty}\left[A_n^3\left(\frac{r_3}{r_3}\right)^n + B_n^3\left(\frac{r_3}{r_3}\right)^{n+1}\right]nP_n(\cos\theta)$$

$$A_n^4\left(\frac{r_3}{r_4}\right)^n + B_n^4\left(\frac{r_4}{r_3}\right)^{n+1} = A_n^3 + B_n^3\,.$$

Inserting the expression for B_n^4, Equation (20), using the notation $r_{ij} \equiv r_i/r_j$:

$$A_n^4\left(r_{34}^n + \frac{n}{n+1}r_{43}^{n+1}\right) = A_n^3 + B_n^3$$

$$\Rightarrow A_n^4 = \frac{n+1}{n}\frac{A_n^3 + B_n^3}{\frac{n+1}{n}r_{34}^n + r_{43}^{n+1}}. \qquad (21)$$

Note that the multiplication factor $\frac{n+1}{n}$ is missing in Nunez and Srinivasan (2006), Appendix G, Equation (G.2.9).

Further, we look at the Neumann boundary condition on the skull boundary, i.e. Equation (3) for $s = 3$, using the notation $\sigma_{ij} \equiv \sigma_i/\sigma_j$:

$$\begin{aligned}
\sigma_4 \frac{\partial \Phi^4}{\partial r}(r_3) &= \sigma_3 \frac{\partial \Phi^3}{\partial r}(r_3) \\
\sigma_4 \left(A_n^4 \frac{n}{r_3} \left(\frac{r_3}{r_4}\right)^n - B_n^4 \frac{n+1}{r_3} \left(\frac{r_4}{r_3}\right)^{n+1} \right) &= \sigma_3 \left(A_n^3 \frac{n}{r_3} \left(\frac{r_3}{r_3}\right)^n - B_n^3 \frac{n+1}{r_3} \left(\frac{r_3}{r_3}\right)^{n+1} \right) \\
n A_n^4 r_{34}^n - (n+1) B_n^4 r_{43}^{n+1} &= \sigma_{34} \left(n A_n^3 - (n+1) B_n^3 \right).
\end{aligned}$$

Inserting Equation (20),

$$n A_n^4 \left(r_{34}^n - r_{43}^{n+1} \right) = \sigma_{34} \left(n A_n^3 - (n+1) B_n^3 \right),$$

and applying Equation (21),

$$n \, \frac{n+1}{n} \frac{A_n^3 + B_n^3}{\frac{n+1}{n} r_{34}^n + r_{43}^{n+1}} \left(r_{34}^n - r_{43}^{n+1} \right) = \sigma_{34} \left(n A_n^3 - (n+1) B_n^3 \right).$$

From this we find that,

$$B_n^3 = \frac{\frac{n}{n+1}\sigma_{34} - \frac{r_{34}^n - r_{43}^{n+1}}{\frac{n+1}{n} r_{34}^n + r_{43}^{n+1}}}{\sigma_{34} + \frac{r_{34}^n - r_{43}^{n+1}}{\frac{n+1}{n} r_{34}^n + r_{43}^{n+1}}} A_n^3,$$

which we can write as:

$$B_n^3 = V_n A_n^3 \qquad \text{where} \qquad V_n = \frac{\frac{n}{n+1}\sigma_{34} - \frac{r_{34}^n - r_{43}^{n+1}}{\frac{n+1}{n} r_{34}^n + r_{43}^{n+1}}}{\sigma_{34} + \frac{r_{34}^n - r_{43}^{n+1}}{\frac{n+1}{n} r_{34}^n + r_{43}^{n+1}}}. \tag{22}$$

Here, the σ_{34}-term in the numerator of V_n differs from Nunez and Srinivasan (2006) (Equation (G.2.1)) and Srinivasan et al. (1998) (Equation (A-2)) in the sense that the multiplication factor is inverted.

For the CSF Dirichlet boundary condition we can follow the same procedure as for the skull Dirichlet boundary condition, and we get,

$$\begin{aligned}
A_n^3 \left(\frac{r_2}{r_3}\right)^n + B_n^3 \left(\frac{r_3}{r_2}\right)^{n+1} &= A_n^2 \left(\frac{r_2}{r_2}\right)^n + B_n^2 \left(\frac{r_2}{r_2}\right)^{n+1} \\
\Rightarrow A_n^3 r_{23}^n + B_n^3 r_{32}^{n+1} &= A_n^2 + B_n^2.
\end{aligned}$$

Inserting the expression for B_n^3 from Equation (22):

$$\begin{aligned} A_n^3\left(r_{23}^n + V_n r_{32}^{n+1}\right) &= A_n^2 + B_n^2 \\ \Rightarrow A_n^3 &= \frac{A_n^2 + B_n^2}{r_{23}^n + r_{32}^{n+1} V_n}\,. \end{aligned} \tag{23}$$

Here, we notice a typographical error in the expression for A_n^3 in Srinivasan et al. (1998), Equation (A-8): there should be an A_n^2-term in the numerator, not A_n^3.

Next, we apply the Neumann CSF boundary condition. Starting out with,

$$\sigma_3 \frac{\partial \Phi^3}{\partial r}(r_2) = \sigma_2 \frac{\partial \Phi^2}{\partial r}(r_2),$$

and making use of the expressions for B_n^3 and A_n^3, we find that,

$$B_n^2 = Y_n A_n^2 \qquad \text{where } Y_n = \frac{\frac{n}{n+1}\sigma_{23} - \frac{\frac{n}{n+1} r_{23}^n - V_n r_{32}^{n+1}}{r_{23}^n + V_n r_{32}^{n+1}}}{\sigma_{23} + \frac{\frac{n}{n+1} r_{23}^n - V_n r_{32}^{n+1}}{r_{23}^n + V_n r_{32}^{n+1}}}. \tag{24}$$

Note that there's a subtle difference between the Y_n presented here, and Nunez and Srinivasan (2006) (Equation (G.2.2)) and Srinivasan et al. (1998) (Equation (A-3)): The second term of the numerator is a fraction. Here, the r_{23}^n factor should not be multiplied by the whole fraction, but rather only the $\frac{n}{n+1}$-term in the numerator.

The Dirichlet boundary condition on the brain boundary is:

$$\begin{aligned} \Phi^2(r = r_1) &= \Phi^1(r = r_1) \\ A_n^2 \left(\frac{r_1}{r_2}\right)^n + B_n^2 \left(\frac{r_2}{r_1}\right)^{n+1} &= A_n^1 \left(\frac{r_1}{r_1}\right)^n + \left(\frac{r_z}{r_1}\right)^{n+1} \\ A_n^2 r_{12}^n + B_n^2 r_{21}^{n+1} &= A_n^1 + r_{z1}^{n+1}. \end{aligned}$$

Inserting the expression for B_n^2 from Equation (24):

$$\begin{aligned} A_n^2\left(r_{12}^n + Y_n r_{21}^{n+1}\right) &= A_n^1 + r_{z1}^{n+1} \\ \Rightarrow A_n^2 &= \frac{A_n^1 + r_{z1}^{n+1}}{r_{12}^n + r_{21}^{n+1} Y_n}. \end{aligned} \tag{25}$$

Finally, we solve the Neumann boundary condition on the brain boundary,

$$\sigma_2 \frac{\partial \Phi^2}{\partial r}(r_1) = \sigma_1 \frac{\partial \Phi^1}{\partial r}(r_1).$$

Inserting the expressions for A_n^2 and B_n^2 from Equations (25) and (24), we find,

$$A_n^1 = \frac{\frac{n+1}{n}\sigma_{12} + Z_n}{\sigma_{12} - Z_n}\, r_{z1}^{n+1} \qquad \text{where } Z_n = \frac{r_{12}^n - \frac{n+1}{n} Y_n r_{21}^{n+1}}{r_{12}^n + Y_n r_{21}^{n+1}}. \tag{26}$$

The A_n^1-term in Srinivasan et al. (1998) (Equation (A-5)) is not consistent with Nunez and Srinivasan (2006) (Equation (G.2.4)) equal to Equation (26): a multiplication factor p/σ_1 is lacking, r_{zl}^{n-1} should be r_{z1}^{n-1}. Moreover, B_n^1 needs to be defined in order for the model description in Srinivasan et al. (1998), Appendix A to give potentials in brain tissue.

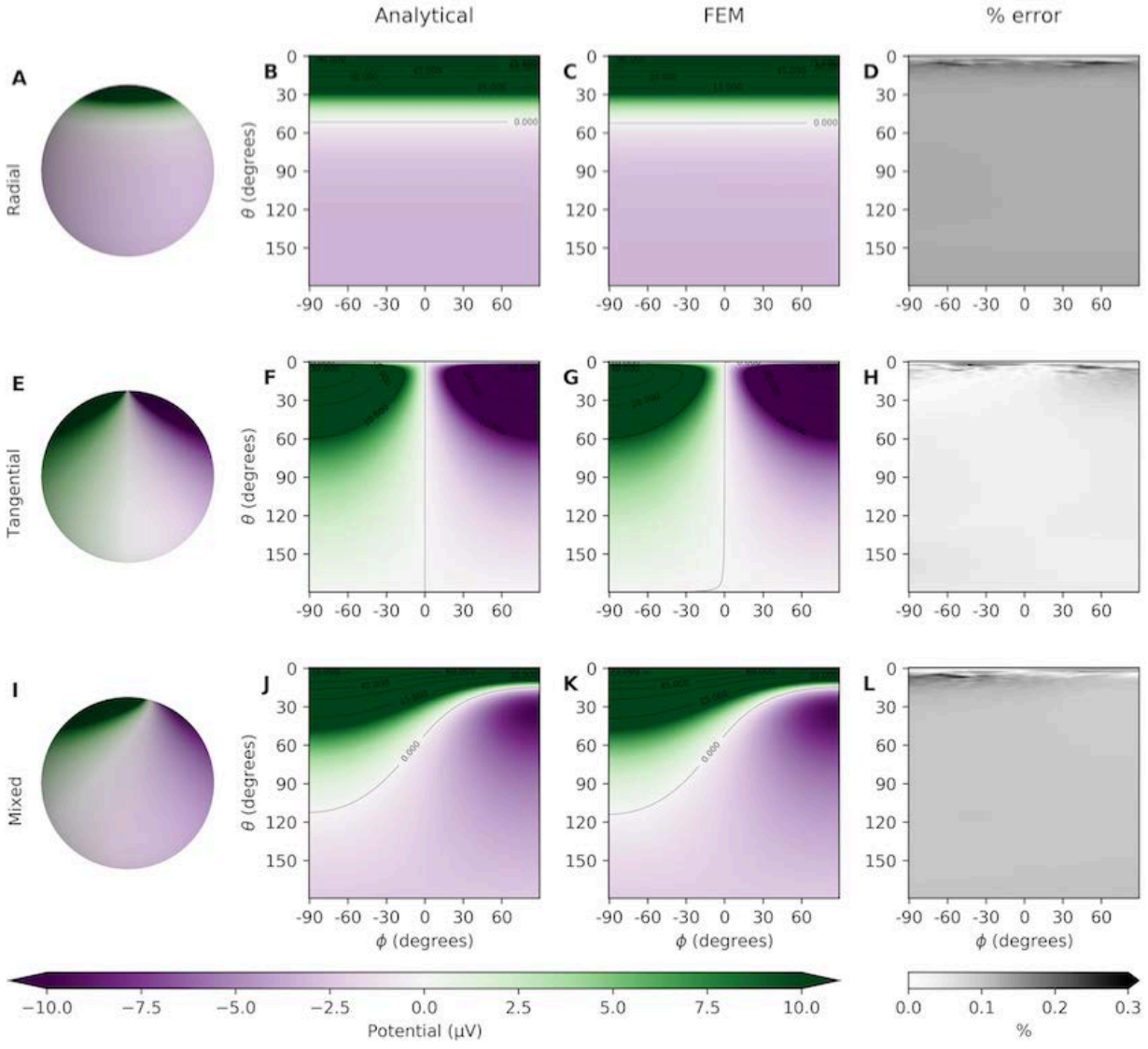
Analytical
FEM
% error
A
B
C
D
Radial
E
F
G
H
Tangential
I
J
K
L
Mixed
θ (degrees)
ϕ (degrees)
0
30
60
90
120
150
-90 -60 -30 0 30 60
0.000
−10.0 −7.5 −5.0 −2.5 0.0 2.5 5.0 7.5 10.0
Potential (μV)
0.0 0.1 0.2 0.3
%

Paper II

Multimodal modeling of neural network activity: computing LFP, ECoG, EEG, and MEG signals with LFPy 2.0

II

frontiers in Neuroinformatics

ORIGINAL RESEARCH
published: 18 December 2018
doi: 10.3389/fninf.2018.00092

Multimodal Modeling of Neural Network Activity: Computing LFP, ECoG, EEG, and MEG Signals With LFPy 2.0

Espen Hagen[1,2*†], *Solveig Næss*[3†], *Torbjørn V. Ness*[2] *and Gaute T. Einevoll*[1,2*]

[1] *Department of Physics, University of Oslo, Oslo, Norway,* [2] *Faculty of Science and Technology, Norwegian University of Life Sciences, Ås, Norway,* [3] *Department of Informatics, University of Oslo, Oslo, Norway*

Recordings of extracellular electrical, and later also magnetic, brain signals have been the dominant technique for measuring brain activity for decades. The interpretation of such signals is however nontrivial, as the measured signals result from both local and distant neuronal activity. In volume-conductor theory the extracellular potentials can be calculated from a distance-weighted sum of contributions from transmembrane currents of neurons. Given the same transmembrane currents, the contributions to the magnetic field recorded both inside and outside the brain can also be computed. This allows for the development of computational tools implementing forward models grounded in the biophysics underlying electrical and magnetic measurement modalities. LFPy (LFPy.readthedocs.io) incorporated a well-established scheme for predicting extracellular potentials of individual neurons with arbitrary levels of biological detail. It relies on NEURON (neuron.yale.edu) to compute transmembrane currents of multicompartment neurons which is then used in combination with an electrostatic forward model. Its functionality is now extended to allow for modeling of networks of multicompartment neurons with concurrent calculations of extracellular potentials and current dipole moments. The current dipole moments are then, in combination with suitable volume-conductor head models, used to compute non-invasive measures of neuronal activity, like scalp potentials (electroencephalographic recordings; EEG) and magnetic fields outside the head (magnetoencephalographic recordings; MEG). One such built-in head model is the four-sphere head model incorporating the different electric conductivities of brain, cerebrospinal fluid, skull and scalp. We demonstrate the new functionality of the software by constructing a network of biophysically detailed multicompartment neuron models from the Neocortical Microcircuit Collaboration (NMC) Portal (bbp.epfl.ch/nmc-portal) with corresponding statistics of connections and synapses, and compute *in vivo*-like extracellular potentials (local field potentials, LFP; electrocorticographical signals, ECoG) and corresponding current dipole moments. From the current dipole moments we estimate corresponding EEG and MEG signals using the four-sphere head model. We also show strong scaling performance of LFPy with different numbers of

OPEN ACCESS

Edited by:
Andrew P. Davison,
FRE3693 Unité de Neuroscience, Information et Complexité (UNIC), France

Reviewed by:
Jorge J. Riera,
Florida International University, United States
Denis A. Engemann,
Inria Saclay - Île-de-France Research Centre, France

****Correspondence:***
Espen Hagen
espen.hagen@fys.uio.no
Gaute T. Einevoll
gaute.einevoll@nmbu

†These authors have contributed equally to this work

Received: *17 March 2018*
Accepted: *21 November 2018*
Published: *18 December 2018*

Citation:
Hagen E, Næss S, Ness TV and Einevoll GT (2018) Multimodal Modeling of Neural Network Activity: Computing LFP, ECoG, EEG, and MEG Signals With LFPy 2.0. Front. Neuroinform. 12:92. doi: 10.3389/fninf.2018.00092

message-passing interface (MPI) processes, and for different network sizes with different density of connections. The open-source software LFPy is equally suitable for execution on laptops and in parallel on high-performance computing (HPC) facilities and is publicly available on GitHub.com.

Keywords: modeling, neuron, neuronal network, local field potential, LFP, ECoG, EEG, MEG

1. INTRODUCTION

Ever since the 1950s, electrical recordings with sharp electrodes have been the most important method for studying *in vivo* activity in neurons and neural networks (Li and Jasper, 1953). In the last couple of decades, however, a host of new measurement methods has been developed and refined. One key development is the new generation of multicontact electrodes allowing for high-density electrical recordings across cortical laminae and areas, and the accompanying resurgence of interest in the low-frequency part of the extracellular signal, the "local field potential" (LFP) (Buzsáki, 2004; Buzsáki et al., 2012; Einevoll et al., 2013). The LFP is a population measure reflecting how dendrites integrate synaptic inputs, insight that cannot be obtained from measurement of spikes from a handful of neurons (Einevoll et al., 2013). Many new optical techniques for probing cortical activity have also been developed. Of particular interest is *two-photon calcium imaging*, which can measure the action potentials of individual neurons deep into cortical tissue (Helmchen and Denk, 2005), and *voltage-sensitive dye imaging (VSDI)*, which measures the average membrane potential across dendrites close to the cortical surface (Grinvald and Hildesheim, 2004). These add to the more established systems-level methods such as *electroencephalography* (*EEG*, Nunez and Srinivasan, 2006), which measures electrical potentials at the scalp, and *magnetoencephalography* (*MEG*, Hämäläinen et al., 1993) which measures the magnetic field outside the head.

A standard way of analyzing such neurophysiological data has been to look for correlations between measurements and how the subject is stimulated or behaves. For example, most of what we have learned about neural representation of visual information in visual cortex has come from receptive-field studies where the correlation between measured spikes and presented visual stimuli is mapped out (Hubel and Wiesel, 1959). The same approach has been used to map out the receptive fields for other sensory modalities (sound, touch, etc.), objects and celebrities (Quiroga et al., 2005), or the spatial location of the animal (O'Keefe and Dostrovsky, 1971; Hafting et al., 2005).

This purely statistical approach has limitations, however. For one, it only provides estimates for the neural representation and gives no direct insight into the circuit mechanisms giving rise to these representations. Secondly, the receptive field is inherently a *linear* measure of activity (Dayan and Abbott, 2001) and cannot in general capture non-linear network dynamics. The receptive field in primary visual cortex depends, for example, strongly on stimulation of the surrounding regions of visual space, an inherently non-linear effect (Blakemore and Tobin, 1972). For other cortical measurements, such as the LFP or VSDI, a statistical analysis is further complicated by the fact that the signals reflect activity in neuron populations rather than individual neurons (Petersen et al., 2003; Einevoll et al., 2013). This makes commonly-used statistical signal measures such as power spectra, correlation, coherence, and functional connectivity difficult to interpret in terms of activity in neurons and networks (Einevoll et al., 2013).

An alternative approach to a purely statistical analysis is, following in the tradition of physics, to formulate candidate hypotheses precisely in mathematics and then compute what each hypothesis would predict for the different types of measurements. Until now candidate cortical network models have typically only predicted spiking activity, thus preventing a proper comparison with measurements other than single-unit and multiunit recordings. To take full advantage of all available experiments, there is a need for biophysics-based forward-modeling tools for predicting other measurement modalities from candidate network models (Brette and Destexhe, 2012), that is, develop software that faithfully models the various types of measurements themselves. To facilitate the forward-modeling of extracellular potentials, both LFPs and spikes [i.e., either single-unit or multi-unit activity (MUA)], we developed LFPy (LFPy.readthedocs.io, Lindén et al., 2014), a Python tool using the NEURON simulator (Carnevale and Hines, 2006) and its Python interface (Hines et al., 2009).

The first release of LFPy (Lindén et al., 2014) implemented a well-established forward-modeling scheme where the extracellular potential is computed in a two-step process (Holt and Koch, 1999): First, the transmembrane currents of multicompartment neuron models are computed using NEURON. Second, the extracellular potential is computed as a weighted sum over contributions from the transmembrane currents from each compartment with weights prescribed by volume-conductor theory for an infinite volume conductor. In LFPy these functions are provided by a set of Python classes that can be instantiated to represent the cell, synapses, stimulation devices and extracellular electric measurement devices. By now this forward-model method has been used in a number of studies, for example to model extracellular spike waveforms (Holt and Koch, 1999; Gold et al., 2006, 2007; Pettersen and Einevoll, 2008; Pettersen et al., 2008; Franke et al., 2010; Schomburg et al., 2012; Thorbergsson et al., 2012; Reimann et al., 2013; Hagen et al., 2015; Ness et al., 2015; Cserpán et al., 2017; Miceli et al., 2017), LFP signals (Pettersen et al., 2008; Lindén et al., 2010, 2011; Gratiy et al., 2011; Makarova et al., 2011; Schomburg et al., 2012; Łęski et al., 2013; Martín-Vázquez et al., 2013, 2015; Reimann et al., 2013; Głąbska et al., 2014, 2016; Mazzoni et al., 2015; Sinha and Narayanan, 2015; Taxidis et al., 2015; Tomsett et al., 2015; Hagen

et al., 2016, 2017; Ness et al., 2016, 2018) and recently axonal LFP contributions (McColgan et al., 2017). Some of these used LFPy to predict extracellular potentials (Łęski et al., 2013; Lindén et al., 2014; Hagen et al., 2015, 2016, 2017; Mazzoni et al., 2015; Ness et al., 2015, 2016, 2018; Tomsett et al., 2015; Miceli et al., 2017; Luo et al., 2018), while in Heiberg et al. (2016) LFPy was used to construct a small-world LGN network without predictions of extracellular potentials. Further, in Uhlirova et al. (2016) LFPy was used to compute neuronal membrane potentials.

Here we present a substantially extended version of LFPy, termed LFPy 2.0, including several new features, that is, support for (i) simulations of networks of multicompartmental neuron models, (ii) computation of LFP/MUA with anisotropic electrical conductivity, (iii) computation of LFP/MUA in the presence of step-wise varying electrical conductivity (such as at the interface between cortical gray matter and white matter), (iv) computation of ECoG signals (i.e., electrical potentials recorded at the cortical surface), (v) computation of EEG signals, and (vi) computation of MEG signals, see illustration in **Figure 1**. To illustrate the computation of these measures by LFPy 2.0 we show in **Figure 2** the LFP, EEG, and MEG signals generated by a single synaptic input onto a single simplified "pyramidal" neuron. As both electric and magnetic signals sum linearly, the recorded signals in real applications will stem from the sum of a large number of such contributions.

Potential uses of LFPy 2.0 include (but are not limited to): Comparison of candidate neuron and network models with arbitrary levels of detail to experiments in order to aid the interpretation of experimental data, validation of data analysis methods by testing them on synthetic (model-based) measurements with known underlying ground truth, and comparison of model predictions from different types of models with different levels of detail.

The manuscript is organized as follows: In section 2 we first review the biophysical forward-modeling scheme used to predict extracellular potentials in different volume-conductor models. Then we describe calculations of current dipole moments and corresponding calculation of EEG and MEG signals. We further describe the implementation of an example network using available data and biophysically detailed cell models from the Blue Brain Project's Neocortical Microcircuit Collaboration (NMC) Portal, and various technical details. In section 3 we investigate the outcome of our example parallel network simulation and corresponding measurements, and assess parallel performance of LFPy when running on HPC facilities. In section 4 we outline implications of this work and discuss possible future applications and developments of the software. In the **Appendix** we describe new LFPy classes and corresponding code examples for set-up of networks.

2. METHODS

2.1. Multicompartment Modeling

2.1.1. Calculation of Transmembrane Currents

The origin of extracellular potentials is mainly transmembrane currents (Buzsáki et al., 2012; Einevoll et al., 2013), even though diffusion of ions in the extracellular space alone also can give rise to such potentials (Halnes et al., 2016). In the presently (and frequently) used forward modeling approach, these transmembrane currents are obtained from spatially discretized multicompartment neuron models (De Schutter and Van Geit, 2009) which allow for high levels of biophysical and morphological detail. Such models have historically been used to model spatiotemporal variations in the membrane voltages $V^{\mathrm{m}}(x,t)$, where x denotes the position along an unbranched piece of dendritic cable. From this cable theory it also follows that the transmembrane current density, that is, the transmembrane current per unit length of membrane, for any smooth and homogeneous cable section is given by (Koch, 1999):

$$i^{\mathrm{m}}(x,t) = \frac{1}{r^{\mathrm{i}}}\frac{\partial^2 V^{\mathrm{m}}(x,t)}{\partial x^2}\,, \tag{1}$$

where r^{i} represents the axial resistance per unit length along the cable. Assuming a homogeneous current density per unit length i^{m} along a single compartment with length Δs, the total transmembrane current $I^{\mathrm{m}} = i^{\mathrm{m}}\Delta s$.

As in the first release of LFPy (Lindén et al., 2014), we rely on the NEURON simulation environment (Carnevale and Hines, 2006) to compute transmembrane currents. As of NEURON v7.4, a faster and direct method of accessing transmembrane currents is provided through its `CVode.use_fast_imem()` method, which we now utilize in an exclusive manner. NEURON's "extracellular" mechanism is thus no longer used to predict extracellular potentials (cf. Lindén et al., 2014, section 5.6). Note, however, that this mechanism itself is still used when an external extracellular potential is imposed as a boundary condition outside each compartment using the `Cell.insert_v_ext()` class method.

2.1.2. Calculation of Axial Currents

To compute the magnetic fields stemming from electrical activity in neurons, the axial currents within cells are needed (Hämäläinen et al., 1993). The axial current for the cable is given by (Koch, 1999):

$$I^{\mathrm{a}}(x,t) = -\frac{1}{r^{\mathrm{i}}}\frac{\partial V^{\mathrm{m}}(x,t)}{\partial x}\,. \tag{2}$$

Assuming homogeneous axial current density between the midpoints of two neighboring compartments n and $n+1$ along the cable, one may obtain the axial current from Ohm's law:

$$I^{\mathrm{a}}_{n,n+1}(t) = \frac{V^{\mathrm{m}}_{n+1}(t) - V^{\mathrm{m}}_{n}(t)}{r^{\mathrm{i}}_{n,n+1}\Delta s_{n,n+1}} = \frac{V^{\mathrm{m}}_{n+1}(t) - V^{\mathrm{m}}_{n}(t)}{R^{\mathrm{i}}_{n,n+1}}\,. \tag{3}$$

Here, V^{m}_{n} and V^{m}_{n+1} are the compartment midpoint membrane potentials, $r^{\mathrm{i}}_{n,n+1}$ the axial resistance per unit length between the two compartments, $\Delta s_{n,n+1}$ the distance between compartment midpoints and $R^{\mathrm{i}}_{n,n+1}$ the corresponding axial resistance.

Further, we outline how axial currents from complex reconstructed neuron morphologies are calculated in LFPy 2.0, and provide the technical implementation details in Algorithm A1 in the **Appendix**. For a more comprehensive explanation, see Næss (2015). The corresponding

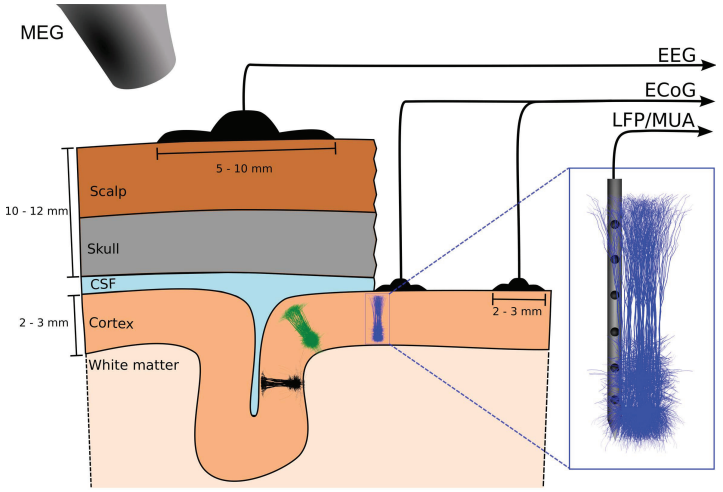

FIGURE 1 | Illustration of measurement signals computed by LFPy 2.0. The figure illustrates the EEG, ECoG, LFP/MUA (linear multielectrode) and MEG recordings of electrical and magnetic signals stemming from populations of cortical neurons. Here three separate cortical populations are depicted. EEG electrodes are placed on the scalp, ECoG electrodes on the cortical surface, while the LFP and MUA both are recorded by electrodes placed inside cortex. In MEG the tiny magnetic fields stemming from brain activity is measured by SQUIDs placed outside the head. The MUA signal, that is, the high-frequency part of the recorded extracellular potential inside cortex, measures spikes from neurons in the immediate vicinity of the electrode contact, typically less than 100 μm away (Buzsáki, 2004; Pettersen and Einevoll, 2008; Pettersen et al., 2008). The "mesoscopic" LFP and ECoG signals will typically contain information from neurons within a few hundred micrometers or millimeters from the recording contact (Einevoll et al., 2013), while the "macroscopic" EEG and MEG signals will have contributions from cortical populations even further away (Hämäläinen et al., 1993; Nunez and Srinivasan, 2006).

implementation is in LFPy 2.0 provided by the class method `Cell.get_axial_currents_from_vmem()`.

In NEURON, a *section* is a continuous piece of cable split into an arbitrary number of *segments* (compartments) indexed by n. Morphologies with branch points must therefore be represented by more than one section. We here denote the relative length from start to end point of each section by $\chi \in [0, 1]$, see **Figure 3A**. All segments within the morphology except the initial segment of the *root* section (typically the somatic section) have a *parent* segment indexed by f. Each segment in a section can have an arbitrary number of *child* segments, thus a parent segment is the segment which connects to the start point of a *child* segment. We also distinguish between start-, mid- and end-point coordinates of each segment (**Figure 3A**).

In **Figures 3B,C** we illustrate the simplest possible calculation of axial current between the midpoints of two neighboring segments f and n belonging to the same section. Their corresponding membrane voltages are V_f^{m} and V_n^{m}, separated by a total (series) axial resistance R_{fn}^{i}. From NEURON we can easily obtain the axial resistance between the segment midpoint and the segment's parent node. The parent node is here the midpoint of the parent segment, as the child and parent belong to the same section. Therefore, NEURON gives us the total axial resistance R_{fn}^{i} directly, in this case. The axial current magnitude between segment midpoints is then trivial to compute using Ohm's law (Equation 3), but as the currents flowing within segments f and n may not lie on the same axis, we differentiate between the current magnitudes I_m^{a} and I_{m+1}^{a}, their axial line element vectors $\mathbf{d}_m$ and $\mathbf{d}_{m+1}$, and the midpoints of each $\mathbf{r}_m$ and $\mathbf{r}_{m+1}$ (**Figure 3C**). The corresponding current indices are denoted by m and $m + 1$ as detailed in Algorithm A1 (**Appendix**).

Figure 3D represents the case where the parent and child segments f and n belong to different sections. The child segment is here the *bottom segment* in a section, and it is connected to the end point of f. As the parent node (the node the child segment connects to on the parent segment) is here located between the two segments, NEURON does in this case not give us the total axial resistance directly. Instead, the total (series) axial resistance $R_{fn}^{\mathrm{i}} = R_f^{\mathrm{i}} + R_n^{\mathrm{i}}$ must first be computed to estimate the axial current. R_f^{i} is here the resistance between the parent midpoint and the connecting node, and R_n^{i} the resistance between the parent node and the segment midpoint.

NEURON allows child sections to be connected anywhere along the parent section ($\chi \in [0, 1]$). Illustrated in **Figure 3E**, a child segment is connected to the point $\chi = 0.5$ and the axial resistance in the parent segment does not enter the calculation of axial current magnitude. LFPy 2.0 still accounts for a virtual axial current I_m^{a} from the parent mid point to the child start point. These virtual currents ensure that the total current dipole

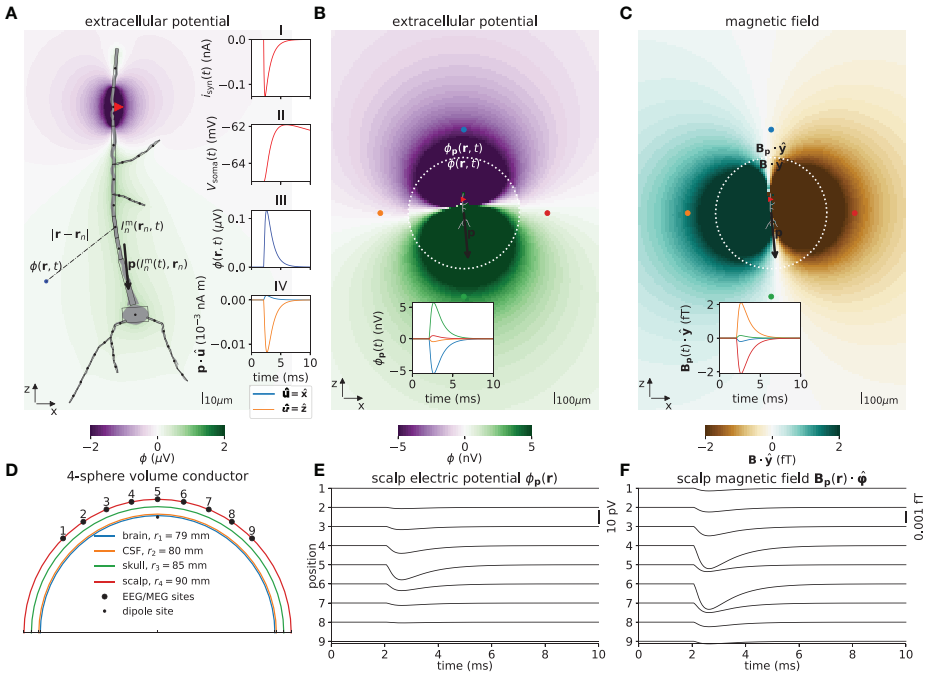

FIGURE 2 | Illustrations of forward model, dipole approximation, EEG and MEG model. **(A)** Illustration of forward-modeling scheme for extracellular potentials from multicompartment neuron models. The gray shape illustrates soma and dendrites of a 3D-reconstructed neuron morphology and the equivalent multicompartment model. A single synaptic input current $i_{\text{syn}}(t)$ (red triangle, inset axes I) results in a deflection of the membrane voltage throughout the morphology, including at the soma ($V_{\text{soma}}(t)$, inset axes II). LFPy allows for computing extracellular potentials ϕ in arbitrarily chosen extracellular locations r (inset axes III) from transmembrane currents ($I_n^{\text{m}}(\mathbf{r}_n, t)$), as well as the components of the current dipole moment p (black arrow, inset axes IV). Compartments are indexed n, r_n denote compartment positions. The image plot shows the extracellular potential in the xz-plane at the time of the largest synapse current magnitude ($t = 2.25$ ms). **(B)** Illustration of the extracellular electric potential calculated both from the current dipole moment and transmembrane currents for the situation in **(A)**. Within a radius $r < 500$ μm from the "center of areas" (see below) of the morphology the panel shows extracellular potentials $\phi(\mathbf{r})$ predicted using the line-source method, while outside this radius the panel shows extracellular potentials $\phi_{\mathbf{p}}(\mathbf{r})$ predicted from the current dipole moment ($\mathbf{p}$, black arrow). Here, an assumption of an homogeneous (same everywhere) and isotropic (same in all directions) extracellular conductivity was used. The 'center of areas' was defined as $\sum_{n=1}^{n^{\text{seg}}} A_n \mathbf{r}_n / \sum_{n=1}^{n^{\text{seg}}} A_n$ where A_n denotes compartment surface area. The time $t = 2.25$ ms as in **(A)**. The inset axis shows the potential as function of time in the four corresponding locations (at $|\mathbf{R}| = 750$ μm) surrounding the morphology (colored circular markers). **(C)** Visualization of magnetic field component $\mathbf{B}_{\mathbf{p}} \cdot \hat{\mathbf{y}}$ (y-component) computed from the current dipole moment, outside a circle of radius $r = 500$ μm (as in **B**). Inside the circle, we computed the same magnetic field component from axial currents. The inset axis shows the y-component of the magnetic field as function of time in the four corresponding locations (at $|\mathbf{R}| = 750$ μm) surrounding the morphology (circular markers). **(D)** Illustration of upper half of the four-sphere head model used for predictions of EEG scalp potentials from electric current dipole moments. Each spherical shell with outer radii $r \in \{r_1, r_2, r_3, r_4\}$ has piecewise homogeneous and isotropic conductivity $\sigma_{\text{e}} \in \{\sigma_1, \sigma_2, \sigma_3, \sigma_4\}$. The EEG/MEG sites numbered 1–9 mark the locations where electric potentials and magnetic fields are computed, each offset by an arc length of $r_4\pi/16$ in the xz-plane. The current dipole position was $\theta = \varphi = 0, r = 78$ mm (in spherical coordinates). **(E)** Electric potentials on the outer scalp-layer positions 1-9 in **(D)**. **(F)** Tangential component of the magnetic field $\mathbf{B}_{\mathbf{p}} \cdot \hat{\varphi}$ in positions 1–9. (Note that at position 5, the unit vector $\hat{\varphi}$ is defined to be directed in the positive y-direction).

moments computed either from transmembrane currents or from axial currents are identical (see section 2.3.1 for details).

At morphology branch points, several child segments may protrude from a parent segment as illustrated in **Figure 3F**. As the segment n and its sibling $\tilde{n}$ both share the same parent f, we estimate the potential $V_{\times}^{\text{m}}$ at the branch node using Ohm's law and Kirchhoff's current law, accounting for the axial resistivities (R_f^{i}, R_n^{i}, $R_{\tilde{n}}^{\text{i}}$) and potentials (V_f^{m}, V_n^{m}, $V_{\tilde{n}}^{\text{m}}$), in order to compute the corresponding axial currents I_m^{a} and I_{m+1}^{a}. The full procedure presently used for computing axial currents in LFPy 2.0 for the cases illustrated in **Figures 3B–F** is provided in full detail in Algorithm A1 (**Appendix**).

2.2. Forward Modeling of LFP and MUA Signals

The relation between transmembrane currents and extracellular potentials is calculated based on volume conduction theory

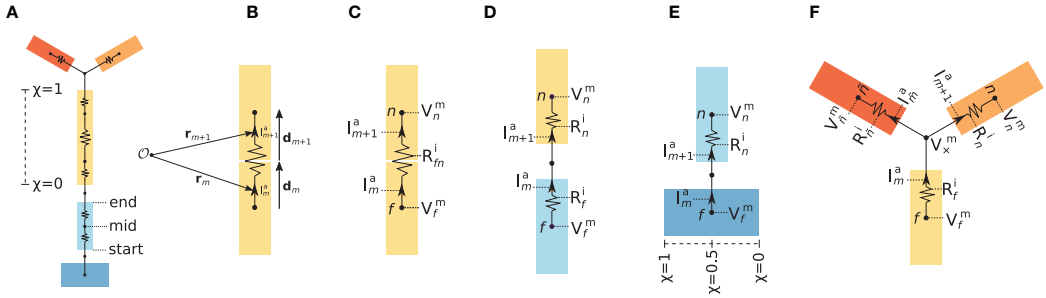

FIGURE 3 | Axial currents in multicompartment neuron models. **(A)** Schematic illustration of sections (colored rectangles), segments and equivalent electric circuit of a simplified multicompartment neuron model. The relative length χ varies between 0 and 1 from start- to end-point of each section. **(B)** Axial current line element vectors ($\mathbf{d}_m, \mathbf{d}_{m+1}$) and corresponding midpoints ($\mathbf{r}_m, \mathbf{r}_{m+1}$) of axial currents ($I^{\mathrm{a}}_m, I^{\mathrm{a}}_{m+1}$) between two connected segments. **(C)** Axial currents ($I^{\mathrm{a}}_m, I^{\mathrm{a}}_{m+1}$), membrane potentials ($V^{\mathrm{m}}_f, V^{\mathrm{m}}_n$), and axial resistance (R^{i}_{fn}) in equivalent electric circuit for a parent segment f and child segment n in a single section. **(D)** Similar to panel B, but parent and child segments belong to two different sections. The total series resistance is here $R^{\mathrm{i}}_f + R^{\mathrm{i}}_n$. **(E)** Illustration of the case where the child segment n is connected to a point $\chi = 0.5$ on the parent section. For children connected at $\chi \in \langle 0, 1\rangle$ the voltage difference ($V^{\mathrm{m}}_n - V^{\mathrm{m}}_f$) is only across the child segment axial resistance R^{i}_n, but the (virtual) current from the node connecting the child start point to the parent midpoint I^{a}_m is still accounted for. **(F)** Illustration of axial currents at branch point between different sections of the morphology. The child segment n has one parent f and one sibling indexed by $\tilde{n}$, where $V^{\mathrm{m}}_{\times}$ denotes the virtual membrane potential at the node connecting the parent end-point to the children start-points. $V^{\mathrm{m}}_{\tilde{n}}$ is the voltage in the midpoint of the sibling segment, while $R^{\mathrm{i}}_{\tilde{n}}$ and $I^{\mathrm{a}}_{\tilde{m}}$ denotes the axial resistance and current between the sibling midpoint and the branch point.

(Nunez and Srinivasan, 2006; Einevoll et al., 2013). At the relatively low frequencies relevant in neurophysiology (below a few thousand hertz), this derivation is simplified by omitting terms with time derivatives in Maxwell's equations (quasistatic approximation, Hämäläinen et al., 1993, p. 426). Further, the extracellular medium is in all situations considered below assumed to be ohmic, that is, linear and frequency-independent (Pettersen et al., 2012; Einevoll et al., 2013; Miceli et al., 2017).

2.2.1. Homogeneous and Isotropic Media

We first consider the simplest situation, where the medium is *homogeneous*, that is, the same in all positions corresponding to an infinite volume conductor, and *isotropic*, that is, the same electrical conductivity in all directions. The medium is then represented by a scalar extracellular conductivity σ_{e}. The extracellular potential $\phi(\mathbf{r}, t)$ at position $\mathbf{r}$ and time t is then given by (Nunez and Srinivasan, 2006; Lindén et al., 2014)

$$\phi(\mathbf{r}, t) = \frac{1}{4\pi\sigma_{\mathrm{e}}} \frac{I(t)}{|\mathbf{r} - \mathbf{r}'|}, \tag{4}$$

where $I(t)$ represents a time-varying point current source at position $\mathbf{r}'$. For transmembrane currents $I^{\mathrm{m}}_{jn}(t)$ of individual compartments $n \in [1, n^{\mathrm{seg}}_j]$ of all cells j in a population of N cells, the extracellular potential can be computed as the linear sum of their contributions as

$$\phi(\mathbf{r}, t) = \frac{1}{4\pi\sigma_{\mathrm{e}}} \sum_{j=1}^{N} \sum_{n=1}^{n^{\mathrm{seg}}_j} \frac{I^{\mathrm{m}}_{jn}(t)}{|\mathbf{r} - \mathbf{r}_{jn}|}, \tag{5}$$

but only under the assumption that each transmembrane current can be represented as a discrete point in space. This point-source assumption can be used in LFPy by supplying the keyword argument and value `method="pointsource"` to the `RecExtElectrode` class (Lindén et al., 2014).

As a homogeneous current distribution along each cylindrical compartment is assumed, we may employ the *line-source* approximation for somatic and dendritic compartments (Holt and Koch, 1999). The formula is obtained by integrating 4 along the center axis of each cylindrical compartment n, and by summing over contributions from every n^{seg}_j compartment of all N cells (Holt and Koch, 1999; Pettersen and Einevoll, 2008; Lindén et al., 2014):

$$\begin{aligned}\phi(\mathbf{r}, t) &= \frac{1}{4\pi\sigma_{\mathrm{e}}} \sum_{j=1}^{N} \sum_{n=1}^{n^{\mathrm{seg}}_j} I^{\mathrm{m}}_{jn}(t) \int \frac{1}{|\mathbf{r} - \mathbf{r}_{jn}|} d\mathbf{r}_{jn} \\ &= \frac{1}{4\pi\sigma_{\mathrm{e}}} \sum_{j=1}^{N} \sum_{n=1}^{n^{\mathrm{seg}}_j} \frac{I^{\mathrm{m}}_{jn}(t)}{\Delta s_{jn}} \ln \left| \frac{\sqrt{h^2_{jn} + r^2_{\perp jn}} - h_{jn}}{\sqrt{l^2_{jn} + r^2_{\perp jn}} - l_{jn}} \right|. \end{aligned} \tag{6}$$

Compartment length is denoted Δs_{jn}, perpendicular distance from the electrode point contact to the axis of the line compartment is denoted $r_{\perp jn}$, longitudinal distance measured from the start of the compartment is denoted h_{jn}, and longitudinal distance from the other end of the compartment is denoted $l_{jn} = \Delta s_{jn} + h_{jn}$. The corresponding keyword argument and value to class `RecExtElectrode` is `method="linesource"` (Lindén et al., 2014).

A final option in LFPy is however to approximate the typically more rounded soma compartments as spherical current

sources, thus the line-source formula (Equation 6) for dendrite compartments is combined with the point-source equation (Equation 4), obtaining (Lindén et al., 2014):

$$\begin{aligned}\phi(\mathbf{r},t) &= \frac{1}{4\pi\sigma_e}\sum_{j=1}^{N}\left(\frac{I^{\mathrm{m}}_{j,\mathrm{soma}}(t)}{|\mathbf{r}-\mathbf{r}_{j,\mathrm{soma}}|}+\sum_{n=2}^{n_j^{\mathrm{seg}}}\int\frac{I^{\mathrm{m}}_{jn}(t)}{|\mathbf{r}-\mathbf{r}_{jn}|}d\mathbf{r}_{jn}\right)\\ &= \frac{1}{4\pi\sigma_e}\sum_{j=1}^{N}\left(\frac{I^{\mathrm{m}}_{j,\mathrm{soma}}(t)}{|\mathbf{r}-\mathbf{r}_{j,\mathrm{soma}}|}+\sum_{n=2}^{n_j^{\mathrm{seg}}}\frac{I^{\mathrm{m}}_{jn}(t)}{\Delta s_{jn}}\ln\left|\frac{\sqrt{h_{jn}^2+r_{\perp jn}^2}-h_{jn}}{\sqrt{l_{jn}^2+r_{\perp jn}^2}-l_{jn}}\right|\right).\end{aligned} \tag{7}$$

The corresponding keyword argument and value is `method="soma_as_point"`.

If the distance between current sources and electrode contacts is smaller than the radius of the segment, unphysical singularities may occur in the computed extracellular potential. Singularities are in LFPy automatically prevented by either setting $r_{\perp jn}$ or $|\mathbf{r}-\mathbf{r}_{jn}|$ equal to the cylindrical compartment radius dependent on the choice of line or point sources.

Electrode contacts of real recording devices have finite spatial extents. A good approximation to the electric potential across the uninsulated surface of metal electrode contact is obtained by computing the spatially averaged electric potential (Robinson, 1968; Nelson et al., 2008; Nelson and Pouget, 2010; Ness et al., 2015), in particular for current sources being located at distances larger than approximately one electrode radius (Ness et al., 2015). The *disc-electrode* approximation to the potential (Camuñas-Mesa and Quiroga, 2013; Lindén et al., 2014; Ness et al., 2015)

$$\phi_{\mathrm{disc}}(\mathbf{u},t) = \frac{1}{A_S}\iint_S \phi(\mathbf{u},t)\,d^2r \approx \frac{1}{m}\sum_{h=1}^{m}\phi(\mathbf{u}_h,t)\,, \tag{8}$$

is incorporated in LFPy, with corresponding parameters for contact radius r_{contact}, number m of random points $\mathbf{u}_h$ on the flat, circular electrode contact surface when averaging (Lindén et al., 2014). The surface normal vector for each electrode contact must also be specified.

2.2.2. Discontinuous and Isotropic Media

Above we described the case for an infinite volume conductor, that is, a constant extracellular conductivity σ_e, as implemented in the initial LFPy release (Lindén et al., 2014). For cases where σ_e vary with position, i.e., $\sigma_e = \sigma_e(\mathbf{r})$, such as for cortical *in vivo* recordings close to the cortical surface (Einevoll et al., 2007) or *in vitro* recordings using microelectrode arrays (MEAs) (Ness et al., 2015), this approximation does not generally hold. Instead a generalized Poisson equation must be solved (Nicholson and Freeman, 1975):

$$\nabla\cdot\big(\sigma_e(\mathbf{r})\nabla\phi(\mathbf{r},t)\big) = -C(\mathbf{r},t), \tag{9}$$

where $C(\mathbf{r},t)$ is the current-source density. This equation can always be solved numerically by means of the Finite Element Method (FEM) (McIntyre and Grill, 2001; Ness et al., 2015) or other mesh-based methods (see for example Tveito et al., 2017).

In the special case where the conductivity σ_e is discontinuous in a single direction, that is, a constant conductivity in the xy-plane and a piecewise constant $\sigma_e(z)$ in the z-direction, the 'Method-of-Images' (MoI) can be used to make analytical formulas for the extracellular potentials, analogous to 4–7 above (Nicholson and Llinas, 1971; Nunez and Srinivasan, 2006; Ness et al., 2015). When applicable, these formulas substantially simplify the modeling of the extracellular potentials compared to FEM modeling.

Electrical potentials across microelectrode arrays (MEAs): The first MoI application is to model recordings in a MEA setting where a slice of brain tissue is put on an insulating recording chip (MEA-chip) and covered with saline (Hagen et al., 2015; Ness et al., 2015). In this three-layer situation separate conductivity values are assigned to the topmost saline layer conductivity σ_S for $z \in [h,\infty]$, the middle tissue layer conductivity σ_T for $z \in [0,h)$ and the lowermost electrode σ_G for $z \in [-\infty,0)$. The parameter h denotes the thickness of the middle tissue layer. The corresponding implementation is provided by the class `RecMEAElectrode`, and has at present the limitations that all current sources (segments) must be contained on the interval $z \in [0,h)$, and that the line-source approximation can only be used when $\sigma_G = 0$ and when computing extracellular potentials for $z = 0$. For other forward-model configurations (for example for $0 \le z \le h$ and/or $\sigma_G > 0$) the point-source approximation can be used. For a detailed derivation of the MoI with two planar electrical boundaries, see Equation (4) in Ness et al. (2015). A corresponding example is provided with LFPy 2.0 (`example_MEA.py`) which illustrates the computation of extracellular potentials as recorded by a MEA following synaptic activation of a pyramidal cell model.

Electrical potentials close to cortical surface: The second MoI application is to model *in vivo* recordings of electrical potentials at or immediately below the cortical surface, that is, the interface between cortical gray matter and dura. Here the extracellular conductivity above the cortical surface σ_S can be higher or lower than the conductivity in cortical gray matter σ_T depending on how the measurements are done, for example whether saline or oil is used to cover an inserted laminar electrode (Einevoll et al., 2007). Such a conductivity jump will affect both the electrical potential recorded at the cortical surface (ECoG recording) as well as the potentials recorded in the top cortical layers (Pettersen et al., 2006). This can be modeled with the same framework as above, that is, by using the class `RecMEAElectrode`, with the cortical surface at height h, while ignoring the lower planar boundary by setting $\sigma_G = \sigma_T$. In this situation the potential at or below the cortical surface at position (x,y,z) for a current source, $I(t)$, positioned at (x',y',z') is given by (Nunez and Srinivasan, 2006; Pettersen et al., 2006; Ness et al., 2015) as:

$$\begin{aligned}\phi(x,y,z,t) = \frac{I(t)}{4\pi\sigma_T}\Bigg(&\frac{1}{\sqrt{(x-x')^2+(y-y')^2+(z-z')^2}}\\ &+\frac{\sigma_T-\sigma_S}{\sigma_T+\sigma_S}\frac{1}{\sqrt{(x-x')^2+(y-y')^2+(z+z'-2h)^2}}\Bigg).\end{aligned} \tag{10}$$

This approach assumes a flat cortical surface. Note, however, that in LFPy 2.0 the ECoG signal can also be modeled by means of the four-sphere EEG head model as described below in section 2.3.4. An example is provided with LFPy 2.0 (`example_ECoG.py`) which illustrates extracellular potentials recorded in the cortex and at the cortical surface following

activation of multiple synapses distributed across a pyramidal cell model.

Electrical potentials in spherical conductor:

LFPy 2.0 also incorporates a spherical conductor model, adapted from Deng (2008), where the conductivity is constant within the sphere and constant outside (class `OneSphereVolumeConductor`). Note that this model is applicable for monopolar current sources, unlike the more complex multi-sphere head models described below in section 2.3 which only apply to dipolar current sources. Although not pursued here, one application of this volume-conductor model could possibly be modeling of LFPs measured in spheroidal brain nuclei.

2.2.3. Homogeneous and Anisotropic Media

For homogeneous media, that is, when the extracellular conductivity is the same at all positions, we also added support for anisotropic media (Nicholson and Freeman, 1975). In this case the extracellular conductivity in 9 must be replaced by a rank 2 (3×3) tensor where the diagonal elements are σ_x, σ_y, and σ_z and the off-diagonal elements are zero (Nicholson and Freeman, 1975). This could for example be used to mimic experimental observations of such anisotropy in cortex (Goto et al., 2010), that is, electric currents flow with less resistance along the depth direction (z-direction) than in the lateral directions (x, y-directions). In this case $\sigma_z > \sigma_x = \sigma_y$ (Ness et al., 2015). The corresponding implementation is based on the description and implementation provided by Ness et al. (2015), and is in LFPy presently supported by the class `RecExtElectrode`, but not the class `RecMEAElectrode`.

2.3. Forward Modeling of EEG, ECoG, and MEG Signals From Current Dipoles

The forward modeling of EEG and MEG signals from current dipoles has a long history (Hämäläinen et al., 1993; Nunez and Srinivasan, 2006). Here the EEG contacts and the MEG magnetometers are located so far away from the neural sources that only the current dipole moments contribute to the measured signals, that is, the contributions from higher-order current multipoles are negligible. From charge conservation, it follows that current monopoles do not exist. To compute the contribution to EEG and MEG signals from detailed neuron models, we thus first need to compute single-neuron current dipole moments as described in section 2.3.1. Next these must be combined with appropriate volume-conductor models for the head.

In LFPy 2.0 we include two "head" models for computing EEG signals from current dipole moments: the (very simplified) infinite homogenous volume-conductor model (section 2.3.2), and the much more involved four-sphere head model where the brain tissue, cerebrospinal fluid (CSF), skull and scalp are represented with different values for the electrical conductivity (Nunez and Srinivasan, 2006; Næss et al., 2017), cf. section 2.3.3. For the MEG signals the forward model is simpler as the magnetic permeability is the same throughout the head as in free space (Hämäläinen et al., 1993). In LFPy 2.0 we include simulation code for computing neural contributions to MEG signals applicable for all head models with spherically-symmetric electrical conductivities, for example, the four-sphere head model, cf. section 2.3.5. While these head models allow for direct calculation of EEG and MEG signals from neurons, it should be noted that the computed current dipole moments also can be used for subsequent calculation of EEG and MEG signals by means of boundary element (BEM) or finite element models (FEM) with anatomically detailed head models (He et al., 2002; Bangera et al., 2010; DeMunck et al., 2012), (Huang et al., 2016).

2.3.1. Calculation of Current Dipole Moments

Current dipole moments from transmembrane currents: The current dipole moment from a single neuron can be computed from transmembrane currents as (Lindén et al., 2010):

$$\mathbf{p}(t) = \sum_{n=1}^{n^{\mathrm{seg}}} \mathbf{r}_n I_n^{\mathrm{m}}(t)\,, \tag{11}$$

where I_n^{m} is the transmembrane current at time t from compartment n at position $\mathbf{r}_n$. For a population of N cells with n_j^{seg} compartments each, the current dipole moment at discrete time steps can be formulated as the matrix product:

$$\begin{bmatrix} p_x(0) & p_y(0) & p_z(0) \\ p_x(dt) & p_y(dt) & p_z(dt) \\ \vdots & \vdots & \vdots \\ p_x(T) & p_y(T) & p_z(T) \end{bmatrix} = \begin{bmatrix} I^{\mathrm{m}}_{11}(0) & I^{\mathrm{m}}_{11}(dt) & \dots & I^{\mathrm{m}}_{11}(T) \\ I^{\mathrm{m}}_{12}(0) & I^{\mathrm{m}}_{12}(dt) & \dots & I^{\mathrm{m}}_{12}(T) \\ \vdots & \vdots & \ddots & \vdots \\ I^{\mathrm{m}}_{jn}(0) & I^{\mathrm{m}}_{jn}(dt) & \dots & I^{\mathrm{m}}_{jn}(T) \\ \vdots & \vdots & \ddots & \vdots \\ I^{\mathrm{m}}_{Nn_j^{\mathrm{seg}}}(0) & I^{\mathrm{m}}_{Nn_j^{\mathrm{seg}}}(dt) & \dots & I^{\mathrm{m}}_{Nn_j^{\mathrm{seg}}}(T) \end{bmatrix}^T \begin{bmatrix} r^{(x)}_{11} & r^{(y)}_{11} & r^{(z)}_{11} \\ r^{(x)}_{12} & r^{(y)}_{12} & r^{(z)}_{12} \\ \vdots & \vdots & \vdots \\ r^{(x)}_{jn} & r^{(y)}_{jn} & r^{(z)}_{jn} \\ \vdots & \vdots & \vdots \\ r^{(x)}_{Nn_j^{\mathrm{seg}}} & r^{(y)}_{Nn_j^{\mathrm{seg}}} & r^{(z)}_{Nn_j^{\mathrm{seg}}} \end{bmatrix}, \tag{12}$$

where $p_u(t)$ is the u-component ($u \in \{x, y, z\}$) of the current dipole moment at time t (thus $\mathbf{p}(t) \equiv p_x(t)\hat{\mathbf{x}} + p_y(t)\hat{\mathbf{y}} + p_z(t)\hat{\mathbf{z}}$), $I^{\mathrm{m}}_{jn}(t)$ the transmembrane currents of segment n of cell j at time t and $r^{(u)}_{jn}$ the corresponding u-coordinates of each segment's midpoint. $\hat{\mathbf{x}}, \hat{\mathbf{y}}$ and $\hat{\mathbf{z}}$ denote the cartesian unit vectors. For more compact notation we here show the transpose (denoted by the raised T) of the matrix containing transmembrane currents. Note that the same formula may be used to also compute current dipole moments $\mathbf{p}_j$ of individual

cells j (or subsets thereof) by slicing the corresponding matrix elements.

Current dipole moments from axial currents: Alternatively, the current dipole moment can be computed from axial currents between neighboring segments (see section 2.1.2). As an example, we consider a two-compartmental dendritic stick model, where segment *one* will act as a current sink, and segment *two* as a current source. The transmembrane current entering segment two I_2^{m} will be the same as the axial current I^{a} between the two segments, which is also equal to the current leaving compartment one I_1^{m}, such that $I_1^{\mathrm{m}} = -I_2^{\mathrm{m}} = I^{\mathrm{a}}$. An axial line element vector $\mathbf{d}$ represents the path traveled by the axial current, which corresponds to the displacement $\mathbf{r}_1 - \mathbf{r}_2$ between the compartment midpoints. From equation 11 it thus follows that the current dipole moment is:

$$\mathbf{p} = \sum_{n=1}^{2} \mathbf{r}_n I_n^{\mathrm{m}} = I^{\mathrm{a}}\mathbf{d}. \tag{13}$$

Multiplying each axial current with the respective current path gives a set of current dipoles:

$$\mathbf{p}_m(t) = I_m^{\mathrm{a}}(t)\mathbf{d}_m. \tag{14}$$

Calculating sets of current dipole moments from neural simulations can be useful, for example for ECoG predictions (see section 2.3.4) or magnetic fields in proximity of the neuron (see section 2.4).

2.3.2. EEG Signal for Homogeneous Volume Conductor

From eletrostatic theory we have that the electric potential outside a spatial distribution of current sinks and sources can be described by a multipole expansion $\phi(r) = C_{\mathrm{monopole}}/R + C_{\mathrm{dipole}}/R^2 + C_{\mathrm{quadrupole}}/R^3 + C_{\mathrm{octupole}}/R^4 + \ldots$, where R is the relative distance from the multipole to measurement location (and the coefficients C depends on the spherical angles). Due to charge conservation, current monopoles do not exist (Nunez and Srinivasan, 2006). For sufficiently large values of R where $C_{\mathrm{dipole}}/R^2 \gg \sum_{q=3}^{\infty} C_{q-\mathrm{pole}}/R^q$, the electric potential of a neuron can be approximated solely from its current dipole moment, as contributions from quadrupolar and higher-order terms become negligible. The electric potential from a current dipole in an ohmic, homogeneous and isotropic medium is given by (Nunez and Srinivasan, 2006)

$$\phi_{\mathbf{p}} = \frac{\mathbf{p}\cdot\mathbf{R}}{4\pi\sigma_{\mathrm{e}}R^3}, \tag{15}$$

where $\mathbf{p}$ is the current dipole moment as defined above, σ_{e} the conductivity of the extracellular medium, $\mathbf{R} = \mathbf{r} - \mathbf{r}'$ the displacement vector between dipole location $\mathbf{r}'$ and measurement location $\mathbf{r}$, and $R = |\mathbf{R}|$. Predictions of extracellular potentials from current dipole moments in homogeneous media are provided by the class `InfiniteVolumeConductor`.

2.3.3. EEG Signal in Four-Sphere Head Model

The computation of EEG signals assuming a homogeneous volume conductor model is obviously a gross approximation as it neglects the large variation in the extracellular conductivity in the head. In order to compute more realistic EEG signals from underlying neuronal sources, we implemented in LFPy 2.0 the inhomogeneous four-sphere head model in class `FourSphereVolumeConductor`. This model is composed of four concentric shells representing brain tissue, cerebrospinal fluid (CSF), skull and scalp, where the conductivity can be set individually for each shell (Srinivasan et al., 1998; Nunez and Srinivasan, 2006). Note that corrections to the original model formulation was recently provided in Næss et al. (2017). LFPy 2.0 incorporates this corrected four-sphere head model.

2.3.4. ECoG Signal From Four-Sphere Head Model

The four-sphere head model is not restricted to EEG predictions, but can also be applied for modeling electric potentials in other layers of the inhomogeneous head model, such as ECoG signals at the interface between the brain tissue and the CSF. In contrast to EEG electrodes, however, the ECoG electrodes are located only micrometers away from the apical dendrites. The electrode's proximity to the neuronal source makes the four-sphere model a less obvious candidate model, as the model is based on the current dipole approximation, giving good predictions only when the measurement point is more than some dipole lengths away from the source (Lindén et al., 2010). However, in the `FourSphereVolumeConductor` class method `calc_potential_from_multi_dipoles()`, this problem can be avoided by taking advantage of the fact that electric potentials sum linearly in ohmic media: Instead of computing a single current dipole moment for the whole neuron, we compute multiple current dipole moments, one for each axial current, as described in section 2.3.1. Since these current dipoles have small enough source separations for the current dipole approximation to be applicable, we can compute the ECoG signal contribution from each current dipole moment separately, using the four-sphere model. The ECoG signal is finally predicted by summing up each contribution. The corresponding LFPy 2.0 example file is `/examples/example_ECoG_4sphere.py`.

2.3.5. MEG Signals in Spherically-Symmetric Head Models

For spherically-symmetric head models the MEG signal can be computed from the current dipole moments set up by intracellular axial currents (Hämäläinen et al., 1993, p. 428). To compute magnetic fields $\mathbf{B}_{\mathbf{p}}$ from current dipole moments we incorporated the special form of the magnetostatic Biot-Savart law (where magnetic induction effects are neglected) (Nunez and Srinivasan, 2006, Appendix C) given as:

$$\mathbf{B}_{\mathbf{p}} = \frac{\mu_0}{4\pi}\frac{\mathbf{p}\times\mathbf{R}}{R^3}. \tag{16}$$

As above, $\mathbf{p}$ is the dipole source, $\mathbf{R} = \mathbf{r} - \mathbf{r}'$ the displacement between dipole location $\mathbf{r}'$ and measurement location $\mathbf{r}$, and $R = |\mathbf{R}|$. For a detailed derivation of this expression see Hämäläinen et al. (1993). The magnetic field $\mathbf{B}$ is related to the commonly

used quantity $\mathbf{H}$ (often also termed magnetic field) through $\mathbf{B} = \mu_0\mathbf{H} + \mathbf{M} = \mu\mathbf{H}$ where $\mathbf{M}$ is the magnetization and μ the magnetic permeability of the material. However, in biological tissues the magnetization $\mathbf{M}$ is very small, and μ is very close to the magnetic constant (i.e., the magnetic permeability of vacuum) μ_0 (Hämäläinen et al., 1993). Predictions of magnetic signals are in LFPy 2.0 incorporated in the class `MEG`, which provides the method `calculate_H` in order to compute the magnetic field from a current dipole moment time series. Its output must be multiplied by μ to obtain the magnetic field $\mathbf{B}_\mathbf{p}$.

Throughout this paper, we show for the four-sphere head model magnetic field components decomposed into tangential and radial components at different positions on spherical surfaces. The tangential components were computed in the direction of the angular unit vectors $\hat{\theta} = \cos\theta\cos\varphi\hat{\mathbf{x}} + \cos\theta\sin\varphi\hat{\mathbf{y}} - \sin\theta\hat{\mathbf{z}}$ and $\hat{\varphi} = -\sin\varphi\hat{\mathbf{x}} + \cos\varphi\hat{\mathbf{y}}$ as $\mathbf{B}\cdot\hat{\theta}$ and $\mathbf{B}\cdot\hat{\varphi}$, respectively. The radial component was computed as $\mathbf{B}_\mathbf{p}\cdot\hat{\mathbf{r}}$ where $\hat{\mathbf{r}}$ denotes the radial unit vector from the center of the sphere in the direction of the contact. Furthermore, we also show tangential and radial components of the surface magnetic field where the underlying dipoles were rotated by an angle $\theta = \pi/2$ around the x-axis, denoted $\mathbf{B}_{R_x(\pi/2)\mathbf{p}}\cdot\hat{\theta}$, $\mathbf{B}_{R_x(\pi/2)\mathbf{p}}\cdot\hat{\varphi}$ and $\mathbf{B}_{R_x(\pi/2)\mathbf{p}}\cdot\hat{\mathbf{r}}$, respectively. For this purpose we used the rotation matrix

$$R_x\left(\frac{\pi}{2}\right) = \begin{bmatrix} 1 & 0 & 0 \\ 0 & 0 & -1 \\ 0 & 1 & 0 \end{bmatrix} \tag{17}$$

multiplied with the current dipole moment $\mathbf{p}$ in cartesian coordinates.

Note that experimental MEG equipment using gradiometers measure changes in the magnetic field across space in units of T/m (Hämäläinen et al., 1993). We here display the time-varying magnitude of magnetic fields in units of T.

2.4. Magnetic Signals Close to Neurons

Most studies of magnetic fields generated by neural activity have been based on MEG recordings where the neuronal sources are so distant from the magnetic-field sensors that the far-field dipole approximation in 16 can be applied. However, probes are also being developed for measuring magnetic fields in direct vicinity of the neurons (Barbieri et al., 2016; Caruso et al., 2017). To compute the magnetic fields in the vicinity of neurons, LFPy 2.0 also implements the relevant Biot-Savart law for this situation (Blagoev et al., 2007):

$$\mathbf{B}(\mathbf{r}) = \frac{\mu_0}{4\pi}\sum_{m=1}^{m_\mathrm{a}} I_m^\mathrm{a}\frac{\mathbf{d}_m\times(\mathbf{r}-\mathbf{r}_m)}{|\mathbf{r}-\mathbf{r}_m|^3}\,. \tag{18}$$

This formula provides the magnetic field for m_a axial currents I_m^a where $\mathbf{d}_m$ are axial line element vectors, and $\mathbf{r}_m$ the midpoint positions of each axial current. The use of this formula assumes that contributions to the magnetic fields from extracellular volume currents are negligible (Hämäläinen et al., 1993, p. 427). Predictions of magnetic signals from axial currents (or equivalently sets of current dipoles) are in LFPy 2.0 facilitated by the corresponding class method `MEG.calculate_H_from_iaxial()`. We show (in **Figure 2**) the y-components of the magnetic fields in vicinity of a model neuron computed as $\mathbf{B}\cdot\hat{\mathbf{y}}$ and $\mathbf{B}_\mathbf{p}\cdot\hat{\mathbf{y}}$ respectively.

2.5. Description of Biophysically Detailed Network in Example Use Case

2.5.1. Neuron Models

Our example network model presented in section 3 comprised about 5500 biophysically detailed multicompartment neurons obtained from The Neocortical Microcircuit Collaboration (NMC) Portal (https://bbp.epfl.ch/nmc-portal, Ramaswamy et al., 2015). The NMC portal provides NEURON code for about 1,000 different single-cell models as well as connectivity data of a reconstruction and simulation of a rat somatosensory cortex column (Markram et al., 2015).

For simplicity of this demonstration, we here use only four different single-cell models as shown in **Figure 2A** for the different network populations. For layers 4 and 5 we chose the most common excitatory cell type and most common inhibitory interneuron cell type, in accordance with statistics of the reconstructed microcircuit of Markram et al. (2015) as provided on the NMC portal. The table in **Figure 4A** summarizes population names (X– presynaptic; Y– postsynaptic) which here coincide with morphology type (m), electric type (e), cell model #, compartment count per single-cell model (n_j^seg), number of cells N_X in each population, occurrence $F_X \equiv N_X/\sum_X N_X$, the number of external synapses on each cell n_ext, rate expectation of external synapses ν_ext and the mean $\overline{z}_X^\mathrm{soma}$ and standard deviation $\sigma_{\overline{z},X}^\mathrm{soma}$ of the normal distribution $\mathcal{N}(\overline{z}_X^\mathrm{soma}, \sigma_{\overline{z},X}^\mathrm{soma})$ from which somatic depths are drawn for each population. The cell type can be derived from the "m" and "e" type in the table. Using the nomenclature of Markram et al. (2015), L4 and L5 are abbreviations for layer 4 and 5; PC – pyramidal cell; LBC – large basket cell; TTPC1 – thick-tufted pyramidal cell with a late bifurcating apical tuft; MC – Martinotti cell; cAD – continuous adapting; dNAC – delayed non-accommodating; bAC – burst accommodating. Thus, L4_PC_cAD corresponds to a layer 4 pyramidal cell with a continuously adapting firing pattern as a response to depolarizing step current and so forth. As multiple variations of the same cell types are provided on the NMC portal, the cell model # can be used to identify the particular single-cell model and corresponding file sets used in the network described here. These single-cell model files can be downloaded one after another from the portal as for example L5_TTPC1_cADpyr232_1.zip, or all together in a single archive. For simplicity we ignore heterogeneity in e-types for each m-type, thus the population counts N_X correspond to the count per m-type in the reconstructed microcircuit. Note for the present network description that $\{X, Y, \mathrm{m}\} \in \{\mathrm{L4\_PC}, \mathrm{L4\_LBC}, \mathrm{L5\_TTPC1}, \mathrm{L5\_MC}\}$.

2.5.2. Population Geometry

The centers of somatic compartments for all cells $i \in X$ were distributed with even probability within a circular radius of 210 μm corresponding to the radius of the reconstructed somatosensory column in Markram et al. (2015). The corresponding depths were drawn from the normal

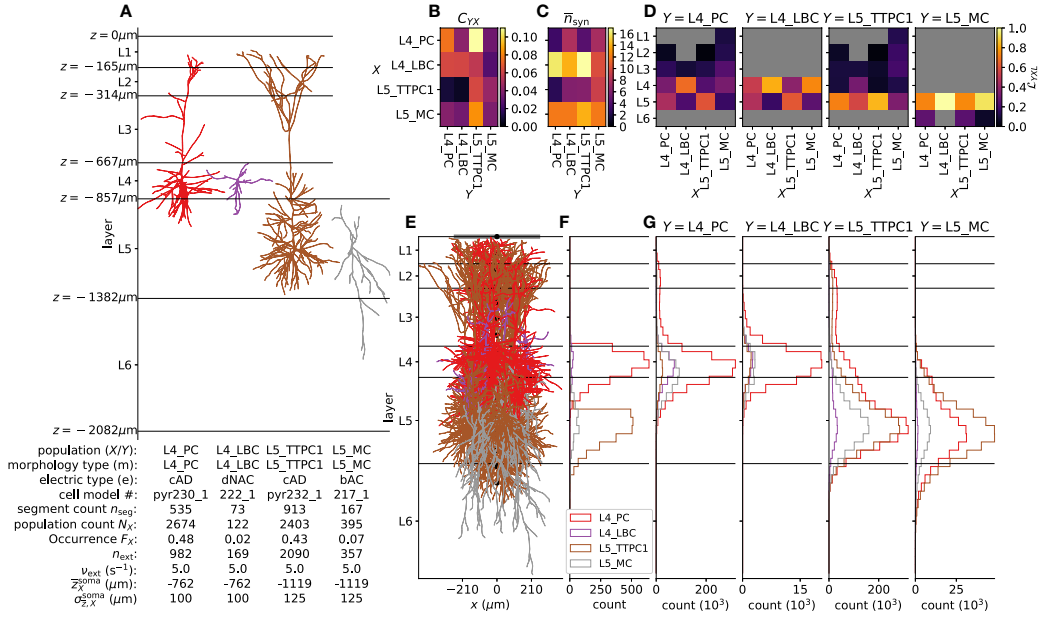

population (X/Y):	L4_PC	L4_LBC	L5_TTPC1	L5_MC
morphology type (m):	L4_PC	L4_LBC	L5_TTPC1	L5_MC
electric type (e):	cAD	dNAC	cAD	bAC
cell model #:	pyr230_1	222_1	pyr232_1	217_1
segment count n_{seg}:	535	73	913	167
population count N_X:	2674	122	2403	395
Occurrence F_X:	0.48	0.02	0.43	0.07
n_{ext}:	982	169	2090	357
ν_{ext} (s^{-1}):	5.0	5.0	5.0	5.0
$\overline{z}_X^{\text{soma}}$ (μm):	-762	-762	-1119	-1119
$\sigma_{z,X}^{\text{soma}}$ (μm):	100	100	125	125

FIGURE 4 | Details of the example network. **(A)** Biophysically detailed neuron models of the network, with depth-values of boundaries of layers 1–6. The lower left table summarizes population names (X – presynaptic; Y – postsynaptic) which here coincide with morphology type (m); electric type (e); cell model #; compartment count per single-cell model (n_j^{seg}); number of cells N_X in each population; occurrence F_X (defined as $N_X / \sum_X N_X$); the number of external synapses on each cell n_{ext}; rate expectation of external synapses ν_{ext}; the expected mean $\overline{z}_X^{\text{soma}}$ and standard deviation $\sigma_{z,X}^{\text{soma}}$ of the normal distribution $\mathcal{N}$ from which somatic depths are drawn. **(B)** Pairwise connection probability C_{YX} between cells in presynaptic populations X and postsynaptic populations Y. **(C)** Average number $\overline{n}^{\text{syn}}$ of synapses created per connection between X and Y. **(D)** Layer specificity of connections $\mathcal{L}_{YXL}$ (Hagen et al., 2016) from each presynaptic population X onto each postsynaptic population Y. Gray values denote $\mathcal{L}_{YXL} = 0$. **(E)** Illustration of cylindrical geometry of populations including a laminar recording device for extracellular potentials (black circular markers) and a single ECoG electrode above layer 1 (gray line). $n = 15$ neurons of each population are shown in their respective locations. **(F)** Laminar distribution of somas for each network population ($\Delta z = 50$ μm) in one instantiation of the circuit. **(G)** Laminar distribution of synapses across depth onto each postsynaptic population Y from presynaptic populations X ($\Delta z = 50$ μm).

distribution $\mathcal{N}(\overline{z}_X^{\text{soma}}, \sigma_{\overline{z},X}^{\text{soma}})$ using population-specific mean and standard deviations given in **Figure 4A**. Neuron positions resulting in any neuron compartments protruding above the hypothetical cortical surface at $z = 0$ or below layer 6 at $z = -2082$ μm were redrawn from the depth distribution. All cells were rotated around their local vertical z-axis by a random angle $\theta \in [0, 2\pi)$.

2.5.3. Synapse Models

For synapses made by cells in a presynaptic population X onto a postsynaptic population Y we used synapse model files provided with the single-cell model files from the NMC portal. There are two base models with connection-specific parameterization which were obtained from the portal. Excitatory synapses are modeled as probabilistic AMPA and NMDA receptors, while inhibitory synapses are modeled as probabilistic GABA_A receptors. Both synapse types were modeled with presynaptic short-term plasticity. The synapse parameterization procedure and validation is described in detail in Markram et al. (2015), with code implementations based on Fuhrmann et al. (2002). The synapse parameters are summarized in **Table 1**, detailing the synapse model names, average synaptic conductances $\overline{g}^{\text{syn}}$ and corresponding standard deviations $\sigma_{\overline{g}}^{\text{syn}}$, release probabilities P_u, relaxation time constants from depression τ_{Dep}, relaxation time constants from facilitation τ_{Fac}, ratios of NMDA vs. AMPA (excitatory connections only), rise and decay time constants τ_U^{r} and τ_U^{d} of the two-exponential conductances of each current type $U \in \{\text{AMPA}, \text{NMDA}, \text{GABAA}\}$, and reversal potentials e^{syn}. Random conductances for each individual synapse were drawn from the capped normal distribution $\mathcal{N}(\overline{g}^{\text{syn}}, \sigma_{\overline{g}}^{\text{syn}})H(g - g_{\min})$. For our network we set the minimum synaptic conductance to be $g_{\min} = 0$ nS.

2.5.4. Extrinsic Input

Synapses from external inputs to the neurons in our network were modeled similarly to excitatory synapses of intrinsic network connections. For inputs to a population Y in layer L

TABLE 1 | Summary of intrinsic synapse parameters.

		Postsynaptic population (Y)			
	Parameter	**L4_PC**	**L4_LBC**	**L5_TTPC1**	**L5_MC**
presynaptic population (X)					
L4_PC	syn. model	ProbAMPANMDA	ProbAMPANMDA	ProbAMPANMDA	ProbAMPANMDA
	$\overline{g}^{\text{syn}}$ (nS)	0.3	0.3	0.3	0.3
	$\sigma_{\overline{g}}^{\text{syn}}$ (nS)	0.11	0.11	0.11	0.11
	P_u	0.859	0.398	0.5	0.093
	τ_{Dep} (ms)	670	560	670	140
	τ_{Fac} (ms)	17	130	17	660
	NMDA ratio	0.4	0.4	0.4	0.4
	$\tau^{\text{r}}_{\text{AMPA}}$ (ms)	0.2	0.2	0.2	0.2
	$\tau^{\text{d}}_{\text{AMPA}}$ (ms)	1.737	1.74	1.742	1.742
	$\tau^{\text{r}}_{\text{NMDA}}$ (ms)	0.29	0.29	0.29	0.29
	$\tau^{\text{d}}_{\text{NMDA}}$ (ms)	43	43	43	43
	e^{syn} (mV)	0	0	0	0
L4_LBC	syn. model	ProbGABAAB	ProbGABAAB	ProbGABAAB	ProbGABAAB
	$\overline{g}^{\text{syn}}$ (nS)	0.89	0.33	0.98	0.33
	$\sigma_{\overline{g}}^{\text{syn}}$ (nS)	1.3	0.15	1.3	0.16
	P_u	0.213	0.254	0.226	0.253
	τ_{Dep} (ms)	730	700	750	710
	τ_{Fac} (ms)	21	21	21	21
	$\tau^{\text{r}}_{\text{GABAA}}$ (ms)	0.2	0.2	0.2	0.2
	$\tau^{\text{d}}_{\text{GABAA}}$ (ms)	7.604	8.373	7.364	8.349
	e^{syn} (mV)	-80	-80	-80	-80
L5_TTPC1	syn. model	ProbAMPANMDA	ProbAMPANMDA	ProbAMPANMDA	ProbAMPANMDA
	$\overline{g}^{\text{syn}}$ (nS)	0.29	0.3	0.31	0.3
	$\sigma_{\overline{g}}^{\text{syn}}$ (nS)	0.11	0.11	0.11	0.11
	P_u	0.5	0.369	0.5	0.092
	τ_{Dep} (ms)	670	550	670	150
	τ_{Fac} (ms)	17	140	17	690
	NMDA ratio	0.4	0.4	0.4	0.4
	$\tau^{\text{r}}_{\text{AMPA}}$ (ms)	0.2	0.2	0.2	0.2
	$\tau^{\text{d}}_{\text{AMPA}}$ (ms)	1.743	1.743	1.744	1.741
	$\tau^{\text{r}}_{\text{NMDA}}$ (ms)	0.29	0.29	0.29	0.29
	$\tau^{\text{d}}_{\text{NMDA}}$ (ms)	43	43	43	43
	e^{syn} (mV)	0	0	0	0
L5_MC	syn. model	ProbGABAAB	ProbGABAAB	ProbGABAAB	ProbGABAAB
	$\overline{g}^{\text{syn}}$ (nS)	0.66	0.33	0.66	0.33
	$\sigma_{\overline{g}}^{\text{syn}}$ (nS)	0.15	0.15	0.15	0.15
	P_u	0.3	0.25	0.299	0.252
	τ_{Dep} (ms)	1200	700	1200	710
	τ_{Fac} (ms)	2.1	21	2.2	21
	$\tau^{\text{r}}_{\text{GABAA}}$ (ms)	0.2	0.2	0.2	0.2
	$\tau^{\text{d}}_{\text{GABAA}}$ (ms)	8.291	8.295	8.271	8.339
	e^{syn} (mV)	-80	-80	-80	-80

we chose to duplicate the synapse parameters of connections made by the presynaptic excitatory population within the same layer (as we were unable to assess what parameters were used for extrinsic connections in Markram et al., 2015). Our synapse parameters are given in **Table 2**. For each cell in the network we created n_{ext} synapses set randomly onto dendritic and apical compartments with compartment specificity of connections $S_{jn}/\sum_{n\in\{\text{dend,apic}\}} S_{jn}$, where S_{jn} denotes surface area of compartment n of cell j. The random activation times of each synapse were set using Poisson processes with rate expectation ν_{ext} for the duration of the simulation. The values for n_{ext} and ν_{ext} are given in **Figure 4A**, and were set by hand in order to maintain spiking activity in all populations.

2.5.5. Connectivity Model

Random connections in our network were set using the Python-implementation of the "connection-set algebra" of Djurfeldt (2012) and Djurfeldt et al. (2014) (github.com/INCF/csa). Using this formalism, we constructed boolean connectivity matrices $\mathbf{C}^{(r)}_{YX}$ for postsynaptic cells $j^{(r)} \subset Y$ distributed across each separate parallel MPI rank (denoted by the superset "(r)" for rank number) and presynaptic cells $i \in X$. Each instance of $\mathbf{C}^{(r)}_{YX}$ had shape $(N_X \times N_{j^{(r)}\subset Y})$, with entries equal to True denoting connections from cell i to $j^{(r)}$, as expressed mathematically by

$$\mathbf{C}^{(r)}_{YX}(C_{YX})(i,j^{(r)}) = \begin{cases} \text{True with probability } C_{YX}\,, \\ \text{False otherwise}\,. \end{cases} \tag{19}$$

TABLE 2 | Synapse parameters for extrinsic input.

			Postsynaptic population (Y)			
		Parameter	**L4_PC**	**L4_LBC**	**L5_TTPC1**	**L5_MC**
Presynaptic pop. (X)	ext	syn. model	ProbAMPANMDA	ProbAMPANMDA	ProbAMPANMDA	ProbAMPANMDA
		$\overline{g}^{\text{syn}}$ (nS)	0.3	0.33	0.31	0.33
		$\sigma_{\overline{g}}^{\text{syn}}$ (nS)	0.11	0.15	0.11	0.15
		P_U	0.859	0.254	0.5	0.252
		τ_{Dep} (ms)	670	700	670	710
		τ_{Fac} (ms)	17	21	17	21
		NMDA ratio	0.4	0.4	0.4	0.4
		$\tau^{\text{r}}_{\text{AMPA}}$ (ms)	0.2	0.2	0.2	0.2
		$\tau^{\text{d}}_{\text{AMPA}}$ (ms)	8.291	8.295	8.271	8.339
		$\tau^{\text{r}}_{\text{NMDA}}$ (ms)	0.29	0.29	0.29	0.29
		$\tau^{\text{d}}_{\text{NMDA}}$ (ms)	43	43	43	43
		e^{syn} (mV)	0	0	0	0

For $X = Y$ and $i = j^{(r)}$, entries in $\mathbf{C}^{(r)}_{YX}$ were set to False (no autapses). We used fixed connection probabilities C_{YX} as obtained from the NMC portal between our chosen m-types.

2.5.6. Multapses

As multiple synapses per connection appear to be a prominent feature in cortical networks (see Markram et al., 2015; Reimann et al., 2015 and references therein), we drew for every connection between presynaptic cell i and postsynaptic cell j a random number of synapses n^{syn} rounded to an integer from the capped normal distribution $\mathcal{N}(\overline{n}^{\text{syn}}, \sigma^{\text{syn}}_{\overline{n}})H(n)$. Conduction delays from action-potential detection (threshold $\theta_{\text{AP}} = -10$ mV) in cell i for each corresponding synapse onto cell j were drawn from the distribution $\mathcal{N}(\overline{\delta}^{\text{syn}}, \sigma^{\text{syn}}_{\overline{\delta}})H(\delta - \delta_{\min})$. For our network we set the minimum delay $\delta_{\min} = 0.3$ ms for all connections.

2.5.7. Layer-specificity of connections

In order to position each individual synapse of a connection on a cell $j \in Y$, in a simplified manner that depended on the degree of overlap between presynaptic axons and postsynaptic dendrites ("Peter's rule"), we calculated for each postsynaptic population Y layer-specificities of connections $\mathcal{L}_{YXL}$ in layer L for synapses made by presynaptic populations X (Hagen et al., 2016), by first computing the sums $\Delta s_{iXL} = \sum_{n \in \text{axon}} \Delta s_{inXL}$, that is, the total axon length of a presynaptic cell type per layer L and sums $\Delta s_{jYL} = \sum_{n \in \{\text{soma,dend}\}} \Delta s_{jnYL}$ of total dendrite and soma length for each postsynaptic cell type across each layer. Then we defined the layer-specificity of connections as

$$\mathcal{L}_{YXL} = \sqrt{\Delta s_{iXL} \Delta s_{jYL}} \Big/ \sum_L \sqrt{\Delta s_{iXL} \Delta s_{jYL}}\,.$$

The sums $\sum_L \mathcal{L}_{YXL} = 1$ for all X and Y. Synapse sites of connections onto cell j were then set randomly with a compartment specificity of connections $S_{jn} \sum_L \Pr_{\mathcal{N}(\mathcal{L}_{YXL}, \Delta L/2)}(z_{nj}) / \sum_n S_{jn}$, where S_{jn} is the surface area of compartment n of the cell j centered at depth z_{nj} and $\Pr_{\mathcal{N}}(...)$ the probability density function of the distribution $\mathcal{N}(\mathcal{L}_{YXL}, \Delta L/2)$. ΔL denotes the thickness of layer L.

All connectivity parameter values ($C_{YX}, \overline{n}^{\text{syn}}, \sigma^{\text{syn}}_{\overline{n}}, \overline{\delta}^{\text{syn}}, \sigma^{\text{syn}}_{\overline{\delta}}, \mathcal{L}_{YXL}$) are summarized in **Table 3**. Visual representations of $C_{YX}, \overline{n}^{\text{syn}}$ and $\mathcal{L}_{YXL}$ are shown in **Figures 4B–D**. **Figure 4E** shows 15 cells in each population X with corresponding distribution of N_X somas across depth ($\Delta z = 50\ \mu$m) in **Figure 4F**. Panel G shows the resulting distribution of synapses across depth for all combinations of Y and X ($\Delta z = 50\ \mu$m).

2.5.8. Computation of Extracellular Potentials Inside Cortical Column

For our multicompartment neuron network we chose to compute the extracellular potential vertically through the center of the column, with the most superficial contact at the top of layer 1 ($z = 0$) to a depth of $z = -1500\ \mu$m within layer 6. The inter-contact distance was $\Delta z = 100\ \mu$m, and contacts were assumed to be circular with radius $r_{\text{contact}} = 5\ \mu$m and surface normal vectors aligned with the horizontal y-axis. For the electrode surface averaging we used $m = 50$ (cf. Equation 8 and Lindén et al., 2014). For the calculation of extracellular potential inside the cortical column we assumed a homogeneous, isotropic, linear and ohmic extracellular conductivity $\sigma_{\text{e}} = 0.3$ S/m.

2.5.9. Computation of ECoG Signal From Method-of-Images

The extracellular potential on top of cortex (ECoG) was computed by means of the Method-of-Images (MOI, see section 2.2.2). In the example, the conductivity below the contact was set as $\sigma_G = \sigma_T = 0.3$ S/m, corresponding to the gray-matter value used above, while the conductivity on top of cortex was to set to be fully insulating, that is, $\sigma_T = 0$ S/m. This could correspond to the situation where a grid of ECoG contacts are embedded in an insulating material (see for example, Castagnola et al., 2014). We further considered a single circular ECoG disk electrode with contact radius $r = 250\ \mu$m with its surface normal vector perpendicular to the brain surface. The disk electrode was centered at the vertical population axis and positioned at the upper boundary of layer 1. For the disk-electrode approximation (cf. Equation 8) we set $m = 500$. (Note that the present MoI implementation requires all transmembrane currents to be represented as point sources confined within the boundaries of the middle (cortical) layer.

TABLE 3 | Summary of connectivity parameters.

			Postsynaptic population (Y)			
		Parameter	**L4_PC**	**L4_LBC**	**L5_TTPC1**	**L5_MC**
Presynaptic population (X)	L4_PC	C_{YX}	0.076	0.042	0.11	0.034
		$\overline{n}_{\text{syn}}$	3.3	7.9	4.3	7.6
		$\sigma_{\overline{n},\text{syn}}$	1.4	3.0	1.7	2.7
		$\overline{\delta}_{\text{syn}}$ (ms)	1.35	1.17	1.433	1.521
		$\sigma_{\overline{\delta},\text{syn}}$ (ms)	0.867	0.763	0.817	0.978
		$\mathcal{L}_{YXL1}$	0.0	0.0	0.0	0.0
		$\mathcal{L}_{YXL2}$	0.058	0.0	0.069	0.0
		$\mathcal{L}_{YXL3}$	0.152	0.0	0.106	0.0
		$\mathcal{L}_{YXL4}$	0.336	0.53	0.105	0.0
		$\mathcal{L}_{YXL5}$	0.454	0.47	0.719	0.73
		$\mathcal{L}_{YXL6}$	0.0	0.0	0.0	0.27
	L4_LBC	C_{YX}	0.063	0.062	0.056	0.027
		$\overline{n}_{\text{syn}}$	16.0	14.0	17.0	10.0
		$\sigma_{\overline{n},\text{syn}}$	6.2	6.0	7.2	3.5
		$\overline{\delta}_{\text{syn}}$ (ms)	1.006	1.076	1.064	1.677
		$\sigma_{\overline{\delta},\text{syn}}$ (ms)	0.367	0.395	0.399	0.494
		$\mathcal{L}_{YXL1}$	0.0	0.0	0.0	0.0
		$\mathcal{L}_{YXL2}$	0.0	0.0	0.0	0.0
		$\mathcal{L}_{YXL3}$	0.1	0.0	0.109	0.0
		$\mathcal{L}_{YXL4}$	0.672	0.818	0.328	0.0
		$\mathcal{L}_{YXL5}$	0.228	0.182	0.563	1.0
		$\mathcal{L}_{YXL6}$	0.0	0.0	0.0	0.0
	L5_TTPC1	C_{YX}	0.011	0.0069	0.063	0.045
		$\overline{n}_{\text{syn}}$	2.5	6.1	6.2	9.2
		$\sigma_{\overline{n},\text{syn}}$	0.89	2.1	2.6	3.1
		$\overline{\delta}_{\text{syn}}$ (ms)	2.374	2.227	1.445	1.372
		$\sigma_{\overline{\delta},\text{syn}}$ (ms)	0.811	0.903	0.653	0.577
		$\mathcal{L}_{YXL1}$	0.0	0.0	0.0	0.0
		$\mathcal{L}_{YXL2}$	0.02	0.0	0.02	0.0
		$\mathcal{L}_{YXL3}$	0.129	0.0	0.078	0.0
		$\mathcal{L}_{YXL4}$	0.244	0.379	0.066	0.0
		$\mathcal{L}_{YXL5}$	0.608	0.621	0.836	0.739
		$\mathcal{L}_{YXL6}$	0.0	0.0	0.0	0.261
	L5_MC	C_{YX}	0.04	0.035	0.083	0.038
		$\overline{n}_{\text{syn}}$	12.0	12.0	14.0	12.0
		$\sigma_{\overline{n},\text{syn}}$	3.9	3.7	5.6	3.4
		$\overline{\delta}_{\text{syn}}$ (ms)	1.91	1.732	2.252	1.341
		$\sigma_{\overline{\delta},\text{syn}}$ (ms)	0.994	0.663	1.549	0.787
		$\mathcal{L}_{YXL1}$	0.111	0.0	0.136	0.0
		$\mathcal{L}_{YXL2}$	0.13	0.0	0.187	0.0
		$\mathcal{L}_{YXL3}$	0.249	0.0	0.209	0.0
		$\mathcal{L}_{YXL4}$	0.329	0.735	0.124	0.0
		$\mathcal{L}_{YXL5}$	0.18	0.265	0.344	0.926
		$\mathcal{L}_{YXL6}$	0.0	0.0	0.0	0.074

2.5.10. Computation of EEG and MEG Signals

The most direct approach for computing EEG and MEG signals would be to (i) compute the per-neuron current dipole moment, (ii) compute the contribution to the signals from each neuron, and (iii) sum these signals to get the total EEG and MEG signals from the entire network. To reduce the computational demands, we instead compute the per-population current dipole moment $\mathbf{p}_X(t)$ using equation 12. The total current dipole moment is then obtained by summing over all populations, that is, $\mathbf{p} = \sum_X \mathbf{p}_X$.

From $\mathbf{p}_X$ we computed the EEG (surface electric potentials on the scalp layer) of the four-sphere head model as described above, and similarly magnetic fields $\mathbf{B}_\mathbf{p}$. For the four-sphere head model we assumed conductivities $\sigma_s \in \{0.3, 1.5, 0.015, 0.3\}$ S/m and radii $r_s \in \{79, 80, 85, 90\}$ mm for brain, cerebrospinal fluid (CSF), skull and scalp, respectively (Nunez and Srinivasan, 2006; Næss et al., 2017). We positioned each population current dipole $\mathbf{p}_X$ below the brain-CSF boundary on the vertical z-axis (thus $x = y = 0$) at $z = r_1 + \overline{z}_X^{\text{soma}}$, where $\overline{z}_X^{\text{soma}}$ was the average soma depth within each population. Surface potentials, that is, EEG potentials, and magnetic fields where computed for polar angles $\theta \in [-\pi/4, \pi/4]$ with angular resolution $\Delta\theta = \pi/16$ as illustrated in **Figure 2D** (azimuth angles $\varphi = 0$), resulting in a contact separation along the arc of $r_4\pi/16 \approx 18$ mm. Different magnetoelectroencephalogram (MEG) equipment may be sensitive to different components of the magnetic field (Hämäläinen et al., 1993). We show different

scalar components of the magnetic field computed on the surface of the four-sphere head model as described above (in section 2.3.5).

2.5.11. Simulation Details

Simulations were run for a total duration of $T = 1,500$ ms with a simulation step size $dt = 0.0625$ ms (16 kHz sampling frequency). The first 500 ms were discarded as startup transient. All neurons were initialized at a membrane voltage $V_{\text{init}}^{\text{m}} = -77$ mV and temperature $T_{\text{celsius}} = 34°\text{C}$ (affecting membrane-channel dynamics).

2.6. Technical Details

2.6.1. Code Availability

All source codes and development history of past and present versions of LFPy are publicly available on GitHub (see github.com/LFPy/LFPy), using "git" (git-scm.com) for code provenance tracking. LFPy is released with an open-source software licence (GPL), which alongside GitHub functionality for listing issues, integration with automated testing, easy forking, local development and merges of upstream changes, facilitates continued, community-based LFPy development.

2.6.2. Requirements

LFPy 2.0 requires Python (continuously tested w. v2.7, v3.4-3.6), an MPI (message-passing interface) implementation such as OpenMPI, NEURON v7.4 or newer compiled with MPI and bindings for Python, Cython, and the Python packages mpi4py, numpy, scipy, h5py, csa (github.com/INCF/csa) and NeuroTools (neuralensemble.org/NeuroTools). In order to run all example files also matplotlib and Jupyter (jupyter.org) have to be installed, but prebuilt Python distributions such as Anaconda (anaconda.com) should provide these common Python packages, or easy means of installing LFPy dependencies (issuing, for example, "conda install mpi4py" on the command line). Detailed instructions for installing dependencies for common operating systems (MacOS, Linux, Windows) are provided in the online LFPy documentation (lfpy.readthedocs.io).

2.6.3. Installation

The latest stable LFPy release on the Python Package Index (pypi.python.org) can be installed by issuing:

```
$ pip install LFPy --user
```

which may prompt the install of also other missing dependencies. The command

```
$ pip install --upgrade --no-deps LFPy --user
```

may be used to upgrade an already existing installation of LFPy (without upgrading other dependencies). In order to obtain all LFPy source codes and corresponding example files, we recommend users to checkout the LFPy source code on GitHub, after installing the git version control software:

```
$ cd <path to repository folder>
$ git clone https://github.com/LFPy/LFPy.git
$ cd LFPy
$ pip install -r requirements --user
$ python setup.py develop --user
```

More detail is provided on lfpy.readthedocs.io.

2.6.4. Reproducibility

The simulated results and analysis presented here were made possible using Python 2.7.11 with the Intel(R) MPI Library v5.1.3, NEURON v7.5 (1472:078b74551227), Cython v0.23.4, LFPy (github.com/LFPy/LFPy, SHA:0d1509), mpi4py v2.0.0, numpy v1.10.4, scipy v0.17.0, h5py v2.6.0, parameters (github.com/NeuralEnsemble/parameters, SHA:v0aaeb), csa (github.com/INCF/csa, SHA:452a35) and matplotlib v2.1.0 running in parallel using 120-4800 cores on the JURECA cluster in Jülich, Germany, composed of two 2.5 GHz Intel Xeon E5-2680 v3 Haswell CPUs per node (2 x 12 cores), running the CentOS 7 Linux operating system. Each node had at least 128 GB of 2133 MHz DDR4 memory. All software packages were compiled using the GNU Compiler Collection (GCC) v4.9.3. All source codes for this study are provided as LFPy example files on GitHub.

3. RESULTS

3.1. Single-Neuron Activity and Extracellular Measurements

The first version of LFPy (Lindén et al., 2014) assumed the model neurons to be embedded in an infinite homogeneous volume conductor and was most suited to compute extracellular potentials (spikes, LFPs) inside the brain. One new feature of LFPy 2.0 compared to the first version of LFPy is that electrical potentials outside cortex (ECoG, EEG), as well as magnetic fields both inside and outside cortex (MEG), can be computed. These new measures are illustrated in **Figure 2** for a single synaptically activated "pyramidal" neuron (composed of soma and dendrite sections only).

Figure 2A presents a basic LFPy simulation example where a passive neuron model with simplified morphology receives a single synaptic input current (inset I). We computed the extracellular potential in the xz-plane (color image plot), using the assumption of line sources for each dendritic compartment, a spherical current source representing the soma, and homogeneous conductivity (7). The postsynaptic response is reflected as a somatic depolarization (inset II) and as a deflection in the extracellular potential in the location $\mathbf{r}$ (blue dot, inset III). The corresponding current dipole moment $\mathbf{p}(\mathbf{r}, t)$ was computed using equation 12 and is illustrated by the black arrow. The x- and z-components ($\mathbf{p} \cdot \hat{\mathbf{x}}, \mathbf{p} \cdot \hat{\mathbf{z}}$) of the current dipole moment are illustrated in inset IV, and we note the much larger dipole moment component in the vertical z-direction compared to the lateral x-direction. We do not show the y-component of the current dipole moment as all segments in this simplified neuronal morphology are located in the xz-plane (hence $\mathbf{p} \cdot \hat{\mathbf{y}} = 0$).

To illustrate the fact that a current dipole potential (Equation 15) gives a good approximation to the extracellular potential ϕ far away from the neuron, we compare with results from using the more comprehensive line-source method (Equation

6) in **Figure 2B**: The line-source potential ϕ is shown inside the dashed circle of radius $r = 500$ μm, while the dipole potential $\phi_{\mathbf{p}}$ is shown outside the circle. The inset shows the dipole potential corresponding to the colored dots located at a distance of 750 μm.

In **Figure 2C** we similarly compute the magnetic field for radii $r > 500$ μm using the current dipole moment (Equation 16), and axial currents inside (Equation 18). The axial currents were computed from per-compartment membrane potentials as described in section 2.1.2. For both color image plot and the inset, we show the dominating magnetic field component, that is, the y-component. As for the electrical potential in **Figure 2B**, we see that the predicted magnetic fields match well at the $r = 500$ μm interface.

Figure 2D illustrates the layout of scalp-layer measurement sites on the four-sphere head model described in section 2.3.3. The numbered points along the outer scalp layer represents measurement locations for EEG and MEG signals. The single current dipole moment is positioned beneath the CSF-brain boundary on the vertical z-axis (see caption for details). **Figure 2E** shows the corresponding scalp surface potentials which is dominated by the z-component of the current dipole moment ($\mathbf{p} \cdot \hat{\mathbf{z}}$, **Figure 2A** inset IV). **Figure 2F** shows the corresponding dominant azimuthal tangential magnetic field component ($\mathbf{B}_{\mathbf{p}} \cdot \hat{\varphi}$) computed from the current dipole moment using equation 16. At the center location (location 5) only the x-component ($\mathbf{p} \cdot \hat{\mathbf{x}}$) contributes to the signal, in the other locations both the x- and y-components contribute.

3.2. Network Activity and Extracellular Measurements

The second main new feature of LFPy 2.0 is the possibility to simulate recurrently connected networks of neurons in parallel. Our exemple network, shown in **Figure 4**, demonstrating this new feature is based on a subset of cortical single-cell models, synapse models and connectivity data from Markram et al. (2015) obtained from The Neocortical Microcircuit Collaboration (NMC) Portal (Ramaswamy et al., 2015). The implementation is described in detail in section 2.5.

In addition to supporting simulations of neuronal networks with simplified or biophysically detailed single-neuron models in parallel, LFPy 2.0 allows for concurrent calculations of extracellular measures of network activity. Specifically, the extracellular potentials at specific positions can be computed at each time step which avoids the memory-demanding process of recording transmembrane currents in all compartments for the duration of the simulation, either to disk or to memory. In the present example, the current dipole moment was calculated at every time step, and this amounted to a useful dimensionality reduction, as only the x, y, z-axis components of $\mathbf{p}$ per population X had to be stored. Assuming serial execution, then for each neuron population X, the total memory consumption is then reduced by a factor $3/(N_X n^{\text{seg}})$ where N_X is the population size and n^{seg} the number of compartments per neuron (see **Figure 4A** for values), compared to storing currents. The per-population current dipole moments were then used to predict EEG scalp surface potentials and MEG signals in the corresponding locations. Note that per-population current dipole moments can be stored, EEG and MEG signal can be computed with other head models at a later stage.

3.2.1. Network Spiking Activity

Figure 5 shows the various predicted measurements for a one-second period of network activity. The spike raster and corresponding spike-count histogram (**Figures 5A,B**) demonstrate the network's tendency to produce synchronous irregular patterns of activity with the parameterization summarized in section 2.5, **Tables 1–3** and **Figure 4**. The per-neuron spike occurrences in the excitatory populations L4_PC and L5_TTPC1 were sparser than for the inhibitory populations L4_LBC and L5_MC. As in the full circuit of Markram et al. (2015), it is possible that an asynchronous network state could have been obtained by modifying extracellular $[Ca^{2+}]_o$-dependent release probabilities P_u for the different synapse types in the model (Borst, 2010; Markram et al., 2015). A modification of release probabilities can shift the effective balance between excitatory and inhibitory synapse activations, but also incorporation of a larger sample of heterogeneous cell types in the model could have brought the network into an asynchronous state, essentially by increasing the amount of inhibitory feedback. In particular interneuron expression in neocortex is known to be more heterogeneous and more dense than demonstrated here (Markram et al., 2004, 2015). However, as our main focus here is to present new simulation technology now incorporated in LFPy, we did not pursue this line of inquiry.

3.2.2. Local Field Potentials (LFPs)

The extracellular potentials as would be measured by a 16-channel laminar probe positioned through the center axis of the cylindrical column, are shown in **Figure 5C**. The computed extracellular potentials are observed to be of the same order of magnitude as experimentally measured spontaneous potentials ($\simeq$0.1–1 mV, see Maier et al., 2010; Hagen et al., 2015; Reyes-Puerta et al., 2016). We further observe that the synchronous events seen in the spiking activity (**Figure 5A**) are reflected as substantial fluctuations in the extracellular potential with amplitudes close to 0.5 mV.

The signals in neighboring channels are further observed to be fairly correlated with comparable amplitudes, irrespective of the presence of somatic compartments at the depths of the contacts (**Figure 4F**). At the superficial channels 1–6, deflections in the electric potential following synchronous network activation are predominantly negative, while a change in sign occur around channel 7 (near the boundary between layer 3 and 4). The strongest deflections of the extracellular potential are typically observed at contacts within layer 5 (ch. 11–13), that is, at depths corresponding to the dense branching of basal dendrites and somas of the large layer 5 pyramidal neuron population. These deflections reflect that the soma compartments and basal dendrites are expected to act as dominant sources of the transmembrane currents setting up the extracellular potential (Lindén et al., 2010). Adding further to this, layers 4 and 5 also had the highest overall densities of excitatory and inhibitory synapses in the present model (**Figure 4G**). Some spike events

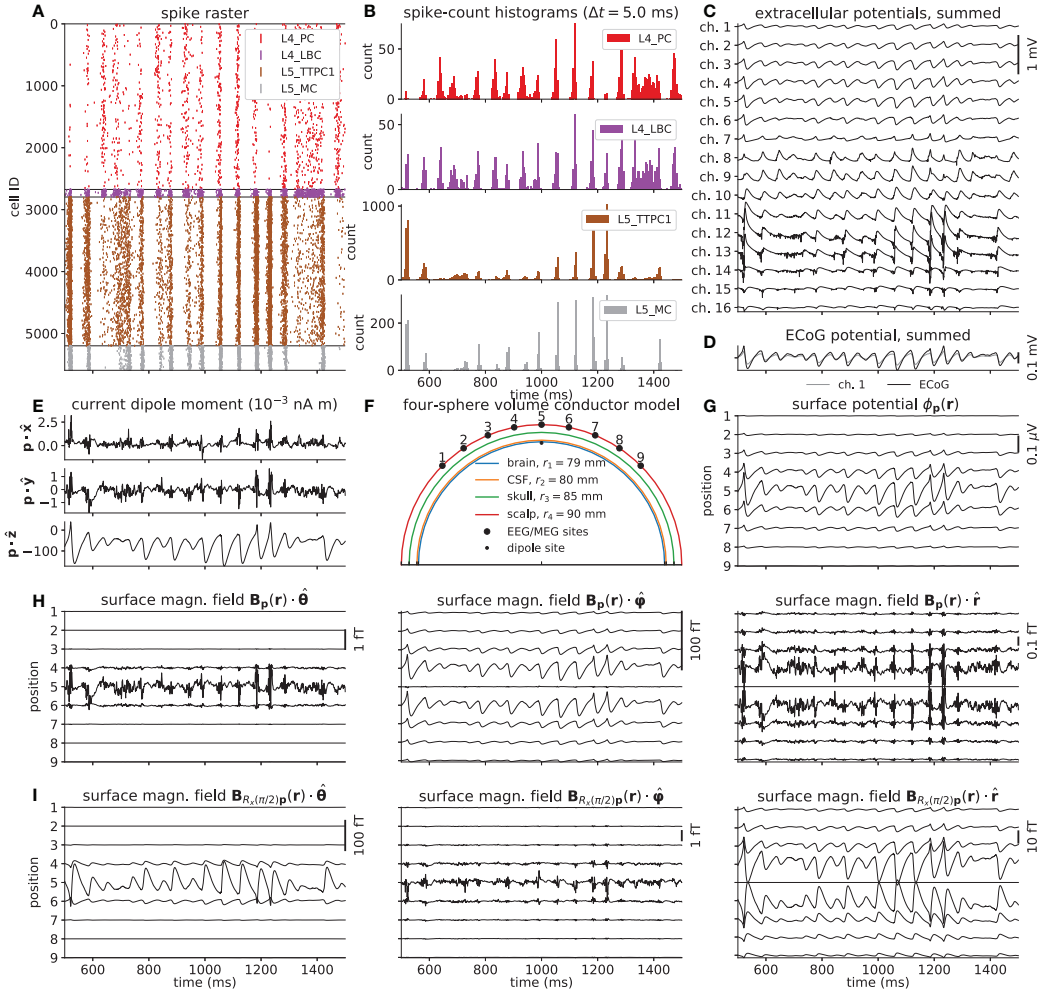

FIGURE 5 | Intra- and extracellular measures of activity in example network. **(A)** Spike raster plot for each population. Each row of dots corresponds to the spike train of one neuron, color coded by population. **(B)** Population spike rates computed by summing number of spike events in each population in temporal bins of width $\Delta t = 5$ ms. **(C)** Extracellular potentials as function of depth assuming an infinite volume conductor. **(D)** Extracellular potential on top of cortex (ECoG) assuming a discontinuous jump in conductivity between brain ($\sigma = 0.3$ S/m) and a non-conducting cover medium ($\sigma = 0$ S/m) and electrode surface radius $r = 250$ μm. The signal is compared to the channel 1 extracellular potential in **(C)** (gray line). **(E)** Component-wise contributions to the total current dipole moment $\mathbf{p}(t)$ summed over population contributions. **(F)** Illustration of upper half of the four-sphere head model (with conductivities $\sigma_S \in \{0.3, 1.5, 0.015, 0.3\}$ S/m and radii $r_S \in \{79, 80, 85, 90\}$ mm for brain, csf, skull and scalp, respectively), dipole location in inner brain sphere and scalp measurement locations. The sites in the *xz*-plane numbered 1–9 mark the locations where electric potentials and magnetic fields are computed, each offset by an arc length of $r_4\pi/16 \approx 18$ mm. **(G)** EEG scalp potentials from multicompartment-neuron network activity with radially oriented populations. **(H)** Tangential and radial components of the head-surface magnetic field (MEG) from multicompartment-neuron network activity with radially oriented population. **(I)** Tangential and radial components of the magnetic field (MEG) on the head surface, with underlying dipole sources rotated by an angle $\theta = \pi/2$ around the *x*-axis (thus with apical dendrites pointing into the plane). (Note that at position 5, the unit vectors $\hat{\varphi}$ and $\hat{\theta}$ are defined to be directed in the positive *y*- and *x*-directions, respectively).

(extracellular signatures of action potentials) are seen in ch. 15, produced by one or several neurons located near the virtual recording device.

Further investigation of the different contributors (**Figures 6A–D**) to the extracellular potential (**Figure 5C**), revealed that most of the signal variance across depth can be

explained by transmembrane currents of the two excitatory populations (**Figure 6E**). Even if the cell numbers in the two pyramidal-cell population were similar, population L5_TTPC1 contributed more to the signal than population L4_PC at all channels except at channels 8-9 (around which the L4_PC somas are positioned).

3.2.3. ECoG Signal

Figure 5D compares the extracellular potential in the topmost channel 1 (gray line), predicted under the assumptions of dendritic line sources, somatic spherical sources and an infinite homogeneous extracellular medium (cf. Equation 7), with our ECoG prediction at the same depth (black line). The ECoG signal was computed assuming a wide contact ($r_{\text{contact}} = 250\ \mu$m) aligned horizontally on top of a flat cortex ($z = 0$). Further, for the ECoG signal the method-of-images (MoI; cf. Equation 11) was used to account for a conductivity discontinuity at the cortical surface. Here, zero conductivity (mimicking, for example, the situation with an insulating mat surrounding the ECoG contact, Castagnola et al., 2014) was assumed above the cortical surface, while the gray-matter value of $\sigma_e = 0.3$ S/m was assumed below.

The amplitude of the ECoG trace was slightly increased compared to the potential measured by the smaller electrode. This amplitude increase can be attributed to the fact that a reduction in conductivity above the boundary would decrease the value of the denominator of equation 11, and hence increase the signal amplitude below insulating cortical surfaces (Pettersen et al., 2006). The expected increased signal amplitude from this conductivity step is here counter-measured by the larger diameter of the ECoG contact ($r_{\text{contact}} = 250\ \mu$m vs. $r_{\text{contact}} = 5\ \mu$m) resulting in an increased average distance from the signal source to the contact point averaged over the contact's surface. Detailed investigation of each signal normalized to the same standard deviation (not shown) revealed virtually indistinguishable features across time and in their power spectra.

3.2.4. Current Dipole Moments

Figure 5E shows the three components of the total current dipole moment **p** stemming from the network activity. The most striking feature is the much larger z-component compared to the lateral x- and y-components. This large difference in component size, about two orders for magnitude, reflects (i) that the vertically aligned pyramidal cell morphologies span across several layers, and (ii) the near rotational symmetry of the model populations around the z-axis. Unlike the z-component, the lateral components largely cancel out. In the same way as for the extracellular potential, the two pyramidal populations are also the dominant sources of the total dipole moment (**Figures 6F–J**). We also note that the z-component of the population current dipole moment generally dominates the other components of the population dipoles, with the exception of the L4_LBC population. Here all components are tiny, reflecting the stellate dendritic morphology and the evenly distributed synapses onto the neurons in this population.

For our model network we note that the maximum magnitude of the current dipole moment is about 0.1 nAm, which is about two orders of magnitude smaller than previously estimated typical "mesoscopic" dipole strengths (Hämäläinen et al., 1993, p. 418).

3.2.5. EEG Signals

As a demonstration of predicting non-invasive electric ("EEG") signals outside of the brain with LFPy 2.0, we utilized the four-sphere head model (as implemented in class `FourSphereVolumeConductor`, see 2) and defined scalp-layer measurement locations as illustrated in **Figure 5F**. We assumed the modeled network to represent a piece of cortical network positioned at the top of a cortical gyrus, so that the population axes were in the radial direction of the spherical head model. The current dipoles (computed above) were positioned below the interface between the CSF and the brain, more specifically the layer-4 and layer-5 population dipoles were positioned at the depth of the center of layer 4 and layer 5, respectively.

As observed in **Figure 5G**, the temporal form of the scalp potentials corresponds directly to the temporal form of the dominant z-component of the current dipole moment in **Figure 5E**. For an infinite volume conductor it follows directly from 15 that the recorded scalp potential will be proportional to this dipole moment at recording positions directly (radially) above the dipole location. Likewise, inspection of the formulas for the four-sphere head model shows that this is also the case for the scalp-potential contributions from both the radial (Næss et al., 2017, Equations 5–6) and tangential (Næss et al., 2017, Equations 17–18) dipole components (although with different proportionality constants for the two components).

For the present example network comprising 5,594 neurons of which 5,077 are pyramidal cells, we observe the magnitudes of the fluctuating scalp potential directly on top of the dipole sites to be on the order of 0.1 μV. This is about two orders of magnitude smaller than the typical size of measured EEG signals of $\sim$10 μV (Nunez and Srinivasan, 2006, Figure 1.1).

The weakly conducting skull layer (compared to the highly conductive brain, spinal fluid and scalp layers) results in a spatial "low-pass filter effect" from volume conduction (Nunez and Srinivasan, 2006, Ch. 6). This low-pass effect accounts for the relatively weak attenuation of the EEG signal with lateral distance from the center position (position 5 in **Figure 5F**) along the head surface, as observed in **Figure 5G**. On the surface of a spherical volume conductor with homogeneous conductivity inside the sphere, but otherwise zero conductivity outside the sphere's surface (1-sphere head model), the potential from a current dipole would decay in amplitude at a higher rate compared to our 4-sphere head-model case with a spherical skull layer with low conductivity. However, in an infinite homogeneous volume conductor the decay in electric potential along the putative sphere's surface would decay with a lower rate than both the 1-sphere and 4-sphere head models, see Nunez and Srinivasan (2006, Ch. 6) for a comparison.

3.2.6. MEG Signals

The computed current dipole moments in **Figure 5E** was also used to compute MEG signals. **Figure 5H** shows the computed

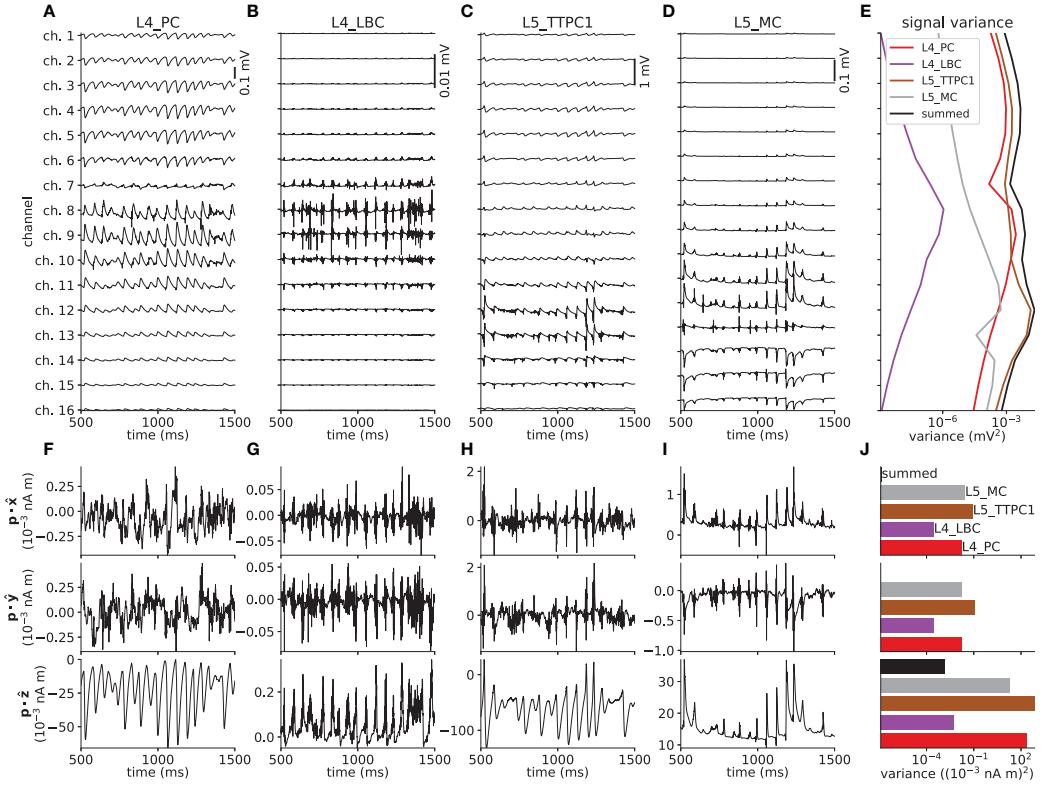

FIGURE 6 | Per-population contributions to the extracellular potential and current dipole moment and corresponding signal variance. **(A–D)** Contributions to the extracellular potential from populations $X \in$ {L4_PC, L4_LBC, L5_TTPC1, L5_MC} in the network across depth. **(E)** Extracellular potential variance across depth for contributions of each population, and for the sum over populations. **(F–I)** x, y, z-components of the per-population contribution to the summed current dipole moment. **(J)** Per-component current dipole moment variance for each population and for summed signals.

magnetic fields for the same set-up providing the EEG signals in **Figure 5G**, that is, radially oriented population current dipoles. In this situation the only sizable magnetic field is directed in the tangential direction around the vertical z-axis. With our spherical coordinates this corresponds to the φ-direction where the unit vector $\hat{\varphi}$ points in counter-clockwise direction. Note also that the magnetic field is almost zero straight above the dipole (position 5), as here the vectors **p** and **R** are near parallel so that the vector product in equation 16 is very small. We also observe that the magnetic field is symmetric around the center position (position 5), so that the field at position 6 is always similar to the field at position 4, and so on.

For EEG signals, equivalent radial dipoles located at the "crowns" of gyri are generally expected to give the largest signal contributions (Nunez and Srinivasan, 2006). For MEG signals, on the other hand, equivalent current dipoles in brain sulci oriented tangentially to the head surface is expected to provide the largest signals (Hämäläinen et al., 1993). In **Figure 5I** we thus show the magnetic field with the current dipole moments directed in a tangential direction (that is, in the y-direction into the paper in **Figure 5F**) rather than in the radial direction. In this situation the largest magnetic field component is in the tangential direction $\hat{\theta}$ (around the y-axis) in position 5. The $\hat{\varphi}$-component is as expected negligible, while the radial component is antisymmetric around position 5, but negligible in position 5 itself.

Typical magnetic fields measured in human MEG are on the order of 50–500 fT (Hämäläinen et al., 1993), and in **Figure 5I** we find that magnetic fields of similar magnitudes (∼100 fT) are predicted when the current dipole moment from our network is oriented in parallel to the cortical surface. Note, however, that in our model set-up, the dipole is only 11 mm away from the closest MEG sensor at position 5, while in human recordings the minimum distance between tangential dipoles in brain sulci and the MEG sensors may be several centimeters (Hämäläinen et al.,

1993). As the magnetic field from a current dipole decays as the square of the distance (see Equation 16), our model likely gives an overestimate of the contribution to the MEG signal from our model network when applied to a human setting.

In **Figure 5H** we also observe sizable magnetic fields (∼20–40 fT) generated by radially-oriented current dipoles. However, the generated fields are in the angular ϕ-direction where the fields have opposite directions on each side of the central position (position 5). Thus, in a setting with several such neighbouring dipoles (generated by neighbouring populations) on cortical gyri, there will be large cancellations effects. Despite the larger distances from the MEG sensors, tangentially oriented dipoles in sulci is therefore expected to dominate the measured MEG in human settings (Hämäläinen et al., 1993).

Animations of EEG surface potentials (color coded) and magnetic field (arrows) of the radially and tangentially oriented current dipole moments are available as **Supplementary Video 1** (radial_dipole.mp4) and **Supplementary Video 2** (tangential_dipole.mp4), respectively. For the case with a tangential dipole the characteristic "butterfly"-like pattern often seen in MEG recordings is observed (see e.g., Figure 5 in Hämäläinen et al., 1993).

3.3. LFPy Parallel Network Performance

In order to assess the performance figures of multicompartment-neuron network implementations in LFPy on a high-performance computing (HPC) facility, we performed a series of simulations with two-population versions of the network presented above. These modified networks consisted only of the layer-5 m-types L5_TTPC1 and L5_MC. We modified cell counts per population N_X and connection probabilities C_{YX} depending on chosen network population sizes N_X as noted in the text below. All other simulation parameters were kept fixed as given in **Tables 1**–**3**.

First, we compared set-up times, creation times of populations and connections, and simulation times for instantiations of similarly sized reference networks ($N^{(1)}_{\text{L5\_TTPC1}} = 2400, N^{(1)}_{\text{L5\_MC}} = 480$) for different number of MPI processes N_{MPI} (**Figure 7A**). N_{MPI} was set identical to the number of available physical cores (no multi-threading). A seed value for the random number generator for each network instantiation was varied to obtain an $N = 3$ sample size for each tested value of N_{MPI}. Both with predictions of extracellular potentials and current dipole moments (continuous lines) and without (dotted lines), the biggest fraction of the total computational time was spent during the main simulation part (red curves), that is, where the simulation is advanced time step by time step. The additional computational cost of computing extracellular potentials and current dipole moments was less than half compared to just simulating the spiking activity in the recurrently connected network. The times spent creating all recurrent connections and synapses (green curves) were between a factor 16 and 32 shorter than the simulation time.

The creation of connections and simulation times scaled strongly with N_{MPI}. An optimal, or strong, log-log-linear scaling curve can be represented as a function $t(N_{\text{MPI}}) \propto N^{-1}_{\text{MPI}}$, in particular for $N_{\text{MPI}} \leq 480$, as these N_{MPI}-values result in an even load balance across parallel processes with the presently used round-robin distribution of cells across MPI processes (see section A2 in **Appendix** for details). Each parallel process has the same number of cells of each m-type, segments (n^{seg}_j) and state variables corresponding to different active ion-channel models. Only variations in per-cell in-degrees (synapse counts) across different processes and simulations occurred due to the random network connectivity model, but even with different random seeds in each trial the trial variability was small (error bars denoting standard deviations are hardly seen).

The creation of populations (orange curves) however showed worse scaling behaviour for $N_{\text{MPI}} > 480$, in part due to uneven load balance. Another possible reason for reduced performance was the increased strain on the file system as all processes simultaneously access the same single-neuron source files upon instantiating individual `NetworkCell` objects. This might have been avoided by creating local copies of the necessary files on each compute node, but we did not pursue this here as the overall time spent instantiating neuron populations was only a fraction of the observed simulation times. The loading of parameters and other needed data (blue curves) was, as expected, fairly constant for different values of N_{MPI} as we did not parallelize the corresponding code.

As a second scaling-performance test, we ran series of simulations with $N_{\text{MPI}} = 480$ but varied the total network size by a factor $b \in \{0.2, 0.25, 0.5, 1, 2, 4\}$ while keeping the expected number of connections K_{YX} (and thus the number of synapses) between pre- and post-synaptic populations X and Y fixed (**Figure 7B**). The expected number of randomly created (binomially distributed) connections K_{YX} was calculated using the relation (Potjans and Diesmann, 2014):

$$C_{YX} = 1 - \left(1 - \frac{1}{N_X N_Y}\right)^{K_{YX}}, \tag{20}$$

with reference network size ($N^{(1)}_{\text{L5\_TTPC1}} = 2400, N^{(1)}_{\text{L5\_MC}} = 480$) and connection probabilities C_{YX} as given in **Table 3**. Similar to the test presented in **Figure 5A**, most of the total computation time was spent during the main simulation part (red curves), followed by creation of connections (green curves) and loading of different parameters (blue curves).

In contrast to the previous case, the creation of cells in the network displayed strong scaling with network size (which implies a relationship $t(r) \propto b$). The supra-optimal scaling seen for connections can be explained by the creation of similar connection counts across different factors b. (Note that supra-optimal scaling implies that $t(r) \propto b^q$ with exponent $q \in (0, 1)$, while sub-optimal scaling implies that $q > 1$.) For the tested factors $b = 0.25$ and $b = 0.5$ we expected sub-optimal scaling for creating populations and connections, as well as for simulation duration. These b-values gave different cell counts and thus inhomogeneous load-balances across MPI processes, which was unavoidable with the presently used round-robin parallelization scheme. A jump in performance was seen for $b = 0.2$ which resulted in only one multicompartment neuron and corresponding calculations on each MPI process.

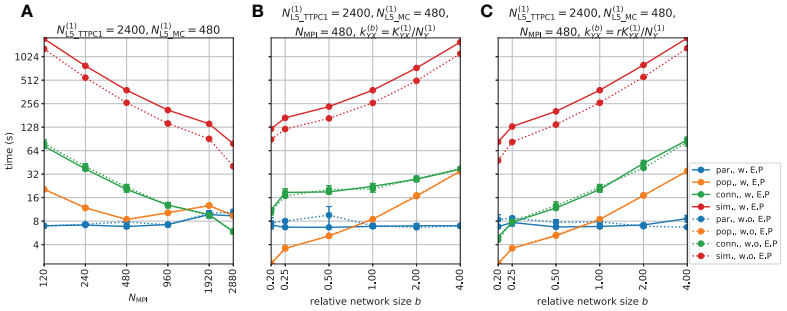

FIGURE 7 | Parallel performance with networks in LFPy. **(A)** Initialization of parameters (par.), population create (pop.), connectivity build (conn.) and main simulation time (sim.) as functions of number of physical CPU cores/MPI processes (N_{MPI}). The reference network population sizes $N_X^{(1)}$ for $X \in \{\mathrm{L5\_TTPC1}, \mathrm{L5\_MC}\}$ are given in the panel title. The network was otherwise constructed with synapse, stimulus and connectivity parameters for each possible connection as given in **Tables 1**–**3**. Times shown with continuous lines were obtained for simulations that included calculations of extracellular potentials and current dipole moments as in **Figures 2**–**6** (w. E.P.), while times shown with dotted lines were obtained for simulations with no such signal predictions (w.o. E.P.). Each data value is shown as the mean and standard deviation of times obtained from $N = 3$ network realizations instantiated with different random seeds. **(B)** Initialization of parameters, population create, connectivity build and main simulation time as functions of network size relative to the reference network population sizes $N_X^{(1)}$ for $X \in \{\mathrm{L5\_TTPC1}, \mathrm{L5\_MC}\}$ as given in the panel title. The superset "(1)" denotes a relative network size $b = 1$. Simulations were run using a fixed MPI process count N_{MPI} and connection probabilities $C_{YX}^{(r)}$ were recomputed for different values of b, such that the expected total number of connections $K_{YX}^{(1)}$ was constant between each simulation (using 20). The set-up was otherwise identical to the set-up in **(A)**. **(C)** Same as **(B)**, but with a fixed expected per-cell synapse in-degree $k_{YX}^{(r)} \equiv rK_{YX}^{(1)}/N_Y^{(1)}$ across different relative network sizes.

As a third scaling-performance test we fixed the mean per-cell synapse in-degree k_{YX} (count of incoming connections per cell) and reran network simulations for different network sizes (**Figure 7C**). The total number of connections was thus set to $bK_{YX}^{(1)}$ and corresponding connection probabilities C_{YX} were recomputed accordingly using equation 20. As expected, this modification mostly affected the time spent creating connections (green curve), and resulted in a near-linear performance curve for scaling factors $b \geq 1$.

As a final performance assessment we repeated the experiment described above with upscaled networks and increased MPI pool sizes. In **Figure 8A** we set the reference network population sizes $N_{\mathrm{L5\_TTPC1}}^{(1)} = 12,000$ and $N_{\mathrm{L5\_MC}}^{(1)} = 2,400$ and varied N_{MPI} between 600 and 4,800. LFPy's parallel performance was strong also here, and **Figure 8A** consequently shows trends similar to the findings for the smaller network. Here, the time spent creating populations (orange curves) was reasonably invariant for different N_{MPI} values, and increased overall by some factor 2–4 compared to the previous case. The parameter loading times were similar, while the time spent connecting the network was increased by a factor ~ 4, but the simulation times increased only by a factor $\lesssim 2$. The differences in connection and simulation times seen here, can be explained by the fact that the typical synapse in-degrees were not preserved. Instead, the synapse in-degrees were increased for the larger network, as we used the connection probability values defined in **Table 3**.

In **Figures 8B,C** we set $N_{\mathrm{MPI}} = 2,400$, and varied the network population sizes relative to the reference network population sizes in **Figure 8A** by the factor $b \in \{0.2, 0.25, 0.5, 1, 2, 4\}$. Again, the performance figures were in qualitative agreement with the previous results for the smaller network and smaller MPI pool sizes. The population creation times and simulation times with and without signal predictions displayed strong scaling with relative network size. The time spent loading parameters was increased by a small amount (by a factor $\lesssim 2$), which likely reflected the increased strain on the file and communication system on the cluster, due to larger MPI pool sizes. The times spent creating the populations were also here near ideally dependent on N_{MPI} in both **Figures 8B,C**. As the total number of connections (and synapses) were conserved across network population sizes in **Figure 8B**, the connection times varied only by a factor two from the smallest to the largest network. In **Figure 8C**, where the number of connections per neuron was kept approximately constant, a doubling in network size resulted in a doubling in connection times. The larger network simulations required approximately twice the amount of time, compared to the smaller network simulations in **Figure 7**. In **Figure 8C**, simulations with LFP predictions consistently failed for the largest network size ($b = 4$), most likely due to lack of available memory to create arrays for storing current dipole moments and extracellular potentials with the increased count of instantiated connections.

4. DISCUSSION

In the present paper we have presented LFPy 2.0, a majorly revised version of the LFPy Python package with several added features compared to its initial release (Lindén et al., 2014).

4.1. New Features in LFPy 2.0

The first version of LFPy only allowed for the computation of electrical measurements from activity in single neurons or,

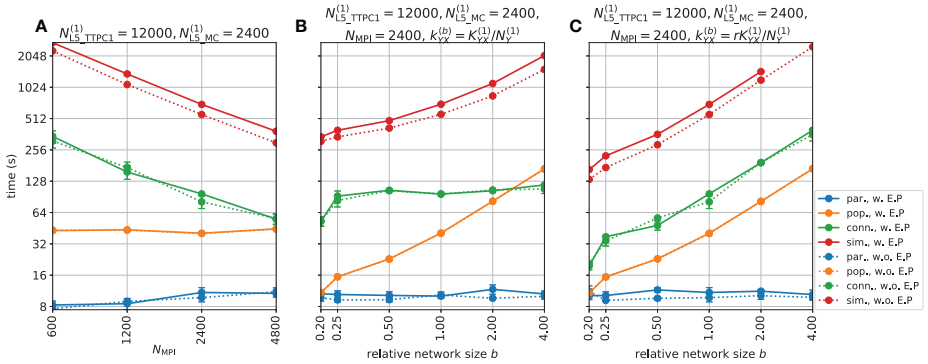

FIGURE 8 | Parallel performance with networks in LFPy II. **(A)** Similar to **Figure 7A**, but with network population sizes upscaled by a factor 5, and a corresponding increase in parallel job sizes. **(B,C)** Similar to **Figures 7B,C**, but with network population sizes and parallel job sizes increased by a factor 5.

by trivial parallellization, populations of neurons only receiving feedforward synaptic input. LFPy 2.0 allows for simulations of recurrently connected neurons as well, for example the types of neuronal networks in cortex. Further, the first version of LFPy was tailored to compute extracellular potentials (spikes, LFPs) inside the brain. Here it was assumed that all active neurons were embedded in an infinite *homogeneous* (i.e., same extracellular conductivity everywhere) and *isotropic* (i.e., same extracellular conductivity in all directions) volume conductor (section 2.2.1). LFPy 2.0 includes several new features and measures of neural activity:

- Stepwise discontinuities in the extracellular conductivity, such as at the cortical surface, can be included by means of the Method-of-Images (section 2.2.2) to compute potentials immediately below or on the cortical surface (i.e., electrocorticographic recordings; ECoG). This approach can also be applied in the computation of potentials recorded by microelectrode arrays (MEAs) (Ness et al., 2015).
- Cylindrical anisotropic conductivity (section 2.2.3) can be included in the computation of spikes and LFPs, reflecting for example that in cortex and hippocampus the conductivity might be larger in the depth direction (along the apical pyramidal-neuron dendrites) than in the lateral directions (Goto et al., 2010).
- Current dipole moments from single neurons and populations of neurons are computed (section 2.3.1) for later use in calculation of signals of systems-level electrical and magnetic recordings (EEG, ECoG, MEG), also for more detailed head models than what is considered presently in LFPy 2.0 (as described in next two items).
- Electrical potentials at the scalp (electroencephalographic recordings; EEG) are computed from the current dipole moments and spherical head models, in particular the four-sphere head model (Nunez and Srinivasan, 2006; Næss et al., 2017), cf. section 2.3.3. This four-sphere head also predicts ECoG signals (section 2.3.4).
- Magnetic fields outside the head (magnetoencephalographic recordings; MEG) can be computed from the current dipole moments assuming a spherically symmetric head model (section 2.3.5). Likewise, magnetic field inside the brain can be computed directly from neuronal axial currents (section 2.4).

LFPy 2.0 also includes much more rigorous code testing with more than 270 unit tests, automated build testing with TravisCI (travis-ci.org/LFPy/LFPy) with different versions of Python (2.7, 3.4-3.6), test coverage of code using coveralls (coveralls.io/github/LFPy/LFPy), automated documentation builds using Read the Docs (lfpy.readthedocs.io), and several updated example files, as well as new examples demonstrating different scientific cases using the new functionalities. The software runs on a wide variety of operating systems, including Linux, Mac OS and Windows.

4.2. Example Applications

To illustrate some of the new measurement modalities incorporated in LFPy 2.0 we showed in **Figure 2** the LFP and EEG signature of a simple pyramidal-like neuron receiving a single excitatory synaptic input on its apical dendrite. In this example the extracellular medium was assumed to be homogeneous, and a characteristic dipolar profile was observed in the extracellular potential (**Figure 2B**). The accuracy of the far-field electrical dipole approximation (Equation 15) for distances of a few millimeters or more away from the neuronal source, was also demonstrated. The corresponding magnetic field set up by the neuron (**Figure 2C**) was quite distinct from the electric potential pattern, but also here far-field magnetic dipole approximation (Equation 16) was observed to be accurate some distance away.

To illustrate the implementation of networks in LFPy 2.0 we show in section A2 (**Appendix**) a code example for a small network using simplified ball-and-stick neurons connected by conductance-based synapses. Our main example applications were on a network of about 5,500 morphologically and

biophysically detailed neuron models from the reconstructed somatosensory cortex column of Markram et al. (2015), connected using probabilistic synapse models with short-term plasticity. For this example, **Figure 5** provided results for a one-second epoch of network activity where spikes (**Figures 5A,B**), LFPs inside the cortical model column (**Figure 5C**), the ECoG signal recorded at cortical surface (**Figure 5D**), and the net current dipole moment (**Figure 5E**) were depicted. The computed current dipole moment was further used to compute the corresponding EEG signal with the four-sphere head model for the situation where the model network was placed on top of a cortical gyrus where the apical dendrites of the pyramidal neurons, and thus the current dipole moment, is pointing in the radial direction (**Figure 5G**). The same current dipole moment was also used to compute the MEG signal, assuming a spherically-symmetric head volume-conductor model, both for the case when the net current dipole is directed perpendicular (**Figure 5H**) and parallel (**Figure 5I**) to the scalp. The latter situation could correspond to the case where the model network is positioned in a cortical sulcus.

While the example network was set up mainly to demonstrate the new features in LFPy 2.0, some of the example results are notable. As expected the two excitatory pyramidal cell populations in the network provided almost all of the recorded LFP signal (except in the deep layers where the layer-5 inhibitory Martinotti-cell population also gave a sizable contribution), cf. **Figure 6E**. Likewise, the two excitatory pyramidal cell populations also gave the dominant contributions to the net current dipole moment providing the EEG and MEG signals (**Figure 6J**).

For the present example network comprising about 5000 pyramidal neurons, we observed the maximum magnitude of the EEG signal to be about 0.1 μV (**Figure 5G**), that is, about two orders of magnitude smaller than the typical size of measured EEG signals of $\sim$10 μV (Nunez and Srinivasan, 2006, Figure 1.1). Thus our example model network appears too small, that is, it incorporates too few pyramidal neurons, to account for the typical experimentally recorded EEG signal amplitudes.

The maximum magnetic field computed at the cortical surface was seen in **Figures 5H,I** to be about 100 fT, that is, similar in magnitude to typical magnetic fields measured by MEG sensors in a human setting ($\sim$50–500 fT, Hämäläinen et al., 1993). However, our model predictions assumed the minimum distance between the current dipoles and the magnetic-field recording device to be only about a centimeter, likely much smaller than the typical minimal distance between the dominant tangential dipoles in cortical sulci and the human MEG sensors. Since the magnetic field around a current dipole decays as the square of the distance, our modeling likely substantially overestimates the magnetic field that would produced by the computed current dipoles in a human setting.

4.3. Use of LFPy

4.3.1. Comparison of Candidate Models With Experiments

An obvious application of LFPy is, following the tradition of physics, to (i) compute predictions of the various available measures of neural activity from different candidate models and (ii) identify which model, or which class of models, is in best agreement with the experimental data. While not always possible, the approach is preferably pursued on multimodal data measured simultaneously (for example simultaneous recordings of spikes, LFP and ECoG). The multi-objective comparison of experimental data with candidate models is a subject on its own, and will not be discussed here (but see, for example, Druckmann et al., 2007).

4.3.2. Validation of Data Analysis Methods

Neuroscience relies on data analysis, and data analysis methods should be validated (Denker et al., 2012). An important application of LFPy could be to provide model-based ground-truth benchmarking data for such validation. This approach has already been used with biophysically detailed neuron models to test methods for spike sorting (Einevoll et al., 2012; Hagen et al., 2015; Lee et al., 2017), neuron classification (Buccino et al., 2017), estimation of firing rates from multi-unit activity (MUA) (Pettersen et al., 2008), current-source density (CSD) analysis (Pettersen et al., 2008; Łęski et al., 2011; Ness et al., 2015), independent component analysis (ICA) (Głąbska et al., 2014) and laminar population analysis (LPA) (Głąbska et al., 2016). Other analysis methods to consider are for example EEG and MEG source localization methods, for example as provided by open-source projects like MNE (martinos.org/mne, Gramfort et al., 2013, 2014), BrainStorm (neuroimage.usc.edu/brainstorm, Tadel et al., 2011), EEGLAB (sccn.ucsd.edu/eeglab, Delorme and Makeig, 2004), Fieldtrip (fieldtriptoolbox.org, Oostenveld et al., 2011), nutmeg (nutmeg.berkeley.edu/, Dalal et al., 2004) and SPM (fil.ion.ucl.ac.uk/spm) where LFPy 2.0 can be used to generate benchmarking data with known "ground truth."

Likewise, LFPy could be used to aid in the interpretation of various statistical measures of electrophysiological activity such as *spike-triggered LFP* or *mutual information* (Einevoll et al., 2013). The interpretation of these measures in terms of the underlying neural network activity is a priori not trivial, but intuition and understanding can be gained by LFPy model investigations where simulation results can be compared with neural activity directly. An example of this was given in Hagen et al. (2016). There the spike-triggered LFP as measured in the model simulation was compared with other ways of accounting for spike-LFP relationships with a simpler physical explanation, that is, the LFP signature following activation of a presynaptic neural population.

It should be noted that the LFPy network model does not necessarily have to be finely tuned to a particular experimental system in order for it to be suitable for validation of data analysis methods: Methods claimed to have fairly general applicability should also be applicable to biologically plausible example network models.

4.3.3. Testing of Simplified Modeling Schemes

LFPy now allows for the concurrent simulation of intracellular (membrane potential) and extracellular signals (spikes, MUA, LFP, EEG, MEG) for recurrent networks of biophysically and morphologically detailed neuron models. Such network

models are computationally demanding to run (Markram et al., 2015), in particular when extracellular signals are computed simultaneously (Reimann et al., 2013). A computationally less demanding alternative is a *hybrid LFP* scheme where the network dynamics, that is, spikes, are modeled with simple point-neuron models such as the integrate-and fire model, and the stored spikes are played back in a second computational step computing the extracellular potentials using multicompartment neuron models (Mazzoni et al., 2015; Hagen et al., 2016).

This scheme requires that salient features of spiking activity of networks of detailed multicompartment neuron models can be accurately captured by point-neuron network models. This was for example demonstrated by Rössert et al. (2016) who reproduced key network behaviour of a reconstructed somatosensory column (Markram et al., 2015) by systematic mapping of synaptic input to somatic responses in generalized leaky integrate-and-fire neurons. Likewise, the accuracy of the second step in the hybrid scheme where the extracellular potential is computed, can be systematically tested by comparing resulting predicted extracellular potential with the ground-truth potentials provided by LFPy. The same approach can also be applied to test other simplified schemes for computing extracellular signals.

4.4. Possible Refinements of Measurement Models in LFPy

4.4.1. Frequency-Dependence of Extracellular Conductivity

The present forward-modeling schemes for electrical potentials assume the extracellular conductivities σ_e to be independent of frequency. If such a frequency dependence is found and described, it can in principle be straightforwardly incorporated by considering each frequency (Fourier) component of recorded signal independently. This was, for example, pursued in Miceli et al. (2017) where each frequency component of the spikes and LFP signals were computed independently (i.e., each frequency component had a specific value of σ_e and a corresponding phase shift required by the Kramers-Kronig relations to preserve causality) and eventually summed to provide the full electric potential. However, on balance the experimental evidence points to at most a weak frequency dependence of σ_e with only minor putative effects on the recorded spikes and LFPs (Miceli et al., 2017). Therefore, the present approximation in LFPy 2.0 to assume a frequency-independent conductivity σ_e, seems warranted.

4.4.2. Modeling of ECoG Signals

LFPy 2.0 provides two different methods for computing ECoG signals, that is, signals at the cortical surface: the method-of-images (MoI) section 2.2.2 and the four-sphere model section 2.3.4 which both have their pros and cons. The MoI method assumes a planar cortical interface and that the media above this interface can be described electrically by means of a single isotropic electrical conductivity. The four-sphere model assumes a spherical cortical surface and uses the far-field dipole approximation which requires the dipolar sources to be sufficiently far away from the recording contacts. With the present use of current dipole moments representing entire neuron populations, this approximation is challenged by the relatively short distance between in particular the most superficial populations and the cortical surface (Næss, 2015). A future project is to systematically explore the accuracy of these two methods for ECoG modeling, for example by comparing their predictions for different situations.

The present forward modeling of electrical potentials are based on stylized spatial (planar/spherical geometries, step-wise varying conductivities) and directional (isotropy/cylindrical anisotropy) variations. More complicated models for the variation of the extracellular conductivity can be accounted for by means of finite-element modeling (FEM, Logg et al., 2012; Lempka and McIntyre, 2013; Ness et al., 2015; Næss et al., 2017) for which the "lead field," that is, the contribution from transmembrane currents or dipole moments to electric signals, always can be computed (Malmivuo and Plonsey, 1995). FEM could, for example, be used to explore in detail how the recording device affects the recorded ECoG signal when a grid of ECoG contacts are embedded in an insulating material (see for example, Castagnola et al. (2014)), in analogy to the study of multielectrode arrays (MEAs) in Ness et al. (2015).

4.4.3. More Complicated Head Models

The current dipole moments computed by LFPy can also be used to compute EEG and MEG signals based on geometrically detailed head models measured by MRI (Bangera et al., 2010; DeMunck et al., 2012; Vorwerk et al., 2014; Huang et al., 2016). Note, however, that geometrically detailed head models do not automatically transfer to electrically detailed head models, and it is thus not always clear how much accuracy is gained by using such models rather than the simpler head models currently implemented in LFPy (see discussion in Nunez and Srinivasan, 2006, Ch. 6).

4.5. Possible Improvements of LFPy Code

While we here demonstrated a relatively strong scaling of parallel network implementations in LFPy, the code itself could be further optimized for improving overall simulation speeds and reduced memory consumption allowing for larger networks for any given MPI pool size.

One common way of improving efficiency of Python applications is rewriting "slow" code to use Cython (C-extensions for Python, cython.org, Smith, 2015). The current LFPy version uses Cython to a limited extent, but remaining code bottlenecks could be identified and addressed accordingly. One potential problem with efficient porting of parts of LFPy's Python code to Cython is repeated calls to NEURON's Python interface, which from a performance point of view should be avoided.

One known bottleneck with parallel implementations of multicompartment neuron networks is uneven load balance, resulting from the fact that individual neurons with very uneven numbers of compartments may be assigned to the different MPI processes. Uneven load balance could potentially be addressed

by incorporating the multi-split method described in Hines et al. (2008), as it appears compatible with the presently used `CVode.use_fast_imem()` method (available since NEURON v7.4). LFPy could then be updated accordingly.

Even without the NEURON multi-split method, distribution of cells among MPI processes using a round-robin scheme could, however, be optimized to level out large differences in compartment counts (and corresponding numbers of state variables). Memory consumption could also be addressed by choosing more efficient memory structures or generators, for example, for connectivity management, and by avoiding in-memory storage of output data wherever possible. File-based I/O operations during ongoing simulations may, however, come at the expense of increased simulation times.

In terms of improved support for simulator-independent (agnostic) model description languages for neuronal models such as NeuroML (Gleeson et al., 2010; Cannon et al., 2014) or NESTML (Plotnikov et al., 2016), LFPy's `TemplateCell` and `NetworkCell` classes already now support loading of active and passive single-neuron model files translated to NEURON's HOC and NMODL languages from NeuroML and NeuroML2 (now in development). A growing number of such single-neuron models is becoming available through, for example the Open Source Brain initiative (opensourcebrain.org), which can readily be used in order to construct new network models. While certainly doable, LFPy is at present not set up for automatic loading of entire neuron networks specified in NeuroML. Also, single-cell and network models specified using LFPy could, in principle, be possible to translate into NeuroML as well, which would allow for executing such models using for example NetPyne (netpyne.org) or LEMS (Cannon et al., 2014).

4.6. Other Measurement Modalities in LFPy

The present version of LFPy only models recording of electric and magnetic brain signals. Optical recording methods are now frequently used in neurophysiology, however, and forward-modeling of such signals would be a natural extension of the present functionality. In voltage-sensitive dye imaging (VSDi), the recorded signals reflects a weighted average of the membrane potentials, and such averages can be readily computed since the membrane voltages in all neuronal compartments are computed during a network simulation simulation (Chemla and Chavane, 2010a,b). This must then be combined with proper forward-modeling of the propagation of the light through the brain tissue (Tian et al., 2011; Abdellah et al., 2015, 2017).

Calcium imaging has become a wide-spread method for measuring neural dynamics (Grienberger and Konnerth, 2012). With the use of neuron models that explicitly includes dynamic modelling of the intracellular calcium concentrations (for example, Hay et al., 2011; Almog and Korngreen, 2014) such signals could be directly modeled as well.

4.7. Alternatives to LFPy

For the purpose of computing extracellular potentials under the assumption of homogeneous extracellular conductivity and networks of multicompartment neuron models, some alternatives to LFPy 2.0 exist. Genesis (genesis-sim.org, Bower and Beeman, 1998) incorporates the simple point-source formalism (Equation 4), while the MATLAB tool Vertex (vertexsimulator.org, Tomsett et al., 2015) allows for computing extracellular potentials but not for multicompartment neuron models with arbitrary levels of detail. The MOOSE simulator (https://moose.ncbs.res.in, Ray and Bhalla, 2008) do not appear to natively incorporate electrostatic forward models. An extension to NEURON named LFPsim (github.com/compneuro/LFPsim, Parasuram et al., 2016) supports single neurons and networks but relies on the NEURON GUI. This may allow for simple evaluation of LFPs generated by small networks, but hampers application to large-scale networks running in parallel.

The Python and NEURON based tools NetPyne (netpyne.org) and BioNet (github.com/AllenInstitute/bmtk, Gratiy et al. (2018)), part of the Allen Brain Institute's Brain Modeling Toolkit, do, however, support biophysically detailed networks of neurons running in parallel with predictions of extracellular potentials, but presently without the wider range of electric and magnetic forward models now provided in LFPy 2.0. Similar to LFPy 2.0, high-level functionality to specify networks are provided to simplify the generation of networks.

Finally, the recent 'Human Neocortical Neurosolver' (hnn.brown.edu) can compute LFP, MEG and EEG signals, but has a focus on signals generated by specific generic cortical network topologies, namely using neurons with few compartments organized in two "cortical layers" 2/3 and 5. In contrast, LFPy 2.0 supports defining networks with an arbitrary number of layers and biophysical detail.

4.8. Outlook

While information in the brain might largely be represented by spike trains, we believe that tools such as LFPy will be instrumental in testing candidate network models aiming to account for this information processing. In the foreseeable future, experimental data against which candidate models can be tested will be a limiting factor. It is thus key that such candidate models can be tested not only against spike trains, but also other measurement modalities.

This updated version of LFPy makes a major step toward being a true multi-scale simulator of neural circuits, allowing for flexible incorporation of highly detailed neuron models at the micrometer scale, yet able to also predict recorded signals such as EEG and MEG at the systems-level scale. The largest network considered here had 57,600 neurons. With the present code, not optimized for numerical efficiency, the simulation of 1.5 s of biological time on this network required about 1,600 CPU hours across 2,400 MPI processes. With optimized code, we expect that much larger networks can soon be addressed routinely as ever more powerful computers gradually become available. The software is also publicly available on GitHub and retains the open-source software license of its initial release, and our hope is that continued development remains driven by needs and contributions of individuals and groups of researchers.

DATA AVAILABILITY STATEMENT

All source codes to reproduce the simulation results of this publication are available as example files in the main LFPy GitHub repository (github.com/LFPy/LFPy). The stable release of LFPy 2.0.0 is deposited on zenodo.org (doi.org/10.5281/zenodo.1401088).

AUTHOR CONTRIBUTIONS

EH and SN wrote the first paper draft. EH, SN, TN, and GE co-wrote the paper. EH implemented and ran all simulations. SN implemented the four-sphere head model for the EEG and axial current calculations. TN implemented the LFP models for anisotropic and inhomogeneous (Method-of-Images) electrical conductivity.

FUNDING

This work received funding from the European Union Horizon 2020 Research and Innovation Programme under Grant Agreement No. 720270 and No. 785907 [Human Brain Project (HBP) SGA1 and SGA2], the Norwegian Ministry of Education and Research through the SUURPh Programme and the Norwegian Research Council (NFR) through COBRA (grant # 250128), CINPLA and NOTUR - NN4661K. Use of the JURECA supercomputer was made possible through VSR computation time grant Brain-scale simulations JINB33.

ACKNOWLEDGMENTS

We thank Tuomo Mäki-Marttunen for useful comments and discussions on the manuscript. We also would like to thank everyone who contributed to LFPy's development.

SUPPLEMENTARY MATERIAL

The Supplementary Material for this article can be found online at: https://www.frontiersin.org/articles/10.3389/fninf.2018.00092/full#supplementary-material

REFERENCES

Abdellah, M., Bilgili, A., Eilemann, S., Markram, H., and Schürmann, F. (2015). Physically-based *in silico* light sheet microscopy for visualizing fluorescent brain models. *BMC Bioinformatics* 16:S8. doi: 10.1186/1471-2105-16-S11-S8

Abdellah, M., Bilgili, A., Eilemann, S., Shillcock, J., Markram, H., and Schürmann, F. (2017). Bio-physically plausible visualization of highly scattering fluorescent neocortical models for *in silico* experimentation. *BMC Bioinformatics* 18:62. doi: 10.1186/s12859-016-1444-4

Almog, M., and Korngreen, A. (2014). A quantitative description of dendritic conductances and its application to dendritic excitation in layer 5 pyramidal neurons. *J. Neurosci.* 34, 182–196. doi: 10.1523/JNEUROSCI.2896-13.2014

Anastassiou, C. A., Perin, R., Markram, H., and Koch, C. (2011). Ephaptic coupling of cortical neurons. *Nat. Neurosci.* 14, 217–223. doi: 10.1038/nn.2727

Bangera, N. B., Schomer, D. L., Dehghani, N., Ulbert, I., Cash, S., Papavasiliou, S., et al. (2010). Experimental validation of the influence of white matter anisotropy on the intracranial EEG forward solution. *J. Comput. Neurosci.* 29, 371–387. doi: 10.1007/s10827-009-0205-z

Barbieri, F., Trauchessec, V., Caruso, L., Trejo-Rosillo, J., Telenczuk, B., Paul, E., et al. (2016). Local recording of biological magnetic fields using giant magneto resistance-based micro-probes. *Sci. Rep.* 6:39330. doi: 10.1038/srep39330

Blagoev, K., Mihaila, B., Travis, B., Alexandrov, L., Bishop, A., Ranken, D., et al. (2007). Modelling the magnetic signature of neuronal tissue. *NeuroImage* 37, 137–148. doi: 10.1016/j.neuroimage.2007.04.033

Blakemore, C., and Tobin, E. A. (1972). Lateral inhibition between orientation detectors in the cat's visual cortex. *Exp. Brain Res.* 15, 439–440. doi: 10.1007/BF00234129

Borst, J. G. G. (2010). The low synaptic release probability *in vivo*. *Trends Neurosci.* 33, 259–266. doi: 10.1016/j.tins.2010.03.003

Bower, J. M., and Beeman, D. (1998). *The Book of GENESIS: Exploring Realistic Neural Models with the GEneral NEural SImulation System, 2nd Edn*. New York, NY: Springer-Verlag.

Brette, R., and Destexhe, A., editors (2012). *Handbook of Neural Activity Measurement*. Cambridge, UK: Cambridge University Press.

Buccino, A. P., Ness, T. V., Einevoll, G. T., Cauwenberghs, G., and Hfliger, P. D. (2017). "Localizing neuronal somata from multi-electrode array *in-vivo* recordings using deep learning," in *2017 39th Annual International Conference of the IEEE Engineering in Medicine and Biology Society (EMBC)* (Piscataway, NJ) 974–977. doi: 10.1109/EMBC.2017.8036988

Buzsáki, G. (2004). Large-scale recording of neuronal ensembles. *Nat. Neurosci.* 7, 446–451. doi: 10.1038/nn1233

Buzsáki, G., Anastassiou, C. A., and Koch, C. (2012). The origin of extracellular fields and currents EEG, ECoG, LFP and spikes. *Nat. Rev. Neurosci.* 13, 407–420. doi: 10.1038/nrn3241

Camuñas-Mesa, L. A., and Quiroga, R. Q. (2013). A detailed and fast model of extracellular recordings. *Neural Comput.* 25, 1191–1212. doi: 10.1162/NECO_a_00433

Cannon, R. C., Gleeson, P., Crook, S., Ganapathy, G., Marin, B., Piasini, E., and Silver, R. A. (2014). LEMS: a language for expressing complex biological models in concise and hierarchical form and its use in underpinning NeuroML 2. *Front. Neuroinformatics* 8:79. doi: 10.3389/fninf.2014.00079

Carnevale, N. T., and Hines, M. L. (2006). *The NEURON Book*. Cambridge, UK: Cambridge University Press.

Caruso, L., Wunderle, T., Lewis, C. M., Valadeiro, J., Trauchessec, V., Rosillo, J. T., et al. (2017). *In vivo* magnetic recording of neuronal activity. *Neuron* 95, 1283–1291.e4. doi: 10.1016/j.neuron.2017.08.012

Castagnola, E., Ansaldo, A., Maggiolini, E., Ius, T., Skrap, M., Ricci, D., et al. (2014). Smaller, softer, lower-impedance electrodes for human neuroprosthesis: a pragmatic approach. *Front. Neuroeng.* 7:8. doi: 10.3389/fneng.2014.00008

Chemla, S., and Chavane, F. (2010a). A biophysical cortical column model to study the multi-component origin of the VSDI signal. *NeuroImage* 53, 420–438. doi: 10.1016/j.neuroimage.2010.06.026

Chemla, S., and Chavane, F. (2010b). Voltage-sensitive dye imaging: technique review and models. *J. Physiol. Paris* 104, 40–50. doi: 10.1016/j.jphysparis.2009.11.009

Cserpán, D., Meszéna, D., Wittner, L., Tóth, K., Ulbert, I., Somogyvári, Z., et al. (2017). Revealing the distribution of transmembrane currents along the dendritic tree of a neuron from extracellular recordings. *eLife* 6:e29384. doi: 10.7554/eLife.29384

Dalal, S. S., Zumer, J. M., Agrawal, V., Hild, K. E., Sekihara, K., and Nagarajan, S. S. (2004). Nutmeg: a neuromagnetic source reconstruction toolbox. *Neurol. Clin. Neurophysiol.* 2004:52.

Dayan, P., and Abbott, L. (2001). *Theoretical Neuroscience*. Cambridge: MIT Press.

De Schutter, E., and Van Geit, W. (2009). "Modeling complex neurons," in *Computational Modeling Methods for Neuroscientists*, Chapter 11, *1st Edn.*, ed E. De Schutter (Cambridge, MA: MIT Press), 260–283.

Delorme, A., and Makeig, S. (2004). EEGlab: an open source toolbox for analysis of single-trial EEG dynamics including independent component analysis. *J. Neurosci. Methods* 134, 9–21. doi: 10.1016/j.jneumeth.2003.10.009

DeMunck, J. C., Wolters, C. H., and Clerc, M. (2012). "EEG and MEG – forward modeling," in *Handbook of Neural Activity Measurement*, eds R. Brette and A. Destexhe (Cambridge, UK: Cambridge University Press), pp. 192–256. doi: 10.1017/CBO9780511979958.006

Deng, S. (2008). Electrostatic potential of point charges inside dielectric prolate spheroids. *J. Electrostat.* 66, 549–560. doi: 10.1016/j.elstat.2008.06.003

Denker, M., Einevoll, G., Franke, F., Grün, S., Hagen, E., Kerr, J., et al. (2012). *Report From 1st INCF Workshop on Validation of Analysis Methods*. Technical report, International Neuroinformatics Coordinating Facility (INCF).

Djurfeldt, M. (2012). The connection-set algebra a novel formalism for the representation of connectivity structure in neuronal network models. *Neuroinformatics* 10, 287–304. doi: 10.1007/s12021-012-9146-1

Djurfeldt, M., Davison, A. P., and Eppler, J. M. (2014). Efficient generation of connectivity in neuronal networks from simulator-independent descriptions. *Front. Neuroinformatics* 8:43. doi: 10.1007/s12021-010-9064-z

Druckmann, S., Banitt, Y., Gidon, A., Schurmann, F., Markram, H., and Segev, I. (2007). A novel multiple objective optimization framework for constraining conductance-based neuron models by experimental data. *Front. Neurosci.* 1:7–18. doi: 10.3389/neuro.01.1.1.001.2007

Einevoll, G. T., Franke, F., Hagen, E., Pouzat, C., and Harris, K. D. (2012). Towards reliable spike-train recordings from thousands of neurons with multielectrodes. *Curr. Opin. Neurobiol.* 22, 11–17. doi: 10.1016/j.conb.2011.10.001

Einevoll, G. T., Kayser, C., Logothetis, N. K., and Panzeri, S. (2013). Modelling and analysis of local field potentials for studying the function of cortical circuits. *Nat. Rev. Neurosci.* 14:770. doi: 10.1038/nrn3599

Einevoll, G. T., Pettersen, K. H., Devor, A., Ulbert, I., Halgren, E., and Dale, A. M. (2007). Laminar population analysis: estimating firing rates and evoked synaptic activity from multielectrode recordings in rat barrel cortex. *J. Neurophysiol.* 97, 2174–2190. doi: 10.1152/jn.00845.2006

Foster, I. (1995). *Designing and Building Parallel Programs: Concepts and Tools for Parallel Software Engineering*. Boston, MA: Addison-Wesley Longman Publishing Co.

Franke, F., Natora, M., Meier, P., Hagen, E., Pettersen, K. H., Linden, H., et al. (2010). "An automated online positioning system and simulation environment for multi-electrodes in extracellular recordings," in *2010 Annual International Conference of the IEEE Engineering in Medicine and Biology* (Piscataway, NJ: IEEE), 593–597.

Fuhrmann, G., Segev, I., Markram, H., and Tsodyks, M. (2002). Coding of temporal information by activity-dependent synapses. *J. Neurophysiol.* 87, 140–148. doi: 10.1152/jn.00258.2001

Głąbska, H., Potworowski, J., Łęski, S., and Wójcik, D. K. (2014). Independent components of neural activity carry information on individual populations. *PLoS ONE* 9:e105071. doi: 10.1371/journal.pone.0105071

Głąbska, H. T., Norheim, E., Devor, A., Dale, A. M., Einevoll, G. T., and Wójcik, D. K. (2016). Generalized laminar population analysis (gLPA) for interpretation of multielectrode data from cortex. *Front. Neuroinformatics* 10:1. doi: 10.3389/fninf.2016.00001

Gleeson, P., Crook, S., Cannon, R. C., Hines, M. L., Billings, G. O., Farinella, M., et al. (2010). NeuroML: a language for describing data driven models of neurons and networks with a high degree of biological detail. *PLoS Comput. Biol.* 6:e1000815. doi: 10.1371/journal.pcbi.1000815

Gold, C., Henze, D. A., and Koch, C. (2007). Using extracellular action potential recordings to constrain compartmental models. *J. Comput. Neurosci.* 23, 39–58. doi: 10.1007/s10827-006-0018-2

Gold, C., Henze, D. A., Koch, C., and Buzsáki, G. (2006). On the origin of the extracellular action potential waveform: a modeling study. *J. Neurophysiol.* 95, 3113–3128. doi: 10.1152/jn.00979.2005

Goldwyn, J. H., and Rinzel, J. (2016). Neuronal coupling by endogenous electric fields: cable theory and applications to coincidence detector neurons in the auditory brain stem. *J. Neurophysiol.* 115, 2033–2051. doi: 10.1152/jn.00780.2015

Goto, T., Hatanaka, R., Ogawa, T., Sumiyoshi, A., Riera, J., and Kawashima, R. (2010). An evaluation of the conductivity profile in the somatosensory barrel cortex of wistar rats. *J. Neurophysiol.* 104, 3388–3412. doi: 10.1152/jn.00122.2010

Gramfort, A., Luessi, M., Larson, E., Engemann, D. A., Strohmeier, D., Brodbeck, C., et al. (2013). Meg and EEG data analysis with mne-python. *Front. Neurosci.* 7:267. doi: 10.3389/fnins.2013.00267

Gramfort, A., Luessi, M., Larson, E., Engemann, D. A., Strohmeier, D., Brodbeck, C., et al. (2014). Mne software for processing meg and eeg data. *NeuroImage* 86, 446–460. doi: 10.1016/j.neuroimage.2013.10.027

Gratiy, S. L., Billeh, Y. N., Dai, K., Mitelut, C., Feng, D., Gouwens, N. W., et al. (2018). BioNet: a python interface to NEURON for modeling large-scale networks. *PLoS ONE* 13:e0201630. doi: 10.1371/journal.pone.0201630

Gratiy, S. L., Devor, A., Einevoll, G. T., and Dale, A. M. (2011). On the estimation of population-specific synaptic currents from laminar multielectrode recordings. *Front. Neuroinformatics* 5:32. doi: 10.3389/fninf.2011.00032

Grienberger, C., and Konnerth, A. (2012). Imaging calcium in neurons. *Neuron* 73, 862–885. doi: 10.1016/j.neuron.2012.02.011

Grinvald, A., and Hildesheim, R. (2004). VSDI: a new era in functional imaging of cortical dynamics. *Nat. Rev. Neurosci.* 5, 874–885. doi: 10.1038/nrn1536

Hafting, T., Fyhn, M., Molden, S., Moser, M.-B., and Moser, E. I. (2005). Microstructure of a spatial map in the entorhinal cortex. *Nature* 436, 801–806. doi: 10.1038/nature03721

Hagen, E., Dahmen, D., Stavrinou, M. L., Lind, H., Tetzlaff, T., van Albada, S. J., et al. (2016). Hybrid scheme for modeling local field potentials from point-neuron networks. *Cereb. Cortex* 26, 4461–4496. doi: 10.1093/cercor/bhw237

Hagen, E., Fossum, J. C., Pettersen, K. H., Alonso, J.-M., Swadlow, H. A., and Einevoll, G. T. (2017). Focal local field potential (LFP) signature of the single-axon monosynaptic thalamocortical connection. *J. Neurosci.* 37, 5123–5143. doi: 10.1523/JNEUROSCI.2715-16.2017

Hagen, E., Ness, T. V., Khosrowshahi, A., Sørensen, C., Fyhn, M., Hafting, T., et al. (2015). ViSAPy: a python tool for biophysics-based generation of virtual spiking activity for evaluation of spike-sorting algorithms. *J. Neurosci. Methods* 245, 182–204. doi: 10.1016/j.jneumeth.2015.01.029

Halnes, G., Mki-Marttunen, T., Keller, D., Pettersen, K. H., Andreassen, O. A., and Einevoll, G. T. (2016). Effect of ionic diffusion on extracellular potentials in neural tissue. *PLoS Comput. Biol.* 12:e1005193. doi: 10.1371/journal.pcbi.1005193

Hämäläinen, M., Hari, R., Ilmoniemi, R. J., Knuutila, J., and Lounasmaa, O. V. (1993). Magnetoencephalography theory, instrumentation, and applications to noninvasive studies of the working human brain. *Rev. Mod. Phys.* 65:413. doi: 10.1103/RevModPhys.65.413

Hay, E., Hill, S., Schürmann, F., Markram, H., and Segev, I. (2011). Models of neocortical layer 5b pyramidal cells capturing a wide range of dendritic and perisomatic active properties. *PLoS Comput. Biol.* 7:e1002107. doi: 10.1371/journal.pcbi.1002107

He, B., Zhang, X., Lian, J., Sasaki, H., Wu, D., and Towle, V. (2002). Boundary element method-based cortical potential imaging of somatosensory evoked potentials using subjects' magnetic resonance images. *NeuroImage* 16, 564–576. doi: 10.1006/nimg.2002.1127

Heiberg, T., Hagen, E., Halnes, G., and Einevoll, G. T. (2016). Biophysical network modelling of the dLGN circuit: different effects of triadic and axonal inhibition on visual responses of relay cells. *PLoS Comput. Biol.* 12:e1004929. doi: 10.1371/journal.pcbi.1004929

Helmchen, F., and Denk, W. (2005). Deep tissue two-photon microscopy. *Nat. Methods* 2, 932–940. doi: 10.1038/nmeth818

Hines, M. L., Davison, A. P., and Muller, E. (2009). NEURON and python. *Front. Neuroinformatics* 3:1. doi: 10.3389/neuro.11.001.2009

Hines, M. L., Markram, H., and Schürmann, F. (2008). Fully implicit parallel simulation of single neurons. *J. Comput. Neurosci.* 25, 439–448. doi: 10.1007/s10827-008-0087-5

Holt, G. R., and Koch, C. (1999). Electrical interactions via the extracellular potential near cell bodies. *J. Comput. Neurosci.* 6, 169–184. doi: 10.1023/A:1008832702585

Huang, Y., Parra, L. C., and Haufe, S. (2016). The New York head - a presise standardized volume conductor model for EEG source localization and tES targeting. *NeuroImage* 140, 150–162. doi: 10.1016/j.neuroimage.2015.12.019

Hubel, D. H., and Wiesel, T. N. (1959). Receptive fields of single neurones in the cat's striate cortex. *J. Physiol.* 148, 574–591. doi: 10.1113/jphysiol.1959.sp006308

Koch, C. (1999). *Biophysics of Computation*. Oxford: Oxford University Press.

Lee, J., Carlson, D., Shokri, H., Yao, W., Goetz, G., Chichilnisky, E., et al. (2017). "YASS: yet another spike sorter," in *Advances in Neural Information Processing Systems 30 (NIPS 2017)* (Red Hook, NY: Curran Associates, Inc.), 4002–4012.

Lempka, S. F., and McIntyre, C. C. (2013). Theoretical analysis of the local field potential in deep brain stimulation applications. *PLoS ONE* 8:e59839. doi: 10.1371/journal.pone.0059839

Łęski, S., Lindén, H., Tetzlaff, T., Pettersen, K. H., and Einevoll, G. T. (2013). Frequency dependence of signal power and spatial reach of the local field potential. *PLoS Comput. Biol.* 9:e1003137. doi: 10.1371/journal.pcbi.1003137

Łęski, S., Pettersen, K. H., Tunstall, B., Einevoll, G. T., Gigg, J., and Wójcik, D. (2011). Inverse current source density method in two dimensions: inferring neural activation from multielectrode recordings. *Neuroinformatics* 9, 401–425. doi: 10.1007/s12021-011-9111-4

Li, C. L., and Jasper, H. (1953). Microelectrode studies of the electrical activity of the cerebral cortex in the cat. *J. Physiol.* 121, 117–140. doi: 10.1113/jphysiol.1953.sp004935

Lindén, H., Hagen, E., Łeski, S., Norheim, E. S., Pettersen, K. H., and Einevoll, G. T. (2014). LFPy: a tool for biophysical simulation of extracellular potentials generated by detailed model neurons. *Front. Neuroinformatics* 7:41. doi: 10.3389/fninf.2013.00041

Lindén, H., Pettersen, K. H., and Einevoll, G. T. (2010). Intrinsic dendritic filtering gives low-pass power spectra of local field potentials. *J. Comput. Neurosci.* 29, 423–444. doi: 10.1007/s10827-010-0245-4

Lindén, H., Tetzlaff, T., Potjans, T. C., Pettersen, K. H., Grün, S., Diesmann, M., et al. (2011). Modeling the spatial reach of the lfp. *Neuron* 72, 859–872. doi: 10.1016/j.neuron.2011.11.006

Logg, A., Mardal, K.-A., and Wells, G. (2012). *Automated Solution of Differential Equations by the Finite Element Method: The FEniCS Book*, Vol. 84. Berlin; Heidelberg: Springer Science & Business Media.

Luo, J., Macias, S., Ness, T. V., Einevoll, G. T., Zhang, K., Moss, C. F. (2018). Neural timing of stimulus events with microsecond precision. *PLoS Biol.* 16:e2006422. doi: 10.1371/journal.pbio.2006422

Maier, A., Adams, G. K., Aura, C., and Leopold, D. A. (2010). Distinct superficial and deep laminar domains of activity in the visual cortex during rest and stimulation. *Front. Syst. Neurosci.* 4:31. doi: 10.3389/fnsys.2010.00031

Makarova, J., Ibarz, J. M., Makarov, V. A., Benito, N., and Herreras, O. (2011). Parallel readout of pathway-specific inputs to laminated brain structures. *Front. Syst. Neurosci.* 5:77. doi: 10.3389/fnsys.2011.00077

Malmivuo, J., and Plonsey, R. (1995). *Bioelectromagnetism*. Oxford, UK: Oxford University Press.

Markram, H., Muller, E., Ramaswamy, S., Reimann, M. W., Abdellah, M., Sanchez, C. A., et al. (2015). Reconstruction and simulation of neocortical microcircuitry. *Cell* 163, 456–492. doi: 10.1016/j.cell.2015.09.029

Markram, H., Toledo-Rodriguez, M., Wang, Y., Gupta, A., Silberberg, G., and Wu, C. (2004). Interneurons of the neocortical inhibitory system. *Nat. Rev. Neurosci.* 5, 793–807.

Martín-Vázquez, G., Benito, N., Makarov, V. A., Herreras, O., and Makarova, J. (2015). Diversity of LFPs activated in different target regions by a common CA3 input. *Cereb. Cortex* 26, 4082—4100.

Martín-Vázquez, G., Makarova, J., Makarov, V. A., and Herreras, O. (2013). Determining the true polarity and amplitude of synaptic currents underlying gamma oscillations of local field potentials. *PLoS ONE* 8:e75499. doi: 10.1371/journal.pone.0075499

Mazzoni, A., Lindén, H., Cuntz, H., Lansner, A., Panzeri, S., and Einevoll, G. T. (2015). Computing the local field potential (lfp) from integrate-and-fire network models. *PLoS Comput. Biol.* 11:e1004584. doi: 10.1371/journal.pcbi.1004584

McColgan, T., Liu, J., Kuokkanen, P. T., Carr, C. E., Hermann, W., and Kempter, R. (2017). Dipolar extracellular potentials generated by axonal projections. *eLife* 6:109918. doi: 10.7554/eLife.26106

McDougal, R. A., Morse, T. M., Carnevale, T., Marenco, L., Wang, R., Migliore, M., et al. (2017). Twenty years of ModelDB and beyond: building essential modeling tools for the future of neuroscience. *J. Comput. Neurosci.* 42, 1–10. doi: 10.1007/s10827-016-0623-7

McIntyre, C. C., and Grill, W. M. (2001). Finite element analysis of the current-density and electric field generated by metal microelectrodes. *Ann. Biomed. Eng.* 29, 227–235. doi: 10.1114/1.1352640

Miceli, S., Ness, T. V., Einevoll, G. T., and Schubert, D. (2017). Impedance spectrum in cortical tissue: implications for propagation of LFP signals on the microscopic level. *eNeuro* 4:ENEURO.0291–16. doi: 10.1523/ENEURO.0291-16.2016

Næss, S. (2015). Biophysical Modeling of EEG Signals From Neurons in the Brain. Master's thesis, Norwegian University of Life Science, Ås.

Næss, S., Chintaluri, H. C., Ness, T. V., Dale, A. M., Einevoll, G. T., and Wójcik, D. K. (2017). Corrected four-sphere head model for EEG signals. *Front. Hum. Neurosci.* 11:490. doi: 10.3389/fnhum.2017.00490

Nelson, M. J., and Pouget, P. (2010). Do electrode properties create a problem in interpreting local field potential recordings? *J. Neurophysiol.* 103, 2315–2317. doi: 10.1152/jn.00157.2010

Nelson, M. J., Pouget, P., Nilsen, E. A., Patten, C. D., and Schall, J. D. (2008). Review of signal distortion through metal microelectrode recording circuits and filters. *J. Neurosci. Methods* 169, 141–157. doi: 10.1016/j.jneumeth.2007.12.010

Ness, T. V., Chintaluri, C., Potworowski, J., Łęski, S., Głąbska, H., Wójcik, D. K., et al. (2015). Modelling and analysis of electrical potentials recorded in microelectrode arrays (MEAs). *Neuroinformatics* 13, 403–426. doi: 10.1007/s12021-015-9265-6

Ness, T. V., Remme, M. W. H., and Einevoll, G. T. (2016). Active subthreshold dendritic conductances shape the local field potential. *J. Physiol.* 594, 3809–3825. doi: 10.1113/JP272022

Ness, T. V., Remme, M. W. H., and Einevoll, G. T. (2018). h-type membrane current shapes the local field potential from populations of pyramidal neurons. *J. Neurosci.* 38, 6011–6024. doi: 10.1523/JNEUROSCI.3278-17.2018

Nicholson, C., and Freeman, J. A. (1975). Theory of current source-density analysis and determination of conductivity tensor for anuran cerebellum. *J. Neurophysiol.* 38, 356–368. doi: 10.1152/jn.1975.38.2.356

Nicholson, C., and Llinas, R. (1971). Field potentials in the alligator cerebellum and theory of their relationship to Purkinje cell dendritic spikes. *J. Neurophysiol.* 34, 509–531. doi: 10.1152/jn.1971.34.4.509

Nunez, P. L., and Srinivasan, R. (2006). *Electric Fields of the Brain: The Neurophysics of EEG*. New York, NY: Oxford University Press.

O'Keefe, J., and Dostrovsky, J. (1971). The hippocampus as a spatial map. Preliminary evidence from unit activity in the freely-moving rat. *Brain Res.* 34, 171–175. doi: 10.1016/0006-8993(71)90358-1

Oostenveld, R., Fries, P., Maris, E., and Schoffelen, J.-M. (2011). Fieldtrip: open source software for advanced analysis of meg, eeg, and invasive electrophysiological data. *Comput. Intell. Neurosci.* 2011:156869. doi: 10.1155/2011/156869

Parasuram, H., Nair, B., D'Angelo, E., Hines, M., Naldi, G., and Diwakar, S. (2016). Computational modeling of single neuron extracellular electric potentials and network local field potentials using LFPsim. *Front. Comput. Neurosci.* 10:65. doi: 10.3389/fncom.2016.00065

Petersen, C. C. H., Grinvald, A., and Sakmann, B. (2003). Spatiotemporal dynamics of sensory responses in layer 2/3 of rat barrel cortex measured *in vivo* by voltage-sensitive dye imaging combined with whole-cell voltage recordings and neuron reconstructions. *J. Neurosci.* 23, 1298–1309. doi: 10.1523/JNEUROSCI.23-04-01298.2003

Pettersen, K. H., Devor, A., Ulbert, I., Dale, A. M., and Einevoll, G. T. (2006). Current-source density estimation based on inversion of electrostatic forward solution: effects of finite extent of neuronal activity and conductivity discontinuities. *J. Neurosci. Methods* 154, 116–133. doi: 10.1016/j.jneumeth.2005.12.005

Pettersen, K. H., and Einevoll, G. T. (2008). Amplitude variability and extracellular low-pass filtering of neuronal spikes. *Biophys. J.* 94, 784–802. doi: 10.1529/biophysj.107.111179

Pettersen, K. H., Hagen, E., and Einevoll, G. T. (2008). Estimation of population firing rates and current source densities from laminar electrode recordings. *J. Comput. Neurosci.* 24, 291–313. doi: 10.1007/s10827-007-0056-4

Pettersen, K. H., Lindén, H., Dale, A. M., and Einevoll, G. T. (2012). "Extracellular spikes and CSD," in *Handbook of Neural Activity Measurement*, eds R. Brette and A. Destexhe (Cambridge, UK: Cambridge University Press). 92–135. doi: 10.1017/CBO9780511979958.004

Plotnikov, D., Rumpe, B., Blundell, I., Ippen, T., Eppler, J. M., and Morrison, A. (2016). NESTML: a modeling language for spiking neurons. arXiv 1606.02882.

Potjans, T. C., and Diesmann, M. (2014). The cell-type specific cortical microcircuit: relating structure and activity in a full-scale spiking network model. *Cereb. Cortex* 24, 785–806. doi: 10.1093/cercor/bhs358

Quiroga, R. Q., Reddy, L., Kreiman, G., Koch, C., and Fried, I. (2005). Invariant visual representation by single neurons in the human brain. *Nature* 435, 1102–1107. doi: 10.1038/nature03687

Ramaswamy, S., Courcol, J.-D., Abdellah, M., Adaszewski, S. R., Antille, N., Arsever, S., et al. (2015). The neocortical microcircuit collaboration portal: a resource for rat somatosensory cortex. *Front. Neural Circuits* 9:44. doi: 10.3389/fncir.2015.00044

Ray, S., and Bhalla, U. S. (2008). PyMOOSE: interoperable scripting in python for moose. *Front. Neuroinformatics* 2:6. doi: 10.3389/neuro.11.006.2008

Reimann, M. W., Anastassiou, C. A., Perin, R., Hill, S. L., Markram, H., and Koch, C. (2013). A biophysically detailed model of neocortical local field potentials predicts the critical role of active membrane currents. *Neuron* 79, 375–390. doi: 10.1016/j.neuron.2013.05.023

Reimann, M. W., King, J. G., Muller, E. B., Ramaswamy, S., and Markram, H. (2015). An algorithm to predict the connectome of neural microcircuits. *Front. Comput. Neurosci.* 9:28. doi: 10.3389/fncom.2015.00120

Reyes-Puerta, V., Yang, J.-W., Siwek, M. E., Kilb, W., Sun, J.-J., and Luhmann, H. J. (2016). Propagation of spontaneous slow-wave activity across columns and layers of the adult rat barrel cortex *in vivo*. *Brain Struct. Funct.* 221, 4429–4449. doi: 10.1007/s00429-015-1173-x

Robinson, D. A. (1968). The electrical properties of metal microelectrodes. *Proc. IEEE* 56, 1065–1071. doi: 10.1109/PROC.1968.6458

Rössert, C., Pozzorini, C., Chindemi, G., Davison, A. P., Eroe, C., King, J., et al. (2016). Automated point-neuron simplification of data-driven microcircuit models. arXiv:1604.00087 [q-bio.NC].

Schomburg, E. W., Anastassiou, C. A., Buzsáki, G., and Koch, C. (2012). The spiking component of oscillatory extracellular potentials in the rat hippocampus. *J. Neurosci.* 32, 11798–11811. doi: 10.1523/JNEUROSCI.0656-12.2012

Sinha, M., and Narayanan, R. (2015). HCN channels enhance spike phase coherence and regulate the phase of spikes and LFPs in the theta-frequency range. *Proc. Natl. Acad. Sci. U.S.A.* 112, E2207–E2216. doi: 10.1073/pnas.1419017112

Smith, K. W. (2015). *Cython: A Guide for Python Programmers*. Sebastopol, CA: O'Reilly Media, Inc.

Srinivasan, R., Nunez, P. L., and Silberstein, R. B. (1998). Spatial filtering and neocortical dynamics: estimates of EEG coherence. *IEEE Trans. Biomed. Eng.* 45, 814–826. doi: 10.1109/10.686789

Tadel, F., Baillet, S., Mosher, J. C., Pantazis, D., and Leahy, R. M. (2011). Brainstorm: a user-friendly application for MEG/EEG analysis. *Comput. Intell. Neurosci.* 2011:879716. doi: 10.1155/2011/879716

Taxidis, J., Anastassiou, C. A., Diba, K., and Koch, C. (2015). Local field potentials encode place cell ensemble activation during hippocampal sharp wave ripples. *Neuron* 87, 590–604. doi: 10.1016/j.neuron.2015.07.014

Thorbergsson, P. T., Garwicz, M., Schouenborg, J., and Johansson, A. J. (2012). Computationally efficient simulation of extracellular recordings with multielectrode arrays. *J. Neurosci. Methods* 211, 133–144. doi: 10.1016/j.jneumeth.2012.08.011

Tian, P., Devor, A., Sakadzić, S., Dale, A. M., and Boas, D. A. (2011). Monte carlo simulation of the spatial resolution and depth sensitivity of two-dimensional optical imaging of the brain. *J. Biomed. Opt.* 16:016006. doi: 10.1117/1.3533263

Tomsett, R. J., Ainsworth, M., Thiele, A., Sanayei, M., Chen, X., Gieselmann, M. A., et al. (2015). Virtual electrode recording tool for extracellular potentials (VERTEX): comparing multi-electrode recordings from simulated and biological mammalian cortical tissue. *Brain Struct. Funct.* 220, 2333–2353. doi: 10.1007/s00429-014-0793-x

Tveito, A., Jæger, K. H., Lines, G. T., Paszkowski, Ł., Sundnes, J., Edwards, A. G., et al. (2017). An evaluation of the accuracy of classical models for computing the membrane potential and extracellular potential for neurons. *Front. Comput. Neurosci.* 11:27. doi: 10.3389/fncom.2017.00027

Uhlirova, H., Kılıç, K., Tian, P., Thunemann, M., Desjardins, M., Saisan, P. A., et al. (2016). Cell type specificity of neurovascular coupling in cerebral cortex. *eLife* 5:e14315. doi: 10.7554/eLife.14315

Vorwerk, J., Cho, J.-H., Rampp, S., Hamer, H., Knösche, T. R., and Wolters, C. H. (2014). A guideline for head volume conductor modeling in EEG and MEG. *NeuroImage* 100, 590–607. doi: 10.1016/j.neuroimage.2014.06.040

Conflict of Interest Statement: The authors declare that the research was conducted in the absence of any commercial or financial relationships that could be construed as a potential conflict of interest.

APPENDIX

A1. Algorithms

Algorithm 1 Axial current calculations in LFPy 2.0

`children` = dict. of child indices n of each parent section `sec`
`connections` = dict. of relative location $\chi \in [0, 1]$ where children connect onto parent section
$\mathbf{R}^{\mathrm{i}}$ = list of axial resistances of child segments to corresponding parent nodes
$\mathbf{V}^{\mathrm{m}}$ = list of membrane potentials at midpoints of each segment
Initialize length $2(n^{\mathrm{seg}} - 1)$ lists $\mathbf{I}^{\mathrm{a}}$, $\mathbf{d}$ and $\mathbf{r}$ indexed by $m \in \{0, 1, \ldots, 2(n^{\mathrm{seg}} - 1) - 1\}$
set current and segment indices $m = n = 0$
set `root_sec = True`
for `sec` in neuron morphology **do**
  if `sec` has parent section **then**
    set parent segment index f from `children` and `connections`
    set `init_seg = True` and `root_sec = False`
  if `count(children[sec])>1` **then**
    set `branch = True`
  set χ =`connections[sec]`
  for `seg` in `sec` **do**
    if `root_sec` **then**
      set $n = 1$ and $f = 0$
      set `init_seg = False` and `root_sec = False`
      continue
    set $R^{\mathrm{i}}_{fn} = \mathbf{R}^{\mathrm{i}}[n]$
    set $V^{\mathrm{m}}_{f} = \mathbf{V}^{\mathrm{m}}[f]$
    set $V^{\mathrm{m}}_{n} = \mathbf{V}^{\mathrm{m}}[n]$
    if not `init_seg` **or** $0 < \chi < 1$ **then**
      compute $\mathbf{I}^{\mathrm{a}}[m] = (V^{\mathrm{m}}_{f} - V^{\mathrm{m}}_{n})/R^{\mathrm{i}}_{fn}$ (see **Figure 3B,C,E**)
    else
      set $R^{\mathrm{i}}_{n} = \mathbf{R}^{\mathrm{i}}[n]$ (axial resistance from mid to start point of segment n)
      set R^{i}_{f} (axial resistance from end to mid point of parent segment f)
      if not `branch` **then**
        compute $\mathbf{I}^{\mathrm{a}}[m] = (V^{\mathrm{m}}_{f} - V^{\mathrm{m}}_{n})/(R^{\mathrm{i}}_{f} + R^{\mathrm{i}}_{n})$ (see **Figure 3D**)
      else
        compute branch point potential

$$V^{\mathrm{m}}_{\times} = \frac{\sum_h V^{\mathrm{m}}_h / R^{\mathrm{i}}_h}{\sum_h 1/R^{\mathrm{i}}_h} \text{ for } h \in \{f, n_1, n_2, \ldots n_{\mathrm{children}}\}$$

        compute $\mathbf{I}^{\mathrm{a}}[m] = (V^{\mathrm{m}}_{\times} - V^{\mathrm{m}}_{n})/R^{\mathrm{i}}_{n}$ (see **Figure 3F**)
    set $\mathbf{I}^{\mathrm{a}}[m+1] = \mathbf{I}^{\mathrm{a}}[m]$
    compute $\mathbf{d}[m]$ by subtracting the midpoint of f from the start point of n
    compute $\mathbf{d}[m+1]$ by subtracting the start point of n from the midpoint of n
    compute $\mathbf{r}[m]$ by subtracting $0.5 \cdot \mathbf{d}[m]$ from the start point of n
    compute $\mathbf{r}[m+1]$ by subtracting $0.5 \cdot \mathbf{d}[m+1]$ from the midpoint of n
    set $f = n$, $n = n + 1$ and $m = m + 2$
    set `branch = False` and `init_seg = False`

A2. New Classes and Network Use-Case Implementation

The first release of LFPy described in Lindén et al. (2014) included a set of Python class definitions for instantiating single-cell models (`Cell`, `TemplateCell`) and corresponding instrumentation of the models with synapse point processes attached to the cell (`Synapse`), patch-clamp electrodes (`StimIntElectrode`) and extracellular recording electrodes (`RecExtElectrode`). Simulations with multiple simultaneous cell-object instances were at the time not supported. Class `TemplateCell` supported the use of template specifications, a requirement for networks in NEURON, but was primarily written to support source codes of 'network-ready' single-cell models such as the Hay et al. (2011) models of layer-5 pyramidal neurons available from, for example, ModelDB (senselab.med.yale.edu/modeldb, McDougal et al. (2017)).

The "one cell at a time" approach may seem limited, in particular when considering ongoing network interactions, but knowing that forward-modeling of extracellular potentials can be decoupled from the network simulation, users could always set up simulations of each individual cell, play back synapse activation times as occurring in the connected network, and sum up the single-cell contributions to the extracellular potential. Thus, the calculation of extracellular potentials can even be dealt with in an "embarrassingly" parallel manner (Foster, 2007; Hagen et al., 2016). These simplifying steps are not possible if the extracellular potential itself affects the cellular dynamics, that is, if mutual interactions between cellular compartments belonging to the same or different cells occur through the extracellular potential, so-called ephaptic interactions (Anastassiou et al., 2011; Goldwyn and Rinzel, 2016; Tveito et al., 2017).

For the present LFPy 2.0 release, we added support for simulations of recurrently connected multicompartment models with concurrent calculations of extracellular potentials and current dipole moments. As described above, the current dipole moment is used for predictions of distal electric potentials (for example scalp surface potentials as in EEG measurements) and magnetic fields (as in MEG measurements). For our example use case, we considered a recurrent network of four populations of multicompartment neuron models. We added a new set of generic class definitions in LFPy to represent the network, its populations and neurons, as well as classes representing different volume-conductor models and measurement modalities as summarized next.

Cells: Each individual neuron in an LFPy network exists as an instantiation of class `NetworkCell`. As this class definition uses class inheritance from the old `TemplateCell` and in turn `Cell` classes, it retains all common methods and attributes from its parent classes. The `NetworkCell` can therefore be instantiated in a similar manner as its parent class (plotted output not shown):

```
#!/usr/bin/env python
"""example_network_cell.py"""
# import modules:
from matplotlib.pyplot import subplot, plot
from LFPy import NetworkCell, StimIntElectrode
# class NetworkCell parameters:
cellParameters = dict(
    morphology='BallAndStick.hoc',
    templatefile='BallAndStickTemplate.hoc',
    templatename='BallAndStickTemplate',
    templateargs=None,
    v_init=-65.
)
# create cell:
cell = NetworkCell(
    tstart=0., tstop=100.,
    **cellParameters
)
# create stimulus device:
iclamp = StimIntElectrode(
    cell=cell,
    idx=0,
    pptype='IClamp',
    amp=0.5,
    dur=80.,
    delay=10.,
    record_current=True
)
# run simulation:
cell.simulate()
# plot cell response:
subplot(2, 1, 1)
plot(cell.tvec, iclamp.i)
subplot(2, 1, 2)
plot(cell.tvec, cell.somav)
```

The morphology and template files referred to above are defined in NEURON "hoc" language files. A "ball and stick" style morphology file with active soma (Hodgkin & Huxley Na^+, K^+ and leak channels) and passive dendrite sections and corresponding template file was written as:

```
/* -------------------------------
BallAndStick.hoc
------------------------------- */
// Create sections:
create soma[1]
create apic[1]
```

```
// Add 3D information:
soma[0] {
    pt3dadd(0, 0, -15, 30)
    pt3dadd(0, 0, 15, 30)
}
apic[0] {
    pt3dadd(0, 0, 15, 3)
    pt3dadd(0, 0, 1015, 3)
}

// Connect section end points:
connect apic[0](0), soma[0](1)

// Set biophysical parameters:
forall {
    Ra = 100.
    cm = 1.
    all.append()
}
soma { insert hh }
apic {
    insert pas
    g_pas = 0.0002
    e_pas = -65.
}
/* ---------------------------- */
```

and

```
/* -------------------------------
BallAndStickTemplate.hoc
------------------------------- */
begintemplate BallAndStickTemplate
public init, soma, apic
public all
objref all
proc init() {
    all = new SectionList()
}
create soma[1], apic[1]
endtemplate BallAndStickTemplate
/* ---------------------------- */
```

In contrast to class `TemplateCell`, class `NetworkCell` has built-in methods to detect somatic action potentials and set-ups of synapses being activated by such threshold crossings in other cells.

Network populations: One step up in the hierarchy, class `NetworkPopulation` represents a size N_X population of `NetworkCell` instantiations of one particular cell type (X) in the network. The class can be used directly as (print output not shown):

```
#!/usr/bin/env python
"""example_network_population.py"""
# import modules
from mpi4py.MPI import COMM_WORLD as COMM
from LFPy import NetworkPopulation, NetworkCell
# class NetworkCell parameters:
cellParameters = dict(
    morphology='BallAndStick.hoc',
    templatefile='BallAndStickTemplate.hoc',
    templatename='BallAndStickTemplate',
    templateargs=None,
    delete_sections=False,
)
# class NetworkPopulation parameters:
populationParameters = dict(
    Cell=NetworkCell,
    cell_args=cellParameters,
```

```
    pop_args=dict(
        radius=100.,
        loc=0.,
        scale=20.),
    rotation_args=dict(x=0., y=0.),
)
# create population:
population = NetworkPopulation(
    first_gid=0, name='E',
    **populationParameters
)
# print out some info:
for cell in population.cells:
    print('RANK {}; pop {}; gid {}; cell {}'.format(
        COMM.Get_rank(), population.name,
        cell.gid, cell))
```

Direct instantiation of class `NetworkPopulation`, however, is of limited use as it does not provide any means of simulation control by itself, and has only one built-in method to draw and set random cell-body positions within a chosen radius (`pop_args['radius']`) and depth from the normal distribution $\mathcal{N}(\overline{u}, \sigma_{\overline{u}})$. In the code example above, `pop_args['loc']` refers to expected mean depth $\overline{u}$ and `pop_args['scale']` to the corresponding standard deviation $\sigma_{\overline{u}}$. A random cell rotation around its own vertical z-axis is applied by default. The integer `cell.gid` value accessed above is a unique global identifier g_{id} of each cell in the network, and is assigned in running order from the number `first_gid`. For parallel execution using MPI, cells will be distributed among threads according to the round-robin rule if the condition $g_{\mathrm{id}} \% N_{\mathrm{MPI}} == k$ is True, where % denotes a division modulus operation, N_{MPI} the MPI pool size and $k \in [0, 1, ..., N_{\mathrm{MPI}} - 1]$ the corresponding rank number.

Networks: The new network functionality is provided through class `Network`. An instantiation of the class sets attributes for the default destination of file output, temporal duration t and resolution dt of the simulation, a chosen initial voltage $V_{\mathrm{init}}^{\mathrm{m}}$ and global temperature control T_{celsius} (which affects channel dynamics). Furthermore, the class instance provides built-in methods to create any number of N_X-sized populations X. Different built-in class methods create random connectivity matrices $\mathbf{C}_{XY}^{(r)}$ (per rank, see *Connectivity Model* in section Section 2.5) between any presynaptic population X and postsynaptic population Y, and connect X and Y using an integer number of synapses per connection n^{syn} drawn from the capped normal distribution $\mathcal{N}(\overline{n}^{\mathrm{syn}}, \sigma_{\overline{n}}^{\mathrm{syn}})H(n)$ where $H(\cdot)$ denotes the Heaviside step function. Similarly, synaptic conductances g^{syn} are drawn from the distribution $\mathcal{N}(\overline{g}^{\mathrm{syn}}, \sigma_{\overline{g}}^{\mathrm{syn}})H(g - g_{\mathrm{min}})$ (where g_{min} denotes minimum synaptic conductance) with connection delays δ^{syn} from $\mathcal{N}(\overline{\delta}^{\mathrm{syn}}, \sigma_{\overline{\delta}}^{\mathrm{syn}})H(\delta - \delta_{\mathrm{min}})$ (where δ_{min} denotes the minimum delay in the network). The network class handles the synapse model in NEURON and corresponding parameters (time constants, reversal potentials, putative synapse locations etc.), and finally provides a simulation control procedure. The simulation control allows for concurrent calculation of network activity and prediction of extracellular potentials as well as the current dipole moment.

In order to set up a complete network simulation we may choose to define `NetworkCell` and `NetworkPopulation` parameters as above, and define parameter dictionaries for our instances of `Network` and extracellular measurement device `RecExtElectrode`:

```
#!/usr/bin/env python
"""example_network.py"""
# import modules
import numpy as np
import scipy.stats as st
from mpi4py import MPI
from LFPy import NetworkCell, Network
import neuron
# relative path for simulation output:
OUTPUTPATH = 'example_network_output'
# class NetworkCell parameters:
cellParameters = dict(**cellParameters)
# class NetworkPopulation parameters:
populationParameters = dict(**populationParameters)
# class Network parameters:
networkParameters = dict(
    dt=2**-4,
    tstop=1200.,
    v_init=-65.,
    celsius=6.5,
    OUTPUTPATH=OUTPUTPATH
```

```
)
# class RecExtElectrode parameters:
electrodeParameters = dict(
    x=np.zeros(13),
    y=np.zeros(13),
    z=np.linspace(1000., -200., 13),
    N=np.array([[0., 1., 0.] for _ in range(13)]),
    r=5.,
    n=50,
    sigma=0.3,
    method="soma_as_point"
)
# method Network.simulate() parameters:
networkSimulationArguments = dict(
    rec_current_dipole_moment=True,
    rec_pop_contributions=True,
)
```

Furthermore, we define population names (X) and corresponding sizes (N_X), as well as one overall connection probability (C_{YX}):

```
# population names, sizez and connection probability:
population_names = ['E', 'I']
population_sizes = [80, 20]
connectionProbability = [[0.05, 0.05], [0.05, 0.05]]
```

Then, we may chose to define the synapse model and corresponding parameters (here using NEURON's built-in two-exponential model `Exp2Syn`) for synapse conductances (weight), delays and synapses per connection (multapses), as well as layer-specificities of connections ($\mathcal{L}_{YXL}$, see Hagen et al., 2016 and below):

```
# synapse model. All corresponding parameters for weights,
# connection delays, multapses and layerwise positions are
# set up as shape (2, 2) nested lists for each possible
# connection on the form:
# [["E:E", "E:I"],
#  ["I:E", "I:I"]].
synapseModel = neuron.h.Exp2Syn
# synapse parameters
synapseParameters = [[dict(tau1=0.2, tau2=1.8, e=0.),
                      dict(tau1=0.2, tau2=1.8, e=0.)],
                     [dict(tau1=0.1, tau2=9.0, e=-80.),
                      dict(tau1=0.1, tau2=9.0, e=-80.)]]
# synapse max. conductance (function, mean, st.dev., min.):
weightFunction = np.random.normal
weightArguments = [[dict(loc=0.002, scale=0.0002),
                    dict(loc=0.002, scale=0.0002)],
                   [dict(loc=0.01, scale=0.001),
                    dict(loc=0.01, scale=0.001)]]
minweight = 0.
# conduction delay (function, mean, st.dev., min.):
delayFunction = np.random.normal
delayArguments = [[dict(loc=1.5, scale=0.3),
                   dict(loc=1.5, scale=0.3)],
                  [dict(loc=1.5, scale=0.3),
                   dict(loc=1.5, scale=0.3)]]
mindelay = 0.3
multapseFunction = np.random.normal
multapseArguments = [[dict(loc=2., scale=.5), dict(loc=2., scale=.5)],
                     [dict(loc=5., scale=1.), dict(loc=5., scale=1.)]]
# method NetworkCell.get_rand_idx_area_and_distribution_norm
# parameters for layerwise synapse positions:
synapsePositionArguments = [[dict(section=['soma', 'apic'],
                                  fun=[st.norm, st.norm],
                                  funargs=[dict(loc=500., scale=100.),
                                           dict(loc=500., scale=100.)],
                                  funweights=[0.5, 1.]
                                 ) for _ in range(2)],
                            [dict(section=['soma', 'apic'],
```

```
                                    fun=[st.norm, st.norm],
                                    funargs=[dict(loc=0., scale=100.),
                                             dict(loc=0., scale=100.)],
                                    funweights=[1., 0.5]
                                   ) for _ in range(2)]]
```

Note that we above relied on Python list-comprehension tricks for compactness. Having defined all parameters, one can then create the network, populations, stimulus, connections, recording devices, run the simulation and collect simulation output:

```
if __name__ == '__main__':
    ######################################################################
    # Main simulation
    ######################################################################
    # create directory for output:
    if not os.path.isdir(OUTPUTPATH):
        if RANK == 0:
            os.mkdir(OUTPUTPATH)
    COMM.Barrier()

    # instantiate Network:
    network = Network(**networkParameters)

    # create E and I populations:
    for name, size in zip(population_names, population_sizes):
        network.create_population(name=name, POP_SIZE=size,
                                  **populationParameters)


        # create excitatpry background synaptic activity for each cell
        # with Poisson statistics
        for cell in network.populations[name].cells:
            idx = cell.get_rand_idx_area_norm(section='allsec', nidx=64)
            for i in idx:
                syn = Synapse(cell=cell, idx=i, syntype='Exp2Syn',
                              weight=0.002,
                              **dict(tau1=0.2, tau2=1.8, e=0.))
                syn.set_spike_times_w_netstim(interval=200.)


    # create connectivity matrices and connect populations:
    for i, pre in enumerate(population_names):
        for j, post in enumerate(population_names):
            # boolean connectivity matrix between pre- and
            # post-synaptic neurons in each population
            # (postsynaptic on this RANK)
            connectivity = network.get_connectivity_rand(
                pre=pre, post=post,
                connprob=connectionProbability[i][j]
                )

            # connect network:
            (conncount, syncount) = network.connect(
                pre=pre, post=post,
                connectivity=connectivity,
                syntype=synapseModel,
                synparams=synapseParameters[i][j],
                weightfun=np.random.normal,
                weightargs=weightArguments[i][j],
                minweight=minweight,
                delayfun=delayFunction,
                delayargs=delayArguments[i][j],
                mindelay=mindelay,
                multapsefun=multapseFunction,
                multapseargs=multapseArguments[i][j],
                syn_pos_args=synapsePositionArguments[i][j],
                )
```

```
# set up extracellular recording device:
electrode = RecExtElectrode(**electrodeParameters)

# run simulation:
SPIKES, OUTPUT, DIPOLEMOMENT = network.simulate(
    electrode=electrode,
    **networkSimulationArguments
)
```

The argument `SPIKES` returned by the final `network.simulate` method call is a dictionary with keys `gids` and `times`, where the corresponding values are lists of global neuron ID's (g_{ID}) and numpy arrays with spike times of each respective unit in the network. The returned `OUTPUT` and `DIPOLEMOMENT` arguments are numpy arrays with structured datatypes (sometimes referred to as record arrays). The array `OUTPUT['imem']` is the total extracellular potential from all transmembrane currents in units of mV, the entries `'E'` and `'I'` contributions from the excitatory and inhibitory neuron populations, respectively. `DIPOLEMOMENT` similarly contains the current dipole moment from populations `'E'` and `'I'`, but not the sum as the current dipole moment of different populations may, in principle, be freely positioned in different locations within a volume conductor. The computed current dipole moments by themselves have no well defined positions in space and must explicitly be assigned a position by the user, unlike the individual compartment positions used when computing the extracellular potential.

The corresponding LFPy 2.0 example files discussed throughout this section are:

- `/examples/example_network/example_network_cell.py`,
- `/examples/example_network/example_network_population.py`
- `/examples/example_network/example_network.py`.

Paper III

Biophysically detailed forward modeling of the neural origin of EEG and MEG signals

III

NeuroImage 225 (2021) 117467

Contents lists available at ScienceDirect

NeuroImage

journal homepage: www.elsevier.com/locate/neuroimage

Biophysically detailed forward modeling of the neural origin of EEG and MEG signals

Solveig Næss[a], Geir Halnes[b], Espen Hagen[c], Donald J. Hagler Jr.[d], Anders M. Dale[d,e], Gaute T. Einevoll[b,c,*], Torbjørn V. Ness[b,*]

[a] Department of Informatics, University of Oslo, Oslo 0316, Norway
[b] Faculty of Science and Technology, Norwegian University of Life Sciences, 1432 Ås, Norway
[c] Department of Physics, University of Oslo, Oslo 0316, Norway
[d] Department of Radiology, University of California, La Jolla, CA 92093, USA
[e] Department of Neurosciences, University of California, La Jolla, CA 92093, USA

A B S T R A C T

Electroencephalography (EEG) and magnetoencephalography (MEG) are among the most important techniques for non-invasively studying cognition and disease in the human brain. These signals are known to originate from cortical neural activity, typically described in terms of current dipoles. While the link between cortical current dipoles and EEG/MEG signals is relatively well understood, surprisingly little is known about the link between different kinds of neural activity and the current dipoles themselves. Detailed biophysical modeling has played an important role in exploring the neural origin of intracranial electric signals, like extracellular spikes and local field potentials. However, this approach has not yet been taken full advantage of in the context of exploring the neural origin of the cortical current dipoles that are causing EEG/MEG signals.

Here, we present a method for reducing arbitrary simulated neural activity to single current dipoles. We find that the method is applicable for calculating extracranial signals, but less suited for calculating intracranial electrocorticography (ECoG) signals. We demonstrate that this approach can serve as a powerful tool for investigating the neural origin of EEG/MEG signals. This is done through example studies of the single-neuron EEG contribution, the putative EEG contribution from calcium spikes, and from calculating EEG signals from large-scale neural network simulations. We also demonstrate how the simulated current dipoles can be used directly in combination with detailed head models, allowing for simulated EEG signals with an unprecedented level of biophysical details.

In conclusion, this paper presents a framework for biophysically detailed modeling of EEG and MEG signals, which can be used to better our understanding of non-inasively measured neural activity in humans.

1. Introduction

Electroencephalography (EEG) is one of the most important non-invasive methods for studying human cognitive function and diagnosing brain diseases (Cohen, 2017; Pesaran et al., 2018). Yet, we know surprisingly little about the neural origin of these electric scalp potentials (Cohen, 2017): On the one hand, we have a relatively good understanding of the biophysics of EEGs, in knowing that these signals originate from cortical current dipoles, and having a well-defined framework for linking such cortical dipoles to electric scalp potentials (Ness et al., 2020; Nunez and Srinivasan, 2006). This has been taken advantage of for a long time in source localization, by inverse modeling of the underlying cortical current dipoles from EEG data. On the other hand, even though these cortical dipoles are assumed to mainly originate from large numbers of synaptic input to cortical pyramidal cell populations (Ilmoniemi and Sarvas, 2019; Lopes da Silva, 2013; Ness et al., 2020; Nunez and Srinivasan, 2006; Pesaran et al., 2018), the precise link between cortical dipoles and the underlying neural activity has remained unclear. In other words, we know very little about exactly which types of neural activity that cause even the most well-studied characteristics of the EEG signal, such as different types of oscillations (e.g., alpha, beta, and gamma waves) and stereotyped EEG shapes in response to sensory stimuli (event-related potentials, ERPs) (Cohen, 2017). Importantly, these different EEG characteristics are affected in predictable ways by various brain conditions, such as sleep and attention (Klimesch et al., 1998; Palva and Palva, 2011; Siegel et al., 2012), and by brain disorders including epilepsy and schizophrenia (Freestone et al., 2015; Light and Näätänen, 2013; Mäki-Marttunen et al., 2019a; Niedermeyer, 2003). This means that a better insight into how different types of brain activity is reflected in cortical current dipoles could help us not only in making better inverse models for source localization, but also in providing a better understanding of the mechanisms of human cortical activity and possibly curing brain diseases (Cohen, 2017; Mäki-Marttunen et al., 2019a; Uhlirova et al., 2016).

The reasons why we lack understanding of the neural origin of EEG signals are many, the main being (i) strong ethical constraints on invasive human brain measurements and (ii) the high number of neurons

* Corresponding author.
E-mail addresses: gaute.einevoll@nmbu.no (G.T. Einevoll), torbjorn.ness@nmbu.no (T.V. Ness).

https://doi.org/10.1016/j.neuroimage.2020.117467
Received 27 June 2020; Received in revised form 28 September 2020; Accepted 12 October 2020
Available online 17 October 2020

that contribute to the signal. However, in recent years there have been major advances in several relevant branches of neuroscience, meaning that a better understanding of the EEG signal may now be within reach (Cohen, 2017; Uhlirova et al., 2016).

To bypass challenge (i), we look to the rapid development in the technology and methods used to study neural activity in lab animals. The possibility to control and manipulate neural activity, while simultaneously recording both intracranial signals like the local field potential (LFP) (Blomquist et al., 2009; Einevoll et al., 2007) and extracranial non-invasive signals like the EEG (Bruyns-Haylett et al., 2017), can be expected to make important contributions to our understanding of non-invasive measurements of human brain activity (Cohen, 2017; Lopes da Silva, 2013; Pesaran et al., 2018; Uhlirova et al., 2016). Furthermore, detailed biophysical modeling of neural activity has become an important tool for understanding intracranial LFP measurements (Einevoll et al., 2013a; Pesaran et al., 2018). Given that EEG is expected to reflect the same basic process as LFP, that is, large numbers of synaptic input to geometrically aligned pyramidal cells (Buzsáki et al., 2012; Nunez and Srinivasan, 2006; Pesaran et al., 2018), it seems likely that detailed biophysical modeling can also help shed light on the neural origin of EEG signals.

As indicated in challenge (ii), EEG signals are expected to reflect the activity of much larger neural populations than the LFPs, making the simulations computationally demanding. Biophysically detailed large-scale simulations of neural networks have, however, been gaining substantial momentum in recent years, thanks to large ongoing neuroscience initiatives like Project MindScope at the Allen Institute for Brain Science, the Blue Brain Project and the EU Human Brain Project (Einevoll et al., 2019). The possibility to calculate EEG signals from such existing and future large-scale biophysically detailed neural simulations could lead to valuable insights into the neural origin of the EEG.

Another complicating aspect of EEG modeling, is that these predictions in general require a head model to account for the widely different electrical conductivities of the brain, cerebrospinal fluid (CSF), skull and scalp (Ilmoniemi and Sarvas, 2019; Nunez and Srinivasan, 2006). While many such head models exist, they tend to take current dipoles as input (Nunez and Srinivasan, 2006; Pesaran et al., 2018), instead of the transmembrane currents that are available from biophysical neural simulations and that form the basis for modeling LFPs (Einevoll et al., 2013b).

Here, we introduce an approach for reducing arbitrary biophysically detailed simulated neural activity to current dipoles, which represents an enormous reduction in term of model complexity when computing brain signals. We verify that the approach gives accurate results when calculating EEG signals, but less so for intracranial electrocorticography (ECoG) signals. Next, we look into how the approach can be applied for investigating the origin of EEG signals, with a particular focus on calcium spikes, before demonstrating how our methods can be applied for pre-existing large-scale network models. Finally, we show how current dipoles can be combined with detailed head models, which enables simulation of EEG signals with unprecedented biophysical detail.

Note that the clear separation between calculation of current dipoles and the corresponding EEG is equally valid for magnetoencephalography (MEG) signals. While we here focus mostly on EEG, the presented approach for calculating current dipoles from neural activity is equally valid for MEG signals, through use of an appropriate forward model (Hagen et al., 2018; Ilmoniemi and Sarvas, 2019).

2. Methods

Neural activity generates electric currents in the brain, which in turn create electromagnetic fields. In this section, we explain how electric brain signals can be modeled in both simple and more complex volume conductors.

2.1. Forward modeling of electric potentials

We assume negligible capacitive effects in the head (Miceli et al., 2017; Pfurtscheller and Cooper, 1975; Ranta et al., 2017) and that electric and magnetic signals effectively decouple. We can then apply the quasistatic approximation of Maxwell's equations for calculating these signals (Hämäläinen et al., 1993; Nunez and Srinivasan, 2006). In other words, for computing extracellular electric potentials, we envision the head as a 3D volume conductor, and combining Maxwell's equations with the current conservation law, we obtain the Poisson equation for computing extracellular potentials (Griffiths, 1999):

$$\nabla \cdot \mathbf{J} = \nabla \cdot (\sigma \nabla \phi), \tag{1}$$

where $\mathbf{J}$ is the electric current density in extracellular space, σ is the extracellular conductivity and ϕ is the extracellular electric potential. The Poisson equation can be solved analytically for simple, symmetric head models, such as an infinitely big space and spherically symmetric models. For more complex head models, numerical methods such as the Finite Element Method (FEM) can be used (Haufe et al., 2015; Logg et al., 2012; Seo et al., 2016; Vorwerk et al., 2014; 2019).

2.1.1. Compartment-based approach

Extracellular potentials generated by transmembrane currents can be calculated with a well-founded biophysical two-step forward-modeling scheme. The first step involves *multicompartmental modeling* and incorporates the details of reconstructed neuron morphologies for calculating transmembrane currents (Sterratt et al., 2011). In the second step, Eq. (1) is solved under the assumption that the extracellular medium is an infinitely large, linear, ohmic, isotropic, homogeneous and frequency-independent volume conductor. The transmembrane currents entering and escaping the extracellular medium can be seen as current sources and sinks, and give the extracellular potential ϕ at the electrode location $\mathbf{r}$ (Ness et al., 2020),

$$\phi(\mathbf{r}) = \frac{1}{4\pi\sigma} \sum_{n=1}^{N} \frac{I_n}{|\mathbf{r} - \mathbf{r}_n|}, \tag{2}$$

where $\mathbf{r}_n$ is the location of transmembrane current I_n, N is the number of transmembrane currents and σ is the extracellular conductivity. This scheme is here referred to as the compartment-based approach, and was applied using the Python package LFPy 2.0 running NEURON under the hood (Carnevale and Hines, 2006; Hagen et al., 2018).

2.1.2. Current dipole approximation

Analogous to how electric charges can create charge multipoles, a combination of current sinks and sources can set up *current* multipoles (Nunez and Srinivasan, 2006). From electrodynamics, we know that extracellular potentials from a volume of current sinks and sources can be precisely described by expressing Eq. (2) as a multipole expansion (Nunez and Srinivasan, 2006):

$$\phi(R) = \frac{C_{\text{monopole}}}{R} + \frac{C_{\text{dipole}}}{R^2} + \frac{C_{\text{quadrupole}}}{R^3} + \ldots, \tag{3}$$

when the distance R from the center of the volume to the measurement point is larger than the distance from the volume center to the most peripheral source (Jackson, 1998). In neural tissue, the current monopole contribution is zero due to current conservation, since the transmembrane currents sum to zero at all times (Koch, 1999; Pettersen et al., 2012). Further, the quadrupole, octopole and higher order terms are negligible compared to the current dipole contribution when R is sufficiently large. In this case, the extracellular potential from a neuron model can be estimated with the second term of the current multipole expansion; an approximation known as the *current dipole approximation* (Nunez and Srinivasan, 2006; Pettersen et al., 2014; Pettersen and Einevoll, 2008):

$$\phi(\mathbf{r}) = \frac{C_{\text{dipole}}}{R^2} = \frac{1}{4\pi\sigma} \frac{|\mathbf{p}| \cos\theta}{|\mathbf{r} - \mathbf{r}_{\text{p}}|^2}. \tag{4}$$

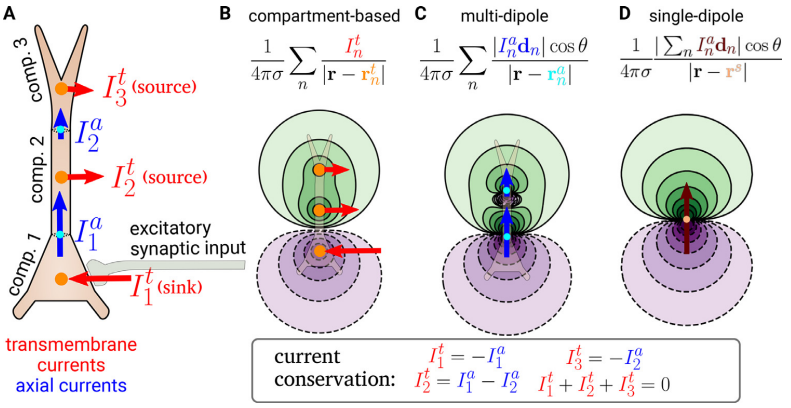

Fig. 1. Illustration of relation between transmembrane currents, axial currents, sources and sinks. A: Schematic illustration of a cell model. This toy model only has three cellular compartments, but note that biophysically detailed neuron models typically have ~ 600–1300 compartments. An excitatory synaptic input initiates a current flow across the membrane and into the neuron. This current consists of an ionic flow of positive ions (e.g., Na^+), in addition to capacitive currents, and is by convention a negative transmembrane current (I^t), also referred to as a current sink. This changes the membrane potential at the location of the synaptic input, initiating axial currents (I^a), that is, currents inside the neuron. The very strong electromagnetic attraction of opposite and repulsion of equal electric charges effectively prevents any charge accumulation, ensuring current conservation. This implies that the same amount of current that goes into a cellular compartment, must also leave the same cellular compartment, enforcing a simple relationship between transmembrane currents and axial currents. Current conservation also ensures that the sum of all transmembrane currents at any given time must sum to zero, which implies that a negative transmembrane current caused by an excitatory synaptic input (current sink), must be exactly balanced by positive transmembrane currents elsewhere on the cell (current sources). **B, C, D**: The extracellular potential around the cell can be calculated either from the transmembrane currents (**B**, Eq. (2)), from the current dipole moments stemming from all the individual axial currents (**C**, Eq. (4)), or from the single summed current dipole moment (**D**, Eqs. (6) and (4)). Note that the single-dipole approximation is only expected to be valid far away from the neuron, see main text for discussion of the validity of this.

Table 1
Radii and electrical conductivities used in the four-sphere model. The radius of each spherical shell in the four-sphere model, with σ denoting the respective electrical conductivities.

	Radius (cm)	σ (S/m)
Brain	8.9	0.276
CSF	9.0	1.65
Skull	9.5	0.01
Scalp	10.0	0.465

Here, $\mathbf{p}$ is the current dipole moment in a medium with conductivity σ, $R = |\mathbf{R}| = |\mathbf{r} - \mathbf{r}_p|$ is the distance between the current dipole moment at $\mathbf{r}_p$ and the electrode location $\mathbf{r}$, and θ denotes the angle between $\mathbf{p}$ and $\mathbf{R}$. The current dipole moment $\mathbf{p}$ can be calculated from an axial current I inside a neuron and the distance vector $\mathbf{d}$ traveled by the axial current: $\mathbf{p} = I\mathbf{d}$, analogous to a charge dipole moment. The current dipole approximation is applicable in the far-field limit, that is when R is much larger than the dipole length $d = |\mathbf{d}|$ (Nunez and Srinivasan, 2006).

Multi-dipole approach From some multicompartmental neuron simulations (Figs. 2–4), we computed multiple current dipole moments, i.e., one for each axial current flowing between neighboring compartments in the neuron:

$$\mathbf{p}_k = I_k^{\text{axial}}\mathbf{d}_k. \tag{5}$$

Here, I_k^{axial} is an axial current traveling along distance vector $\mathbf{d}_k$, resulting in a current dipole moment $\mathbf{p}_k$. By inserting all the current dipole moments from a neuron simulation into the current dipole approximation (Eq. (4)), we get a good estimate of the extracellular potential at any electrode location where the distance between the electrode and the nearest dipole is sufficiently large (Nunez and Srinivasan, 2006). See Fig. 1 for an illustration of the relation between these different approached for calculating extracellular potentials. Note that the length of each (multi-)dipole is equal to half the length of its corresponding neuronal compartment. The calculation of multi-dipoles from simulated neural activity was implemented in LFPy 2.0, and can be used through the function `Cell.get_multi_current_dipole_moments` (Hagen et al., 2018).

Single-dipole approximation From each multicompartmental neuron simulation, we computed one single current dipole moment. This can either be done by summing up the multiple current dipole moments,

$$\mathbf{p}(t) = \sum_{k=1}^{M}\mathbf{p}_k(t) = \sum_{k=1}^{M} I_k^{\text{axial}}(t)\mathbf{d}_k, \tag{6}$$

where M is the number of axial currents, or equivalently from a position-weighted sum of all the transmembrane currents (Hagen et al., 2018; Lindén et al., 2010):

$$\mathbf{p}(t) = \sum_{k=1}^{N} I_k^{\text{trans}}(t)\mathbf{r}_k, \tag{7}$$

where N is the number of compartments in the multicompartmental neuron model and $\mathbf{r}_k$ is the position of transmembrane current $I_k^{\text{trans}}(t)$. For calculating EEG signals a location for the current dipole must be chosen, and unless otherwise specified we positioned the dipole halfway between the position of the soma and the position of the synaptic input (for multiple synaptic inputs, we used the average position of the synaptic inputs). Note, however, that the large distance from the neuron to the EEG electrode (~ 10 mm) implies that the EEG signal is relatively insensitive to small changes in the dipole location within cortex. The calculation of current-dipole moments from simulated neural activity was implemented in LFPy 2.0, and can be used through `Cell.current_dipole_moment` (Hagen et al., 2018).

2.2. Head models

Electric potentials will be affected by the geometries and conductivities of the various parts of the head (Nunez and Srinivasan, 2006), which is especially important for electrode locations outside of the brain. This can be incorporated into our extracellular potential calculations by applying simplified or complex head models.

2.2.1. Four-sphere head model

The four-sphere head model is a simple analytical model consisting of four concentric shells representing brain tissue, cerebrospinal fluid (CSF), skull and scalp, where the conductivity can be set individually for each shell (Nunez and Srinivasan, 2006; Srinivasan et al., 1998). The model solution is given in Næss et al. (2017) and is found by solving the

Poisson equation subject to boundary conditions ensuring continuity of current and electric potentials over the boundaries, as well as no current escaping the outer shell. This model is based on the current dipole approximation. The parameters used in this paper (Table 1) were taken from Huang et al. (2013) to be consistent with the parameters used in the construction of the more complex New York head model (see next section).

2.2.2. New York Head model

The New York Head model is a detailed head model based on high-resolution, anatomical MRI-data from 152 adult heads (Huang and Parra, 2015). The model was constructed by taking advantage of the reciprocity theorem, stating that the position of the electrode and the dipolar source can be switched without affecting the measured potential (Rush and Driscoll, 1969). This means, that virtually injecting current at the locations of the EEG electrodes and using the finite element method (Logg et al., 2012) to compute the resulting potential anywhere in the brain, gives the link between current dipoles in the brain and the resulting EEG signals (Dmochowski et al., 2017; Huang et al., 2016; Malmivuo and Plonsey, 1995; Ziegler et al., 2014). This link was captured in a matrix known as the *lead field* **L** (Nunez and Srinivasan, 2006):

$$\mathbf{L} = \frac{\mathbf{E}}{I} \tag{8}$$

Here, I is the injected current at the electrode locations and $\mathbf{E}$ is the resulting electric field in the brain. The lead field matrix gives us the precise link between a current dipole moment $\mathbf{p}$ in the brain and the resulting EEG signals $\mathbf{\Phi}$ (Nunez and Srinivasan, 2006):

$$\mathbf{\Phi} = \mathbf{L} \cdot \mathbf{p}. \tag{9}$$

We applied the New York Head model by downloading the lead field $\mathbf{L}$ from https://parralab.org/nyhead/. The units incorporated in the lead field matrix was not immediately obvious. However, from Dmochowski et al. (2017) and Huang et al. (2013) it appears that an injected current I of 1 mA gives an electric potential E in V/m, meaning that a current dipole moment $\mathbf{p}$ in the unit of mAm gives EEG signals in the unit of V.

2.3. Simulation of neural activity

All neuron simulations were performed using the python package LFPy 2.0, running NEURON under the hood (Hagen et al., 2018). For investigations of single-cell contributions to extracellular potentials, we applied three different morphologically reconstructed cell models: The human layer-2/3 pyramidal cell from Eyal et al. (2018), the layer-5 pyramidal cell from rat cortex constructed by Hay et al. (2011) and a rat layer-5 chandelier cell; an interneuron model developed by Markram et al. (2015).

The pyramidal cell models were downloaded from http://www.senselab.med.yale.edu/modeldb/, with accession numbers 238347 (2013_03_06_cell03_789_H41_03) and 139653 (cell1) respectively, while we found the interneuron at the Neocortical Microcircuit Collaboration Portal (http://www.bbp.epfl.ch/nmc-portal/microcircuit) under layer-5, Chandelier Cell (ChC), continuous Non-accomodating (cNAC), (rp110201_L_idA_-_Scale_x1.000_y0.975_z1.000_-_Clone_3).

For all simulations with passive ion channels only (Figs. 2–4), we used the following cell parameters: membrane resistance of 30000 Ωcm^2, axial resistance of 150 Ωcm (Mainen and Sejnowski, 1996) and a membrane capacitance of 1 μF/cm^2 (Gentet et al., 2000; Sterratt et al., 2011). When active mechanisms were included in the simulations (Fig. 5), all cell properties were incorporated as described in the specific cell's documentation.

Neural simulations shown in Figs. 2–5 received synaptic input modeled as conductance-based, two-exponential synapses (`Exp2Syn` in NEURON). The rise time constant was set to 1 ms and the decay time constant was 3 ms, synaptic reversal potential was 0 mV and the synaptic weight was set to 0.002 μS, unless otherwise specified.

Table 2
Population names and sizes in large-scale neural network model The number of neurons in each population. E=excitatory, I=inhibitory, and TC=thalamocortical.

Name	Population size
L2/3E	20,683
L2/3I	5834
L4E	21,915
L4I	5479
L5E	4850
L5I	1065
L6E	14,395
L6I	2948
TC	902

2.3.1. Large-scale network model

For modeling of network activity (Figs. 6 and 7), we used the so-called hybrid scheme proposed by Hagen et al. (2016). Here, the neural network activity is first simulated with point neurons in NEST (Linssen et al., 2018) and the resulting spiking activity of all neurons saved to file. Afterwards, the neurons are modeled with detailed multicompartment morphologies and the spike times of the presynaptic neurons are used as activation times for synaptic input onto these neurons in a simulation where the extracellular potentials are calculated (Hagen et al., 2016; Senk et al., 2018). The simulation was unmodified from the results presented by Hagen et al. (2016) with transient thalamocortical input (their Figs. 1 and 7), except that all single-cell current dipole moments were recorded, and the EEG signals calculated. Briefly, the network model consists of 8 neural populations across four cortical layers (L2/3, L4, L5 and L6), with one excitatory and one inhibitory population in each of the four layers. The number of neurons in each population is given in Table 2, and the connectivity between the different populations is based on anatomical data (Binzegger et al., 2004; Potjans and Diesmann, 2014), and given in Hagen et al. (2016) (their Table 5). For the first step, simulating the network activity, the cortical neurons were modeled as leaky integrate-and-fire neurons, connected with static current-based exponential synapses. External input was supplied both in the form of a constant current input with a population specific strength, and thalamocortical input, which in the present example correspond to simultaneous activation of all thalamocortical neurons (t=900 ms), which are projecting to neural populations in layer 4 and layer 6. In the second step for calculating LFP and EEG signals, all cell models were passive, with population specific morphologies. The excitatory populations were pyramidal cells in L2/3, L5 and L6, and stellate cells in L4. All pyramidal cells were oriented with the apical dendrite along the depth axis of cortex (z-axis), and randomly rotated around this axis. Other cell types (stellate cells and interneurons) were randomly rotated around all axes. To ensure some variability in the morphologies, the 8 cortical populations were further divided into a total of 16 subpopulations with different morphologies (although some of these subpopulations used the same morphology).

For a full description of simulation details and parameters used for the large-scale network model, we refer to Hagen et al. (2016).

2.4. Code availability

Simulation code to reproduce all figures in this paper is freely available from https://github.com/solveignaess/EEG.git. For a more general and detailed documentation and examples of how to calculate current dipoles and EEG signals for biophysically detailed cell models, we refer the reader to the LFPy documentation (https://lfpy.rtfd.io).

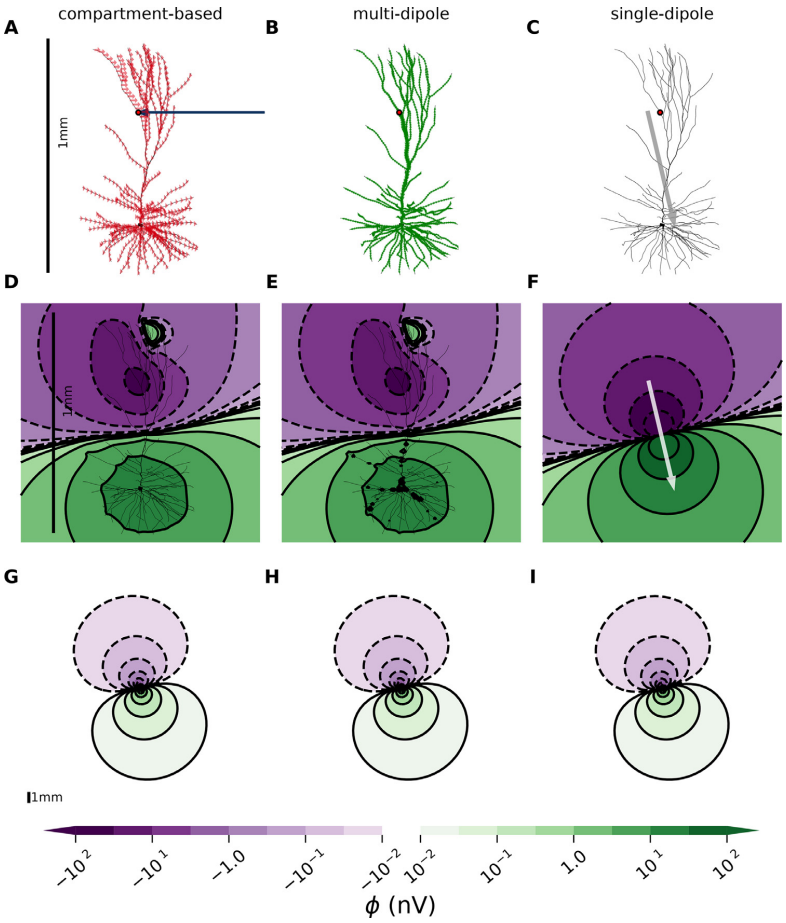

Fig. 2. Extracellular potentials become dipolar in the far field limit. A: Passive layer-2/3 pyramidal cell from human (Eyal et al., 2016) with an excitatory, conductance-based, two-exponential synapse placed on apical dendrite (red dot), see Methods (2.3) for parameters. The resulting transmembrane currents for each compartment are shown as a blue arrow (input current) and red arrows (return currents). **B**: Green arrows represent the multiple current dipole moments between neighboring neural compartments. **C**: Gray arrow illustrates the total current dipole moment, that is, the vector sum of the dipoles in B. **D-F**: Extracellular potential in immediate proximity of the neuron, computed with the compartment-based approach, multi-dipole approach and single-dipole approximation, respectively. Note that the multi-dipole results differ slightly from the compartment-based approach when the distance from the measurement point to the nearest current dipole moment is short compared to the dipole length. **G-I**: Same as D-F, but at a larger spatial scale (zoomed out). See 1 mm scalebar in panel A, D and G. The colorbar is shared for panels D-I.

3. Results

We introduce an approach for modeling electroencephalography (EEG) and magnetoencephalography (MEG) signals from detailed biophysical multicompartment cell models. The approach involves two steps: First, current dipole moments are extracted from activity in neurons or networks. Second, the extracted current dipoles are used as sources in established forward models. Here we only demonstrate the approach by computing EEG signals, but the current dipoles are equally applicable for computing MEG signals using the appropriate magnetic-field forward models (Hagen et al., 2018; Hämäläinen et al., 1993; Ilmoniemi and Sarvas, 2019). For illustration, we first consider EEG signals stemming from single synaptic input onto single neurons in an infinite homogeneous head model, before moving on to a simple, generic head model. Finally, we study EEGs from large-scale simulated network activity, also applying a detailed head model.

3.1. At sufficiently large distances, extracellular potentials become dipolar

When modeling electric potentials within the brain, we can apply the well-established compartment-based approach assuming a homogeneous volume conductor (Section 2.1.1) (Einevoll et al., 2013a; Holt and Koch, 1999). However, this assumption is no longer valid when it comes to modeling EEG signals on the scalp, which calls for an inhomogeneous head model (Ilmoniemi and Sarvas, 2019). Such head models typically take current dipoles as input, as opposed to individual current sinks/sources, and must be based on the current dipole approximation (Nunez and Srinivasan, 2006). Here, we introduce an approach for computing current dipoles from arbitrary simulated neural activity, and compare current-based and dipole-based modeling of electric potentials generated by a single cell receiving excitatory synaptic input. Excitatory synaptic input initiates a negative current at the synapse location, since positive ions flow into the cell. Due to current conservation (Koch, 1999), this negative current is exactly balanced by spatially distributed positive currents along the cellular membrane, as illustrated in Fig. 2**A** for a single apical excitatory synaptic input to a passive human cortical layer-2/3 pyramidal cell model (Eyal et al., 2016). See Methods 2.3 for simulation details. In the standard procedure for modeling extracellular potentials, here referred to as the *compartment-based approach*, the transmembrane current in each cellular compartment corresponds to a point current source/sink. Another strategy is to consider the axial current of each cellular compartment as a small current dipole (see Eq. (6)), which we refer to as the *multi-dipole approach* (Fig. 2**B**). By vector summation of all these dipoles into one single dipole at a specific position, we obtain the *single-dipole approximation* (Fig. 2**C**). For the sake of comparing these modeling approaches, we have assumed that the cell is po-

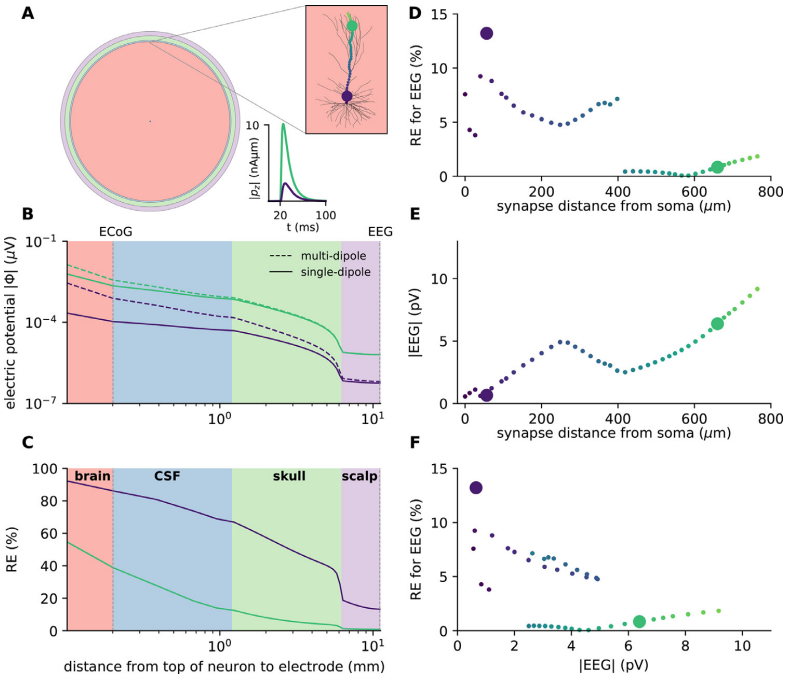

Fig. 3. Single-dipole approximation is justified for EEG but not ECoG signals. A: Illustration of four-sphere head model, where the pink, blue, green and purple spherical shells represent the brain, CSF, skull and scalp respectively, see Table 1. The pink inset shows the human layer-2/3 neuron (Eyal et al., 2016) located in the brain, 88.0 mm above head center. 41 simulations lasting 100 ms with a single synaptic input after 20 ms to cell with passive ion channels only, were performed for varying input locations, see colored dots. The z-component of the resulting current dipole moments for two synaptic input locations (large colored dots) are shown in inset below as functions of time. The results presented in this figure are computed at the simulation time points producing the largest current dipole moment for each synaptic input location. **B**: Magnitude of extracellular potential $|\phi|$ as function of distance from the top of the neuron, shown for two simulations with synaptic input locations marked by large colored dots in upper inset of A. In each simulation, we consider the time point with the largest current dipole moment. Dashed lines show extracellular potentials computed with multi-dipole, and full lines show single-dipole calculations. **C**: Relative error RE comparing the single-dipole model to the multi-dipole model, as function of distance from top of neuron to measurement point. **D**: Relative error RE showing how single-dipole model deviates from multi-dipole model EEG calculations, as function of distance from soma to synapse location. **E**: Magnitude of EEG signal, |EEG|, as function of distance from soma to synaptic input location. **F**: Relative error, RE, showing how EEG calculations performed with the single-dipole approximation deviates from multi-dipole approach as a function of amplitude of the EEG signal, |EEG|.

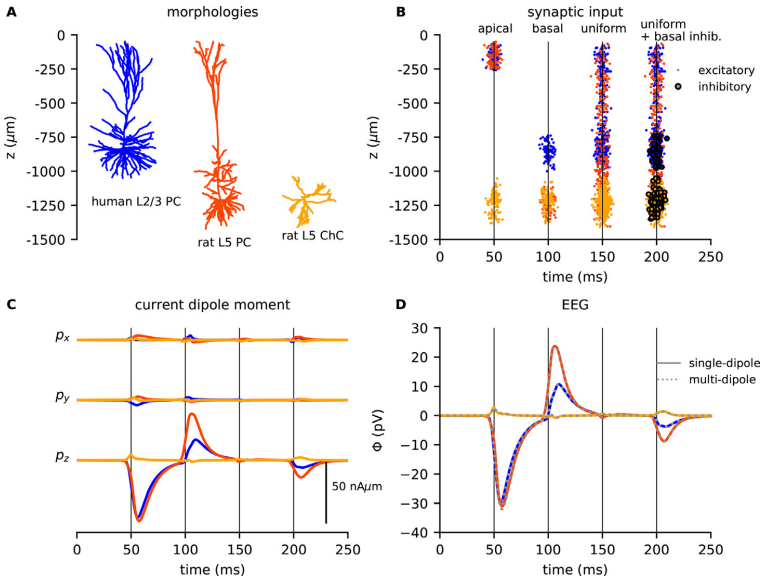

Fig. 4. EEG signals and current dipole moment from three different cell types with various synaptic input. A: The morphologies of a human L2/3 pyramidal cell (blue; Eyal et al. (2016)), a rat L5 pyramidal cell (red; Hay et al. (2011)), and a rat L5 interneuron (orange; Markram et al. (2015)). The remaining panels display data connected to each cell type, see cell-specific colors. **B**: Each dot represents an excitatory synaptic input at a specific time (x-axis) at a specific height of the neuron (z-axis, corresponding to panel A) for a specific cell type (color). The bigger dots with black borders mark inhibitory synaptic input. The four input bulks represent 1) 100 apical excitatory synaptic inputs, 2) 100 basal excitatory synaptic inputs, 3) 400 homogeneously spread-out excitatory synaptic inputs and 4) 400 homogeneously spread-out excitatory synaptic inputs and 50 inhibitory basal synaptic inputs. The synaptic weights sum to 0.01 μS for all sets of excitatory / inhibitory synapses in each wave (see Section 2.3 for details). For the interneuron, which doesn't have typical "apical" or "basal" zones, the synapses were spread out all over the morphology for all input types. **C**: The x-, y- and z-components of the current dipole moment $\mathbf{p}$ for the three different cell types. **D**: EEG signals, ϕ from the three cell types computed with the four-sphere model.

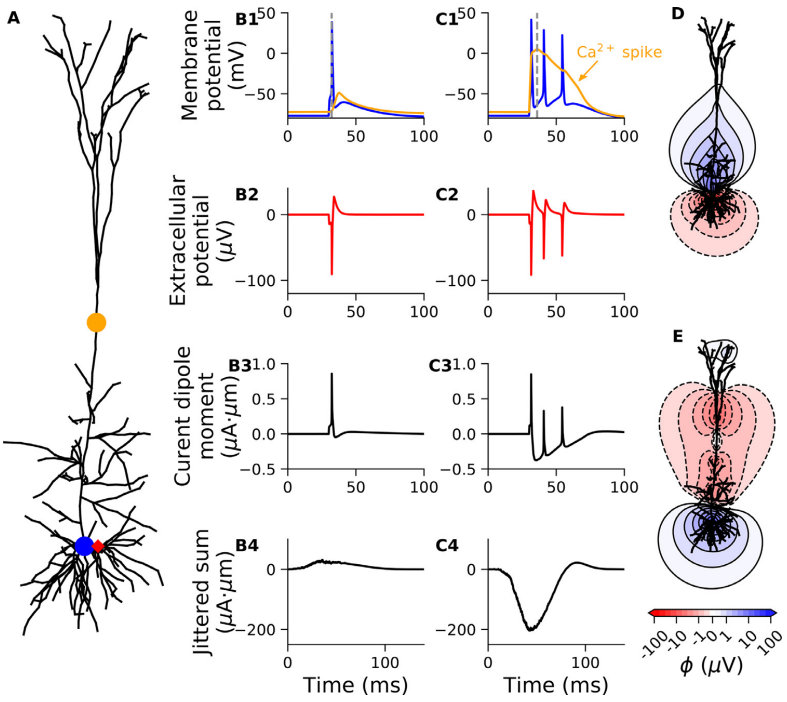

Fig. 5. Current dipole moment expose dendritic calcium spikes. A: Layer-5 cortical pyramidal cell model from rat (Hay et al., 2011), receiving either a single excitatory synaptic input to the soma evoking a single somatic action potential (blue dot, results in **B1-4**), or in addition an excitatory synaptic input to the apical dendrite, evoking a dendritic calcium spike and two additional somatic spikes (orange dot, results in **C1-4**). **B1, C1**: Membrane potential at the two positions indicated in **A. B2, C2**: Extracellular potential 30 μm away from the soma (red diamond in **A**), assuming for illustration an infinite homogeneous extracellular medium. **B3, C3**: Single-cell current dipole moment. **B4, C4**: Sum of 1000 instances of the single-cell current dipole moment (from **B3, C3**), that has been randomly shifted in time with a normally distributed shift with a standard deviation of 10 ms. **D:** Contour lines of extracellular potential around neuron at a snapshot in time during the somatic spike in **B1** (t=32.2 ms; time marked by dashed line). **E:** Contour lines of extracellular potential around neuron at a snapshot in time during the calcium spike in **C1** (t=36.0 ms; time marked by dashed line). The synaptic weight was 0.07 and 0.15 μS for the somatic and apical input location, respectively.

sitioned in an infinite homogeneous electric medium. Very close to the neuron, the extracellular potential will strongly depend on the exact distribution of transmembrane currents across the cellular morphology and will, therefore, typically not take a purely dipolar shape (Fig. 2 **D,E** versus **F**). However, since the dipole contribution will dominate when we are further away from the current sources (see Eq. (3)), the extracellular potential becomes more and more dipolar with increasing distance from the cell (Lindén et al., 2010). This implies that for the purpose of calculating extracellular potentials far away from the cell, the single-dipole approximation might be well justified (Fig. 2**G-I**). Note that there can be small differences between the results from the compartment-based and the multi-dipole approaches for electrode locations in the immediate vicinity of the current sources, due to the approximations inherent in using the current dipole model (Fig. 2D versus Fig. 2E).

3.2. Single-dipole approximation is justified for EEG, but not ECoG signals

In order to test the applicability of the single-dipole approximation for calculating ECoG and EEG signals, we applied the four-sphere head model (Hagen et al., 2018; 2019; Næss et al., 2017). Since the four-sphere head model takes current dipoles as input, the multi-dipole approach was used as benchmark: an assumption that should be well justified for the cell-to-electrode distances considered, see Section 3.1.

For different locations of a single excitatory synaptic input to a human cortical layer-2/3 pyramidal cell model (Eyal et al., 2016) (Fig. 3**A**), we calculated the electric potential at point-electrode positions spanning from 100 μm above the top of the cell, to the surface of the head, using both the multi-dipole approach and the single-dipole approximation (Fig. 3**B**). In the simulations shown, we used conductance-based synapses and included only passive membrane conductances, but we confirmed that using current-based synapses or a fully active cell model gave very similar results.

The electric potential decreased steeply with distance when crossing the different layers of the head model, most strongly across the low-conducting skull (Fig. 3**B**). For all synaptic input locations, we observed that the electric potential calculated with the single-dipole approximation markedly deviated from the multi-dipole approach directly above the neuron, but the difference strongly decreased with distance from the neuron (Fig. 3**B**, full versus dashed lines for two selected synapse locations). We quantified the model dissimilarities by looking at the relative error at the timepoint of the maximum current dipole moment, and for a chosen distal synaptic input the relative error was 38.9% and 0.839% at the position of the ECoG and EEG electrodes respectively (Fig. 3**C**, green line). For a specific proximal synaptic input we observed a relative error of 86.1% at the ECoG position, and 13.2% at the EEG position (Fig. 3**C**, purple line). Inserting a single strong synaptic current (synaptic weight 0.05 μS) into the soma of the same layer-2/3 pyramidal cell with active mechanisms (Eyal et al., 2018), resulting in a somatic spike, gave relative errors of 34.2% and 0.813% for the computed ECoG and EEG signals, respectively (results not shown). We found that calculating EEG signals with the single-dipole approximation gave relative errors peaking for synaptic locations $\sim$ 60 and 400 μm above the soma, with a sharp drop in the relative error for synaptic inputs further away from the soma than $\sim$ 400 μm (Fig. 3**D**). Here, synaptic inputs slightly distal to 400 μm away from soma resulted in the majority of the return currents escaping the cell below the synaptic input (closer to the soma). This gave a distinctly dipole-like source/sink distribution, and thereby low relative errors ($\sim$ 0.4%). Synaptic inputs slightly proximal to 400 μm away from soma instead resulted in almost balanced return currents above and below the synaptic input. This gave a multipole-like source/sink distribution, and thereby larger relative errors ($\sim$ 7%). Note, however, that the synaptic input locations that resulted in higher relative errors, also gave relatively weak EEG signals (Fig. 3**E**). This demonstrates that the relative error of the single-dipole approximation is negatively correlated with the amplitude of the scalp potential (Fig. 3**F**). This is as ex-

pected, given that the strongest EEG signals are expected to be caused by dipole-like source/sink distributions (section 2.1.2). In summary, the single-dipole approximation can result in substantial errors at the position of the ECoG electrodes, but gives small errors at the position of the EEG electrodes for synaptic locations leading to strong EEG signals.

3.3. Single-dipole approximation simplifies estimate of EEG contribution

In the previous section, we showed that the single-dipole approximation was applicable for calculation of EEG signals, and in this section we demonstrate that the single-dipole approximation can substantially simplify the analysis of the biophysical origin of EEG signals.

Pyramidal cells have a preferred orientation along the depth axis of cortex (here the z-axis), and the direction of the current dipole moment $\mathbf{p}$ can be expected to align with this axis since radial symmetry will tend to make the orthogonal components (p_x, p_y) cancel at the population level (Hagen et al., 2018). In contrast, interneurons show much less of a preferred orientation, and are therefore expected to give a negligible contribution to the EEG signal, except indirectly through synaptic inputs onto pyramidal cells (Hagen et al., 2016). We illustrated this by applying the single-dipole approximation to three different cell types (Fig. 4**A**), each receiving a large number of synaptic inputs with target regions on the cells set up to vary over time (Fig. 4**B**).

For the previously used human layer-2/3 cell (Fig. 4**A**, blue; Eyal et al. (2016)) receiving a volley of 100 excitatory synaptic inputs that were restricted to the uppermost 200 μm of the cell (t=50 ms; Fig. 4**B**, blue dots), we observed a negative deviation of p_z (Fig. 4**C**, blue line). For 100 basal synaptic inputs (t=100 ms; Fig. 4**B**, blue line), the polarity of p_z was instead positive, but of slightly lower amplitude than for apical input, as can be expected because the large area of the somatic region will cause strong return currents in the immediate vicinity of the synaptic inputs, and therefore an overall weaker current-dipole moment.

A uniform distribution of 400 synaptic inputs across the cell membrane with area-weighted probability (t=150 ms; Fig. 4**B**, blue line), only gave rise to small ripples in p_z, due to the substantial cancellation of current dipoles of opposite polarity. It is sometimes assumed that excitatory input is relatively uniformly distributed onto pyramidal cells, while inhibitory input is more directed to the perisomatic region (Mazzoni et al., 2015; Skaar et al., 2020; Teleńczuk et al., 2020; 2020). As expected, we found that this combination of uniformly distributed excitatory synaptic input and perisomatic inhibitory input gave rise to a clear negative response in p_z (t=200 ms; Fig. 4**B**, blue line), which could be part of the explanation why inhibitory synaptic input in some cases has been found to dominate the LFP (Hagen et al., 2016; Teleńczuk et al., 2017).

For a rat cortical layer-5 pyramidal cell model (Fig. 4**A**, red; Hay et al. (2011)), the resulting current dipole moment was very similar in shape to the previously described current dipole moment from the human layer-2/3 cell model. The amplitude was however somewhat larger, which was expected because the longer apical dendrite will tend to give larger current dipole moments (Fig. 4**C**, red line). Lastly, we used a rat cortical layer-5 interneuron model (Fig. 4**A**, orange; Markram et al. (2015)), but since the dendrites of interneurons are not structured into the same distinctive zones as pyramidal cells, the synaptic input caused very small net current dipole moments.

We calculated the EEG signals with the four-sphere head model, using both the multi-dipole (Fig. 4**D**, dotted lines) and the single-dipole (Fig. 4**D**, solid lines) approach. To compare the approaches, we computed the relative error as a function of time, that is, the absolute difference between the results from the two approaches, normalized by the maximum EEG magnitude computed with the multi-dipole approach. The single-dipole approach gave a maximum error of 2.14%, 3.27% and 0.313% for the human layer-2/3 cell, the rat layer-5 cell and the rat interneuron, respectively. Importantly, the EEG signal is essentially fully described by the z-component of the current dipole moment p_z, that is, a single time-dependent variable. This reduction in signal description represents a massive simplification in the understanding of the biophysical origin of the EEG signal, compared to considering the transmembrane currents and position of each cellular compartment.

3.4. Current dipole moment expose dendritic calcium spikes

Suzuki and Larkum (2017) recently demonstrated that dendritic calcium spikes can be recorded experimentally at the cortical surface, and that the signal amplitudes can be similar to contributions from synaptic inputs. This demonstrates that active conductances may play an important role in shaping ECoG and EEG signals. Furthermore, it suggests that information about calcium dynamics might be present in such signals, and that this information could potentially be taken advantage of when studying learning mechanisms associated with dendritic calcium spikes (Suzuki and Larkum, 2017).

The previously introduced rat layer-5 cortical pyramidal cell model from Hay et al. (2011) can exhibit dendritic calcium spikes. When this cell model received a single excitatory synaptic input to the soma (Fig. 5**A**, blue dot), strong enough to elicit a somatic action potential (Fig. 5**B1**, blue), a small depolarization was also visible in the apical dendrite (Fig. 5**B1**, orange). Even so, this did not initiate any dendritic calcium spike. However, when combining the same somatic synaptic input with an additional excitatory synaptic input to the apical dendrite, 400 μm away from the soma (Fig. 5**A**, orange dot), we observed a dendritic calcium spike. This calcium spike did, in turn, induce two additional somatic spikes (Fig. 5**C1**). For both synaptic input strategies described above, the extracellular potential simulated 30 μm away from the soma took the shape of stereotypical extracellular action potentials: that is, a sharp negative peak followed by a broader and weaker positive peak (Fig. 5**B2, C2**). Further, we observed that the slow dendritic calcium spike was not reflected in the extracellular potential close to the soma (Fig. 5**C2**). We found that for the case with only a somatic spike and no calcium spike, the single-cell current dipole moment resembled the inverse of the extracellular potential (Fig. 5**B3**), while for the case with both somatic and dendritic spiking, a pronounced slow component was also present in the single-cell current dipole moment (Fig. 5**C3**). Somatic action potentials are typically not expected to contribute significantly to EEG signals (but see Teleńczuk et al. (2015)), because the very short duration of spikes with both a positive and a negative phase implies that extreme synchrony is needed for spikes to sum constructively, and spikes that are only partially overlapping tend to sum destructively. The same cannot be expected to hold for the calcium spikes, which are not only longer-lasting but also predominately cause a negative response in the current current dipole moment. To mimic a neural network scenario with multiple cells spiking at slightly different times, we calculated the sum of 1000 instances of the single-cell current dipole moment that was jittered (shifted) in time (normally distributed, standard deviation=10 ms). We found that the case with the dendritic calcium spike now had a 6.6-fold larger maximum amplitude than the case with only the somatic spike (Fig. 5 **B4** versus **C4**, $\max|\mathbf{p}|$ = 30.8 μAμm and 204.2 μAμm respectively). This demonstrates that dendritic calcium spikes are much more capable of summing constructively for a population of cells, and substantiates the role of dendritic calcium spikes in affecting ECoG/EEG/MEG recordings.

The amplitude of the slow component of the current dipole moment from the calcium spike was about 0.5 μAμm (Fig. 5**C3**), and later (Sec. 3.5) we will present results from a simulated neural network where the average event-related current dipole moment of layer 5 pyramidal cells were found to be about 0.1 μAμm (Fig. 6**D**, bottom right). This indicates that our results are compatible with the claim by Suzuki and Larkum (2017) that signal amplitudes from calcium spikes could be similar in amplitude to contributions from synaptic input.

We can make a very rough estimate of the number of simultaneous calcium spikes required to cause a measurable EEG response: A cur-

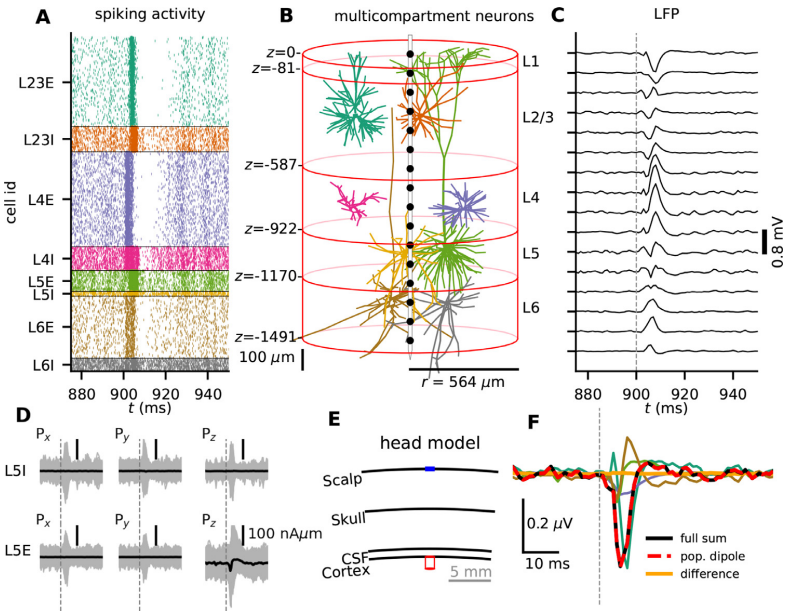

Fig. 6. Large-scale neural simulations can be used to probe biophysical origin of EEG signals. A: Stimulus-evoked spiking activity from thalamic input (time t = 900 ms, denoted by thin vertical line) in the cortical microcircuit model from Potjans and Diesmann (2014). Dots indicate spike times of individual neurons, and populations are represented in different colors (I=inhibitory, E=excitatory). **B**: Multicompartment model neurons used to produce the measurable signals, with colors corresponding to panel **A**, showing one example morphology per population. Layer boundaries are marked at depths relative to cortical surface, z = 0. A laminar recording electrode with 16 contacts separated by 100 μm (black dots) is positioned in the center of the population. **C**: LFPs calculated at depths corresponding to black dots in **B. D**: For the two L5 populations (L5I and L5E), the three components of the current dipole moment is shown for all individual cells (gray), together with the population average (black). **E**: Illustration of the four-sphere head model, with the red column corresponding the the outline of the population in panel **B. F**: The EEG signal from each population found by summing the single-cell EEG contribution of all individual cells within each population (different colors, same color scheme as in **A**,**B**), together with the total summed EEG signal (black). The simplified EEG signal was found by first summing the z-component of the current dipole moments for all pyramidal cells, that is L2/3E, L5E and L6E, and calculating the EEG from these population dipoles (red dashed).

rent dipole moment of 1 μAμm gives an EEG amplitude on the order of 10^{-3} μV (see for example Fig. 4 **C** and **D**, note different scales). Assuming that an EEG contribution must exceed $\sim$ 10 μV to be detectable (Hagen et al., 2018; Nunez and Srinivasan, 2006) implies a minimum needed current dipole moment of $\sim 10^4$ μAμm. A number of perfectly synchronous calcium spikes would each contribute with $\sim$ 0.5 μAμm (Fig. 5**C3**), suggesting that about 20,000 synchronous calcium spikes would be needed to cause a measurable EEG response. Further, considering that the signal amplitude decreases by about 100-fold from cortical surface to scalp (Fig. 3**B**) and assuming a similar detection threshold, indicates that a few hundred simultaneous calcium spikes would be detectable by ECoG electrodes.

It might initially seem surprising that the dendritic calcium spike is so strongly reflected in the single-cell current dipole moment, given that the transmembrane currents associated with the somatic action potential are much larger than those associated with the dendritic calcium spike: the maximum amplitude of the transmembrane currents of the somatic compartment was 45.1 nA, compared to just 0.30 nA for the compartment in the apical dendrite (Fig. 5**A**, blue and orange dots). However, the current dipole moment is given as the product between the amplitude of the current and the separation between the source and sink ($\mathbf{p} = I\mathbf{d}$; Eq. (6)). While the currents associated with the somatic action potential will for the most part be contained within the somatic region, giving very small sink/source separations, the currents associated with the dendritic calcium spike will be distributed over a much larger part of the cell membrane. This effect can be illustrated by comparing the spatial profile of the extracellular potentials around the neuron at a snapshot in time during a somatic spike or during a calcium spike (Fig. 5 **D** versus **E**).

3.5. EEG from large-scale neural network simulations

So far, we have only considered EEG contributions from single cells, but real EEG signals are expected to reflect the activity of hundreds of thousands to millions of cells (Cohen, 2017; Nunez and Srinivasan, 2006). Biophysically detailed modeling of large populations is still in its infancy (Einevoll et al., 2019) and at present typically include "only" a few tens of thousands of biophysically detailed cells (Billeh et al., 2020; Markram et al., 2015). Networks of point neurons, on the other hand, are regularly used to simulate hundreds of thousands (Billeh et al., 2020) or even millions of cells (Schmidt et al., 2018; Senk et al., 2018), but LFP, ECoG, EEG or MEG signals can not be computed directly from point neurons (Einevoll et al., 2013a; Ness et al., 2020). To investigate EEG signals generated by neuronal networks, we therefore used a hybrid scheme (Hagen et al., 2016; Senk et al., 2018; Skaar et al., 2020), where the network activity is first simulated in a highly computationally efficient manner with point neurons in NEST (Linssen et al., 2018) and the resulting spiking activity of each neuron saved to file. Afterwards, each cell is modeled with biophysically detailed multicompartment morphologies and the stored spikes of all the presynaptic neurons are used as activation times for synaptic input onto these neurons in a simulation where the extracellular potentials are calculated (Hagen et al., 2016; Senk et al., 2018).

We used the large-scale point-neuron cortical microcircuit model from Potjans and Diesmann (2014) and Hagen et al. (2016). This model has $\sim$ 80,000 neurons divided into 8 different cortical populations, that is, one excitatory and one inhibitory population in each of the four layers L2/3 - L6 (see Section 2.3.1). This model can exhibit a diverse set of spiking dynamics including different oscillations and asynchroneous irregular network states (Brunel, 2000; Hagen et al., 2016). We here chose to focus on the scenario with transient thalamocortical input for mimicking event-related potentials (ERPs). However, focusing on different neural oscillations (brain waves) or spontaneous activity would have served equally well for our purposes. The only difference from the original simulation by Hagen et al. (2016) was the added calculation of current dipole moments and EEG signals. We simulated transient thalamic synaptic input to layers 4 and 6 (Fig. 6**A**), and after the spikes had been mapped onto the multicompartment cell models (Fig. 6**B**), we cal-

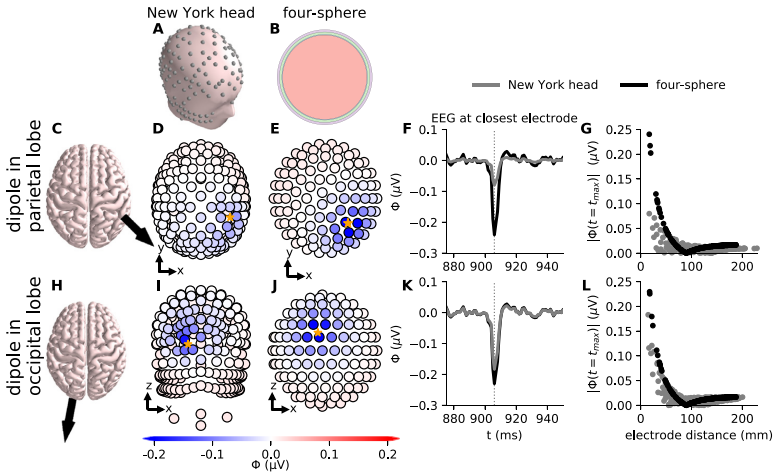

Fig. 7. EEG signals from cortical column network with simple or complex head models. EEG signals from the population dipole from the cortical microcircuit model (same as in Fig. 6), can be used both with the complex New York Head model (**A**), or the simple four-sphere head model (**B**). The dipole was located either in the parietal lobe (**C-G**) or in the occipital lobe (**H-L**). **C**: The dipole location and orientation in the parietal lobe is illustrated with black arrow on the cortical surface of the New York Head model. **D, E**: EEG signals (ϕ) on scalp surface electrodes computed with the New York Head model (**D**) or the four-sphere head model (**E**), seen from above. The data is from the time point of the strongest current dipole moment $|\mathbf{p}|$. Dipole location is marked by orange star, with coordinates in the New York Head model (55, -49, 57) mm. **F**: EEG trace computed with the New York Head model (gray) or the four-sphere head model (black) on the scalp surface electrode with the shortest distance to the dipole location. The distances were 16.76 mm (New York Head) and 16.78 mm (four-sphere). **G**: Absolute value of EEG signals from panel **D,E** as a function of distance from dipole to measurement electrode. **H-L**: Same as for **C-G**, but with the dipole located in the occipital lobe. Note that panel **I, J** are rotated to show the back of the head. The dipole coordinates in the New York Head model were (-24.3, -105.4, -1.2) mm, and the distance to the closest electrode in panel **K** was 14.64 mm (New York Head) and 17.51 mm (four-sphere).

culated the LFP (Fig. 6**C**) similarly to Hagen et al. (2016) (their Fig. 1), in addition to the current dipole moments of each cell.

For all cell populations, we found that the current dipole moments from individual cells could show large transient responses to thalamic input (Fig. 6**D**; gray lines show current dipole moment from individual cells in two example populations: L5 inhibitory (L5I) and L5 exitatory (L5E)), but for all inhibitory populations, as well as for the excitatory stellate cells in L4, the thalamic response was not visible in the average current dipole moment (Fig. 6**D**; black lines, L5I). The same was true for the current dipole moment components perpendicular to the depth axis for excitatory populations (Fig. 6**D**; L5E, p_x, p_y, black lines), but not for the component along the depth axis which had a substantial average response to the thalamic input (Fig. 6**D**; L5E, p_z, black line). These observations imply, as previously noted, that only the z-component of the current dipole moment from excitatory pyramidal cell populations can be expected to contribute significantly to the EEG signal.

Our findings invite a simplified approach to calculate the EEG signal: The original approach involves calculating all the $\sim$ 80,000 single-cell EEG contributions and summing them, taking into account the position of the individual cells, similarly to what is done for the LFP signal. A much simpler alternative would be to compute a single summed p_z-component from all neurons in each pyramidal cell population (L2/3E, L5E and L6E), and place it in the center of the given pyramidal cell population (with a population-specific depth). We can then calculate the resulting simplified EEG signal from these population dipoles. This approximation can be expected to be accurate when the population radius is small compared to the distance from the population center to the EEG electrode. Note that the distance from the top of cortex to the top of the head is typically $\sim$ 10 mm, while the diameter of the present simulated population is only $\sim$ 1 mm (Fig. 6; population outline in **B** is drawn in red in **E**).

To test this simplified approach, we combined the current dipole moments with the four-sphere head model (Fig. 6**E**). We calculated the EEG signal by the simplified approach, that is, from one time-dependent array, p_z, for each pyramidal cell population, located in the center of the given population. We then compared this simplified approach with the original approach, that is, the sum of EEG contributions from all $\sim$ 80,000 cells at their respective positions. The simplified approach gave a maximum relative error of 1.1% (maximum absolute difference normalized by maximum value of EEG from original approach) (Fig. 6**F** black versus red dashed line). This implies that the EEG signal from the simulated cortical activity can be nearly fully represented by a single time-dependent variable for each pyramidal cell population. Further, summing these population dipoles into one single dipole, and locating it in the center of the population column at 1 mm depth, instead gave a maximum relative error of 6.6%. This highlights that the exact position of different pyramidal cell populations are relatively unimportant for shaping the EEG signal.

We also compared the relative amplitude of the EEG signal from each population, and found that for the present example, the excitatory population of L2/3 was the dominant source of the EEG signal (Fig. 6**F**). Note, however, that we expect this observation to be somewhat model-dependent, and that strong general claims about the contribution of different pyramidal cell populations to the EEG signal cannot be made from this example study alone.

3.6. Dipole approximation in complex head models

Even though the four-sphere head model is convenient for generic EEG studies, many applications such as accurate EEG source analysis, may require more detailed head models (Dale et al., 1999; Vorwerk et al., 2014). The construction of such complex head models is dependent on expensive equipment, that is magnetic resonance imaging (MRI), to map the electrical conductivity of the entire head at resolutions of $\sim$ 0.5–1.0 mm^3 (Huang and Parra, 2015; Huang et al., 2016). Afterwards, numerical techniques such as the Finite Element Method (FEM) (Logg et al., 2012) can be used to calculate the signal at the EEG electrodes for arbitrary arrangements of current dipoles in the brain, but at a high computational cost. The number of computing hours is, however, reduced by applying the reciprocity principle of Helmholtz. The reciprocity principle states, in short, that switching the location of a current source and a recording electrode will not affect the measured potential (Dmochowski et al., 2017; Huang et al., 2016; Malmivuo and Plonsey, 1995; Ziegler et al., 2014). This implies that it suffices to use

FEM to calculate the lead field in the brain from virtual current dipoles placed at each of the EEG electrodes. From the lead field matrix, we can infer the potential at the EEG electrodes, given an arbitrary arrangement of current dipoles in the brain. Luckily, several such pre-solved complex head models are freely available, and one example is the *New York Head* (NYH) (Fig. 7**A**), which we have applied here (Huang et al. (2016); https://parralab.org/nyhead/).

To illustrate the use of pre-solved complex head-models, we inserted the current dipole moment obtained from the cortical column model in Section 3.5 into the New York Head model (Fig. 7**A**), at two manually chosen positions: one in the parietal lobe (Fig. 7**C and D**), and one in the occipital lobe (Fig. 7**H and I**). In both cases, the current dipole moment was oriented along the normal vector of the brain surface, and the EEG signal was calculated. For comparison with a simplified head model, we inserted the same current dipole moment into the four-sphere head model (Fig. 7**B**) at locations comparable to the dipole positions chosen in the occipital and parietal lobe in the NYH model: the locations in the four-sphere model were chosen close to the brain surface, such that the distance from dipole position to the closest electrode (Fig. 7**E and J**) and the brain surface normal vectors were similar to the respective positions in the NYH model.

The two head models generated EEG signals of the same temporal shape, which is expected, given that neither of the models included any temporal filtering (Miceli et al., 2017; Pfurtscheller and Cooper, 1975; Ranta et al., 2017). The computed EEG signals from the two head models also gave comparable results in both spatial shape and amplitude (Fig. 7 **D** versus **E; I** versus **J**). The relative difference between the EEG signals calculated with the four-sphere model and the NYH model at the time of maximum signal amplitude was 201% and 25.2% for the positions in the parietal and occipital lobe respectively (Fig. 7**F and K**). Note that while the four-sphere head model gave very similar EEG amplitudes for the two different dipole locations (as expected from symmetry), the EEG amplitudes from the complex head model was much more variable, even for similar distances to the closest electrode (Fig. 7**F** and**K**).

The higher variability of the complex head model was also apparent in the decay of the maximum EEG amplitude with distance, which was perfectly smooth, exponential-like (Nunez and Srinivasan, 2006), and very similar for the two locations in the four-sphere model, but very variable for the complex head model, although with the same general shape (Fig. 7**G** and **L**).

Note that despite the complexity, the NYH model is substantially faster than the four-sphere model. In order to simulate the EEGs from a dipole moment vector containing 1200 timesteps, the NYH model execution times were $\sim$ 0.3 s, while the four-sphere model needed $\sim$ 0.9 s.

4. Discussion

4.1. Summary

In this paper, we have introduced an approach for reducing arbitrary simulated neural activity from biophysically detailed neuron models to single current dipoles (Fig. 2). We verified that the approach was applicable for calculating EEG, but generally not for ECoG signals (Figs. 3 and 4), and gave examples of how reducing neural activity to a single dipole can be a powerful tool for investigating and understanding single-cell EEG contributions (Figs. 4 and 5). Furthermore, we demonstrated that the presented approach could easily be integrated with existing large-scale simulations of neural activity. Moreover, we showed how single dipoles are useful for constructing compact representations of the EEG contributions from entire neural populations, with methods still firmly grounded in the underlying biophysics (Fig. 6). Finally, we demonstrated how the simulated current dipoles, from single cells or large neural populations, can be directly inserted into complex head models for calculating more realistic EEG signals (Fig. 7).

4.2. Application of current dipoles for computing EEG, MEG and ECoG signals

We have highlighted that the calculation of current dipoles from neural activity is cleanly separated from the calculation of the ensuing EEG signals. Since MEG sensors like EEG electrodes are positioned far away from the neural sources, the same is true for MEG signals. The calculated current dipoles can therefore also be used in combination with simplified or detailed frameworks for calculation of MEG signals, for example by following methods outlined in Hagen et al. (2018) and Ilmoniemi and Sarvas (2019).

ECoG electrodes are in general positioned closer to the neural sources. For our example simulations of the ECoG signal generated by individual neurons, we found that use of the single-dipole approximation gave substantial errors (Fig. 3). Thus for computation of ECoG signals, the standard compartment-based formalism or the multi-dipole approach (Fig. 2) requiring much more computational resources, may be required. Here an alternative to using full head models is to use the method of images, taking into account the discontinuity of electrical conductivity at the cortical surface (Hagen et al., 2018; Pettersen et al., 2006). A further complication of ECoG signals is that since the electrodes are both relatively large and close to the neural current sources, the ECoG electrodes themselves might be expected to substantially impact the measured signals (Ness et al., 2015; Rogers et al., 2020; Vermaas et al., 2020).

Note that while we here used LFPy 2.0 (Hagen et al., 2018; 2019), a python interface to NEURON (Carnevale and Hines, 2006), calculation of current dipole moments can easily be implemented into any framework where the transmembrane currents are available, through the simple formula given in eq. (7).

4.3. Generalization to non-compartmental models

EEG and MEG recordings reflect neural activity at the systems-level (Einevoll et al., 2019; Pesaran et al., 2018). Here, we have focused on calculating current dipoles from detailed multi-compartment neuron models, but neural modeling at the systems-level is often based on higher levels of abstraction, like point neurons (Linssen et al., 2018) or firing rate populations (Sanz-Leon et al., 2013). Calculation of electric or magnetic signals from such higher-level neural simulations must in general rely on some kind of approximation trick, since neurons require a spatial structure to be capable of producing electromagnetic signals (Einevoll et al., 2013a). One such trick that we took advantage of here is the hybrid scheme (Hagen et al., 2016). This two-step scheme involves neural network activity first being simulated by point neurons, before the resulting spike trains are replayed onto multi-compartment neuron models for calculating LFP and EEG signals (Section 3.5; Fig. 6).

Further, the hybrid scheme can be generalized to also allow for calculation of EEG/MEG signals from firing-rate models by using the so-called kernel method, which has previously been successfully applied to the LFP (Hagen et al., 2016; Skaar et al., 2020; Teleńczuk et al., 2020). In practice, this can be done in two steps: First, simultaneously activating all outgoing synapses from a specific (presynaptic) simulated population, and recording the total current dipole moment of the response (the kernel) (Hagen et al., 2016). Second, computing the EEG/MEG contribution stemming from this (presynaptic) population by convolving the kernel with the population firing rate, and applying an appropriate forward model. Here, the firing rate would be obtained separately in point neuron network models or firing-rate models. In this way, the basic biophysics of EEG and MEG signals from synaptic activation of multi-compartment neuron models is included, avoiding, however, computationally heavy multicompartmental modeling of spiking dynamics. The calculated current-dipole kernels should be applicable for different kinds of input to the original network model, but would in general have to be recomputed for changes to cell or synaptic parameters.

4.4. Connection to other work

Calculation of current dipole moments from morphologically complex cell models has been pursued before, for example to study the EEG and MEG contribution of spiking single cells (Murakami and Okada, 2006), or to study how the synaptic input location affects the current dipole (Ahlfors and Wreh II, 2015; Lindén et al., 2010). Important work on EEG interpretation in terms of the underlying neural activity has also previously been done through use of "minimally sufficient" biophysical models, see for example Murakami et al. (2003, 2002), Jones et al. (2009, 2007), Sliva et al. (2018) and Neymotin et al. (2020). Here, "minimally sufficient" means that the cell models only had minimally needed multi-compartment spatial structure (point neurons cannot produce current dipole moments), only considered a few cell types, and employed simple synaptic connection rules. In particular, the Human Neocortical Neurosolver (HNN) (Neymotin et al., 2020) enables researchers to link measured EEG or MEG recordings to neural activity through a pre-defined canonical neocortical column template network. HNN comes with an interactive GUI, designed for users with little or no experience in computational modeling, and might therefore be an appropriate choice for researchers seeking to gain a better understanding of their EEG/MEG data. However, while the use of such minimally sufficient models allows for quick and direct comparison between simulated and recorded EEG signals, it is not (presently) compatible with simulating EEG or MEGs from biophysically detailed single cell- or network models, constructed from detailed experimental data (Arkhipov et al., 2018; Billeh et al., 2020; Egger et al., 2014; Gratiy et al., 2018; Hagen et al., 2016; Markram et al., 2015; Reimann et al., 2013).

A more high-level approach for simulating MEG/EEG signals from the underlying neural activity has been pursued through neural field or neural mass models (Bojak et al., 2010; Coombes, 2006; David and Friston, 2003; Deco et al., 2008; Jirsa et al., 2002; Ritter et al., 2013), which aim to model the evolution of coarse-grained variables such as the mean membrane potential or the firing rate of neuron populations. Such coarse-graining drastically reduces the number of parameters and the computational burden of the simulation, and can be used to study the interplay among entire brain regions, and indeed run whole-brain simulations. The Virtual Brain (TVB) is an excellent example of a software for whole-brain network simulations (Ritter et al., 2013; Sanz-Leon et al., 2015; 2013), where detailed and potentially personalized head models can be combined with tractography-based methods identifying the connectivity between brain regions (Sanz-Leon et al., 2013). To calculate measurement modalities like MEG and/or EEG signals from neural field or neural mass models, it is typically assumed that the population current dipole moments are roughly proportional to, for example, the average excitatory membrane potential (Bojak et al., 2010; Ritter et al., 2013). Further, EEGs can be calculated from the resulting current dipole moments in combination with head models as presented in this paper, or through other softwares or techniques (Gramfort et al., 2014). This suggests an intriguing future development, where one could apply the above-mentioned kernel method based on biophysically detailed neuron models to substantially increase the accuracy of LFP, EEG and MEG predictions from high-level large-scale simulations of neural activity.

4.5. Outlook

EEG and, later, MEG signals have been an important part of neuroscience for a long time, but still very little is known about the neural origin of the signals (Cohen, 2017). A better understanding of these signals could lead to important discoveries about how the brain works (Ilmoniemi and Sarvas, 2019; Lopes da Silva, 2013; Pesaran et al., 2018; Uhlirova et al., 2016), and provide new insights into mental disorders (Mäki-Marttunen et al., 2019a; Sahin et al., 2019). This work lays some of the foundation for obtaining a better understanding of EEG/MEG recordings, by allowing easy calculation of the signals from arbitrary neural activity. The presented formalism is well suited for modeling EEG/MEG contributions from various potential neural origins, including different cell types, different ion channels and different synaptic pathways. For example, to study the effect of calcium spikes (Suzuki and Larkum, 2017), I_h currents (Kalmbach et al., 2018; Ness et al., 2016; 2018), or gene expression on EEG signals (Mäki-Marttunen et al., 2019b), one only needs to know how the z-component of the resulting population current dipole is affected. This decoupling of the current dipole moment and head model allows for easier investigation and improved understanding of the origin of the EEG/MEG signal.

This study has only considered how one can calculate EEG/MEG signals from the underlying neural activity (so-called forward modeling). EEG/MEG measurements are, however, often used for source localization (so-called inverse modeling), aiming to identify the underlying cortical current dipoles (Gramfort et al., 2014; Ilmoniemi and Sarvas, 2019; Nunez and Srinivasan, 2006). However, such reconstructed current dipoles are generic in the sense that they are typically not intended to represent specific neural populations. By allowing for calculation of current dipoles from cortical populations, the work presented here takes a step towards consolidating the, so far, mostly separate scientific disciplines of neural modeling and EEG/MEG data analysis (but see also Neymotin et al. (2020)).

The main challenge in inverse modeling, is that the problem is mathematically ill-posed, because the number of possible current sinks/sources is much larger than the number of recording electrodes. This implies that unique solutions can in general not be found, without making additional assumptions on cortical current dipole distributions (Pettersen et al., 2012). In practice, this means that the performance of inverse methods will depend on design choices that need testing. The presented approach can be used to create simulated EEG/MEG data with known underlying current dipoles, which can be used for benchmarking inverse methods for source localization, similar to what has previously been done for current source density estimations (Pettersen et al., 2006). Further, Pettersen et al. (2006) demonstrated that an improved inverse method for LFP analysis, the so-called iCSD method, could be made by building the forward model into the inverse model. Going one step further, we can envision incorporating the presented approach into an EEG inverse model, aiming to identify synaptic input regions to different pyramidal cell populations instead of cortical current dipoles.

While there are many examples of detailed biophysical modeling of neural activity improving interpretation of measured intracranial extracellular potentials in lab animals (Blomquist et al., 2009; Chatzikalymniou and Skinner, 2018; Einevoll et al., 2007; Luo et al., 2018; McColgan et al., 2017; Teleńczuk et al., 2020), much less has been done for human EEG/MEG signals. This is natural given that studies of healthy human brains necessarily are limited to non-invasive technologies (Cohen, 2017; Lopes da Silva, 2013; Uhlirova et al., 2016). However, given all the valuable insights that could be gained from an increased understanding of non-invasive measurements of neural activity in humans, an important challenge in modern neuroscience is to build on the mechanistic insights from animal studies and use them for understanding non-invasive signals in humans (Cohen, 2017; Einevoll et al., 2019; Lopes da Silva, 2013; Mäki-Marttunen et al., 2019a; Uhlirova et al., 2016). The approach for calculating EEG/MEG signals in this paper should therefore ideally be used in combination with animal studies simultaneously measuring multisite laminar LFP (and MUA) signals within cortex, as well as EEG/MEG signals (see for example Bruyns-Haylett et al., 2017; Cohen, 2017).

Today, we have a reasonably good understanding of how single neurons operate, that is, how they respond to synaptic input, and how multitudes of synaptic inputs combine to produce action potentials (Einevoll et al., 2019). Similarly, we can, to a high degree, explain the measurement physics of EEG/MEG, that is, how neural currents affect electromagnetic brain signals recorded outside of the head (Cohen, 2017; Ilmoniemi and Sarvas, 2019; Nunez and Srinivasan, 2006). The challenge of understanding EEG/MEG signals is therefore closely related to the greatest challenge in modern neuroscience: understanding neural

networks. Making sense of such complicated dynamical systems typically requires computational modeling (Einevoll et al., 2019), but the complexity of neurons, and the complexity and size of the neural networks involved in even the simplest of cognitive tasks, makes this a daunting challenge. The steady increase in available computing power, in combination with the ever-increasing knowledge on synaptic connectivity patterns is, however, making this approach more and more attractive (Arkhipov et al., 2018; Billeh et al., 2020; Egger et al., 2014; Gratiy et al., 2018; Hagen et al., 2016; Markram et al., 2015; Reimann et al., 2013; 2019): Today, there are several ongoing research projects pursuing such modeling efforts, for example at the Allen Institute for Brain Science and in the Human Brain Project (Einevoll et al., 2019). While biophysically detailed, large-scale neural simulations are still in their infancy, we expect these simulations to become an increasingly important research tool in neuroscience (Einevoll et al., 2019). The presently described method enables EEG/MEG simulations combining detailed neural simulations with realistic head models. We believe that this approach will help shedding light on the neural origin of EEG/MEG signals, and help us take full advantage of these important brain signals in the future.

Credit authorship contribution statement

Solveig Næss: Conceptualization, Software, Data curation, Formal analysis, Methodology, Visualization, Investigation, Validation, Writing - original draft, Writing - review & editing. **Geir Halnes:** Conceptualization, Methodology, Supervision, Writing - review & editing. **Espen Hagen:** Conceptualization, Software, Methodology, Supervision, Writing - review & editing. **Donald J. Hagler Jr.:** Conceptualization, Methodology, Software, Supervision, Writing - review & editing. **Anders M. Dale:** Conceptualization, Methodology, Supervision, Writing - review & editing. **Gaute T. Einevoll:** Conceptualization, Methodology, Funding acquisition, Project administration, Supervision, Resources, Writing - review & editing. **Torbjørn V. Ness:** Conceptualization, Data curation, Formal analysis, Methodology, Project administration, Supervision, Software, Visualization, Validation, Writing - original draft, Writing - review & editing.

Acknowledgements

This work received funding from the European Union Horizon 2020 Research and Innovation Programme under Grant Agreement No. 785907 and No. 945539 [Human Brain Project (HBP) SGA2 and SGA3], the Norwegian Ministry of Education and Research through the SUURPh Programme and the Norwegian Research Council (NFR) through COBRA (No. 250128), NOTUR (No. NN4661K) and DigiBrain (No: 248828).

References

Ahlfors, S.P., Wreh II, C., 2015. Modeling the effect of dendritic input location on MEG and EEG source dipoles. Med. Biol. Eng. Comput. 53 (9), 879–887. doi:10.1007/s11517-015-1296-5.

Arkhipov, A., Gouwens, N.W., Billeh, Y.N., Gratiy, S., Iyer, R., Wei, Z., Xu, Z., Abbasi-Asl, R., Berg, J., Buice, M., Cain, N., da Costa, N., de Vries, S., Denman, D., Durand, S., Feng, D., Jarsky, T., Lecoq, J., Lee, B., Li, L., Mihalas, S., Ocker, G.K., Olsen, S.R., Reid, R.C., Soler-Llavina, G., Sorensen, S.A., Wang, Q., Waters, J., Scanziani, M., Koch, C., 2018. Visual physiology of the layer 4 cortical circuit in silico. PLoS Comput. Biol. 14 (11), e1006535. doi:10.1371/journal.pcbi.1006535.

Billeh, Y.N., Cai, B., Gratiy, S.L., Dai, K., Iyer, R., Gouwens, N.W., Abbasi-Asl, R., Jia, X., Siegle, J.H., Olsen, S.R., Koch, C., Mihalas, S., Arkhipov, A., 2020. Systematic integration of structural and functional data into multi-scale models of mouse primary visual cortex. Neuron 106, 1–16. doi:10.2139/ssrn.3416643.

Binzegger, T., Douglas, R.J., Martin, K.A.C., 2004. A quantitative map of the circuit of cat primary visual cortex.. J. Neurosci. 24 (39), 8441–8453. doi:10.1523/JNEUROSCI.1400-04.2004.

Blomquist, P., Devor, A., Indahl, U.G., Ulbert, I., Einevoll, G.T., Dale, A.M., 2009. Estimation of thalamocortical and intracortical network models from joint thalamic single-electrode and cortical laminar-electrode recordings in the rat barrel system. PLoS Comput. Biol. 5 (3). doi:10.1371/journal.pcbi.1000328.

Bojak, I., Oostendorp, T.F., Reid, A.T., Kötter, R., 2010. Connecting mean field models of neural activity to EEG and fMRI data. Brain Topogr. 23 (2), 139–149. doi:10.1007/s10548-010-0140-3.

Brunel, N., 2000. Dynamics of sparsely connected networks of excitatory and inhibitory neurons. J. Comput. Neurosci. 8, 183–208.

Bruyns-Haylett, M., Luo, J., Kennerley, A.J., Harris, S., Boorman, L., Milne, E., Vautrelle, N., Hayashi, Y., Whalley, B.J., Jones, M., Berwick, J., Riera, J., Zheng, Y., 2017. The neurogenesis of P1 and N1: a concurrent EEG/LFP study. NeuroImage 146, 575–588. doi:10.1017/CBO9781107415324.004.

Buzsáki, G., Anastassiou, C.A., Koch, C., 2012. The origin of extracellular fields and currents–EEG, ECoG, LFP and spikes.. Nat. Rev. Neurosci. 13 (6), 407–420. doi:10.1038/nrn3241.

Carnevale, N.T., Hines, M.L., 2006. The NEURON Book. Cambridge University Press, Cambridge.

Chatzikalymniou, A.P., Skinner, F.K., 2018. Deciphering the contribution of oriens-lacunosum/ moleculare (OLM) cells to intrinsic θ rhythms using biophysical local field potential (LFP) models. eNeuro 5 (4). doi:10.1523/ENEURO.0146-18.2018.

Cohen, M.X., 2017. Where does EEG come from and what does it mean? Trends Neurosci. 40 (4), 208–218. doi:10.1016/j.tins.2017.02.004.

Coombes, S., 2006. Neural fields. Scholarpedia 1 (6), 1373. doi:10.4249/scholarpedia.1373. Revision #138631

Dale, A.M., Fischl, B., Sereno, M.I., 1999. Cortical surface-based analysis segmentation, I reconstruction, surface. NeuroImage 9, 179–194.

David, O., Friston, K.J., 2003. A neural mass model for MEG/EEG: coupling and neuronal dynamics. NeuroImage 20 (3), 1743–1755. doi:10.1016/j.neuroimage.2003.07.015.

Deco, G., Jirsa, V.K., Robinson, P.A., Breakspear, M., Friston, K., 2008. The dynamic brain: from spiking neurons to neural masses and cortical fields. PLoS Comput. Biol. 4 (8). doi:10.1371/journal.pcbi.1000092.

Dmochowski, J.P., Koessler, L., Norcia, A.M., Bikson, M., Parra, L.C., 2017. Optimal use of eeg recordings to target active brain areas with transcranial electrical stimulation. NeuroImage 157 (May), 69–80. doi:10.1016/j.neuroimage.2017.05.059.

Egger, R., Dercksen, V.J., Udvary, D., Hege, H.-C., Oberlaender, M., 2014. Generation of dense statistical connectomes from sparse morphological data. Front. Neuroanat. 8 (November), 1–18. doi:10.3389/fnana.2014.00129.

Einevoll, G.T., Destexhe, A., Diesmann, M., Grün, S., Jirsa, V., de Kamps, M., Migliore, M., Ness, T.V., Plesser, H.E., Schürmann, F., 2019. The scientific case for brain simulations. Neuron 102, 735–744. doi:10.1016/j.neuron.2019.03.027.

Einevoll, G.T., Kayser, C., Logothetis, N.K., Panzeri, S., 2013. Modelling and analysis of local field potentials for studying the function of cortical circuits. Nat. Rev. Neurosci. 14.

Einevoll, G.T., Lindén, H., Tetzlaff, T., Łęski, S., Pettersen, K.H., (Ed), R.Q.Q., (Ed), S.P., 2013. Principles of Neural Coding, Local Field Potentials Biophysical Origin and Analysis. CRC Press, Florida.

Einevoll, G.T., Pettersen, K.H., Devor, A., Ulbert, I., Halgren, E., Dale, A.M., 2007. Laminar population analysis: estimating firing rates and evoked synaptic activity from multielectrode recordings in rat barrel cortex.. J. Neurophysiol. 97 (3), 2174–2190. doi:10.1152/jn.00845.2006.

Eyal, G., Verhoog, M.B., Testa-Silva, G., Deitcher, Y., Benavides-Piccione, R., DeFelipe, J., De Kock, C.P., Mansvelder, H.D., Segev, I., 2018. Human cortical pyramidal neurons: from spines to spikes via models. Front. Cell. Neurosci. 12, 181.

Eyal, G., Verhoog, M.B., Testa-Silva, G., Deitcher, Y., Lodder, J.C., Benavides-Piccione, R., Morales, J., DeFelipe, J., de Kock, C.P., Mansvelder, H.D., Segev, I., 2016. Unique membrane properties and enhanced signal processing in human neocortical neurons. e-Life.

Freestone, D.R., Karoly, P.J., Peterson, A.D., Kuhlmann, L., Lai, A., Goodarzy, F., Cook, M.J., 2015. Seizure prediction: science fiction or soon to become reality? Curr. Neurol. Neurosci. Rep. 15 (11). doi:10.1007/s11910-015-0596-3.

Gentet, L.J., Stuart, G.J., Clements, J.D., 2000. Direct measurement of specific membrane capacitance in neurons. Biophys. J. 79 (1), 314–320.

Gramfort, A., Luessi, M., Larson, E., Engemann, D.A., Strohmeier, D., Brodbeck, C., Parkkonen, L., Hämäläinen, M.S., 2014. MNE software for processing MEG and EEG data. NeuroImage 86, 446–460. doi:10.1016/j.neuroimage.2013.10.027.

Gratiy, S.L., Billeh, Y.N., Dai, K., Mitelut, C., Feng, D., Gouwens, N.W., Cain, N., Koch, C., Anastassiou, C.A., Arkhipov, A., 2018. BioNet: a Python interface to NEURON for modeling large-scale networks. PLoS One 13 (8), e0201630. doi:10.1371/journal.pone.0201630.

Griffiths, D.J., 1999. Introduction to Electromagnetism 10, P429.

Hagen, E., Dahmen, D., Stavrinou, M.L., Lindén, H., Tetzlaff, T., Van Albada, S.J., Grün, S., Diesmann, M., Einevoll, G.T., 2016. Hybrid scheme for modeling local field potentials from point-neuron networks. Cereb. Cortex 26 (12), 4461–4496. doi:10.1093/cercor/bhw237.

Hagen, E., Næss, S., Ness, T.V., Einevoll, G.T., 2018. Multimodal modeling of neural network activity: computing LFP, ECoG, EEG and MEG signals with LFPy 2.0. Front. Neuroinform. 12 (92). doi:10.3389/fninf.2018.00092.

Hagen, E., Næss, S., Ness, T.V., Einevoll, G.T., 2019. LFPy - multimodal modeling of extracellular neuronal recordings in Python. In: Encyclopedia of Computational Neuroscience. Springer, New York, NY, p. 620286. doi:10.1007/978-1-4614-7320-6_100681-1.

Hämäläinen, M., Haari, R., Ilmoniemi, R.J., Knuutila, J., Lounasmaa, O.V., 1993. Magnetoencephalography – theory, instrumentation, and application to noninvasive studies of the working human brain. Rev. Modern Phys. 65.

Haufe, S., Huang, Y., Parra, L.C., 2015. A highly detailed FEM volume conductor model based on the ICBM152 average head template for EEG source imaging and TCS targeting. Conf. Proc. IEEE Eng. Med. Biol. Soc. 2015, 5744–5747.

Hay, E., Hill, S., Schürmann, F., Markram, H., Segev, I., 2011. Models of neocortical layer 5b pyramidal cells capturing a wide range of dendritic and perisomatic active properties. PLoS Comput. Biol. 7 (7).

Holt, G.R., Koch, C., 1999. Electrical interactions via the extracellular potential near cell bodies. J. Comput. Neurosci. 6.

Huang, Y., Dmochowski, J.P., Su, Y., Datta, A., Rorden, C., Parra, L.C., 2013. Automated MRI segmentation for individualized modeling of current flow in the human head. J. Neural Eng. 10 (6), 066004.

Huang, Y., Parra, L.C., 2015. Fully automated whole-head segmentation with improved smoothness and continuity, with theory reviewed. PLoS One 10 (5), 1–34. doi:10.1371/journal.pone.0125477.

Huang, Y., Parra, L.C., Haufe, S., 2016. The New York Head–A precise standardized volume conductor model for EEG source localization and tES targeting. NeuroImage 140, 150–162. doi:10.1016/j.neuroimage.2015.12.019.

Ilmoniemi, R.J., Sarvas, J., 2019. Brain Signals: Physics and Mathematics of MEG and EEG. MIT Press.

Jackson, J.D., 1998. Classical Electrodynamics, third ed. Wiley.

Jirsa, V.K., Jantzen, K.J., Fuchs, A., Kelso, J.A., 2002. Spatiotemporal forward solution of the EEG and MEG using network modeling. IEEE Trans. Med. Imaging 21 (5), 493–504. doi:10.1109/TMI.2002.1009385.

Jones, S.R., Pritchett, D.L., Sikora, M.a., Stufflebeam, S.M., Hämäläinen, M., Moore, C.I., 2009. Quantitative analysis and biophysically realistic neural modeling of the MEG mu rhythm: rhythmogenesis and modulation of sensory-evoked responses.. J. Neurophysiol. 102 (6), 3554–3572. doi:10.1152/jn.00535.2009.

Jones, S.R., Pritchett, D.L., Stufflebeam, S.M., Hämäläinen, M., Moore, C.I., 2007. Neural correlates of tactile detection: a combined magnetoencephalography and biophysically based computational modeling study. J. Neurosci. 27 (40), 10751–10764. doi:10.1523/JNEUROSCI.0482-07.2007.

Kalmbach, B.E., Buchin, A., Long, B., Close, J., Nandi, A., Miller, J.A., Bakken, T.E., Hodge, R.D., Chong, P., de Frates, R., Dai, K., Maltzer, Z., Nicovich, P.R., Keene, C.D., Silbergeld, D.L., Gwinn, R.P., Cobbs, C., Ko, A.L., Ojemann, J.G., Koch, C., Anastassiou, C.A., Lein, E.S., Ting, J.T., 2018. h-Channels contribute to divergent intrinsic membrane properties of supragranular pyramidal neurons in human versus mouse cerebral cortex. Neuron 100 (5), 1194–1208.e5. doi:10.1016/j.neuron.2018.10.012.

Klimesch, W., Doppelmayr, M., Russegger, H., Pachinger, T., Schwaiger, J., 1998. Induced alpha band power changes in the human EEG and attention. Neurosci. Lett. 244 (2), 73–76. doi:10.1016/S0304-3940(98)00122-0.

Koch, C., 1999. Biophysics of Computation. Oxford Univ Press, Oxford.

Light, G.A., Näätänen, R., 2013. Mismatch negativity is a breakthrough biomarker for understanding and treating psychotic disorders. PNAS 110 (38), 15175–15176. doi:10.1073/pnas.1313287110.

Lindén, H., Pettersen, K.H., Einevoll, G.T., 2010. Intrinsic Dendritic Filtering Gives Low–pass Power Spectra of Local Field Potentials. J. Comput. Neurosci. 29, 423–444.

Linssen, C., Lepperød, M. E., Mitchell, J., Pronold, J., Eppler, J. M., Keup, C., Peyser, A., Kunkel, S., Weidel, P., Nodem, Y., Terhorst, D., Deepu, R., Deger, M., Hahne, J., Sinha, A., Antonietti, A., Schmidt, M., Paz, L., Garrido, J., Ippen, T., Riquelme, L., Serenko, A., Kühn, T., Kitayama, I., Møk, H., Spreizer, S., Jordan, J., Krishnan, J., Senden, M., Hagen, E., Shusharin, A., Vennemo, S. B., Rodarie, D., Morrison, A., Graber, S., Schuecker, J., Diaz, S., Zajzon, B., Plesser, H. E., 2018. Nest 2.16.0. 10.5281/zenodo.1400175

Logg, A., Mardal, K.-a., Wells, G.N., 2012. Automated solution of differential equations by the finite element method. Vol. 84 of Lecture Notes in Computational Science and Engineering. Springer, Berlin, Heidelberg doi:10.1007/978-3-642-23099-8.

Lopes da Silva, F., 2013. EEG and MEG: relevance to neuroscience. Neuron 80 (5), 1112–1128. doi:10.1016/j.neuron.2013.10.017.

Luo, J., Macias, S., Ness, T.V., Einevoll, G.T., Zhang, K., Moss, C.F., 2018. Neural timing of stimulus events with microsecond precision. PLoS Biol. 16 (10), 1–22.

Mainen, Z.F., Sejnowski, T.J., 1996. Influence of dendritic structure on firing pattern in model neocortical neurons. Nature 382.

Mäki-Marttunen, T., Kaufmann, T., Elvsåshagen, T., Devor, A., Djurovic, S., Westlye, L.T., Linne, M.-l., Rietschel, M., Schubert, D., Borgwardt, S., Efrim-budisteanu, M., Bettella, F., Halnes, G., Hagen, E., 2019. Biophysical psychiatry–how computational neuroscience can help to understand the complex mechanisms of mental disorders. Front. Psychiatry 10 (534), 1–14. doi:10.3389/fpsyt.2019.00534.

Mäki-Marttunen, T., Krull, F., Bettella, F., Hagen, E., Næss, S., Ness, T.V., Moberget, T., Elvsåshagen, T., Metzner, C., Devor, A., et al., 2019. Alterations in schizophrenia-associated genes can lead to increased power in delta oscillations. Cereb. Cortex 29 (2), 875–891.

Malmivuo, J., Plonsey, R., 1995. Bioelectromagnetism - Principles and Applications of Bioelectric and Biomagnetic Fields. Oxford University Press.

Markram, H., Muller, E., Ramaswamy, S., Reimann, M.W., Abdellah, M., Sanchez, C.A., Ailamaki, A., Alonso-Nanclares, L., Antille, N., Arsever, S., Kahou, G.A.A., Berger, T.K., Bilgili, A., Buncic, N., Chalimourda, A., Chindemi, G., Courcol, J.-D., Delalondre, F., Delattre, V., Druckmann, S., Dumusc, R., Dynes, J., Eilemann, S., Gal, E., Gevaert, M.E., Ghobril, J.-P., Gidon, A., Graham, J.W., Gupta, A., Haenel, V., Hay, E., Heinis, T., Hernando, J.B., Hines, M., Kanari, L., Keller, D., Kenyon, J., Khazen, G., Kim, Y., King, J.G., Kisvarday, Z., Kumbhar, P., Lasserre, S., Le Bé, J.-V., Magalhães, B.R., Merchán-Pérez, A., Meystre, J., Morrice, B.R., Muller, J., Muñoz-Céspedes, A., Muralidhar, S., Muthurasa, K., Nachbaur, D., Newton, T.H., Nolte, M., Ovcharenko, A., Palacios, J., Pastor, L., Perin, R., Ranjan, R., Riachi, I., Rodríguez, J.-R., Riquelme, J.L., Rössert, C., Sfyrakis, K., Shi, Y., Shillcock, J.C., Silberberg, G., Silva, R., Tauheed, F., Telefont, M., Toledo-Rodriguez, M., Tränkler, T., Van Geit, W., Díaz, J.V., Walker, R., Wang, Y., Zaninetta, S.M., DeFelipe, J., Hill, S.L., Segev, I., Schürmann, F., 2015. Reconstruction and simulation of neocortical microcircuitry. Cell 163 (2), 456–492. doi:10.1016/j.cell.2015.09.029.

Mazzoni, A., Lindèn, H., Cuntz, H., Lansner, A., Panzeri, S., Einevoll, G.T., 2015. Computing the Local Field Potential (LFP) from integrate-and-fire network models. PLOS Comput. Biol. 11 (12), e1004584. doi:10.1371/journal.pcbi.1004584.

McColgan, T., Liu, J., Kuokkanen, P.T., Carr, C.E., Wagner, H., Kempter, R., 2017. Dipolar extracellular potentials generated by axonal projections. eLife 6, e26106. doi:10.7554/eLife.26106.

Miceli, S., Ness, T.V., Einevoll, G.T., Schubert, D., 2017. Impedance Spectrum in Cortical Tissue: Implications for Propagation of LFP Signals on the Microscopic Level. eNeuro 4 (1), 1–15.

Murakami, S., Hirose, A., Okada, Y.C., 2003. Contribution of ionic currents to magnetoencephalography (MEG) and electroencephalography (EEG) signals generated by guinea-pig CA3 slices.. Jo. Physiol. 553 (Pt 3), 975–985. doi:10.1113/jphysiol.2003.051144.

Murakami, S., Okada, Y., 2006. Contributions of principal neocortical neurons to magnetoencephalography and electroencephalography signals.. J. Physiol. 575 (Pt 3), 925–936. doi:10.1113/jphysiol.2006.105379.

Murakami, S., Zhang, T., Hirose, a., Okada, Y.C., 2002. Physiological origins of evoked magnetic fields and extracellular field potentials produced by guinea-pig CA3 hippocampal slices. J. Physiol. 544 (1), 237–251. doi:10.1113/jphysiol.2002.027094.

Ness, T.V., Chintaluri, C., Potworowski, J., Łęski, S., Głąbska, H., Wójcik, D.K., Einevoll, G.T., 2015. Modelling and analysis of electrical potentials recorded in microelectrode arrays (MEAs). Neuroinformatics 13 (4), 403–426. doi:10.1007/s12021-015-9265-6.

Ness, T. V., Halnes, G., Næss, S., Pettersen, K. H., Einevoll, G. T., 2020. Computing extracellular electric potentials from neuronal simulations. arXiv 2006.16630.

Ness, T.V., Remme, M.W.H., Einevoll, G.T., 2016. Active subthreshold dendritic conductances shape the local field potential. J. Physiol. 594 (13), 3809–3825. doi:10.1113/JP272022.

Ness, T.V., Remme, M.W.H., Einevoll, G.T., 2018. h-type membrane current shapes the local field potential from populations of pyramidal neurons. J. Neurosci. 38 (26), 6011–6024. doi:10.1523/JNEUROSCI.3278-17.2018.

Neymotin, S.A., Daniels, D.S., Caldwell, B., McDougal, R.A., Carnevale, N.T., Jas, M., Moore, C.I., Hines, M.L., Hämäläinen, M., Jones, S.R., 2020. Human Neocortical Neurosolver (HNN), a new software tool for interpreting the cellular and network origin of human MEG/EEG data. eLife 9, e51214.

Niedermeyer, E., 2003. The clinical relevance of EEG interpretation. Clin. Electroencephalogr. 34 (3), 93–98. doi:10.1177/155005940303400303.

Nunez, P.L., Srinivasan, R., 2006. Electric Fields of the Brain, second ed. Oxford University Press, New York.

Næss, S., Chintaluri, C., Ness, T.V., M.Dale, A., Einevoll, G.T., Wójcik, D., 2017. Four–sphere head model for EEG signals revisited. Front. Hum. Neurosci..

Palva, S., Palva, J.M., 2011. Functional roles of alpha-band phase synchronization in local and large-scale cortical networks. Front. Psychol. 2 (SEP), 1–15. doi:10.3389/fpsyg.2011.00204.

Pesaran, B., Vinck, M., Einevoll, G.T., Sirota, A., Fries, P., Siegel, M., Truccolo, W., Schroeder, C.E., Srinivasan, R., 2018. Investigating large-scale brain dynamics using field potential recordings: analysis and interpretation. Nat. Neurosci. 21, 903–919. doi:10.1038/s41593-018-0171-8.

Pettersen, K., Lindén, H., Tetzlaff, T., Einevoll, G.T., 2014. Power laws from linear neuronal cable theory: Power spectral densities of the soma potential, soma membrane current and single-neuron contribution to the EEG. PLoS Comput. Biol. 10.

Pettersen, K.H., Devor, A., Ulbert, I., Dale, A.M., Einevoll, G.T., 2006. Current-source density estimation based on inversion of electrostatic forward solution: effects of finite extent of neuronal activity and conductivity discontinuities.. J. Neurosci. Methods 154 (1–2), 116–133. doi:10.1016/j.jneumeth.2005.12.005.

Pettersen, K.H., Einevoll, G.T., 2008. Amplitude variability and extracellular low-pass filtering of neuronal spikes. Biophys. J. 94.

Pettersen, K.H., Lindén, H., Dale, A.M., Einevoll, G.T., 2012. Extracellular spikes and CSD. Handb. Neural Act. Meas..

Pfurtscheller, G., Cooper, R., 1975. Frequency dependence of the transmission of the EEG from cortex to scalp. Electroencephalogr. Clin.Neurophysiol. 38 (1), 93–96. doi:10.1016/0013-4694(75)90215-1.

Potjans, T.C., Diesmann, M., 2014. The cell-type specific cortical microcircuit: relating structure and activity in a full-scale spiking network model.. Cereb. Cortex 24 (3), 785–806. doi:10.1093/cercor/bhs358.

Ranta, R., Le Cam, S., Tyvaert, L., Louis-Dorr, V., 2017. Assessing human brain impedance using simultaneous surface and intracerebral recordings. Neuroscience 343, 411–422. doi:10.1016/j.neuroscience.2016.12.013.

Reimann, M.W., Anastassiou, C.A., Perin, R., Hill, S.L., Markram, H., Koch, C., 2013. A biophysically detailed model of neocortical local field potentials predicts the critical role of active membrane currents. Neuron 79 (2), 375–390. doi:10.1016/j.neuron.2013.05.023.

Reimann, M.W., Gevaert, M., Shi, Y., Lu, H., Markram, H., Muller, E., 2019. A null model of the mouse whole-neocortex micro-connectome. Nat. Commun. 10 (3903), 1–38.

Ritter, P., Schirner, M., Mcintosh, A.R., Jirsa, V.K., 2013. The virtual brain integrates computational modeling and multimodal neuroimaging. Brain Connect. 3 (2), 121–145. doi:10.1089/brain.2012.0120.

Rogers, N., Thunemann, M., Devor, A., Gilja, V., 2020. Impact of brain surface boundary conditions on electrophysiology and implications for electrocorticography. Front. Neurosci. 14 (763). doi:10.3389/fnins.2020.00763.

Rush, S., Driscoll, D.A., 1969. EEG electrode sensitivity - an application of reciprocity. IEEE Trans. Biomed. Eng. BME-16 (1), 15–22.

Sahin, M., Jones, S.R., Sweeney, J.A., Berry-Kravis, E., Connors, B.W., Ewen, J.B., Hartman, A.L., Levin, A.R., Potter, W.Z., Mamounas, L.A., 2019. Discovering translational biomarkers in neurodevelopmental disorders. Nat. Rev. Drug Discov. 18, 235–236. doi:10.1038/d41573-018-00010-7.

Sanz-Leon, P., Knock, S.A., Spiegler, A., Jirsa, V.K., 2015. Mathematical framework for large-scale brain network modeling in The Virtual Brain. NeuroImage 111, 385–430. doi:10.1016/j.neuroimage.2015.01.002.

Sanz-Leon, P., Knock, S.A., Woodman, M.M., Domide, L., Mersmann, J., Mcintosh, A.R., Jirsa, V., 2013. The Virtual Brain: a simulator of primate brain network dynamics. Front. Neuroinform. 7 (10). doi:10.3389/fninf.2013.00010.

Schmidt, M., Bakker, R., Shen, K., Bezgin, G., Diesmann, M., van Albada, S.J., 2018. A multi-scale layer-resolved spiking network model of resting-state dynamics in macaque visual cortical areas. PLoS Comput. Biol. 14, 1–38. doi:10.1371/journal.pcbi.1006359.

Senk, J., Hagen, E., van Albada, S. J., Diesmann, M., 2018. Reconciliation of weak pairwise spike-train correlations and highly coherent local field potentials across space. arXiv, 1–44. http://arxiv.org/abs/1805.10235

Seo, H., Kim, D., Jun, S.C., 2016. Effect of anatomically realistic full-head model on activation of cortical neurons in subdural cortical stimulation-a computational study. Sci. Rep. 6 (May), 1–12. doi:10.1038/srep27353.

Siegel, M., Donner, T.H., Engel, A.K., 2012. Spectral fingerprints of large-scale neuronal interactions. Nat. Rev. Neurosci. 13 (2), 121–134. doi:10.1038/nrn3137.

Skaar, J.-E.W., Stasik, A.J., Hagen, E., Ness, T.V., Einevoll, G.T., 2020. Estimation of neural network model parameters from local field potentials (LFPs). PLoS Comput. Biol. 16 (3), e1007725. doi:10.1101/564765.

Sliva, D.D., Black, C.J., Bowary, P., Agrawal, U., Santoyo, J.F., Philip, N.S., Greenberg, B.D., Moore, C.I., Jones, S.R., 2018. A prospective study of the impact of transcranial alternating current stimulation on EEG correlates of somatosensory perception. Front. Psychol. 9 (NOV), 1–17. doi:10.3389/fpsyg.2018.02117.

Srinivasan, R., Nunez, P.L., Silberstein, R.B., 1998. Spatial filtering and neocortical dynamics: estimates of EEG coherence. IEEE Trans. Biomed. Eng..

Sterratt, D., Graham, B., Gillies, A., Willshaw, D., 2011. Principles of Computational Modeling in Neuroscience. Cambridge University Press, Cambridge.

Suzuki, M., Larkum, M.E., 2017. Dendritic calcium spikes are clearly detectable at the cortical surface. Nat. Commun. 8 (276), 1–10. doi:10.1038/s41467-017-00282-4.

Teleńczuk, B., Baker, S.N., Kempter, R., Curio, G., 2015. Correlates of a single cortical action potential in the epidural EEG. NeuroImage 109, 357–367. doi:10.1016/j.neuroimage.2014.12.057.

Teleńczuk, B., Quyen, M.L.V., Cash, S.S., Hatsopoulos, N.G., Destexhe, A., Neurosciences, D., National, C., Recherche, D., 2017. Local field potentials primarily reflect inhibitory neuron activity in human and monkey cortex. Sci. Rep. 7 (40211), 1–16. doi:10.1101/052282.

Teleńczuk, B., Telenczuk, M., Destexhe, A., 2020. A kernel-based method to calculate local field potentials from networks of spiking neurons. J. Neurosci Methods 344, 108871.

Teleńczuk, M., Teleńczuk, B., Destexhe, A., 2020. Modelling unitary fields and the single-neuron contribution to local field potentials in the hippocampus. J Physiol 598, 3957–3972.

Uhlirova, H., Kilic, K., Tian, P., Sakadz, S., Saisan, P.A., Gagnon, L., Thunemann, M., Nizar, K., Yasseen, M.A., Jr, D.J.H., Vandenberghe, M., Djurovic, S., Andreassen, O.A., Silva, G.A., Masliah, E., Kleinfeld, D., Vinogradov, S., Buxton, R.B., Einevoll, G.T., Boas, D.A., Dale, A.M., Devor, A., Devor, A., 2016. The roadmap for estimation of cell-type- specific neuronal activity from non-invasive measurements. Proc. R. Soc. Lond. Ser.B Biol. Sci. 371 (August). doi:10.1098/rstb.2015.0356.

Vermaas, M., Piastra, M.C., Oostendorp, T., Ramsey, N., Tiesinga, P.H.E., 2020. When to include ECoG electrode properties in volume conduction models. J. Neural Eng. doi:10.1088/1741-2552/abb11d.

Vorwerk, J., Cho, J.H., Rampp, S., Hamer, H., Knösche, T.R., Wolters, C.H., 2014. A guideline for head volume conductor modeling in EEG and MEG. NeuroImage 100, 590–607. doi:10.1016/j.neuroimage.2014.06.040.

Vorwerk, J., Hanrath, A., Wolters, C.H., Grasedyck, L., 2019. The multipole approach for EEG forward modeling using the finite element method. NeuroImage 201 (February), 116039. doi:10.1016/j.neuroimage.2019.116039.

Ziegler, E., Chellappa, S.L., Gaggioni, G., Ly, J.Q., Vandewalle, G., André, E., Geuzaine, C., Phillips, C., 2014. A finite-element reciprocity solution for EEG forward modeling with realistic individual head models. NeuroImage 103, 542–551. doi:10.1016/j.neuroimage.2014.08.056.

Appendices

Appendix A

Comments on the four-sphere model

A.1 Agreement with Cuffin, 1979

In Paper I, we compare the corrected analytical solution with the formulations by Srinivasan, 1998 [33] and Nunez and Srinivasan, 2006 [1]. Another solution of the four-sphere model, that only gives the electric potential on the scalp, is provided by Cuffin, 1979 [28]. We found that our solution agrees with the Cuffin, 1979-solution (see Figure A.1).

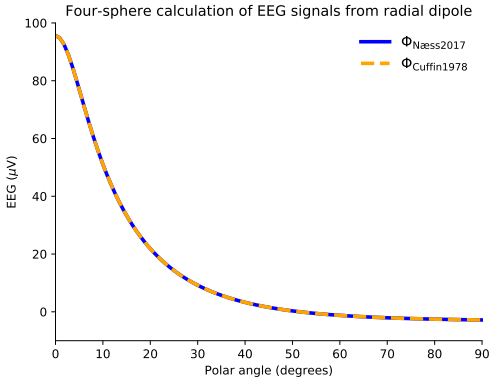

Fig A.1. Comparison of EEG calculations with four-sphere model solution by Cuffin and Cohen 1979. Radial dipole of size 10^{-7} Am at 7.8 cm above sphere center. Model parameters as in Paper 1.

A.2 Note on convergence

It is known that the four-sphere model can converge slowly for specific locations of the current dipole and the measurement electrode. By looking at the summation terms in Equation (5), (6), (17) and (18) in Paper III, we see that the following terms must all converge:

$$A_n^1 \left(\frac{r}{r_1}\right)^n n, \tag{A.1}$$

$$\left(\frac{r_z}{r}\right)^{n+1} n, \tag{A.2}$$

for the electrode location in the brain, $s = 1$, and

$$A_n^s \left(\frac{r}{r_s}\right)^n n, \tag{A.3}$$

$$B_n^s \left(\frac{r_s}{r}\right)^{n+1} n, \tag{A.4}$$

for $s = 2, 3, 4$. The convergence rate μ can be found as follows:

$$\mu = \lim_{n\to\infty} \frac{x_{n+1} - L}{x_n - L},$$

where $L = \lim_{n\to\infty} x_n$. For the terms listed above, we found two expressions: μ_1 for (A.1) and (A.3) and μ_2 for (A.2) and (A.4):

$$\mu_1 = \frac{r\ r_z}{r_s^2},$$

$$\mu_2 = \frac{r_\mathrm{z}}{r},$$

where $s = 1, 2, 3, 4$.

The four-sphere head model solution will converge slowly when μ_1 or μ_2 is close to 1. Looking at μ_2, we see that we will experience slow convergence if the measurement point r is close to the dipole location r_z. This should not really be a problem, since the current dipole approximation is not meant for computing electric potentials very close to the dipole. From μ_1, we see that the convergence is slow if the product $rr_z \sim r_s^2$. This confirms our experience with very slow convergence when the dipole is placed close to the brain surface, and the measurement location is close to the brain surface, that is either in brain tissue, or in the CSF layer. If the diameters of the different media are relatively similar, for example if the brain, CSF, skull and scalp diameters are unreasonably large, this can also lead to large μ_1 and slow convergence. To avoid slow convergence for the four-sphere model implementation in LFPy, we recommend to keep a 1 μm buffer between the current dipole moment and the brain surface, and between the electrode and any layer surface.

For approximations of multi-sphere models avoiding the slow convergence, see DeMunck, 1993 [30], Zhang, 1995 [31] and Sun, 1997 [32].